# ULTRAFAST SPECTROSCOPY OF WIDE BANDGAP SEMICONDUCTOR NANOSTRUCTURES

THÈSE N$^{O}$ 6713 (2015)

PRÉSENTÉE LE 25 AOÛT 2015

À LA FACULTÉ DES SCIENCES DE BASE
LABORATOIRE D'OPTOÉLECTRONIQUE QUANTIQUE
PROGRAMME DOCTORAL EN PHOTONIQUE

ÉCOLE POLYTECHNIQUE FÉDÉRALE DE LAUSANNE

POUR L'OBTENTION DU GRADE DE DOCTEUR ÈS SCIENCES

PAR

Mehran SHAHMOHAMMADI

acceptée sur proposition du jury:

Prof. H. P. Herzig, président du jury
Prof. B. M. J. Deveaud, Dr J.-D. Ganière, directeurs de thèse
Prof. C. Weisbuch, rapporteur
Prof. . J. Christen, rapporteur
Prof. E. Matioli, rapporteur

ÉCOLE POLYTECHNIQUE
FÉDÉRALE DE LAUSANNE

Suisse
2015

An experiment is a question which science poses to Nature,
and a measurement is the recording of Nature's answer.
Max Planck

To my parents,
and
to my love.

# Acknowledgements

Without the help of countless people, this thesis would have not been possible. To all these people I owe my sincere gratitude.

First and foremost, I would like to thank my academic advisor, professor Benoît Deveaud, for the support and guidance he has provided me throughout my dissertation. His scientific intuitions and insights were always a shortcut path for me. He always gave me precise advices, but also the freedom to choose my research direction. Despite his very busy schedule, he had always a time slot on his calendar for me to meet and discuss my experimental results. I have always admired the positive and encouraging atmosphere he brought to our meetings, as well as his precise and carefully evaluating manner. I have truly learned a lot during my thesis, which goes beyond science itself. Thanks Benoît for all.

Then, I would like to thank my thesis co-supervisor, Dr. Jean-Daniel Ganière. It has been a great honor for me to work with him, with lots of experimental skills and ideas on CL spectroscopy. I enjoyed working closely with Jean-Daniel, as his last PhD student, on many different projects and research proposals.

I am eternally indebted to Dr. Gwénolé Jacopin, the ambitious and motivated postdoc, whom I worked with during my PhD. With his friendly, supportive, and motivated manner, he passed me his passion and knowledge. Indeed, he has a big share on all experimental and computational achievements in my thesis. In addition to the scientific side, he has also provided me with invaluable help in carefully planning and managing research projects. Working together and sharing so many adventures in the lab has simply been a great pleasure for me.

I am then much indebted and grateful to Dr. Pierre Corfdir for patiently guiding me in my first steps in the laboratory. From time to time, I had chance to meet him at EPFL or conferences, and to have fruitful discussions on my PhD results.

I would like to thank the members of my jury, prof. Claude Weisbuch, prof. Jürgen Christen, prof. Elison Matioli, and prof. Hans Peter Herzig for taking the time to review this dissertation and for providing valuable comments and discussions. It has been a great honor for me to have such a competent evaluation of my work.

I would like then to express my sincere gratitude to Nicolas (prof. Nicolas Grandjean), with whom I had the opportunity to have very close and fruitful collaborations. He provided me great insights into a different area, like for instance, the growth of nitrides. I truly enjoyed our many stimulating and interesting discussions. Moreover, It was my pleasure to collaborate with his group (LASPE) members, including Marlene, Etienne, Noelia, Jacques, and .... My special thanks goes to Lise (Dr. Lise Lahourcade) and Dr. Jean-François, for growing the state-of-the-art high quality samples during my PhD.

My special thanks go to Dr. Raphaël Butté for our long and fruitful discussions, that started from the beginning of my PhD. He indeed helped me a lot on our scientific discussions. With his precise and critical reading and reviewing my articles, he improved the quality of what we published together. I would like to express my sincere gratitude to Georg (Dr. Georg Rossbach), with whom I had the opportunity to have close and fruitful collaboration on the main part of my thesis. He was the most serious and at the same time friendly PhD student I met in my PhD. It has been a real pleasure to know you and work with you.

I owe many thanks to my coworkers from Attolight start-up, and especially Dr. Jean Berney, Dr. Samuel Sonderegger, and Dr. Malik Benameur for providing our lab a functional time resolved cathodoluminescence system, and for continuously developing and maintaining the system. I would like to thank all my colleagues and friends from Peking University, Dr. Xuewen Fu and prof. Dapeng Yu, for our collaboration on ZnO materials.

I am grateful to the members of LOEQ for the friendly, and unique scientific atmosphere I worked in during these last four years. Many thanks to LOEQ secretary, Claire Lyse, that without her, literally no one could do any thing in our lab. I would like to thank my current and former LOEQ colleagues: Claudéric, Fauzia, Albert, Naotomo, Verena, Roland, Mitchell, Grǵory, François, and Marc-André. I would like to specially thank Daniel and Marcia, our close family friends, with whom I felt not far from my family. I am grateful to my great officemates Mahmood and Wei for friendly and helpful discussions. It was really a pleasure to share office with you guys, and sometimes work in lab with you. I should thank Gwénolé, once again here, but this time for translating the English abstract to French résumé.

I would like to express as well my thanks to the technical staff: Nicolas Leiser, Yoan and Damien Trolliet, and Roger Rochat.

On the path to the world of research, I would like to thank my previous supervisor prof. Mohajer. Indeed, he had a serious impact on my previous and future carrier and life.

Outside of EPFL, I am grateful to my friends in Lausanne, with whom I shared lots of exciting, and enjoyable memories. I am also thankful to them for all their helps.

Last but not least, I wish to thank a special group of people. My deepest gratitude goes to my parents, for their unconditional love and endless support through all my life. I would like to thank my brothers (Mehdi and Mohsen), my sister (Negar), my brother-in-law (Hosein), and my parents-in-law as well.

Finally, I am grateful to Hadis, my love. Indeed, meeting her was the most influential event over my entire life. She enriched my life in many aspects, and gave me the real taste of enjoying my life. Her understanding, kindness, patience, support, and encouragement are only few minor things I can cite here. This work is dedicated to you.

*Lausanne, 7 July 2011*
Mehran Shahmohammadi

# Abstract

Group III-nitrides have been considered a promising choice for the realization of optoelectronic devices since 1970. Since the first demonstration of the high-brightness blue light-emitting diodes (LEDs) by Shuji Nakamura and coworkers, the fabrication of highly efficient white LEDs has passed successful developments. A serious physical issue still remained, which prevents their use for high power and highly efficient LEDs: the drop of external quantum efficiency (EQE) of III-nitride LEDs when increasing the driving current, the so-called ”efficiency droop” problem. In order to have a fast expansion to the lighting market, the cost-per-lumen of packaged LEDs must rapidly decrease. This indeed demands for having LED chips operating with high EQE under the high current operation.

Besides the industrial interest of III-nitrides, owing to their large direct bandgap, they feature some interesting optical properties such as large exciton binding energy and large oscillator strength of excitons. However, when the carrier density raised in a semiconductor, a transition should occur from an insulating state consisting of a gas of excitons to a conductive electron-hole plasma, that is called the Mott transition. This crossover can drastically affect the optical and electrical characteristics of semiconductors and may, for instance, drive the transition from a polariton laser to a vertical cavity surface-emitting laser. More interestingly, even if biexcitons are frequently seen to dominate the emission of III-nitride heterostructures when the density is raised, no clear experimental report is available on the role of biexcitons in the Mott transition in a two-dimensional (2D) nanostructure.

In the first part, the emission properties of high-quality GaN/AlGaN single quantum wells (QWs) at high-carrier densities are examined. They are of crucial importance to provide a deeper insight into the operating conditions of III-nitride based lasers and LEDs, as well as the transition from strong to weak coupling regime of exciton-polaritons in semiconductor microcavities. Employing the same technique then to investigate some InGaN/GaN QWs, the droop signature was investigated comprehensively in both polar and non-polar QWs. Having an accurate estimation of the carrier density in the QWs, the contribution of several non-radiative processes were quantitatively examined. These experiments can indeed provide a deeper insight on the physical phenomena responsible for the efficiency droop in III-nitride LEDs, and can stimulate several theoretical and experimental on this subject.

The second part focuses on the transport mechanisms of excitons in ZnO and III-nitride based nano-structures. The transverse movement of donor-bound excitons in a purely bent ZnO microwire as a function of temperature have been investigated, owing to the high spatial, spectral and temporal resolutions of our original time resolved cathodoluminescence system. The movement mechanism was modeled by a hopping process of excitons. Our results pave the way to new experiments allowing to reveal the physics at play at the nanoscale in different materials. However, in case of highly disordered systems, one should take into account more complex considerations, as in the case of InGaN core-shell QW structures studied in the last chapter, the large energy fluctuations prevent excitons to move along the energy gradient at low temperatures.

Key words: Gallium nitride, III-nitrides, quantum wells, external quantum efficiency, excitons, biexcitons, electron-hole plasma, Mott-transition, strong and weak coupling regime, polariton lasing, exciton binding energy, exciton oscillator strength, polar and non-polar QWs, ZnO, exciton hopping, core-shell QW structures, donor-bound excitons, pure bending.

# Résumé

Les nitrures d'éléments III ont été considérés comme un choix prometteur pour la réalisation de dispositifs optoélectroniques depuis 1970. Depuis la démonstration de la première LED bleue de forte luminosité par Shuji Nakamura et ses co-auteurs, la fabrication de LEDs blanches très efficaces a connu de très fructueux développements. Cependant, certains problèmes physiques persistent et empêchent la fabrication de LEDs extrêmement efficaces et puissantes. Une d'elles est particulièrement importante : la chute d'efficacité quantique externe (EQE) à haut courant d'injection. Afin d'avoir une croissance rapide du marché de l'éclairage, le coût par lumen des LEDs doît rapidement baisser dans les prochaines années ce qui demande d'avoir des LEDS fonctionnant avec une efficacité élevée à fort courant d'injection.

En plus de la large bande interdite des nitrures d'éléments III, qui intéressent les industriels, cette famille de matériaux se distingue par certaines propriétés optiques telles qu'une large énergie de liaison de l'exciton ainsi qu'une force d'oscillateur d'exciton importante. Cependant, lorsque la densité de porteurs augmente dans un semiconducteur, une transition doit se produire d'un état isolant consistant en un gaz d'excitons en un plasma conducteur d'électrons-trous, appelé la transition de Mott. Ce changement de phase peut drastiquement affecter les caractéristiques optiques et électriques des semiconducteurs et peut par exemple, conduire à une transition d'un laser à polaritons en un laser à cavité verticale émettant par la surface. Plus intéressant encore, si les biexcitons dominent souvent l'émission des hétérostructures d'éléments III quand la densité augmente, aucune expérience ne reporte le rôle des biexcitons dans la transition de Mott dans des nanostructures bidimensionnelles.

Dans une première partie, les propriétés d'émission de puits quantiques uniques GaN/AlGaN sous forte injection sont étudiées. Ces structures sont extrêmement intéressantes pour la compréhension des propriétés optiques des structures à microcavités et peut permettre une compréhension plus en détails des diodes laser et des LEDs ainsi que de la transition du régime de couplage fort à couplage faible des polaritons dans les microcavités semiconductrices. En employant la même technique pour des puits quantiques InGaN/GaN, la signature de la chute d'efficacité a été étudiée dans le cas de puits polaires et non-polaires. La contribution de différents processus non radiatifs a été estimée grâce à l'obtention d'une estimation précise de la densité de porteurs dans les puits quantiques. Cette partie de notre étude permet d'avoir une meilleure compréhension de l'origine de la chute d'éfficacité dans les nitrures d'éléments

III et peut stimuler d'autres travaux expérimentaux et théoriques sur le sujet.

La seconde partie s'intéresse aux mécanismes de transport des excitons dans les nanostructures de ZnO et de nitrures d'éléments III. Nous reportons pour la première fois l'observation directe du mouvement des excitons liés au donneur dans des microfils de ZnO purement en flexion en fonction de la température grâce aux hautes résolutions spatiales, temporelles et spectrales de notre système original de cathodoluminescence résolue en temps. Le mécanisme de ce mouvement a été étudié et modélisé par un mécanisme de saut des excitons. Nos conclusions sur l'étude de ce mouvement des excitons dans un champ de contrainte inhomogène doivent être générales et peuvent s'appliquer à la plupart des semiconducteurs à température cryogénique. Cependant, les résultats sur ce type de transport ne s'appliquent pas nécessairement aux systèmes désordonnés comme démontré dans le dernier chapitre pour le cas des hétérostructures cœur-coquille InGaN/GaN Dans ce cas, même en présence d'un gradient d'énergie le long du nanofil, les larges fluctuations d'énergie empêchent les excitons de se déplacer à basse température.

Mots clefs : Nitrure de Gallium, nitrure d'éléments III, puits quantiques, efficacité quantique externe, excitons, biexcitons, plasma électrons-trous, transition de Mott, condensat de polaritons, régime de couplage fort, laser à polaritons, condensation de Bose-Einstein, energie de liaison de l'exciton, force d'oscilateur d'exciton, puits quantiques polaires et non-polaires, ZnO, saut d'exciton, hétérostructures cœur-coquille, exciton lié à un donneur, flexion pure.

# Contents

# Introduction

To make an efficient light emitting device based on a semiconductor material, it should possesses three main characteristics: (i) an efficient radiative efficiency, (ii) an appropriate energy bandgap and (iii) efficient p- and n-type doping with low resistivities. In order to have light emitting devices in the blue range of visible spectrum, then, III-nitride materials have been considered as the most promising choice, since they fulfill all these all these criteria with success. Moreover, by means of alloying, their bandgap can span over a broad range of wavelengths from the ultra-violet (UV) down to the infrared (IR). In 1994 Nakamura *et al.* realized a breakthrough with the first candela-class blue InGaN-based light emitting device (LED) [1]. Since that time, IIII-nitrides have been considered for a broad range of applications from everyday-life technologies to specific industrial required equipments such as, e.g., domestic solid-state lighting devices or optical players and optical data storage devices. Therefore, III-nitrides became the second most important semiconductor family just after silicon as far as commercial devices are concerned. III-nitride LEDs have already saturated the LCD backlighting market, they started to penetrate to the general illumination market owing to their record luminous efficiencies. However, some physical issues remain unsolved, which prevent their use for high power and highly efficient LEDs. One of a peculiar importance is the drop of external quantum efficiency (EQE) of an LED at high driving currents, a problem that is so-called the ”efficiency droop”. In order to expand to the lighting market as projected by [2], the cost-per-lumen of packaged LEDs must rapidly decrease within the next few years. This requires being able to produce LED chips operating with high EQE at high driving currents.

Besides the largely tunable bandgap, effective p- and n-type doping, and highly efficient luminescence, that makes III-nitrides a promising candidate for industrial applications, they feature some interesting optical properties such as large exciton binding energy, and large oscillator strength of excitons. The observation of polariton condensation up to room temperature has already been realized in properly designed structures grown under optimal conditions [3, 4]. This makes III-nitrides the most promising candidate also for the realization of polariton laser diodes [5]. However, when raising the carrier density, a transition should occur from an insulating state consisting of a gas of excitons to a conductive electron-hole plasma, the so-called the Mott transition [6]. As the Mott transition marks the crossover between bosonic and fermionic nature of a system, a clearer and deeper insight into that is of crucial importance for description of multi-particle effects relying on the Bose-statistics [7, 8, 9]. For instance, in case of the polariton condensation, It can define the carrier density regime at which the transition occurs from a polariton laser to a vertical cavity surface-emitting laser [9, 10].

More interestingly, biexcitons are frequently observed to dominate the emission of the high quality III-nitride heterostructures when the density is raised [11, 12], thanks to the larger binding energy of these excitonic molecules in those heterostructures. Nevertheless, very few reports exist on the study on the crossover to the Mott transition in the presence of biexcitons in case of GaAs-based T-shape quantum wires[13, 14], no clear experimental report is available on the role of biexcitons in the Mott transition in a two-dimensional (2D) nanostructure.

A major part of this thesis is devoted to the investigation of the carrier dynamics III-nitride QWs with picosecond time resolved (tr) photoluminescence (PL) technique, and under high injection condition. We aim at the investigation on the evolution of the QW PL emission as a function of the carrier density. Several criteria have been examined to determine the carrier density at which the Mott transition occurs. We pay a particular attention to the role that can be played by biexcitons at the Mott transition. Afterwards, the same characterization techniques will be applied to InGaN/QW, in orders to investigate the droop of internal quantum efficiency (IQE) in those structures.

Additionally, semiconductors with reduced dimensionality have raised a huge interest of the scientific community for several years. This interest arises form the fact that in the low-dimensional semiconductors, one can vastly tune the electronic properties of confined electrons and holes. Moreover, some mechanical and optical properties of semiconductors are modified by reduction of their size [15]. For instance, strain becomes an unavoidable phenomenon and shows an enhanced impact on the properties of semiconductor nanostructures [16, 17, 18]. Therefore, a proper design of semiconductor devices based on the strain effect needs to fully account for the strain effects on the electronic and optical properties of the semiconductor nanostructures. To exemplify the importance that strain may have on the electro-optical properties in semiconductors we can point out the strain induced Stark shift of the emission energy in III-Nitride heterostructures [19], the strained silicon application in mobility enhanced transistors [18], and bandgap engineering of nanowires with core-shell structure with strain [20].

In this context, semiconductor nanowires are interesting for fundamental studies of strain effects, since a large range of both compressive and tensile strain can be applied to them by simply bending the nanowires without introducing dislocations, owing to their higher elastic strain limits [15]. Applying the large values of tensile strain is another advantage of micro/nanowires, while this is not easy to reach in bulk structures [21]. In fact, tensile strain in bulk structures can only be achieved in strained epitaxial layers, but is limited to small values. Recently, the mechanical-optical coupling properties of ZnO micro/nanowires have raised a huge interest for application in piezoelectric-optical devices as well as photon-mechanical devices [16].

In this context, we aim at investigating the dynamics of excitons in various wide bandgap semiconductor nanostructures by picosecond time resolved (tr) photoluminescence (PL) and cathodoluminescence (CL). These techniques allow us generating a population of hot excitons at a given part of a nanostructure and monitor their transport and energy relaxation. We will pay a particular interest to the transport of donor-bound excitons in presence of an energy gradient. In case of purely bent ZnO microwire, this energy gradient originates form the variation of the bandgap caused by the applied uniform strain gradient. Owing to the high spatial, spectral and temporal resolutions of our original tr-CL system, we can measure directly the speed of excitons created by pulsed electron beams. Moreover in some InGaN core-shell QW structures, we have investigated the exciton transport in presence of an energy field along the QW, caused by the In composition variation along the nanowire [22]. The large potential disorders, caused by the fluctuations of either In composition or the QW well thickness along the nanowire, modifies drastically the excitons transport along the energy gradient.

## Outline

The first part of the present work is devoted to the presentation of physical and optical properties of wide bandgap semiconductor materials, including III-nitride and ZnO materials, and the description of the spectroscopy techniques and tools employed to investigate their optical properties in this thesis.

- **Chapter 1: Wide bandgap materials.** The first chapter briefly presents the properties of III-nitride based semiconductors as well as ZnO semiconductors, including structural, optical and electrical ones. For heterostructures grown along the polar *c*-orientation, the impact of the built-in electric field is addressed.

- **Chapter 2: Experimental setups.** The second chapter deals with the details of the experimental setups used within this thesis. First the tr-PL system is introduced, which allows probing optical properties of nanostructures over a wide range of carrier densities with a temporal resolution of few picoseconds. Afterwards, the continuous wave (cw) CL and the tr-CL setups will be introduced.

The second part of the present work is devoted to the optical properties of III-nitride QWs under high injection condition.

- **Chapter 3: High injected GaN/AlGaN Quantum wells above the Mott transition.**

The content of this chapter deals with the PL investigation of single GaN/AlGaN QWs under high injection conditions. The state-of-the-art quality of the investigated sample as well as the large binding energy of exciton in these QWs allows observing the well-defined excitonic levels and probing the PL properties over a wide range of carrier densities and temperatures. A special attention is paid to the role of biexcitons at high injection densities. Afterwards, the temperature dependence of the Mott transition is discussed, with a main focus on determining the carrier density at which the Mott transition occurs and its dependence on temperature.

- **Chapter 4: Efficiency droop signature in III-Nitrides LEDs: a time resolved PL investigation on InGaN/GaN QWs.**

The content of this chapter deals with the tr-PL spectroscopy of InGaN/GaN QWs, in order to investigate the IQE in these QWs. The aim of this chapter is to provide a more clear picture of carrier dynamics in those QWs, when the injection density increases. First, some intrinsic differences in dynamics of the InGaN QWs and GaN QWs are highlighted. Then, the carrier dynamics in InGaN samples are discussed, with an attention to discriminate the role of several physical phenomena on the IQE. The experimental technique is the same as the one applied for GaN QWs in the previous chapter, which allows us determining accurately the carrier density in the QW, and hence have a quantitative estimation of various recombination rates in InGaN QWs under high injection condition.

The third part of the present work is devoted to the investigation of the exciton transport in ZnO and III-nitride semiconductor nanostructures by means of tr-CL techniques.

- **Chapter 5: Exciton hopping under a uniform strain gradient in ZnO microwires.**

This chapter deals with the exciton dynamics in bent ZnO microwires under a uniform strain gradient at low temperatures. Starting with the evidence of exciton movement under a strain gradient, it then focuses on a theoretical model to explain the mechanism of this movement, taking into account the fact that the majority of excitons are bound to donors at low temperatures in our samples. Eventually, the validity of the proposed model is examined by performing measurements on a sample with different design, and over a larger range of temperatures.

- **Chapter 6: Excitonic diffusion in InGaN/GaN core-shell nanowires.**

This chapter deals with an investigation of the carrier diffusion in a graded InGaN/GaN QW nanowire. Despite the presence of an energy gradient along the nanowire, the energy landscape stems from the localization centers preventing the long distance diffusion of carriers at low temperatures. The temperature dependence of the dynamics, however, shows that the exciton localization can be modified by a thermally activated relaxation into the deeper localized states. An analytical model based on an effective medium approximation was used to model the observed dynamics as a function of temperature.

In the last part of this manuscript, we finally provide a summary of our results, as well as perspectives for further investigations.

# 1 Wide band gap materials: III-nitride and ZnO

In this chapter we try to address the main optical, mechanical and electrical properties of the wide bandgap materials investigated in this thesis, i.e. III-nitrides and ZnO. Although the main focus in this chapter is III-nitrides, owing to the similarity of the crystalline structure of ZnO and III-nitrides, they share most of the presented properties. Therefore, in addition to the physical parameters for III-nitrides, we try also to provide those of ZnO. We pay a special attention to the presence of spontaneous polarization field along the $c$-axis in III-nitirdes, caused by the lack of inversion symmetry in their wurtzite cell.

## 1.1 Structural properties

### 1.1.1 Crystalline structure

A detailed description of the solid crystalline structure is of special interest as many of the material physical properties, such as electronic and mechanical ones, can be drawn from symmetry arguments by applying group theory. Any crystalline structure can be obtained by a periodic repetition of an elementary pattern (called base) in all three directions of space, by three primitive translation vectors labeled $\mathbf{a}_1$, $\mathbf{a}_2$ and $\mathbf{a}_3$. These repetitions of the basis by the primitive translation vectors generates a lattice, called Bravais lattice. Directions and planes in a crystal are expressed in this basis by a set of integers $h$, $k$ and $l$ called the Miller indices. Any vector $\mathbf{R}$ of the Bravais lattice can thus be expressed by $\mathbf{R} = h\mathbf{a}_1 + k\mathbf{a}_2 + l\mathbf{a}_3$.

Even if III-nitrides can crystallize in the zinc-blende structure [24] only the wurtzite one is thermodynamically stable. Its lattice corresponds to an hexagonal close packed (hcp) structure with a two-atom basis: the metal atoms $M \in [In, Ga, Al]$ are located at positions (0,0,0) and $(\frac{1}{3}, \frac{2}{3}, \frac{1}{2})$ and the N-atoms at $(\frac{1}{3}, \frac{2}{3}, u + \frac{1}{2})$ and $(0, 0, u)$ . Here, $u$ is the internal parameter, which defines the M-N bond length according to $\Delta(M - N) = u.c$, where $c$ is the distance between two equivalent planes in the stacking direction.

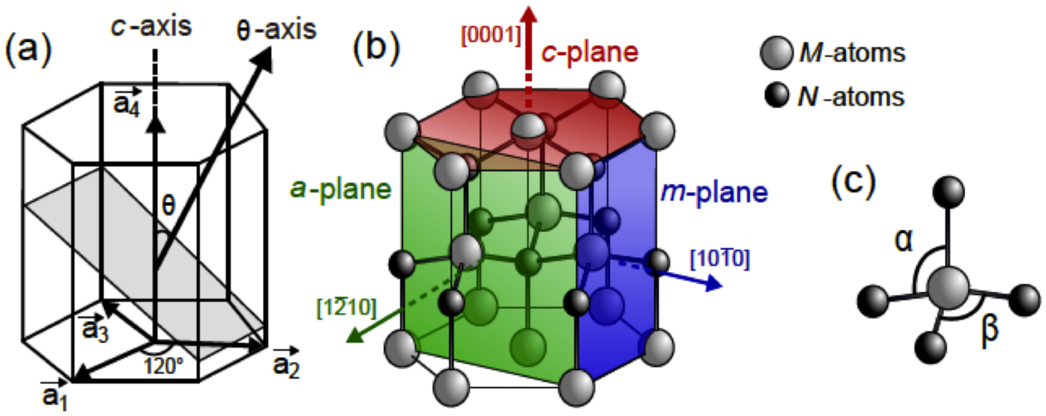

Figure 1.1 – **(a)** The basis of the Bravais cell for wurtzite structure ($a_1$, $a_2$, $a_3$, $a_4$). The gray plain represents a random semi-polar plain forming the angle of $\theta$ degree with the $c$-axis. **(b)** Metal (gray) and Nitrogen (black) atoms form a hexagonal close-packed sub-lattice. Each atom is surrounded tetrahedrally by four complementary atoms. **(c)** Angles between Nitrogen (N) and metal (M) atoms. Figure adapted from [23].

These four positions form the primitive unit cell for the entire wurtzite family and every vector of the wurtzite Bravais cell can be expressed in the basis ($\mathbf{a}_1, \mathbf{a}_2, \mathbf{a}_4$) (see Fig. 1.1(a)), where $\mathbf{a}_4$ is parallel to the high symmetry direction labeled as $c$-axis, and has a norm given by the lattice constant $c$. $\mathbf{a}_1$ and $\mathbf{a}_2$ have the same length and form an angle of 120° between them in the orthogonal plane. It is common to use a four-vector basis due to the hexagonal symmetry of the wurtzite cell, and introduce an additional in-plane vector $\mathbf{a}_3 = -(\mathbf{a}_1 + \mathbf{a}_2)$. In this basis, planes and directions are given by a four-index notation. Note that crystal planes are labeled as $(hklm)$ and directions as $[hklm]$.

The hcp 3D lattice can be seen as a stack of spheres arranged by hexagonal symmetry in plane. After the first plane (labeled as A) the second one (B) is deposited in order to minimize the total volume. This bilayer stack is then repeated to generate the full 3D-crystalline structure with the period sequence ABABAB... . Labeling a the distance between two adjacent spheres within a given layer, $a$, $c$ and $u$ constants in a perfect hcp structure satisfy the relations:

$$\begin{aligned} \frac{c}{a} &= \sqrt{\frac{8}{3}} \approx 1.633, \\ u &= \frac{3}{8} = 0.375. \end{aligned} \tag{1.1}$$

The two angles between the bonds in the tetrahedron, $\alpha$ and $\beta$ (see Fig. 1.1(c)), are equal in an ideal structure, i.e. $\alpha = \beta = 109.47°$. However, due to non-idealities in the as-grown samples

Table 1.1 – Lattice parameters for wurtzite GaN, InN, AlN, ,and ZnO at room temperature. Due to the iconicity of the bonding $u$ and $c/a$ parameters deviate from those of the ideal wurtzite cell. From [28, 29]

| | GaN | InN | AlN | ZnO | ideal |
|---|---|---|---|---|---|
| a | 3.189 | 3.545 | 3.112 | 3.249 | – |
| c | 5.185 | 5.703 | 4.982 | 5.206 | – |
| c/a | 1.6259 | 1.6087 | 1.6009 | 1.633 | 1.602 |
| u | 0.3769 | 0.3787 | 0.3814 | 0.375 | 0.382 |

and the strong ionicity of the bonds, these ideal values slightly differ from the experimentally observed for all ternary compounds of III-nitrides [25, 26, 27]. Table 1.1 summarize the lattice parameters for wurtzite GaN, InN, AlN, and ZnO at 300 K as well as the the parameters for an ideal wurtzite cell.

### 1.1.2 Crystalline orientation for growth of III-nitrides

Growth of III-nitride heterostructures along the $c$-axis possesses serious advantages due to its mature technology, and the availability of large-area substrates with a relatively low threading dislocation density ($\sim 10^5 - 10^6 cm^{-2}$). However, growth along other crystal orientations also attracted some interest due to their own advantages, despite a poorer crystalline quality. Recently, the research focuses mainly on three different types of crystal orientations:

• **The polar $c$-axis**: The $c$-axis is always referred to as the polar axis, due to the presence of spontaneous polarization along the growth direction. Thanks to the higher growth quality and in-plane isotropic properties, it is considered as the preferential growth axis for both academic and industrial purposes. However, the radiative efficiency of heterostructures is strongly impacted by spontaneous and piezoelectric polarization effects in the active medium. This effect, referred to as quantum confined Stark effect (see section 1.4.3), detrimentally affects the exciton oscillator strength and binding energy due to the separation of electron and hole wave-functions.

• **The non-polar axis (a-axes and m-axes)**: In contrast to $c$-plane case, growth along non-polar orientations allows to get rid of the quantum confined Stark effect, owing to the fact that the projection of the polarization along the growth direction is equal to zero [30, 31]. Moreover, due to the in-plane optical anisotropy, the emitted light is spontaneously polarized, which might present some advantages for devices such as liquid crystal display screens [32]. The use of non-polar grown heterostructures for LEDs has been considered as an alternative to reduce the carrier density in the active medium for a given driving current, thanks to the shorter radiative lifetime of carriers compared to their polar counterparts [33]. Eventually, non-polar orientations are very promising to reduce the threshold current density for UV laser diodes [34].

- **The semi-polar axes**: A last category of crystal orientation, which has recently attracted a lot of interest in the community is the semi-polar one, the intermediate situation of polar and non-polar case that seems very promising for the realization of LEDs and laser diodes in the green spectral range due to the higher indium incorporation that allows reaching longer wavelengths [35]. For instance, an electrically injected continuous-wave green laser diode ($\lambda = 520 nm$) was demonstrated on the (20$\bar{2}$1)-plane [36]. Another serious advantage of these orientations is that the piezoelectric field along the growth direction can be strongly reduced depending on the alloy composition and the strain state [37].

## 1.2 Mechanical properties

Due to the large lattice-mismatch between III-nitride compounds and the commercially available substrates, in order to have a proper sample design, one should fully account for strain effects on the material properties. Strain affects the electronic and optical properties since it modifies the equilibrium position of the atoms in the primitive cell. A good understanding of the crystal mechanical properties provides a direct way of tuning the properties of optoelectronic devices by strain management, e.g. via a careful choice of the crystal orientation, alloy composition, and layer thicknesses.

Crystal deformation generates internal forces that are identified as stress, i.e. the force responding to strain per unit area [38]. Strain ($\varepsilon$) and stress ($\sigma$) are tensors proportional to each other in the linear elastic theory limit. For a crystal, Hooke's law is generalized by introducing a tensor displaying the elastic stiffness $C_{ijkl}$, which linearly relates stress and strain components. Due to the crystal symmetries the $C_{ijkl}$ tensor can be reduced to a 6×6 matrix $C_{ij}$. For wurtzite crystals, only five elastic constants are necessary to describe the mechanical properties, given by:

$$C_{ij} = \begin{pmatrix} C_{11} & C_{12} & C_{13} & 0 & 0 & 0 \\ C_{12} & C_{11} & C_{13} & 0 & 0 & 0 \\ C_{13} & C_{13} & C_{33} & 0 & 0 & 0 \\ 0 & 0 & 0 & C_{44} & 0 & 0 \\ 0 & 0 & 0 & 0 & C_{44} & 0 \\ 0 & 0 & 0 & 0 & 0 & \frac{(C_{11}-C_{12})}{2} \end{pmatrix} \tag{1.2}$$

As $\varepsilon$ and $\sigma$ are symmetric tensors, they can be reduced to 6-component vectors with the notation convention xx→1, yy→2, zz→3, yz =zy→4, xz =zx→5, and xy = yx→6. Therefore, Hooke's law for solids defines the stress according to:

$$\sigma_i = \sum_j C_{ij}\epsilon_j - \sum_k e_{ik}F_k \approx \sum_j C_{ij}\epsilon_j \tag{1.3}$$

where $e_{ik}$ is the piezoelectric tensor and $F_k$ is the electric field along the k-direction. All latin subscripts run over the three spatial directions x, y and z. Note that, in this expression, the second term representing the converse piezoelectric effect is neglected. Indeed, this is justified by the small deviations (~2%) from the complete calculation by neglecting this term in the case of heterostructures [39]. Table 1.2 summarizes the value of the different elements of the elastic modulus $C$ for III-nitrides binary elements as well ZnO.

Table 1.2 – Elastic constants for III-nitride binary compounds [40] and ZnO [41].

| | GaN | AlN | InN | ZnO |
|---|---|---|---|---|
| $C_{11}(GPa)$ | 390 | 396 | 223 | 217 |
| $C_{12}(GPa)$ | 145 | 137 | 115 | 117 |
| $C_{13}(GPa)$ | 106 | 108 | 92 | 121 |
| $C_{33}(GPa)$ | 398 | 378 | 224 | 225 |
| $C_{44}(GPa)$ | 105 | 116 | 48 | 50 |

## 1.3 Optical properties: Bandgap

In a semiconductor, the bandgap energy $E_g$ is defined as the energy difference between the edge energies of the conduction and valence band. A large fraction of III-nitrides having a direct bandgap, that encompasses a large range of energies from the mid-infrared for InN up to the deep UV for AlN. At 10 K, the $E_g$ of unstrained GaN is estimated to be 3.504 eV [42], and it changes to 6.089 eV for AlN [43]. In case InN composition, after a long-standing controversy, its $E_g$ has been finally admitted to be around 0.7 eV [44].

Contrary to the lattice parameters, the bandgap of III-nitride ternary alloys do not show a linear dependence on the composition $x$. This is mainly due to the distorted lattice of ternary alloys ($A_xB_{1-x}N$) compared to the lattices of the AN and BN binary alloys. The deviation from the linear dependence of $E_g$ ($A_xB_{1-x}N$) with $x$ is characterized with the so-called bowing parameter $b$:

$$E_g(A_xB_{1-x}N) = xE_g(AN) + (1-x)E_g(BN) - bx(1-x), \tag{1.4}$$

with $b$ value of 1, 2.5, and 5.4 in case of $Al_xGa_{1-x}N$, $In_xGa_{1-x}N$, and $Al_xIn_{1-x}N$, respectively [28].

### 1.3.1 Temperature dependence of the Bandgap

When raising the temperature, the lattice dilatation leads to reduction of the $E_g$. This behavior can be described by the semi-empirical relation suggested by Varshni's law [45]:

$$E_g(T) = E_g(0) - \frac{\alpha T^2}{\beta + T}, \tag{1.5}$$

where $\alpha$ and $\beta$ are material dependent parameters. Typical values reported in the literature for the case of III-Nitride compounds and ZnO are listed in Tab. 1.3.

Table 1.3 – Bandgap values for wurtzite crystalline phase of III-nitride compounds and ZnO, taken from Ref. [46, 40, 47].

| | GaN | AlN | InN | ZnO |
|---|---|---|---|---|
| $\alpha(meV/K)$ | 0.909 | 1.799 | 0.245 | 0.505 |
| $\beta(K)$ | 832 | 1462 | 624 | 900 |

## 1.4 Polarization in III-nitride heterostructures

The anisotropy of the wurtzite structure has strong consequences on the electronic properties of III-nitrides compared to the other III-V semiconductors. The most critical consequence of anisotropy appears in heterostructures. GaN exhibits an internal polarization aligned along the $c$-axis. The polarization discontinuities at the interfaces of heterostructures, such as quantum wells (QWs) or quantum dots, grown along the $c$-axis generate strong built-in electric fields, and thus producing the quantum confined Stark effect. In this section, we discuss the impacts of the quantum confined Stark effect on the emission properties of (Al,Ga)N/GaN QWs grown along the polar $c$-axis.

### 1.4.1 Spontaneous polarization

Due to the non-centrosymmetry of wurtzite binary crystals, the barycenters of positive and negative charges are not superimposed. This leads to a spontaneous polarization along the $c$-axis., while the amplitude of this spontaneous polarization depends on the structural properties of the crystal such as the lattice parameter $c$ and the internal parameter $u$ [48]. When changing from GaN to InN and AlN, the crystal structure deviates from the ideal wurtzite structure and thus the amplitude of the spontaneous polarization increases (see Tab. 1.1).

The spontaneous polarization of the ternary alloys $Al_xGa_{1-x}N$ and $In_xGa_{1-x}N$ has a strong non-linear dependence on $x$ value [49]. Non-linearities originates from three distinct mechanisms: (i) volume deformation of the crystal unit cell, (ii) internal strain effects due to variation in the cation-anion separation, and (iii) disorder caused by the random incorporation of the atoms. Spontaneous polarization in case of $\mathrm{Al}_x\mathrm{Ga}_{1-x}\mathrm{N}$ and $\mathrm{In}_x\mathrm{Ga}_{1-x}\mathrm{N}$ ternary alloys can be expressed to the second order of $x$ [29]:

$$P_{sp}(Al_xGa_{1-x}N) = -0.090x - 0.034(1-x) + 0.019x(1-x), \tag{1.6}$$

$$P_{sp}(In_xGa_{1-x}N) = -0.042x - 0.034(1-x) + 0.038x(1-x). \tag{1.7}$$

### 1.4.2 Piezoelectric polarization

Owing to the lattice mismatch between different compounds of III-nitrides, in general, growing the III-nitride heterostructures, their crystal will undergo a deformation inducing a modification of the whole polarization. The difference between the polarization of a strained crystal and that of the relaxed one is the piezoelectric polarization $P_{pz}$. In presence of biaxial strain, the piezoelectric polarization along [0001] is given by:

$$P_{pz} = \left(2e_{31} + 2\frac{C_{13}}{C_{33}}e_{33}\right)\varepsilon_{xx}, \tag{1.8}$$

where $C_{ij}$ and $e_{ij}$ denote the elasticity and piezoelectric tensors of the strained compound. The piezoelectric polarization of ternary alloys can be given by a linear interpolation of the polarization of the two binary compounds [49].

### 1.4.3 Quantum confined Stark effect (QCSE)

During the growth of III-nitrides based heterostructures, materials with different internal polarization are stacked successively on each other. For instance, let us consider a layer of AlN deposited on a layer of GaN, while the interface between the two media is perpendicular to the polar $c$-axis. Assuming the layers to be semi-infinite, owing to the continuity of the displacement vector $D$ at the interface between the two dielectric media, there is an accumulation of charges at the interface between GaN and AlN. The charge density $\sigma$ at this interface is given by:

$$\sigma = \overrightarrow{n}(\overrightarrow{P}_{GaN} - \overrightarrow{P}_{AlN}) \tag{1.9}$$

where $\overrightarrow{n}$ is the normal vector of the interface between GaN and AlN and parallel to the $c$-axis. This interface can be seen as an infinite plane charged with $\sigma$, that creates an electric fields F in both the GaN and the AlN layers. The amplitude of $F$ in GaN layer, then, can be written as:

$$\overrightarrow{F}_{GaN} = -\frac{\sigma}{2\varepsilon_{GaN}}\overrightarrow{n}, \tag{1.10}$$

, in the AlN layer, the electric field amplitude is given by:

$$\vec{F}_{AlN} = +\frac{\sigma}{2\varepsilon_{AlN}}\vec{n}. \tag{1.11}$$

In case of a single GaN/AlN QW, where a GaN layer is embedded between two AlN barriers, the two GaN/AlN interfaces are oppositely charged, and hence from the superposition principle, the amplitude of the electric field can be described as:

$$\vec{F}_{GaN} = -\frac{\sigma}{\varepsilon_{GaN}}\vec{n} = \frac{\vec{P}_{AlN} - \vec{P}_{GaN}}{\varepsilon_{GaN}}. \tag{1.12}$$

The influence of built-in electric fields on the emission properties of an exciton confined in a polar QW can be modeled by envelope function calculations, by adding the electrostatic energy caused the built-in electric fields $F$ to the crystal potentials $V_e(z_e)$ and $V_h(z_h)$. The major consequences of built-in electric fields on the emission energy of $Al_xGa_{1-x}N$/GaN single QWs are illustrated in Fig. 1.2. In case of very thin QWs (typically thinner than 2.5 nm), the built-in electric fields have almost no influence on the emission properties of the exciton (see Fig. 1.2(a)). However, in case of a 7.5 nm thick QW (see Fig. 1.2(b)), the electron hole wave-function overlap is dramatically decreased, and the QW emission energy is redshifted compared to the case of polarization free QWs to the values even below the bulk GaN bandgap [50]. This redshift, known as Stark shift, is in first approximation given by $qF_{GaN}L_{GaN}$. Accordingly, the QW emission energy can be given by:

$$E_G^{QW} = E_G^{bulk} + E_e^{conf} + E_h^{conf} - qF_{GaN}L_{GaN}, \tag{1.13}$$

where $E_{e,h}^{conf}$ is the confinement energy of the electron (hole) extracted from the envelope function calculation [23].

The built-in electric field separates the electron and hole wave-functions, and thus reduces the electron hole wave-function overlap (see Fig. 1.2(c)). Therefore, it can severely increase the radiative lifetime of electron-hole pairs. This impact on the exciton radiative lifetime can be quite significant, as it can change, for instance, the lifetime of a 3.5 nm thick GaN quantum dot embedded in AlN barrier to 100 $\mu s$ [51]. Note that this increase of the radiative lifetime is not necessary an advantage, since at room temperature, charge carriers suffer from efficient non-radiative recombinations with short non- radiative lifetime (typically 10 ps - 10 ns [52, 53, 54] in case of III-nitride QWs). Therefore, this effect can considerably reduce the radiative efficiency of thick QWs.

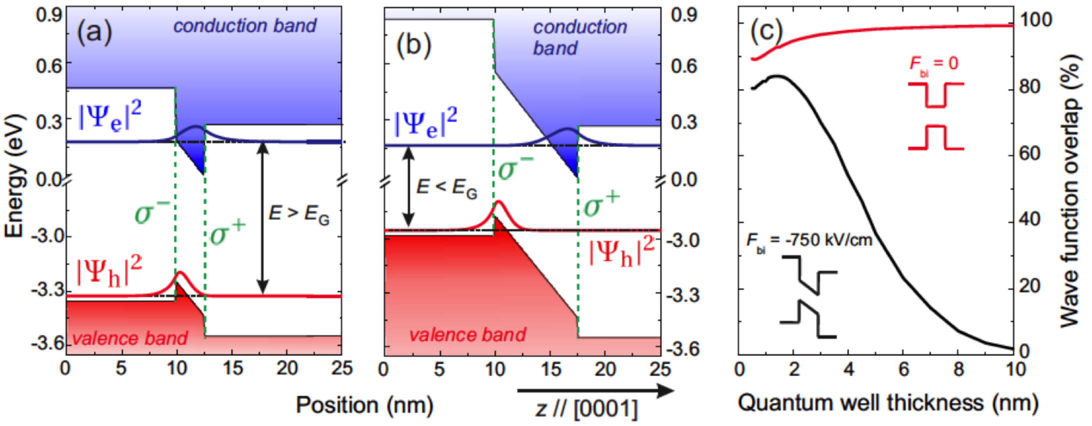

Figure 1.2 – **(a)** Impact of the quantum confined Stark effect on the electronic properties of a single GaN/$Al_{0.2}Ga_{0.8}N$ QW embedded between infinitely large barriers: **(a)** $L_Q W$ = 2.5 nm, in which the emission energy is above the bulk bandgap ($E_G$), **(b)** $L_{QW}$ = 7.5 nm, in which the emission energy is below $E_G$. Electron (blue) and hole (blue) presence probability $|\Psi_e|^2$ and $|\Psi_h|^2$ are calculated within the envelope wave-function calculations. The charge planes at the QW interfaces are indicated by $\sigma+$ and $\sigma-$ (green dashed lines). **(c)** The value of electron and hole wave-function overlap as a function of the QW thickness, in the presence (absence) of a 750 kV/cm large built-in electric field black (red). Adapted from [23].

## 1.5 Excitonic effect

In the previous sections, when discussing the electron-hole recombination, we systematically neglected the Coulomb interaction between these two particles. When the Coulomb interaction between electrons and holes is considered, the first excited state is still described by a single electron in the conduction band and a hole in the valence band but they are now correlated and form a bound state called an exciton.

Table 1.4 – Experimental excitonic parameters for bulk GaAs, CdTe, GaN, AlN, and ZnO for T <10K.

| | GaAs | CdTe | GaN | AlN | ZnO |
|---|---|---|---|---|---|
| $E_G(eV)$ | 1.519 [55] | 1.606 [56] | 3.499 [55] | 6.25 [48] | 3.44 [47] |
| $a_B(nm)$ | 11.2 [55] | 7 [57] | 2.7 [58] | 1.2 [58] | 0.9 [47] |
| $E^b_{X,3D}(meV)$ | 3.9 [55] | 9.5 [56] | 24.8 [59] | 44 [48] | 60 [47] |

The Hamiltonian of an exciton is the sum of that of the electron and the hole with the Coulomb interaction term:

$$\hat{\mathscr{H}}_X^{bulk} = -\frac{\hbar^2\nabla_e^2}{2m_e^*} - \frac{\hbar^2\nabla_h^2}{2m_h^*} - \frac{e^2}{4\pi\varepsilon_0\varepsilon_r\|\mathbf{R}_e - \mathbf{R}_h\|}, \tag{1.14}$$

where $\mathbf{R}_{e,h}$ denotes the coordinate of the electron (hole), $\nabla^2_{e,h}$ is the Laplacian operator expressed in terms of the particle coordinates, $\varepsilon_0$ is the vacuum permittivity and $\varepsilon_r$ is the relative permittivity of the material.

In a first order approximation, this problem resembles the one of the hydrogen atom, where the hole plays the role of the proton. To express the solution of the excitonic problem in terms of that of the hydrogen one, one should rescale the physical quantities of interest, i.e., the binding energy $E^b_{X,3D}$ and the Bohr radius $a_B$ according to:

$$\begin{aligned} E^b_{X,3D} &= \frac{\mu}{m_0\varepsilon_r^2}R_y = \frac{\mu}{m_0\varepsilon_r^2} \times 13.6eV, \\ a^B_{X,3D} &= \frac{m_0\varepsilon_r}{\mu}a^H_B = \frac{m_0\varepsilon_r}{\mu} \times 0.53nm, \end{aligned} \tag{1.15}$$

where the indices $X$ and $H$ refer to the exciton and hydrogen cases, respectively, and $\mu$ is the exciton reduced mass given by $\mu = (\frac{1}{m_e^*} + \frac{1}{m_h^*})^{-1}$, and $R_y$ is the Rydberg constant. The eigenenergies for exciton in bulk system then given by:

$$E_n^{bulk} = E_G + \frac{\hbar^2 K^2}{2M_X} - \frac{E^b_{X,3D}}{n^2}, \tag{1.16}$$

where $M_X = m_e^* + m_h^*$ is the exciton translational mass, $K$ is the center of mass wave vector and $n = 1,2,3...$ is the principal quantum number. Note that the quantity $E^{b,n}_{X,3D} = \frac{E^b_{X,3D}}{n^2}$ corresponds to the exciton binding energy for a bulk exciton with principal quantum number $n$. In Tab. 1.4, values for $E_G$ at low temperature ($T < 10K$), $a_B$ and $E^b_{X,3D}$ are given for the 1s exciton (n =1) for various semiconductor materials. One can identify a correlation between the exciton binding energy and the band gap energy, that suggests that wide bandgap semiconductor materials such as GaN and ZnO are well adapted for the observation of excitonic effects at elevated temperatures.

### 1.5.1 The quantum well exciton

In case of QWs, the exciton binding energy and the oscillator strength are enhanced due to quantum confinement. This contributes to the high efficiency of the excitonic luminescence in QW-based structures. Contrary to bulk excitons, the translation symmetry is broken along the growth direction QWs, leading to the energy renormalization of the electron and hole states due to quantum confinement.

The Hamiltonian for 2D-excitons should be thus modified with respect to Eq. 1.14 by adding the electron and hole confinement potentials along the growth direction $z$, according to:

$$\hat{\mathscr{H}}_X^{2D} = -\frac{\hbar^2\nabla_e^2}{2m_e^*} - \frac{\hbar^2\nabla_h^2}{2m_h^*} + \hat{V}_e^{conf}(Z_e) + \hat{V}_h^{conf}(Z_h) - \frac{e^2}{4\pi\varepsilon_0\varepsilon_r \|\mathbf{R}_e - \mathbf{R}_h\|} \tag{1.17}$$

For simplicity, we separate the electron (hole) motion in the plane of the QW ($\rho_{e,h}$) from that along the growth direction ($z_{e,h}$). This is justified by the fact that, the width of the studied QWs ($L_{QW}$) in this thesis, are generally comparable or smaller than the bulk exciton Bohr radius ($L_{QW} \approx a_B$) [60]. In this case, the 1s exciton wave-function can be written in the form[60]:

$$\Psi(\mathbf{R}_e, \mathbf{R}_h) = \frac{1}{\sqrt{S}} exp(ik_\parallel \rho) f_e(z_e) f_h(z_h) \Phi(\rho), \tag{1.18}$$

where $S$ is the surface of the QW plane, $k_\parallel = k_e + k_h$ and $\rho = \frac{m_e^*\rho_e + m_h^*\rho_h}{m_e^* + m_e^*}$ are the in-plane components of the exciton wave vector and the position of its center-of-mass. $f_{e,h}(z_{e,h})$ is the envelope function for the electron (hole) obtained by solving the 1D-dimensional Schrödinger equation for the confinement potential along the growth direction $z$. $\Psi(\rho)$ is the solution of the 2D hydrogenoid-like Hamiltonian, which in case of the 1s exciton is given by:

$$\Psi_{1s}(\rho) = \frac{1}{a_B}\sqrt{\frac{2}{\pi}} exp(-\frac{\rho}{a_B}), \tag{1.19}$$

where $a_B$ is the effective 2D Bohr radius. Therefore, in the 2D-limit, the eigenenergies of theHamiltonian in Eq. 1.17 are given by:

$$E_n^{QW}(k_\parallel) = E_G + E_e^{conf} + E_h^{conf} + \frac{\hbar^2 k_\parallel^2}{2M_X} - \frac{E_{X,3D}^b}{(n - \frac{1}{2})^2}. \tag{1.20}$$

Note that the exciton binding energy is now expressed as $\frac{E_{X,3D}^b}{(n-\frac{1}{2})^2}$, meaning that for the 1s exciton, the binding energy is enhanced by a factor of 4 with respect to the bulk case for $n = 1$. However, this situation corresponds to the perfect 2D-case when $L_{QW} \to 0$ and confinement effects progressively vanish when the structure dimension tends to the bulk case [60].

# 2 Experimental setups

This chapter deals with the details of the experimental setups, used within this thesis, to investigate the dynamics of carriers in wide bandgap semiconductor nanostructures. To begin with, the time resolved (tr) photoluminescence (PL) system shall be introduced, which allows probing optical properties of nanostructures over a wide range of carrier densities and with a temporal resolution of few picosecond. However, tr-PL measurement technique is basically limited by the poor spatial resolution defined at best by the diffraction limit. Afterwards, the continuous wave (cw) cathodoluminescence (CL) will be introduced, which benefits from a good spatial resolution in the range of few nanometers.

Since we are interested in the carrier transport dynamics as well as their recombination dynamics, another measurement technique with simultaneous temporal and spatial resolution is needed. These characterizations of semiconductor can be realized using our time resolved (tr) cathodolumuinescence (CL), which, thanks to its spatial and temporal resolutions, allows probing the relaxation and the transport of free electron-hole pairs and excitons. The purpose of this chapter is not, however, to give the reader a thorough description of each experimental machine, but rather to provide him with the key characteristics of each setup, including their advantages and limitations.

## 2.1 Time resolved photoluminescence

To investigate the dynamics of carrier relaxations and recombinations, that usually occurs in picosecond time scales in direct band gap semiconductors such as GaAs and GaN heterostructure, picosecond luminescence spectroscopy can be a powerful technique[61]. One therefore needs ultrafast excitation techniques combined with an ultrafast detection with minimized temporal jitter to be able to track these dynamics. The former is done in our experimental system by means of the harmonics of a mode-locked Ti: Sapphire laser, while the latter is provided by a synchronous streak camera locked to our excitation laser to reduce the jitter effect over long acquisition measurements. The overall temporal resolution of our tr-PL system is estimated to be better than 10 ps, which is basically limited by the diffraction of the collected signal with gratings. The spatial resolution is, however, defined by the size of the excitation spot that can be between 5 and 50 $\mu m$, depending on the objective used for the excitation. In the following, the two main parts of the tr-PL system will be introduced in respective order: the excitation path and the collection path.

### 2.1.1 Excitation path

The optical excitation is performed by a picosecond mode-locked Ti:Sapphire laser, optically pumped by a frequency-doubled Nd:$YVO_4$ laser ($\lambda$ = 532 nm). The emission band of the Ti: $Al_2O_3$ ranges from 600 to 1080 nm, with a maximum gain at 670 nm. This amplification medium is located in an optical cavity formed by a high-reflectivity mirror and an output coupler with 80% reflectivity. The length of the cavity amounts to L = 1.86 m, which makes the longitudinal mode separation of $\Delta\nu = c/2L$, where c denotes the speed of light, and the path of the light through the Ti: $Al_2O_3$ rod was neglected in the first order approximation.

The longitudinal modes that fall in the emission band of the Ti: Sapphire crystal are usually uncoupled and have a random phase under cw operation of the laser. In order to obtain ultra-short laser pulses, the modes of the laser have to be mode-locked with a well-defined phase difference to obtain a constructive interference at the output. Providing the suitable phase difference between modes for mode-locking conditions, the periodicity of the pulse trains of the laser is defined by the round-trip travel time for laser pulses in the cavity, $T = 2L/c \approx 12.4ns$ in our system.

In a Ti: Sapphire, mode-locking can be achieved passively thanks to the optical Kerr effect. Indeed, the refractive index of the Ti: Sapphire rod depends on the intensity of the laser beam. It is, therefore, possible to design the optical cavity in order to favor the propagation of intense light pulses. The losses are then higher in cw than in pulsed mode, leading to mode-locking that has originally been called ”magic” mode-locking. However, in order to ensure reliable mode-locked operation, the phase relation between longitudinal modes is in fact achieved by an acousto-optic modulator at laser start-up. It allows mode-locked operation of the laser over an extended period, that is not the case in passive mode-locking operation. This acousto-optic modulator is driven by a radio-frequency signal with a fixed frequency of about 80 MHZ.

The width of the pulse is proportional to the number of phase-locked modes, i.e.,the higher is the number of modes that interfere constructively, the shorter is the pulse width. Assuming that all the modes within the gain region of the Ti:Sapphire rod (670 and 1080 nm) can interfere, we obtain that $2 \times 10^6$ modes oscillating in phase and would correspond to a pulse width of less than 2 fs. However, in practice, much smaller number of modes contribute to the pulse due to, for instance, the imperfection in the mirror coatings over the full wavelength range of 670 to 1080 nm, or the presence of modes that are not necessarily locked in phase. Presence of any dispersion will also reduce the number of modes that are locked in phase. As a matter of fact, the most drastic reduction in the number of modes is produced by the birefringent filter present in the cavity that allows the tuning of the laser wavelength. Such a filter is made of two or three birefringent plates and only those modes whose polarization remain linear after traveling through the plates can propagate back and forth in the cavity without losses. Each pulse results finally from the constructive interference between only ~3000 longitudinal modes, allowing for the generation of 2 ps pulses (average energy of 12 nJ per pulse). One should also note that the group velocity dispersion due to the propagation of the beam into the non-linear Ti: Sapphire rod is compensated by a Gires-Tournois interferometer, which is placed at the end of the laser cavity.

In order to excite wide bandgap semiconductors, we use the third harmonic of the picosecond Ti: Sapphire mode-locked laser. The second harmonic is obtained by focusing the laser on a uniaxial birefringent crystal that gives the second-harmonic by non-linear effect in the crystal. To obtain the third harmonic, the second harmonic and the fundamental one are focused on a second non-linear crystal with proper spatial and temporal overlap. Indeed, optimal harmonic generation is obtained when the mode matching is respected. Experimentally, this angle tuning is obtained by rotating the non-linear crystals.

As already mentioned, lasing action is possible for wavelengths between 670 and 1080 nm. However, the mirror coatings of the frequency doubler/tripler limit us to excitation wavelengths in the range of 270 to 330 nm at third harmonic and 400 to 480 nm at second harmonic. At the exit of the frequency tripler, the beam is far from being Gaussian since the laser beam passes through thick non-linear crystals in the harmonic generation process. As a consequence, the crystals can in no way be considered as point sources for the second and the third harmonics and at the exit of the tripler, the beam exhibits an elongated shape. Therefore, a cylindrical lens was used inside the tripled and right after the second non-linear crystal to retrieve the shape of the laser beam. However, in order to obtain a perfect Gaussian beam, we had to filter spatially the beam with pinholes with approximate diameter of $\phi$ = 1-2 $mm$. To excite the sample, two different objectives were used with the following specifications:

- An achromatic lens L1, with focal length of $f$ = 9.7 cm. Neglecting the divergence of the laser beam, astigmatism and spherical aberration, the diameter of the excitation spot is given by $\Phi = f(2.4\lambda/\phi)$, which results in an excitation spot diameter of about 50 $\mu m$.

- An achromatic objective lens OL1, with focal length of $f$ = 0.25 cm, and a numerical aperture of NA = 0.55 that allows for an excitation spot diameter below 5 $\mu m$.

Considering our excitation power is typically set between 10 $\mu$W and 2 mW for excitation wavelength of $\lambda$ = 280 nm, the density of the uniform photo-generated electron-hole pairs per pulse within the excitation spot is comprised between $8 \times 10^9$-$1.5 \times 10^{11} cm^{-2}$ using L1, and $8 \times 10^{11}$-$1.5 \times 10^{13} cm^{-2}$ using OL1.

### 2.1.2 Collection path

Our PL setup works in illumination-collection mode, i.e., the excitation laser and the PL are focused and collected by the same lens L1/OL1 (see Fig. 2.1). The beam-splitter (BS) is used to deflect the excitation beam by 90 degrees towards the sample. The reflection of this BS at 280 nm is about 75%. The transmitted part of the laser is measured with a power meter on the back-side of the BS, in order to measure the excitation power.

The PL is then focused by a second lens (L2) on a spatial filter (pinhole) with a diameter of either 50 or 100 $\mu m$. The use of such a pinhole allows for the analysis of a uniformly excited area of the sample, which is of key importance when interpreting excitation dependent measurements or extracting from PL spectra the effective temperature of charge carriers, as is the case for all studies in chapter 3 and 4. As shown in the inset of Fig. 2.1, the excitation spot is imaged on the pinhole and only its central area passes through the pinhole for analysis. The dimension of the analyzed spot is given by the diameter of the pinhole and by the magnification of the excitation spot, i.e., the ratio between the focal lengths of L2 and L1/OL1 (~ 3 or 100 when using L1 or OL1, respectively).

The PL is then analyzed spectrally with a 32 cm focal length monochromator. In this thesis, two sets of diffraction grating have been used. We have used a set of 1 inch wide 300, 600, 1200 grooves/mm gratings, all blazed at wavelength of 350 nm, whereas the second set of gratings consists of 1 inch wide 150, 300, and 1200 grooves/mm gratings blazed at wavelength of 500 nm. There is the possibility to change from one set of gratings to another in the spectrometer. The experimentally obtained spectral resolutions with these gratings are in order of few meV, mainly limited by the size of the entrance slit of the spectrometer [62]. Nevertheless, these spectral resolutions are enough to study III-nitride QWs, because the emission linewidth is dominated by inhomogeneous broadening and is of the order of a few meV in the stat-of-the-art samples.

The temporal analysis of the luminescence signal was obtained by a streak camera that converts the time information into a spatial one (see Fig. 2.2). At the exit of the monochromator, the spectrally dispersed luminescence is sent through a slit (the temporal slit of the streak camera) on a photocathode. The electrons photo-generated by photocathode are then deflected by a sinusoidal electric field, which is synchronized with the laser, and hit the multi-channel plate (MCP) to be amplified. Therefore, the early electrons arrive on one side of the MCP, while the late ones are displaced according to their delay towards the other side. The signal is

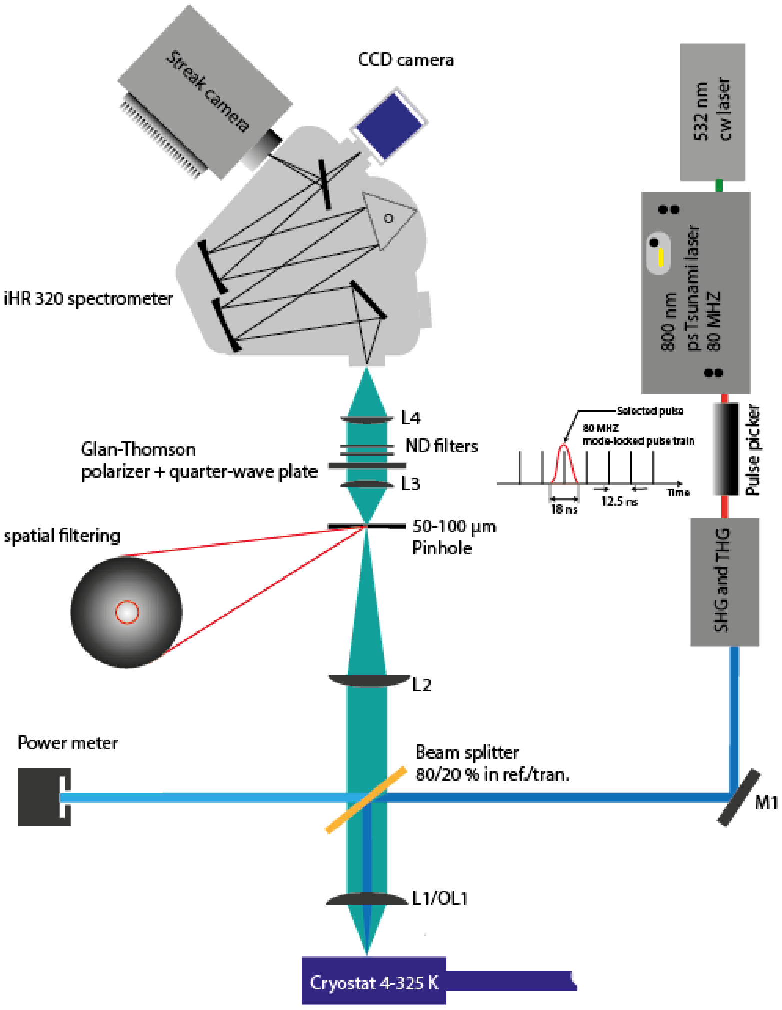

Figure 2.1 – The schematics of the tr-PL experimental system, illumination-collection mode. We use the third harmonic of a pulsed Ti:Sapphire laser to excite the luminescence of wide bandgap semiconductors. The pulsed picker before the harmonic generator allows reducing the repetition of the laser from 80 MHZ down to 80 HZ. The PL signal is collected by a lens (L1/OL1), if necessary attenuated or polarization-analyzed, and then sent to a monochromator and a streak camera synchronized with the mode-locked laser. The pinhole placed in the collection path allows spatial filtering of the uniform part of the excitation spot, as it is shown in the inset of the figure.

amplified in the MCP by multiple avalanches and is finally sent to a phosphor plate. The final image of the screen is captured by a CCD on the back-side of the phosphor plate. At this stage, each pixel of the CCD provides the intensity of the signal for a given time and wavelength, while the amplitude of the deflecting electric field defines the total time range covered by the CCD at the end-side of the streak.

The synchronous method helps to reduce the sensitivity of the measurements to instabilities

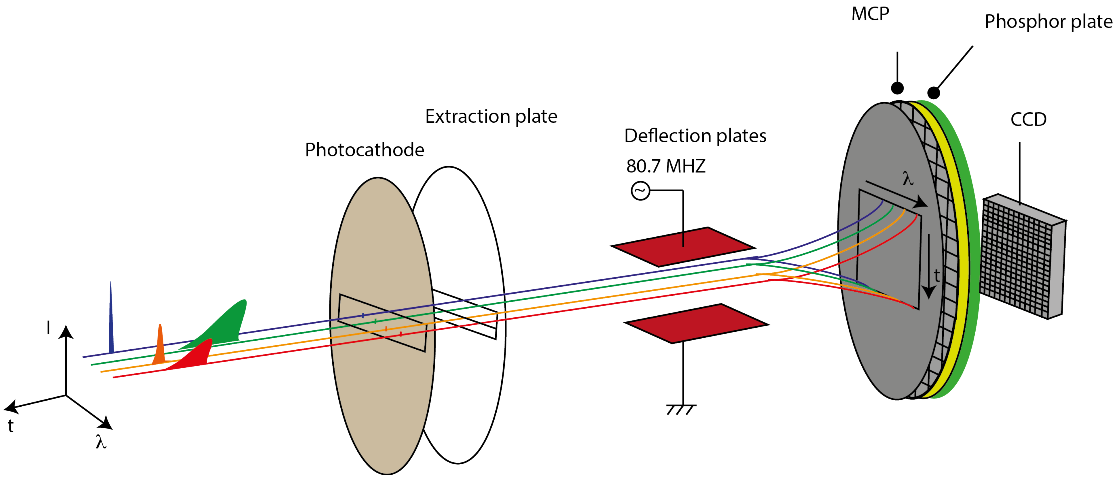

Figure 2.2 – Schematics of the operation mechanism of a streak camera. The temporal dispersion of a spectrally resolved luminescence signal by a streak camera in synchroscan mode is shown.

of the laser occurring over few pulses. However, we cannot eliminate small continuous drifts in the laser repetition rate that spoil the time resolution of the camera when long integrations are performed. Moreover, the intrinsic temporal resolution of the streak camera (~ 2ps) can hardly be achieved in our experiments due to using diffraction gratings. One should also take into account other experimental limits such as jitter, laser instabilities, laser pulse width to estimate the temporal resolution of the system, which in overall leads to a temporal resolution of 10-20 ps.

Eventually, it worth mentioning the pulse picker unit used in the excitation path, that allows reaching lower laser repetition rates. The used pulsed picker is based on an electro-optical modulator, which suppresses the linear polarized laser pulses at off duration and rotate the polarization in on duration (See Fig. 2.1). The used pulsed picker combined with the slow scan unit used for synchronization of the streak camera allows preforming measurements with much longer time-scales up to few ms. This possibility is of practical interest, for instance, to study high In content InGaN/GaN QWs, where the large built-in electric field combined with the localization effect leads to very long decay time of the QW emission [63].

## 2.2 Continuous wave cathodoluminescence

### 2.2.1 Inelastic interactions between an electron beam and a semiconductor

The interaction of high-energy electrons (~ few keV) with a semiconductor leads to a wide range of elastic and inelastic scattering events. A large portion of incident electrons are scattered, elastically or not, by the atoms of the solid and re-emitted with an energy comparable with the primary electrons. These electrons are called backscattered electrons. However, some electrons, called secondary electrons, can undergo several inelastic scatterings and end up with energy of typically few eV. The particles excited by an inelastic electron/atom scattering can cover a wide range of energies. If the energy of the incoming electron is sufficiently high, it can promote electrons in the atomic shells from a deep energy level to a higher energy one, for instance from K to L orbital, that results in X-ray emissions during relaxation process.

However, if the energy loss of the incident electron is only of a few eV it can only excite an electron from the valence to the conduction band, i.e., generate an electron-hole pair in the lattice. In the case of semiconductors, the excited electron relaxes towards the bottom of the conduction band, and the hole to the top of the valence band, and then can recombine radiatively. The light emission subsequent to the excitation by an electron beam is called cathodoluminescence.

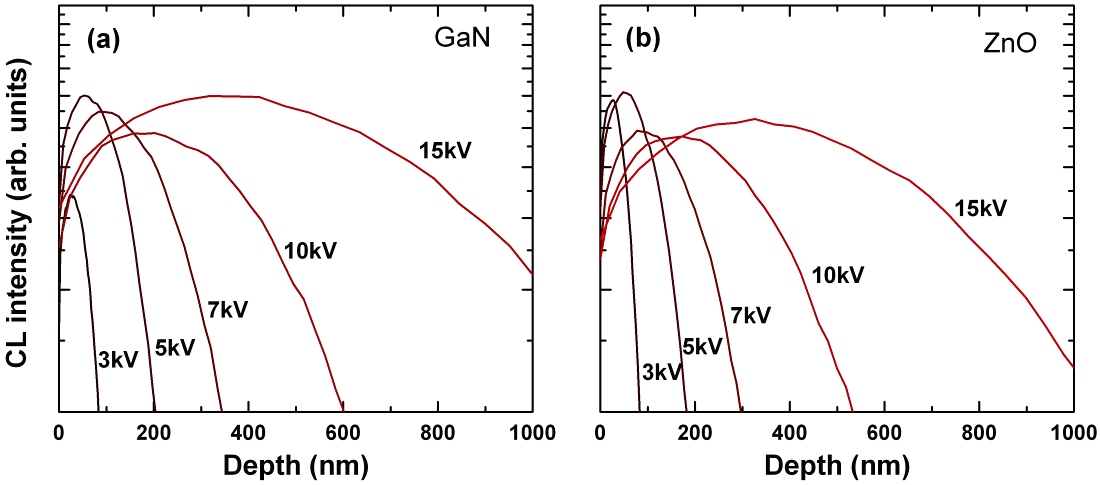

Figure 2.3 – Monte-Carlo simulation of depth of the CL generation volume at different acceleration voltage, preformed with Casino software, for GaN (a) and ZnO (b) bulk material, respectively.

Dependent on their energies, electrons can experience very complex and long trajectories that involve both types of elastic and inelastic scatterings. Therefore, the spatial distribution of generated electron-hole pairs is a volume -the so-called generation volume. The radius and depth of the generation volume can be determined either analytically [64], or by means of Monte-Carlo simulations [65]. The generation volume is strongly dependent on the incident electron beam energy and on the chemical nature of the material.

It is possible to estimate the density of electron-hole pairs generated in a semiconductor by an electron beam. Indeed, there is a fundamental difference between PL and CL: whereas in single photon absorption, one photon can generate only one electron hole pair, a high-energy electron in CL can generate thousands of electron-hole pairs in the excitation volume. The generation factor, i.e. the number of electron-hole pairs generated per incident electron, is given by:

$$G = E_b(1-\gamma)/E_i, \tag{2.1}$$

where $E_b$ is the excitation beam energy, $E_i$ is the ionization energy (energy needed for formation of an electron-hole pair), and the term $1-\gamma$ represent the fraction of electrons loss $via$ backscattering electrons. The ionization energy is a function of the bandgap energy $E_G$ and is given by the following generally accepted relation:

$$E_i = 2.8E_g + M, \tag{2.2}$$

where 0<M<1 eV is a material dependent parameter [66, 67]. The results of a Monte-Carlo simulation, preformed with casino software, to estimate the depth of the CL generation volume at different acceleration voltage in case of bulk ZnO and bulk GaN are shown in Fig. 2.3(a) and (b), respectively. In these simulations, 20000 electrons were used in order to obtain the distribution profiles, while the depth of CL generation volume increases with increasing the acceleration voltage. It is thus, for instance, possible to distinguish by depth-resolved CL the emission of near-surface states from that of the underlying material. The slight difference in the simulation results originates from the material dependence of electron scatterings. Eventually, it is also important to emphasize the difference in the excitation volumes of a thin sample (i.e., thinner than the depth of generation volume) and a bulk sample, while in the former generation volume is defined by the dimension of the structure. For instance, in a 10 nm thick NW, the generation volume is defined by the size of the electron beam spot along the NW and the diameter of the NW in vertical direction.

In order to collect the CL signal in our cw-CL system, a parabolic mirror is introduced between the sample and the polar piece (objective lens) of the microscope (see Fig. 2.4). Apart from experimental difficulties to align this parabolic mirror in order to have the best collection efficiency, two other important drawbacks yielded by the presence of the mirror are: (i) reduction of the number of secondary electrons reaching the Everhart-Thornley detector, thus decreasing the signal-to-noise ratio of the secondary electron mapping, and (ii) increase in the working distance and therefore decreasing the spatial resolution of the set-up.

The CL signal is then sent to a monochromator followed by a photomultiplier tube or a CCD. As is the case for secondary electron (SE) imaging, CL mappings are obtained by scanning the electron beam on the surface of the sample while detecting in parallel the CL signal. However, the spatial resolution of CL is more difficult to estimate, as one has to care not only for the extension of the generation volume, but also for the diffusion of charge carriers [68].

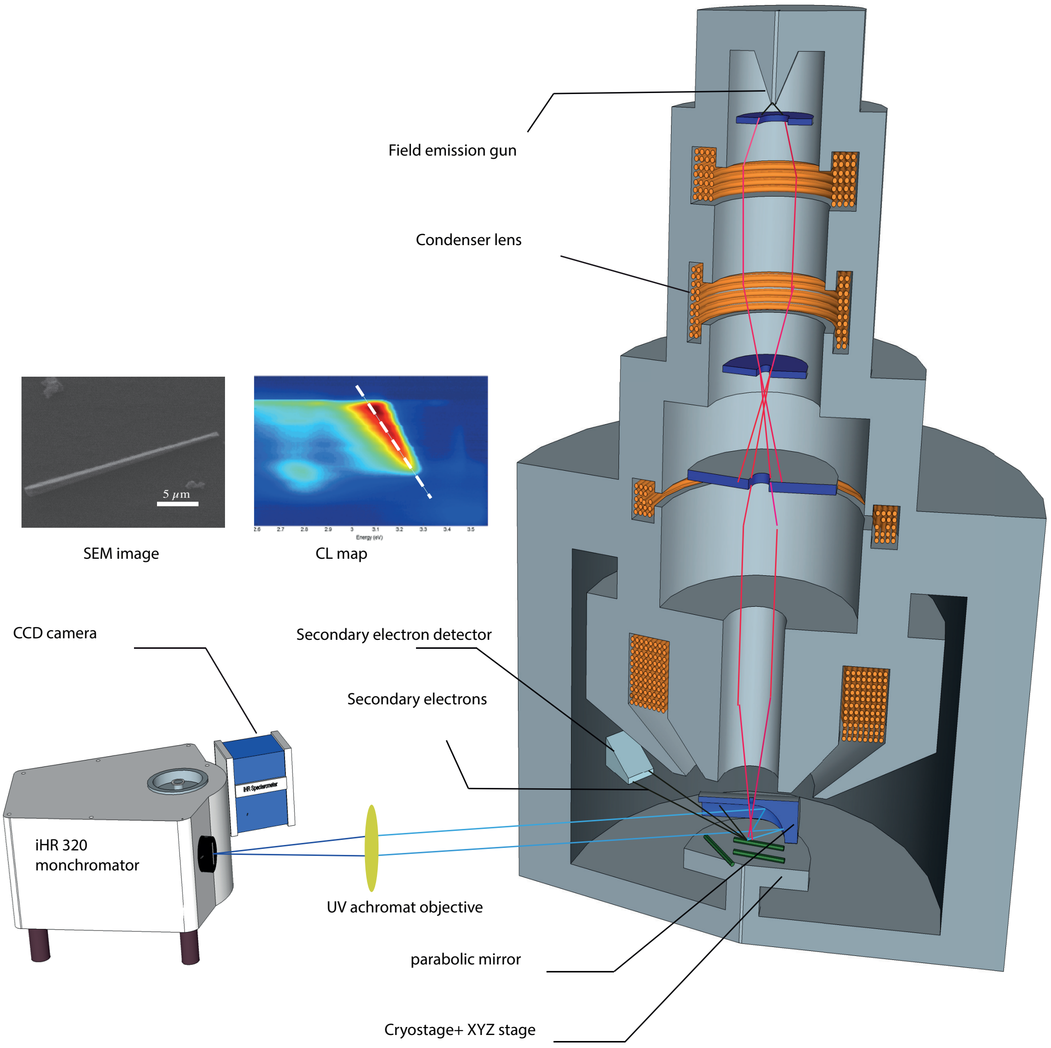

Figure 2.4 – Schematics of the cw-CL set-up: electrons are emitted from a field emission gun and accelerated along the column of the microscope. The CL is collected by a parabolic mirror and sent to a monochromator equipped by a CCD. The inset shows the SEM and the CL linescanning spectra for an InGaN QW core-shell QW nanowire.

## 2.3 Time resolved cathodoluminescence

In the previous two sections, the two experimental systems, i.e., tr-PL and cw-CL techniques, were briefly introduced. As it was mentioned, each technique has its own advantages and limits: wheres tr-PL can provide us a good temporal resolution, it is limited in the spatial resolution, while the cw-CL technique having good spatial resolution, provides no temporal information. The purpose of the tr-CL is to combine the temporal resolution of tr-PL (a few ps) with the spatial resolution of cw-CL (a few nm), to obtain a more clear image of the underlying physics of the investigated semiconductor nanostructures (cf. chapter 6 and 7 for applications).

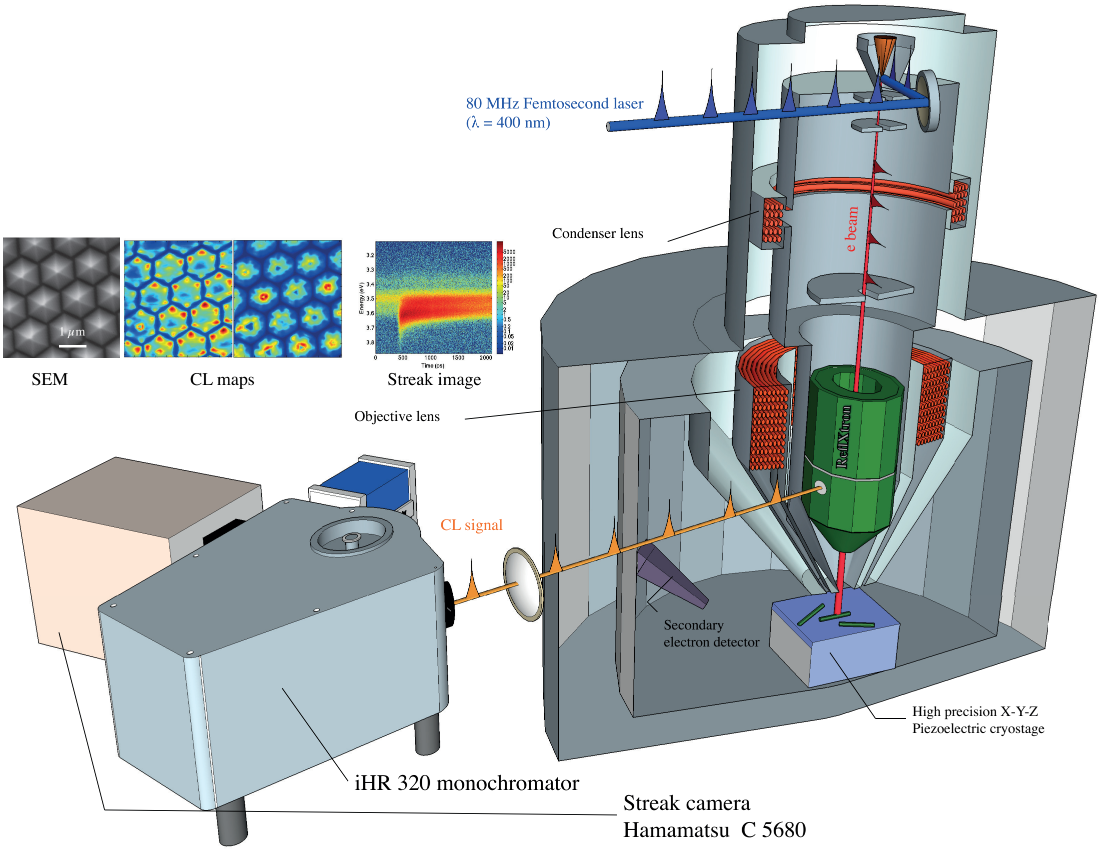

Figure 2.5 – Schematics of the tr-CL set-up, where the second harmonic of a fs pulsed Ti: Sapphire laser is focused on the tip of the electron microscope to create electron pulses. The electrons are then accelerated along the column of the microscope. The CL is collected by the integrated optics inside the electron microscope column and dispersed in a monochromator followed by a streak camera for energy and time resolved analysis. A SEM image of some GaN pyramids, and the corresponding CL intensity maps for different emission energies as well as the recorded streak image are shown.

The first realization of a tr-CL with a time resolution in the nanosecond scale has been reported by [69], where electron pulses were obtained by a beam blanking technique, i.e., the electron beam was deflected by an electric field oscillating perpendicularly to the column of the electron microscope. However, technically, the length of these electron pulses cannot be below several ns. The latter put a limit on the observation of dynamics that occurs at time scale faster than ns. For instance, the dynamics of excitons in bulk GaN trapped by point or extended defects occurs within 100 ps [70, 71], and such long pulses do not allow for the study of charge carrier transport.

Alternatively, one can use the short optical pulses (few ps/fs) to pulsed electron beam taking the advantage of the photoelectric effect. The first successful demonstration of this technique was reported in Ref. [72], where a pulsed electron beam was obtained, exciting a 50 nm thick gold photocathode by the third harmonic of a mode-locked Ti: Sapphire. The extracted electrons are then accelerated along the column of the microscope with an acceleration voltage set between 3 and 10 kV and focused on the surface of the sample. In this thesis, we have used an Attolight Alalin Chronos 4027 microscope to perform the tr-CL measurements (see Fig. 2.5). The integrated optics within the microscope column, with its large numerical aperture, allows performing measurements in a much more efficient way. The brighter electron source of the microscope, with designed electron optics to reduce the cross over points in the electron column helps also to have higher excitation density and therefore, a higher signal to noise ratio compared to the first demonstrated experimental system.

Compared to cw-CL setup, the main drawback of this tr-CL apparatus is the low current of the probe, while it is estimated to be below 1-10 pA. When increasing the electron density, the inelastic collisions of primary electrons can results in both temporal- and spatial-expansion of the electron beam. The latter impact was not verified experimentally in our system, while the laser excitation power was always kept by an order of magnitude below the damage threshold of the field emission gun of our electron microscope.

The CL spectra as well as streak images have been recorded in a pulsed mode operation (~1ps electron pulse, the repetition rate of 80.5 MHz, and average electron current ~10 pA). In all the measurements the excitation voltage was set to 6kV, which can provide a reasonable generation volume in order to have a good spatial resolution in our tr-CL measurements. The Attolight Alalin Chronos 4027 microscope, allows also switching from tr- to cw-CL operation by eliminating the laser excitation and heating the electron microscope gun, while in the previous version of the system, this was not possible.

Similar to our tr-PL setup, the luminescence is sent to a monochromator, which is equipped on one exit slit with a CCD camera to record the time-integrated spectra and on other exit with a Hamamatsu streak camera in synchronous mode to analyze temporally and spectrally the CL signal. The temporal resolution of the set-up has been measured by excitation at 300 K of a highly defective GaN layer. From the rise-time of GaN CL, which is expected to be of the order or below 1 ps, the temporal width of the electron pulses was estimated to be roughly 10 ps [72].

Finally, to be able to perform tr-CL measurements at low temperatures, our tr-CL microscope is equipped with a very low-vibration and low-drift cryogenic stage in close loop control configuration. The latter allows precisely addressing the desired points on a nanostructure with a resolution better than 100 nm, while small drifts during acquisitions could be compensated by simultaneous monitoring of the sample position *via* SEM image. This stage, consisting of a copper sample holder cooled down by liquid helium, allows us to routinely reach temperatures as low as 8 K.

# 3 High-injected GaN/AlGaN Quantum wells above the Mott transition

The content of this chapter deals with the PL investigation of single GaN/AlGaN quantum wells (QWs) under high injection conditions. The state-of-the-art quality of the investigated sample as well as the large binding energy of exciton in these QWs allows observing the well-defined excitonic levels and probing the PL properties over a wide range of carrier densities and temperatures. The arrangement of the chapter is as it follows. An introduction to the Mott transition, a brief literature review on biexciton recombination, and the modeling of the electron-hole plasma (EHP) PL lineshape will be provided in section 3.1. The modified details of the experimental framework compared to the PL experimental system introduced in the last chapter will be discussed in section 3.2. Afterwards, in section 3.3, the results of a high injection PL investigation of a GaN/AlGaN will be presented, with the main focus on the role of biexcitons at high carrier injections. In section 3.4, the temperature dependence of the Mott transition will be discussed with examining several criteria to define the Mott density. Eventually, the carrier dynamics at high injection densities, which gives evidence for the absence of Auger recombination in our investigated GaN/AlGaN QWs, will be presented.

The results shall be discussed in this chapter were previously published in the following papers:

- *Biexcitonic molecules survive excitons at the Mott transition*
M. Shahmohammadi, G. Jacopin, G. Rossbach, J. Levrat, E. Feltin, J.-F. Carlin, J.-D. Ganière, R. Butté, N. Grandjean, and B. Deveaud, Nat. Commun. **5**, 5251 (2014).

- *High-temperature Mott-transition in wide band-gap semiconductor quantum wells*
G. Rossbach, J. Levrat, G. Jacopin, M. Shahmohammadi, J.-F. Carlin, J.-D. Ganière, R. Butté, B. Deveaud, and N. Grandjean, Phys. Rev. B **90**, 201308 (2014).

## 3.1 The Mott transition

The metal-insulator transition in electron-hole (e-h) systems, the so-called Mott transition (MT), has attracted a lot of interest over the years, both theoretically and experimentally [73, 74, 75]. The importance of the MT arises from its close link with the onset of gain opening up the operation regime of conventional laser diodes, but also from the fact that it defines the crossover from bosonic to fermionic quasi-particles in a semiconductor medium. Therefore, it additionally sets the injection limit for the operation of polariton lasers [9, 10]. For instance, cavity-polariton condensation takes place below the MT, but relies on a very dense exciton gas already giving rise to saturation effects [9, 10]. In such a case, clear frontiers between quantum effects and conventional lasing due to gain arising from an inverted e-h population tend to wash out [10]. A similar motivation also exists for a potential condensation of excitons or exciton lasing [76, 77].

For device applications, a comprehensive understanding of the MT and thus of the electronic characteristics of III-nitride based QWs close to the transparency limit should provide essential information on the operating principle and the carrier-injection regime of blue lasers. A particular interest also arises in light-emitting diodes (LEDs), while the commonly observed and highly-debated efficiency droop of InGaN-based LEDs occurring at high driving currents [78, 79, 80].

Well-established theories exist for the dilute excitonic gas regime, i.e. insulating regime [81], as well as for the dense EHP regime, i.e. conducting regime [74]. However, a comprehensive theory for that encompasses these two density regimes, and even more importantly the transition between the two regimes, does not exist yet [13]. It is still debated whether the MT should be a first- or a second-order transition. There are some experimental reports that claim to evidence the first-order nature of the MT [82, 83], however, most of the experimental reports favor the second option based on the absence of any observation of a sharp threshold [84, 85, 86].

In the regime of low carrier density $n$, and for sufficiently low temperature, free electrons and holes in a semiconductor bind together and form neutrally charged quasiparticles, the so-called excitons. The excitons represent the fundamental electronic excitation of a semiconductor and obey Bose statistics in the low-density limit. However, when increasing temperature or $n$ beyond a certain limit, the exciton complexes get ionized and the system switches from an insulating state to a conductive EHP. The exciton dissociation induced by a hot phonon bath represents a classical process and occurs when the thermal energy becomes of the order of the exciton binding energy $E_X^b \approx k_B T$.

However, the ionization of excitons due to an increasing carrier population relies on much more complex mechanisms. The generally accepted picture of the semiconductor MT follows the idea of a complex interplay between phase space-filling effects, the progressive broadening of the resonance *via* collisions, and the screening of Coulomb interactions between the exciton constituents, when the carrier density increases. In simplified terms, when $n$ approaches the hard-sphere limit, that is, when the interparticle distance is reduced to the order of the exciton Bohr radius $a_B$ [73], the fermionic properties of the exciton constituents become dominant. Therefore, Coulomb screening and phase-space filling cause a reduction of the exciton binding energy $E_X^b$ and eventually around a certain critical density $n_{\text{crit}}$ the exciton energy coincides with the renormalized bandgap and the exciton resonance disappears within the broad response of the plasma [87]. Note that the hard-sphere limit can only provide a crude estimation of $n_{\text{crit}}$ , that is usually an overestimated value [76].

Figure 3.1, represent schematically the evolution of the exciton emission energy (black solid line), and its corresponding lower and upper half maximum energies (black dashed lines) as well as the expected bandgap energy (green) and electron-hole Fermi level separation (blue) as a function of the carrier density in a GaN/AlGaN QW. The parameters for this graph are the experimental values deduced for sample SQW-3, which will be investigated thoroughly in section 3.4. Various physical effects are involved in the variation of the exciton emission energy, that shall be discussed hereafter. Excitons consist of charged particles, interacting *via* Coulomb forces. Owing to the fermionic nature of exciton constituents, they interact with each other *via* both direct and exchange Coulomb interactions. It is usually assumed that the bandgap of continuum states monotonously redshifts with increasing the $n$, due to the interplay of exchange and multi-particle correlation effects [88, 89]. This renormalized bandgap is expected to follow a cubic-root density dependence in 2D and 3D systems according to [86, 90, 90]:

$$E_{\text{BGR}}(n) = E_X(0) + E_X^b(0) + \Delta E_{QW}(n) - \alpha_{\text{BGR}} n^{1/3}, \tag{3.1}$$

where $E_X(0)$ and $E_X^b(0)$ denote the exciton emission energy and the exciton binding energy at zero carrier density, and the term $\Delta E_{QW}(n)$ denotes the density-dependent of the QW bandgap, mainly affected by the screening of the built-in electric field in the QW. The term $\alpha_{\text{BGR}}$ denotes a material and dimensionality dependent constant, which can be estimate in 2D system [90]:

$$\alpha_{\text{BGR}} = 3.1.a_B^{2/3} E_X^b. \tag{3.2}$$

At the same time, the exciton binding energy is expected to decrease due to the mutual effect of the phase-space filling and carrier-carrier interactions [87]. Some works predict a linear density dependence for the exciton bing energy [92, 93], however, most of the experimental reports evidence only a marginal shift of the exciton energy up to very high carrier densities [86, 94, 95]. This independence of the exciton energy to the carrier density can be interpreted as a perfect compensation between the BGR and the reduction of exciton binding energy.

Figure 3.1 – Schematics of the Mott transition defining criteria according to $E_X = E_{\mathrm{BGR}}$ and $\Delta E_{\mathrm{F}} = E_{\mathrm{BGR}}$. The Mott density corresponding to these criteria are marked by red dashed lines. $E_X$ is given by the black solid line and the gray dashed lines mark upper and lower QW half maximum energies (adapted from Ref. [91]).

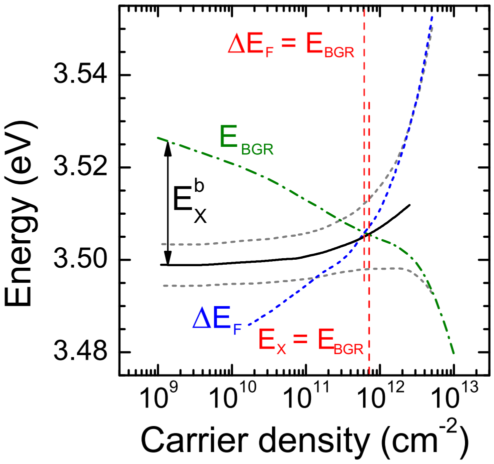

Considering the quantum confined Stark effect (QCSE) in our investigated *c*-plane QWs, both exciton emission energy and exciton binding energy can be modified when increasing the carrier density. Screening of the QCSE directly leads to blueshift of the QW ground state. At the same time, increase of the electron-hole wave-function due to QCSE screening leads to an increase of the exciton binding energy, and correspondingly increases the complexity of the problem. Therefore, neglecting the reduction of the exciton binding energy due to exchange between carriers, one can write:

$$E_X(n) = E_X(0) + \Delta E_{QW}(n) - \Delta E_X^b(n) = E_X(n) + \Delta E_{QCSE}^X(n). \tag{3.3}$$

In that case, one can simply define a criterion for the Mott transition as:

$$E_X(n_{crit}) = E_{\mathrm{BGR}}(n_{crit}). \tag{3.4}$$

The crossing between $E_X$ and $E_{\mathrm{BGR}}$ means the density at which the exciton merges with the continuum states, i.e., when the exciton binding energy $E_X^b$ vanishes and the exciton resonance disappears within the broad response of the plasma [89, 88].

Another criterion for the Mott transition can be defined according to the transparency limit $\Delta E_{\mathrm{F}} = E_{\mathrm{BGR}}$, i.e., when the quasi-Fermi level separation exceeds the band-edge. The latter defines also the onset of gain from an EHP [96], a purely fermionic effect that excludes any excitonic absorption at the band-edge. As can be seen in Fig. 3.1, both criteria lead to similar threshold densities.

Some other criteria based on, for instance, the lineshape and the high energy slope of the QW emission were examined in our study to define the Mott density, and will be discussed in detail in section 3.4.

### 3.1.1 The role of biexcitons in the Mott transition

Interestingly, even if biexcitons are frequently seen to dominate the emission of semiconductor structures when $n$ is raised according to the mass action law, and this is particularly true for GaN-based heterostructures [12], no clear experimental report is available on the role of biexcitons in the MT in a two-dimensional (2D) systems. A comprehensive study treating the MT in the presence of biexcitons can only be found for T-shaped GaAs-based quantum wires [14].

There are some other reports in the literature about the important role of biexciton at high-injected direct bandgap semiconductors. For instance, the observed gain at the transparency limit in ZnCdSe/ZnSe multiple QWs by means of pump-probe measurements [97], that was attributed to the biexciton transition. Another example can be the observed biexcitonic transition and the electron hole plasma *via* time-integrated PL in CdTe/CdMnTe multiple QWs, performed by means of quasi cw-PL measurements [98].

Nevertheless, the above-mentioned works are based on experiments carried out on multiple QW structures and therefore suffer from mixing various carrier densities in the different QWs due to the variation of the absorption profile in depth of the sample . This problem can be significant also in the case of time integrated PL measurements. Hence, it is hard to extract some conclusive and quantitative information from these reports since they integrate the photoluminescence signal over a large range of carrier densities. Nevertheless, both reports suggest the possibility of robust biexciton transitions at high carrier densities in II-VI compounds.

The same argument is valid for experimental reports based on optically-probed bulk systems, whereas the exponential absorption profile leads to an emission signal that mixes inhomogeneously injected regions and may conceal certain characteristics of the MT. This drawback can be circumvented in 2D systems, where the excitation profile density can be clearly identified both laterally and vertically [94].

Considering the hard-sphere approximation, the $n_{\mathrm{crit}}$ for the injection-induced dissociation of biexcitons is expected to be smaller than its excitonic counterpart owing to the larger biexciton Bohr radius [99]. In section 3.3, the results of a high-injection PL investigation on samples featuring the biexcitonic transition, and a crossover between a mixed exciton-biexciton gas and a conductive EHP will be discussed. Our experiments directly address the dynamics and stability of biexcitons in the high carrier-density regime, and highlight the need of development of new theories for getting a comprehensive understanding of the operation mechanism of nitride-based blue lasers.

### 3.1.2 Temperature dependence of the Mott density

There are few experimental studies concerning the temperature dependence of the MT. In a simple framework, an increasing Debye-screening length gives good reasons to expect a rise in $n_{\mathrm{crit}}$ with temperature. Even if such a behavior was claimed for bulk Ge in Ref. [86], controversial reports exist in the literature, due to the inconsistencies arising when the MT is described by static screening [76], and the expected impact of dynamic screening effects [87, 100]. Hence, the MT and in particular its temperature dependence require further experimental investigation owing to its importance.

Wide bandgap semiconductor QWs provide an ideal system, in which to study Coulomb correlations such as excitons and biexcitons since the relatively small dielectric constant and large effective masses result in binding energies of the order of few tens of meV [101]. Such large binding energies are comparable to both the room temperature thermal energy $k_B T$ and the LO-phonon energy. The results of the temperature dependence of the MT will be discussed in section 3.4 of this chapter, while the results of an investigated GaN/AlGaN Qw with narrow emission linewidth and large $E_X^b$ of about 30-40 meV will be represented over a wide range of the temperature from $0K$ up to $150K$. The dominant radiative recombination over the whole studied temperature range is warranted by the high quality of the sample.

### 3.1.3 Model of the EHP emission lineshape

In order to model the EHP emission, we employed a pure fermionic model in our study to reproduce the lineshape of the QW emission spectrum. This model allows deducing precisely the carrier density $n$ and the carrier temperature $T_{\mathrm{car}}$ in the QW. The details of this model are the followings: the matrix element is assumed to be independent of the wave vector $k$. Thus, the spontaneous recombination rate $R_{spont}$ can be written as:

$$R_{spont}(E) \propto \sum_{j=A,B} \frac{1}{\tau_{rad,j}} D_j^{cv} . f_{e,j}(E) f_{h,j}(E), \tag{3.5}$$

where $f_e$ and $f_h$ are the conduction and valence band Fermi-Dirac functions, respectively, $\tau_{rad,j}$ is the $k$-independent radiative decay time for the different transitions j, $D_j^{cv}(E)$ denotes the 2D joint density of states convoluted with a Gaussian function for taking into account the inhomogeneous broadening of the emission from the QW. The A and B denotes the contribution of the heavy-hole (HH) and light-hole (LH) valence band. The transitions were assumed to be separated in energy with a difference deduced from our PLE measurements, and to have identical radiative decay times according to the almost equal oscillator strengths observed in PLE measurements. Following momentum conservation the electron and hole

Fermi-functions are defined by:

$$f_{e,j}(E) = \left[\exp\left(\frac{\frac{m_{h,j}}{m_{e,j}+m_{h,j}}(E-E_m)-E_{f,e}}{k_B T_{\text{car}}}\right)+1\right]^{-1}, \tag{3.6}$$

$$f_{h,j}(E) = \left[\exp\left(\frac{\frac{m_{e,j}}{m_{e,j}+m_{h,j}}(E-E_m)-E_{f,h}}{k_B T_{\text{car}}}\right)+1\right]^{-1}, \tag{3.7}$$

where $E_{f,e}$ and $E_{f,h}$ denote the respective electron and hole quasi Fermi-energies. For a single conduction and valence band, $E_{f,e}$ and $E_{f,h}$ are simply defined by [102]:

$$E_{f,e} = k_B T_{\text{car}} \ln\left[exp\left(\frac{\pi\hbar^2 n}{m_e k_B T_{\text{car}}}\right)-1\right], \tag{3.8}$$

$$E_{f,h} = k_B T_{\text{car}} \ln\left[exp\left(\frac{\pi\hbar^2 n}{m_h k_B T_{\text{car}}}\right)-1\right]. \tag{3.9}$$

Here, $k_B$, $\hbar$, and $e$ represent the Boltzmann-constant, the reduced Planck-constant, and the elementary charge of the electron, respectively. However, when including two non-degenerate valence bands, the $E_{f,h}$ calculation requires an iterative approach to account for the sum of the density of states of each of the valence bands, the total carrier density, and the carrier temperature. The effective electron and hole masses in the QW-plane were estimated from the $k.p$ simulations.

Eventually, there is a lifetime-broadening effect evidenced on the low-energy side of the PL spectra at high injection densities (see Fig. 3.2(a), for the results obtained on sample SQW-1, which will be discussed in details in section 3.3). In order to account for this lifetime-broadening mainly induced by carrier-carrier scatterings, the PL spectra have been convoluted with a Lorentzian of energy-dependent width $\Gamma$. To take into account the variation of this lifetime broadening with emission energy, Landsberg suggested a rather complex function [103]. Its application was only justified by the close agreement of the experimental results and the computed lineshape. Since a full theoretical interpretation of the broadening of the low-energy side still has to be given [104], we have preferentially chosen a simple Gaussian function in agreement with [105, 106] in our analysis, which its value is maximum at $E_m$ and reduces to a nonzero value at $\Delta E_\text{F}$, where $\Delta E_\text{F} = E_m + E_{f,e} + E_{f,h}$ denotes the separation of the quasi-Fermi levels of electrons and holes. A good agreement was observed between the experimental spectra and the modeled lineshape, applying this simple phenomenological function for the energy dependence of the homogenous broadening. Nevertheless, It worth commenting that this broadening function mainly affects the fitting on the low energy tail

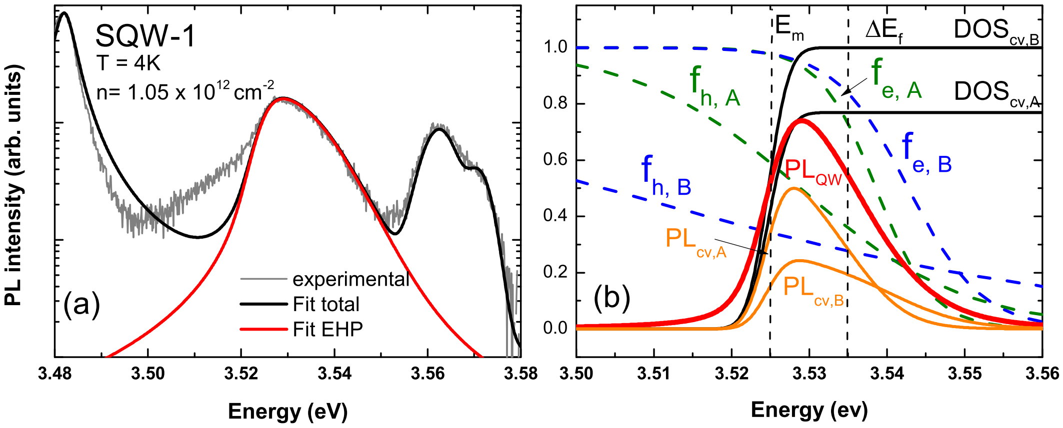

Figure 3.2 – **(a)** tr-PL spectrum obtained at a delay time of 250 ps after the excitation for sample SQW-1, under high injection condition at T= 4K (gray), compared to the electron-hole plasma modeling (black). The emission spectrum of the QW is fitted with a degenerate EHP profile considering Fermi filling of the conduction and valence bands with effective electron and hole masses taken equal to $m_e^* = 0.2m_0$, $m_A^* = 1.8m_0$, and $m_B^* = 0.45m_0$, as deduced from k.p simulations. The carrier density was estimated be around $1.05 \times 10^{12} cm^{-2}$. In order to reproduce the full PL spectrum, the barrier emission at about 3.56 eV was modeled by two Gaussian functions, and a Lorentzian function was used to account for the emission of the GaN substrate at 3.48 eV. A good agreement was observed between the modeled and experimentally observed emission lineshape of the QW. **(b)** The electron and hole Fermi distribution for A (B) valence band are shown in green (blue) dashed lines. The position of the modeled bandgap $E_m$ and the separation of the electron-hole Fermi level is marked by black dashed lines. The black solid lines show the joint density of states corresponding to A and B valence band. The PL stem from contribution of each valence band (orange) and the sum of the two (red) are also shown.

of the PL spectrum, and has a marginal effect on the fitting results, and in particular on the deduced carrier densities.

The fitting parameters, then, are the carrier bath temperature $T_{\mathrm{car}}$, the two-dimensional carrier density n, the modeled bandgap $E_m$, the homogenous broadening $\Gamma$, and a scaling factor to match the experimentally observed PL amplitude. As already indicated, the accuracy of the present modeling critically depends on the homogeneity of the probed carrier density. Along the growth axis this condition is naturally fulfilled by the single QW structure, whereas laterally the spatial filtering ensures collection from the homogeneous center of the excitation spot only. Figure 3.2(a) shows the results of this lineshape fitting for sample SQW-1, under high injection condition. The electron and hole Fermi distribution for A (B) valence band are shown in green (blue) dashed lines. The black solid lines show the joint density of states corresponding to A and B valence bands. The PL stems from contribution of each valence band (orange) and the sum of the two (red) are also shown.

## 3.2 The experimental framework

To study the sample at high carrier injection, both cw-PL and tr-PL experiments have been performed. Power-dependent PL spectra have been recorded by exciting the sample with a frequency-doubled cw $Ar^+$-laser ($\lambda$ = 244 nm). For tr-PL experiments, the sample was excited with the third harmonic ($\lambda$ = 280 nm) of a picosecond mode-locked Ti:sapphire laser. The excitation beam was focused on the sample by means of a 3 mm focal length UV objective (NA = 0.55), that allows for an excitation spot diameter below 5 $\mu m$.

A key issue for the present measurements, where the luminescence signal critically depends on the excitation power density, is to carefully position a spatial filter in the collection path. To have a homogeneous excitation density, the center of the PL spot on the sample was 100 times magnified and sent through a 50 $\mu m$ pinhole placed in the collection line, which allowed us to probe a region with a quite uniform excitation density. It is worth noticing that slightly misplacing the spatial filter leads to the contribution of a wide range of carrier densities in the PL signal critically concealing the main characteristics of the MT. While the mentioned spatial filtering well define the carrier density distribution in the lateral direction, using single QWs in our investigation yield a unique carrier distribution along the depth of the sample.

The collected PL was analyzed spectrally and temporally using a 32 cm focal length monochromator equipped with a CCD and a streak camera. A 600 and 1200 groove/mm grating were used to disperse the PL spectra, which allows us to reach a spectral resolution better than 1 meV. For the tr-PL analysis, the streak camera was used with a temporal resolution of about 5 ps in synchronous scan mode.

## 3.3 The role of biexciton in the Mott transition

In this section, by probing two thin and high quality single GaN/AlGaN QWs at high-injection densities, we will investigate the role of the biexcitons in the Mott transition. The difference between the samples probed in this section (named SQW-1 and SQW-2) and the one in the section 3.4 (SQW-3), is the presence of the biexciton in the former ones, while, due to QCSE effect (see discussions in section 3.3.8), the biexciton transition is suppressed in the latter one.

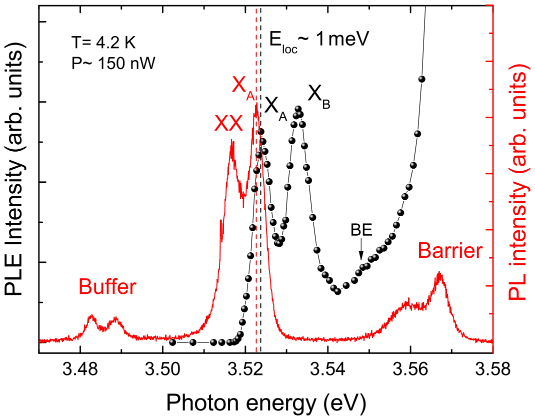

Figure 3.3 – PLE (black dots, solid line is a guide to the eye) and PL (red solid line) spectrum of SQW-1 at moderate excitation. The localization energy of ~1 meV is deduced by comparing the exciton energy in the PLE and the PL spectra.

### 3.3.1 Sample structure

The sample investigated here (SQW-1) is a 3 nm thick GaN/$Al_{0.05}Ga_{0.95}N$ single QW grown by metal organics vapor phase epitaxy (MOVPE) on a *c*-plane sapphire and sandwiched in between GaN/$Al_{0.05}Ga_{0.95}N$ barriers with respective top and bottom barrier thicknesses of 50 nm and 200 nm. The *c*-plane sapphire substrate was overgrown by a 3 $\mu m$ thick GaN buffer layer prior to the growth of the QW. More details on the growth of this sample can be found in Ref. [107].

The high quality of the sample SQW-1 is confirmed by the small localization energy of about 1 meV, deduced from the energy difference between the PL and the excitation PL (PLE) measurements (see Fig. 3.3). The PLE spectrum of the sample, shown by black color in Fig. 3.3, contains two fundamental transitions of the QW at 3.534 eV and 3.545 eV attributed to $X_A$ and $X_B$ excitons, respectively. The barrier absorption appears as a strong absorption in the PLE spectrum at about 3.560 eV. The small kink in the PLE intensity that appears right before the barrier signature might originate from the continuum band-edge (BE) transition in the QW. Indeed, its energy position is in good agreement with the estimated exciton binding energy in our structure. Nevertheless, the strong absorption of the barrier hampers a conclusive assignment to this transition.

The small localization energy, in addition to the narrow emission linewidth of the QW (~ 5 meV) allow us to observe the biexciton (XX) transition, that appears at the low energy side of the exciton transition. As shown in Fig. 3.3, the PL spectrum recorded at a moderate injection density (red) is dominated by $X_A$ transition at 3.533 eV, and XX transition at about 8 meV below the exciton transition at 3.525 eV.

The exciton binding energy $E_X^b$ in our sample was estimated to 30 meV, deduced from a Schrödinger-Poisson (SP) simulation according to Ref. [10]. Indeed, the reduced electron-hole wave-function overlap due to the QCSE was considered within this model. This effect is more prominent at low carrier densities, while increasing the $n$ can progressively screen the electric field in the QW. Indeed, when raising the carrier density, other impacts such as the carrier-carrier interaction on the exciton binding energy should be considered. However, these effects are neglected in our SP simulations.

Assuming the electric field in the QW to be 180 kV/cm [50], the $E_X^b$ deduced from these SP simulations of about 30 meV at zero carrier densities. The biexciton binding energy $E_{XX}^b$ can be estimated from the energy difference between the exciton and biexciton transition, which is given by:

$$E_{XX}^{PL} = E_X^{PL} - E_{XX}^b, \tag{3.10}$$

where $E_{XX}^{PL}$ and $E_X^{PL}$ denote the respective PL emission energy of the XX and $X_A$ transition. From our cw-PL measurements (cf. Fig. 3.4 (a)), $E_{XX}^b$ amounts to around 8 meV. It worth mentioning that, in the presence of a large localization energy, more complicated considerations should be considered to estimate the $E_{XX}^b$ from PL energies [108], while the localization energy can be different for excitons and biexcitons. However, thanks to the negligible localization energy in sample SQW-1, we can safely exclude this effects. Applying more complicated line-shape modeling for the biexciton emission (as it will be discussed in section 3.3.3), however, will not modify significantly our estimated value of $E_{XX}^b$.

Therefore, the ratio of the exciton binding energy to that of the biexciton in our sample is about 0.26, a value close to the 0.228 expected for weakly disordered structures [109, 110]. This confirms that the luminescence in our sample stems from free excitons and their biexcitonic counterparts at low densities.

### 3.3.2 Continuous wave PL measurements

The biexciton transition was identified from our power dependent cw-PL measurements. As shown in Fig. 3.4(a), at low excitation densities, the PL emission of the SQW-1 is dominated by a single narrow emission at 3.533 eV attributed to $X_A$ exciton. The substrate emission can be identified as the emission at 3.480 eV, while the emission lines at around 3.560 originate from the $Al_xGa_{1-x}N$ barriers ($x$=5%). Increasing the excitation power, the biexciton peak at low-energy side of the QW starts to increase super-linearly with respect to the PL intensity of the $X_A$. The PL intensity of the QW emissions at 3.533 and 3.525 eV, deduced from a careful fitting to the PL spectra at different excitation power densities are plotted in Fig. 3.4(b). The measured slope of ~1 and ~2 for the PL intensities versus the excitation power confirm the origin of these two emissions: 3.533 is attributed to $X_A$, while the emission at 3.525 eV originates from biexciton emission. Indeed, due to the mass action law, the biexciton density is proportional to square of the exciton density at equilibrium [108, 111]. In addition to the power dependence in our cw-PL measurements, the origin of the biexciton transition in SQW-1 was further confirmed from our forthcoming tr-PL measurements (section 3.3.4), and from the dependence of the $E_{XX}^{b}$ to the QW thickness due to QCSE (section 3.3.8). The impact of QCSE on the biexciton binding energy was thoroughly investigated in the same sample in Ref. [11].

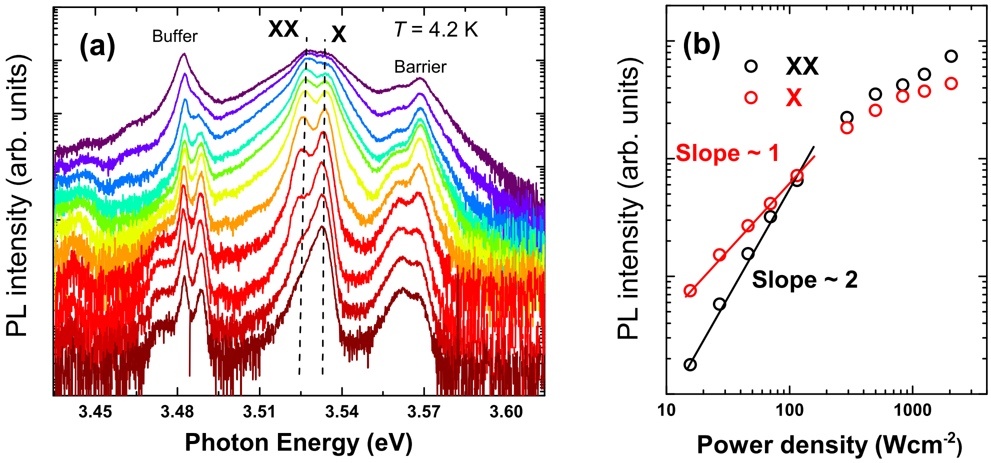

Figure 3.4 – **(a)** Power dependent PL spectra of the sample under cw laser excitation. The excitation power density changes from 3 $W/cm^2$ up to 3000 $W/cm^2$ from the lowest to the highest spectrum, respectively. **(b)** PL intensity of the exciton (red) and biexciton (black) peaks as a function of excitation power density. The linear and quadratic dependencies of the exciton and biexciton PL intensities at low injection confirm the assignment of these two peaks to excitons and biexcitons, respectively.

Another aspect of our cw-PL measurements is the onset of hot carrier effects, when raising the excitation power. Indeed, an increase of the injection power density, in our cw-PL measurements, leads directly to an increase of the carrier density in the QW, but also raises the temperature of carriers owing to the constant feeding of hot carriers in the QW. The latter effect appears as an increase in the slope of the high-energy tail of the QW emission (see Fig. 3.4(a)). At the same time, as the high energy tail of the QW reaches the barrier energy, a clear change in the slope of high energy tail of the barrier emission emerges. This observation can be understood as an efficient carrier exchange between the QW and the barrier at high injection densities.

In order to reach the Mott density in cw-PL measurements, one needs to overcome the leakage of hot carriers to the barrier at high injection power densities and the short radiative lifetime of carriers in SQW-1. Whereas, applying those injection power densities causes the heating of the sample. Therefore, employing the lineshape fitting according to an EHP emission model is not fully applicable to our cw-PL spectra, even though the onset of saturation in the PL intensity has already appeared in the last two high excitation density spectra. Note further that at the highest excitation power, the biexciton transition is clearly distinguishable, which provides a clear contrast to the intuitive picture of a lower biexciton stability due to its reduced binding energy.

### 3.3.3 Lineshape fitting of the exciton and biexciton transitions

It worth commenting on our lineshape fitting to the biexciton emission at low and moderate injection power densities. Although, a simple Voigt function was applied to fit the exciton and biexciton lineshape in all our study, more complicated models could be considered. Indeed, the difference between the effective mass of exciton and biexciton leads to a difference in their dispersion curves (see Fig. 3.5(a)). In the two- dimensional (2D) case, the energy of biexciton before recombination and for a given in-plane $k$-vector ($k_{\parallel}$) is given by:

$$E_{XX} = 2E_X - E^b_{XX} + \frac{\hbar^2 k^2_{\parallel}}{2M_{XX}}, \tag{3.11}$$

where $E_X$ denotes the exciton energy, $M_{XX}$ and $E^b_{XX}$ denote the biexciton effective mass and binding energy, respectively. For exciton, the energy can be given by:

$$E_X = E_{X0} + \frac{\hbar^2 k^2_{\parallel}}{2M_X}. \tag{3.12}$$

For a reasonable approximation, the biexciton effective mass can assumed to be twice of the exciton effective mass $M_X$. For the case in which $k_{\parallel}$ is greater than the photon momentum, after recombination of a biexciton, the total energy is $\hbar\omega + E_X + \hbar^2 k^2_{\parallel}/2M_X$, which gives the photon energy as:

$$\hbar\omega = E_X - E^b_{XX} + \frac{\hbar^2 k^2_{\parallel}}{4M_X}. \tag{3.13}$$

Considering a Boltzmann distribution of kinetic energies, this leads to a model lineshape for biexciton with a characteristic thermal tail on its low-energy side according to [112, 113, 114]:

$$I_{XX}(E) = I_0 exp\big[-\big(\frac{\hbar^2 k^2_{\parallel}}{4M_X}\big)/k_B T\big] = I_0 exp\big[-\frac{E_X - E^b_{XX} - E}{k_B T}\big], \quad \text{for } E < E_X - E^b_{XX}, \tag{3.14}$$

with a sharp cutoff at $E_X - E^b_{XX}$, corresponding to the limit of biexciton zero kinetic energy.

Figure 3.5(b-f) shows the results of the fitting of cw-PL spectra, when the carrier injection density varied over one order of magnitude. The biexciton binding energy and carrier bath temperature were tuned as fitting parameters. Despite the simplicity of the model, a good

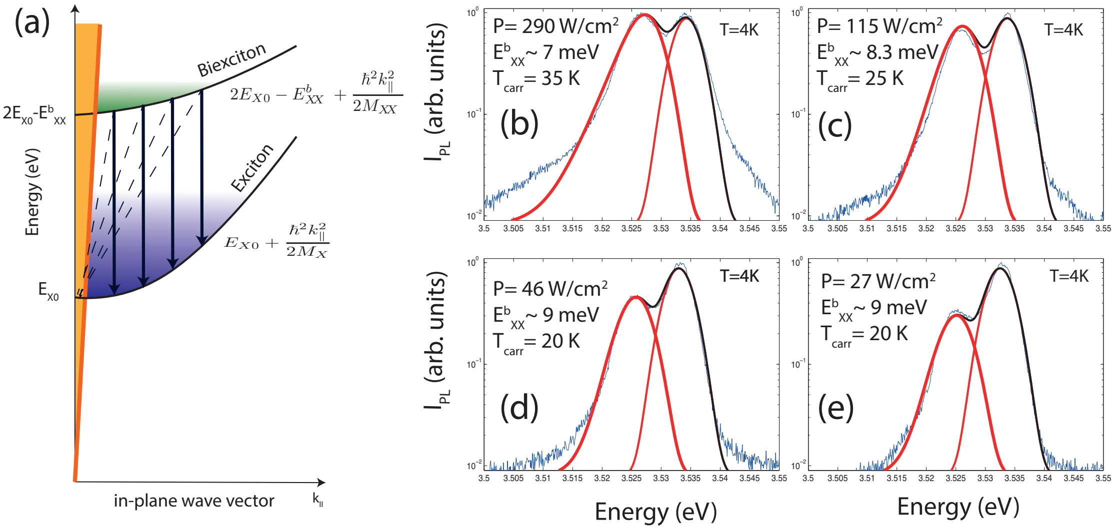

Figure 3.5 – **(a)** Schematics of biexciton recombination: the recombined biexciton leaves one exciton with the same k-vector on the excitonic branch and one exciton in the light cone, which recombine radiatively. The light cone is shown by orange solid line. **(b)** The results of the lineshape fitting for cw-PL spectra at moderate injection densities. The total fitted lineshape is shown in black and PL lineshape of the exciton and biexciton emission is shown in red.

agreement was observed between the modeled lineshape and the experimentally obtained spectra. Nevertheless, the biexciton binding energy estimated from this fitting does not vary significantly from the one extracted by fitting of the exciton and biexciton emission simply with two Voigt functions: the estimated value from this lineshape fitting varies between 7 meV to 9 meV, which is in close agreement with the deduced value from fitting with Voigt functions (~8 meV). There might be some uncertainty in the estimated value, due to other homogenous or inhomogeneous broadenings neglected in this model. Since, the results of our fittings are marginally affected by these details, in our study we preferentially chose Voigt functions for fitting the exciton and biexciton lineshape.

### 3.3.4 Time resolved PL measurements

In this section, we will discuss the results obtained by tr-PL measurements. Owing to the low repetition rate of the laser excitation, it is possible to reach a higher carrier density with such measurements without heating the sample. The representative streak image recorded at 4.2 K is shown in Fig. 3.6. The excitation laser pulse arrives at zero time delay with a peak excitation density of 150 $\mu J/cm^2$.The emission energies of the substrate, the barrier and the exciton and biexciton are labeled on the streak image. The QW emission undergoes dramatic time-dependent changes: whereas it is a broad emission at early delays, extended up to the barrier energy, its linewidth narrows with increasing delay time and it converts to two narrow emission lines at long delay times.

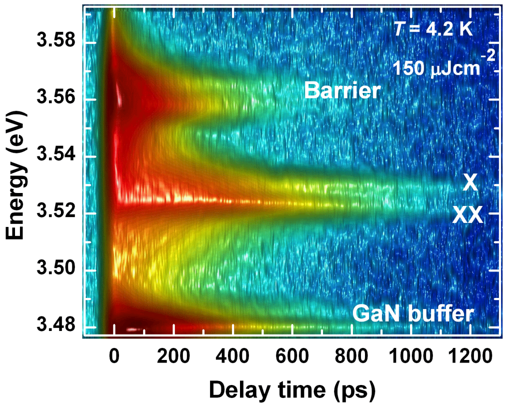

Figure 3.6 – Streak image of the tr-PL measurements recorded at 4.2 K. The GaN buffer layer, exciton, biexciton and barrier emission energy are labeled. Note that the color code was not provided due to the lightening effect that has been applied to enhance the visibility of the XX transition at longer delays. The quantitative data extracted from this streak image are represented in Fig. 3.7.

To reveal better the dynamics, the PL spectra from the streak image in Fig. 3.6 corresponding to different time delays are depicted in Fig. 3.7(a). The PL intensity decay corresponding to energies of $X_A$, XX and barrier are plotted in Fig. 3.7(b). The PL spectrum measured 50 ps after the excitation (the uppermost spectrum) features a broad plateau-like emission, extending from the QW emission energy up to the emission energy of the barrier. This saturation of the PL spectrum in energy evidences the $k$-space filling of the constant 2D density-of-states (DOS), i.e. the presence of a degenerate EHP in the QW [94]. At longer times delays, the carrier density in the QW reduces through radiative recombination of the e-h pairs. At time delays up to 300 ps, while the PL spectrum has still the saturation characteristics on the low energy side of the QW emission (see Fig. 3.7(a)), the high-energy emission of the QW shrinks down progressively, following to the decrease in the carrier density in the QW.

A line-shape fitting based on the EHP model, discussed in section 3.1.3, can still reproduce the PL spectra up to this time delay. The result of this fitting is exemplified by the black curve in Fig. 3.7(a). The A and B valence bands were considered to be separated by 11 meV in energy, a value deduced from our PLE measurements. The effective masses of the electron and holes in the A and B valence band were taken equal to $m_{e^*} = 0.2m_0$, $m_A^* = 1.8m_0$, and $m_B^* = 0.45m_0$, respectively, following $k.p$ simulations, with $m_0$ denoting the free electron mass. This fitting allows the pair density in the QW to be extracted precisely, and the agreement between modeling and experimental data confirms the dominant fermionic nature of the carriers at these time delays in our tr-PL measurements. Notice that the above-mentioned modeling is only applicable for carrier densities above the critical density of the Mott transition, i.e. when luminescence stems from the EHP.

Surprisingly, only for time delays longer than 300 ps, a distinct peak at the biexciton energy appears. Even though, we cannot observe the band-edge emission in our samples, the pure exponential tail of the QW emission at this time delay indicates the dominant population of

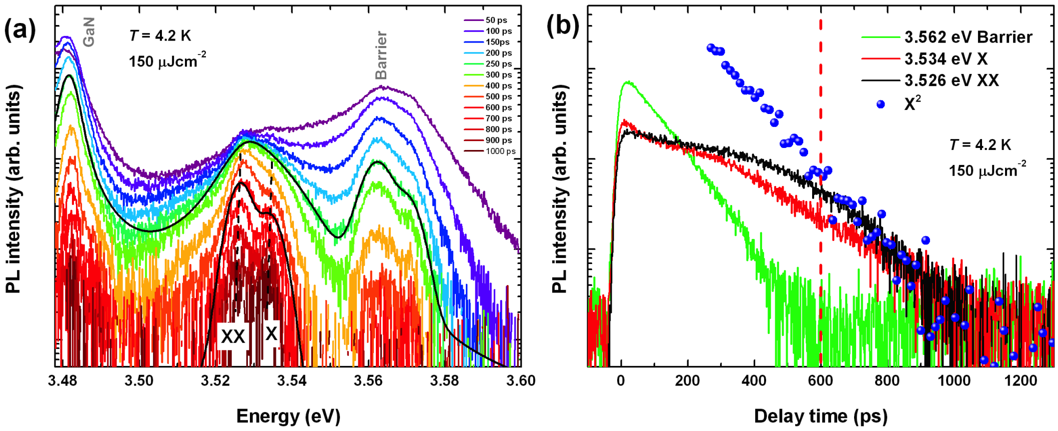

Figure 3.7 – **(a)** tr-PL spectra at different time delays from 50 to 1000 ps in semi-logarithmic scale at T = 4.2 K, extracted from streak image in Fig. 3.6. The estimated carrier density (in $cm^{-2}$) in the QW corresponding to each spectrum from the upper to the lower one, respectively, is equal to: $2.83 \times 10^{12}$, $2.20 \times 10^{12}$, $1.73 \times 10^{12}$, $1.37 \times 10^{12}$, $1.07 \times 10^{12}$, $8.40 \times 10^{11}$, $5.02 \times 10^{11}$, $3.00 \times 10^{11}$, $1.85 \times 10^{11}$, $1.16 \times 10^{11}$, $7.51 \times 10^{10}$, $4.96 \times 10^{10}$, $3.22 \times 10^{10}$. For the PL spectra at 250 and 600 ps time delay, fittings with the EHP lineshape model and two Voigt functions are shown for comparison (black).**(b)** Decays of the PL intensity corresponding to the energy of the biexciton (3.526 eV), the exciton (3.534 eV) and the barrier (3.562 eV) in semi-logarithmic scale. The square of the PL intensity at the exciton energy (blue spheres) is also reported to show the thermodynamic equilibrium between excitons and biexcitons at long delays after the excitation. The red dashed line shows the delay time at which thermodynamic equilibrium between excitons and biexcitons is reached.

fermionic carriers at this time delay [94]. At still longer delays, however, the QW emission linewidth reduces continuously and a peak at the exciton energy position appears. In other words, when raising the carrier density in the QW, the excitonic resonance disappears at a smaller carrier density than the biexcitonic one. This observation stands in contrast to the intuitive expectation exposed above: high-density effects should first screen the biexciton resonance, because of its larger Bohr radius and its smaller binding energy[99, 109]. It is also noticeable that the EHP evolves from the biexciton resonance and not from excitons as the low energy edge of the plasma emission shows. Moving to the excitonic regime for delay time of about 600 ps, the PL intensity corresponding to the biexciton energy starts to follow the square slope of the exciton PL intensity, evidencing the thermodynamic equilibrium between excitons and biexcitons [108].

### 3.3.5 Estimation of the carrier density

The results of the estimated carrier density in the QW deduced from EHP lineshape fitting are shown as black circles in Fig. 3.8. The maximum carrier density in the QW deduced from

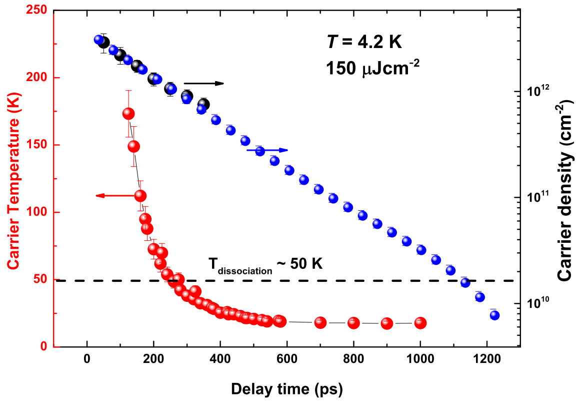

Figure 3.8 – Extrapolated QW carrier density (blue) and carrier density values extracted from the EHP modeling procedure at early time delays (black) as a function of the time delay after excitation. The correspondingly deduced effective carrier temperatures are shown in addition (red). The black dashed line marks the temperature limit according to Saha's law, where biexcitons are ionized according to their binding energy (8 meV).

this lineshape fitting of the QW emission amounts to $3 \times 10^{12} cm^{-2}$. This value is basically limited by the finite height of the barrier. To extrapolate the carrier density at longer delays, the extracted carrier density from the lineshape modeling at early delays was scaled for each time delay based on the overall captured QW emission PL intensity in the streak image according to:

$$I_{PL} \propto \frac{dn}{dt}. \tag{3.15}$$

More precisely, for each time delay the PL intensity recorded on the streak image, which is integrated spectrally of the QW emission and temporally from the considered time delay to infinity, was multiplied by the deduced carrier density at early time delays (cf. Ref. [94]).

Assuming a negligible contribution of non-radiative recombinations in this high quality sample at low temperature, this method can provide a reasonably accurate estimation of the carrier density in the QW. Owing to the rapid decay of the barrier, the accuracy of this estimated carrier density is also marginally affected by refilling of carriers from the barriers to the QW. The carrier diffusion outwards of the excitation spot could also modify the estimated carrier density, as it was observed in case of GaAs QWs in Ref. [115]. However, this effect should be negligible in our case, owing to the lower mobility of excitons in GaN due to higher effective masses and larger excitation spot (~5 $\mu m$) in our measurements. Nevertheless, considering all the above-mentioned effects, our estimated carrier density stays reasonably accurate, which allows us transposing the time-resolved experiments into carrier density dependent plots.

### 3.3.6 Analysis and discussion

To estimate the emission energy and the full width at half maximum (FWHM) of the exciton and biexciton transition from our tr-PL measurements, two Voigt functions were employed for both emissions. The inhomogeneous contribution, i.e. the broadening of the Gaussian function, was estimated from fittings at very low carrier densities and kept constant for fitting all other spectra, whereas the broadening of the Lorentzian part was tuned to fit well the homogeneous broadening induced by the carrier-carrier collisions [116, 92]. Figure 3.9(a) and (b) depict the results of this fitting for excitons and biexciton emission energies as well as their lower and upper FWHM energies (red and black dashed lines, respectively) as a function of the carrier density. The data points are the results of fitting of the time resolved spectra with a Voigt profile for carrier densities below $8 \times 10^{11} cm^{-2}$.

At carrier densities higher than $8 \times 10^{11} cm^{-2}$, the exciton peak becomes asymmetric on its high-energy tail and gradually moves to an EHP. Simultaneously, the biexciton transition broadens on the low-energy side. Thus, it was not possible to continue this fitting procedure beyond those densities. Indeed, more complex profiles should be used both for the exciton and the biexciton transition, but the main results of the present fit would not be modified by such details for which no complete theory exists over the full density range studied here (cf. discussion in section 3.3.3).

To rephrase our findings in terms of the carrier density in the SQW-1, up to densities of $5 \times 10^{11} cm^{-2}$, the PL of GaN QWs is dominated by excitonic recombination. Increasing the density further, the excitonic emission disappears as a shoulder of the biexcitonic emission, until a clear EHP emission is observed at densities in excess of $1 \times 10^{12} cm^{-2}$. Similarly to what is observed in GaAs-based QWs, the MT appears to be a smooth transition, occurring at carrier densities around $10^{12} cm^{-2}$ in our structure. However, contrary to the GaAs system, here the plasma builds up from the biexciton resonance rather than from the exciton resonance.

Schrödinger-Poisson simulations were used to model the characteristics of our 3 nm thick GaN/$Al_{0.05}Ga_{0.95}N$ QW with a built-in electric field of 180 kV/cm in agreement with Ref. [19]. It allowed extracting the change in the e-h wave-function overlap and the exciton energy shift (Fig. 3.9(a)). The normalized wave-function overlap changes from 0.64 at zero carrier density to 0.95 at the carrier density of $5 \times 10^{12} cm^{-2}$. Neglecting screening effect at high carrier densities, the exciton binding energy is expected to increase from 30 to 40 meV for the mentioned carrier densities. The total shift in exciton energy observed in the experimental results is in good agreement with the value estimated from SP simulations up to moderate carrier densities as shown in Fig. 3.9(a), which is given by Eq. 3.3.

At carrier densities above $3 \times 10^{11} cm^{-2}$, however, the experimentally observed shift of the exciton energy deviates from the one deduced from the model, originating from the fact that in our SP simulations, exciton screening and phase space filling are not considered.

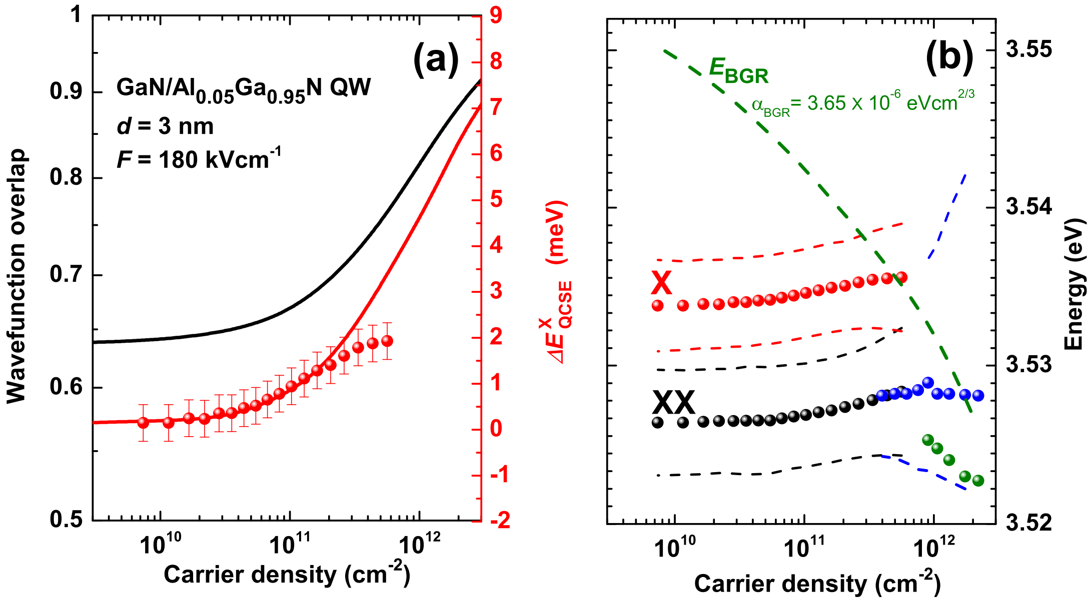

Figure 3.9 – **(a)** Results of Schrödinger-Poisson simulations for the e-h wave-function overlap (black curve) and shift in exciton energy due to screening of the built-in electric field in the QW (red solid curve) compared with the experimental values of the exciton emission energy shift (red circles). **(b)** Energy of the exciton and biexciton transitions (red and black circles) in addition to their FWHM energies (shown by dashed lines) as a function of the QW carrier density. The energy difference between exciton and biexciton energies, i.e., the biexciton binding energy, remains constant over the entire power density range. The green circles represent the values of the bandgap extracted from EHP emission modeling. Beyond the MT, the QW emission peak and FWHM energies are shown with blue dots and blue dashed lines, respectively. It is obvious, that they emerge from the biexciton emission band. The green dashed line shows the expected evolution of the band-edge due to BGR with $\alpha_{\mathrm{BGR}} = 3.65 \times 10^{-6} eVcm^{2/3}$ in agreement with Refs. [90, 91]

Figure 3.9(b) shows that the PL linewidth, at moderate carrier densities, is larger for biexcitons (6 meV) than that of excitons (4 meV). Towards higher carrier densities, both exciton and biexciton linewidths start to significantly increase due to collisional broadening [117]. As observed in Fig. 3.9(b) the exciton (and biexciton) emission energy blueshifts by about 2.5 meV with increasing injection from $6 \times 10^{10}$ to $8 \times 10^{11} cm^{-2}$. The observed shift is in close agreement with the energy shift due to screening of the built-in electric field in the QW expected from SP simulations. The expected evolution of the bandgap energy $E_{\mathrm{BGR}}$ versus the carrier density $n$ is shown also in Fig. 3.9(b), according to Eq. 3.1. The $\alpha_{\mathrm{BGR}}$ is a material and dimensionality dependent constant, which was chosen to be equal to $3.65 \times 10^{6} eVcm^{2/3}$ in agreement with Refs. [90, 91].

Although, from theoretical predictions [118, 119], we expect a change in the exciton energy due to the reduction in its binding energy and BGR effect, no measurable shift was observed. This is presumably due to a perfect compensation between BGR and the reduction in $E_X^b$ [90]. When the carrier density approaches the critical value of $1 \times 10^{12} cm^{-2}$, the exciton binding energy should be considerably reduced. Assuming that Haynes rule [110] is valid at these carrier densities, a pronounced decrease in the biexciton binding energy is expected. However, we observed almost no change in the energy difference between the exciton and the biexciton (Fig. 3.9(b)), which implies a remarkable stability of biexcitons at high carrier densities.

In summary, a crossover from excitons to biexcitons and finally to an EHP in a 2D system as function of carrier density was observed in our experimental results. The stability of biexciton molecules against the Coulomb screening and collisions at high carrier density was traced back to the robustness in the biexciton binding energy. The appearance of an EHP emission spectrum from the biexciton energy implies the important role can be played by biexcitons in the Mott transition.

At first sight the robustness of biexcitonic molecules might seem surprising if one considers their smaller binding energy compared to that of excitons. However, one should consider also a more complex interplay between correlation and exchange processes occurring in those molecules built from four particles, when interacting with nearby carriers. In most of the existing theories on the Mott transition, the existence of biexcitons was neglected [120, 100], likely because of their reduced stability in smaller bandgap QW heterostructures like GaAs (cf. section 3.3.7). Therefore, our results call for more theoretical investigations considering the important role that can be played by those quasiparticles across the Mott transition.

### 3.3.7 Saha's law and the higher biexciton stability in GaN QWs compared to GaAs QWs

The population of excitons, biexcitons and free carriers at thermal equilibrium can be described according to mass action laws [121, 108, 122, 123, 124]:

$$e + h \xleftrightarrow{K_X} X \qquad \Longrightarrow \qquad \frac{n_e n_h}{n_X} = K_X(T) = \frac{\mu k_B T}{2\pi\hbar^2} \exp\left(-\frac{E_X^b}{k_B T}\right) \tag{3.16}$$

$$X + X \xleftrightarrow{K_{XX}} XX \qquad \Longrightarrow \qquad \frac{n_X^2}{n_{XX}} = K_{XX}(T) = \frac{M_X k_B T}{\pi\hbar^2} \exp\left(-\frac{E_{XX}^b}{k_B T}\right), \tag{3.17}$$

where $n_e$, $n_h$, $n_X$, and $n_{XX}$ denote the population density of electrons, holes, excitons, and biexcitons, respectively. The terms $\mu$ and $M_X$ are the exciton reduced and translational mass, respectively. Charge conservation in our undoped QW, then implies that $n_e = n_h = n_{free}$, where $n_{free}$ is the thermal free electron population density. Considering the total carrier density in the QW ($n_{tot}$), one can write:

$$2n_{XX} + n_X + n_{free} = n_{tot}. \tag{3.18}$$

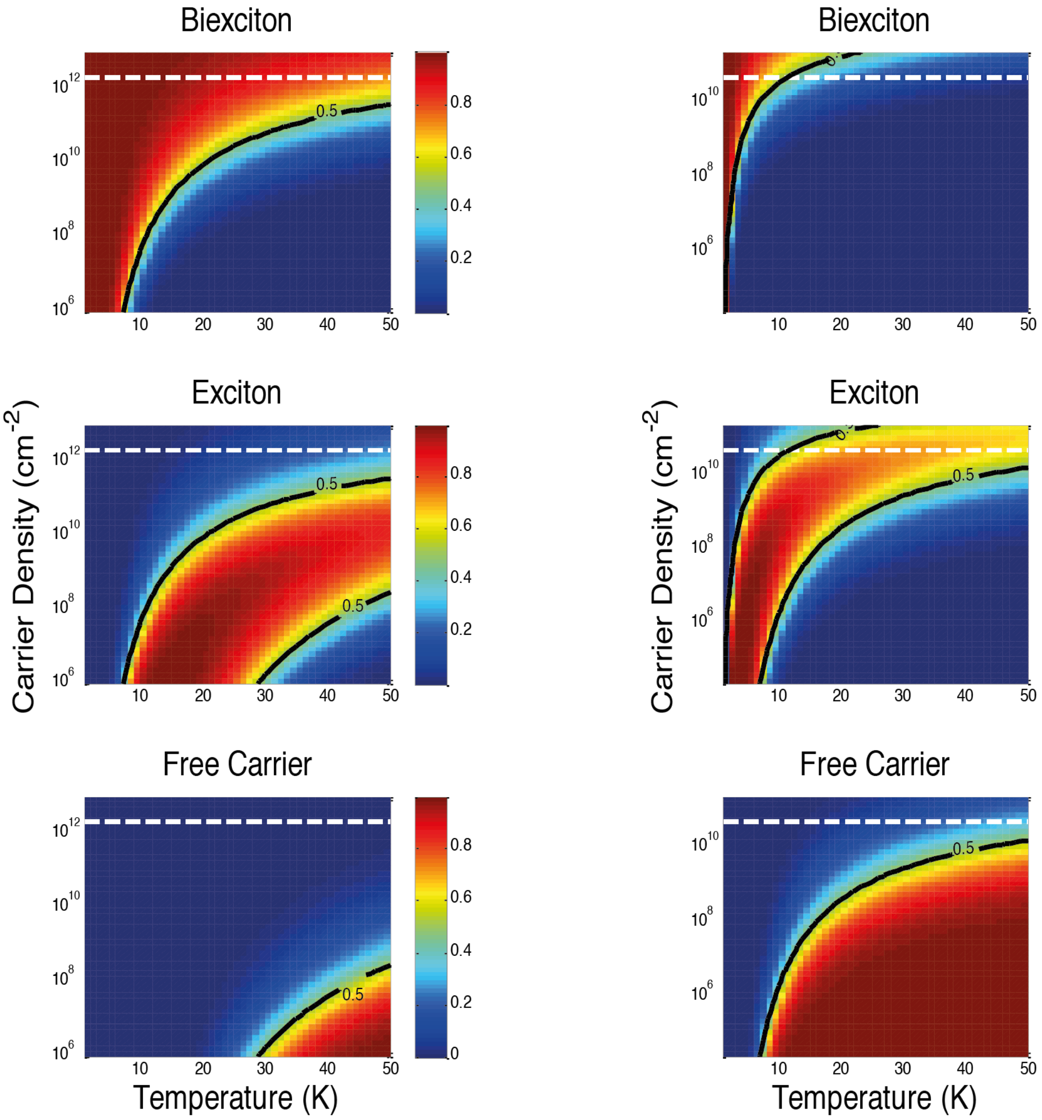

Figure 3.10 – Evolution of the biexciton ($n_{xx}/n_{tot}$), exciton ($n_x/n_{tot}$) and free carrier ($n_{e-h}/n_{tot}$) population density ratio to the total carrier density ($n_{tot}$) in the QW versus the lattice temperature and total carrier density $n_{tot}$, simulated for typical binding energies for exciton and biexciton in the case of GaN QW (left column) and GaAs QW (right column), respectively. The borders of transition between dominant populations are marked by black solid lines, while the horizontal white dashed line marks the approximate $n_{\text{crit}}$ in each case.

Solution of Eqs. 3.16 to 3.18 for different lattice temperatures and different values of $n_{tot}$ are shown in Fig. 3.10, with the typical values of exciton and biexciton binding energy in GaN QWs (left column) and GaAs QWs (right column), respectively. The general behavior of the relative densities in both cases remain the same: at low temperatures, there is crossover from exciton to biexciton majority population with rising the carrier density. Rising the temperature for a given value of $n_{tot}$, however, leads to ionization of biexciton into exciton, and into free carriers upon a further increase of the temperature.

Hence the increased stability of biexcitons at high injection can be tentatively explained through this mass action law. However, in case of GaAs QWs, the most studied system so far because of its high quality and technological importance, no biexciton has ever been observed close to the Mott transition in these 2D structures. One possible explanation might be that in all experiments an increase in carrier density is linked to an increase in carrier temperature: excitons become more stable compared to biexcitons at high carrier density because of the related increase in temperature.

As shown in the Fig. 3.10, this effect is more detrimental for GaAs heterostructures where the biexciton binding energy is smaller (for instance, ~1.5 meV [125]) than in our investigated SQW-1, that allows the stability of biexcitons up to temperatures of 20K. However, in our investigated same (SQW-1), biexcitons can survive at temperatures up to 50 K, thanks to their large binding energy of 8 meV. Additionally, as shown in Fig. 3.8, owing to the efficient phonon-cooling, the effective carrier temperature in our measurements remains below 50K up to carrier densities $\approx 10^{12} cm^{-2}$, which allows the formation of biexcitons.

### 3.3.8 The impact of QCSE on the biexciton binding energy

In this section, the results of tr-PL measurements on a single GaN/$Al_{9\%}Ga_{91\%}N$ QW grown on $c$-plane sapphire will be discussed, while the wedge thickness of the QW (1 nm < $L_{QW}$< 1.5 nm) allows probing the effect of QCSE on the biexciton binding energy. Whereas the impact of QCSE on biexciton binding energy was thoroughly investigated in Ref. [11] on SQW-1 and SQW-2 at low carrier injection, we recall some important features of this study at high injection densities here.

The streak images and the time delay slices are reported in Fig. 3.11. Clearly, the biexciton binding energy increases with decreasing QW thickness from (a) to (c). The dependence of the biexciton binding energy on the QW thickness can be understood from the following argument: while keeping the Al composition in the barrier constant, an increase in the QW thickness leads to a reduction in the electron-hole wave-function overlap due to the QCSE. The built-in electric field, indeed, leads to a preferential orientation of the excitonic dipoles

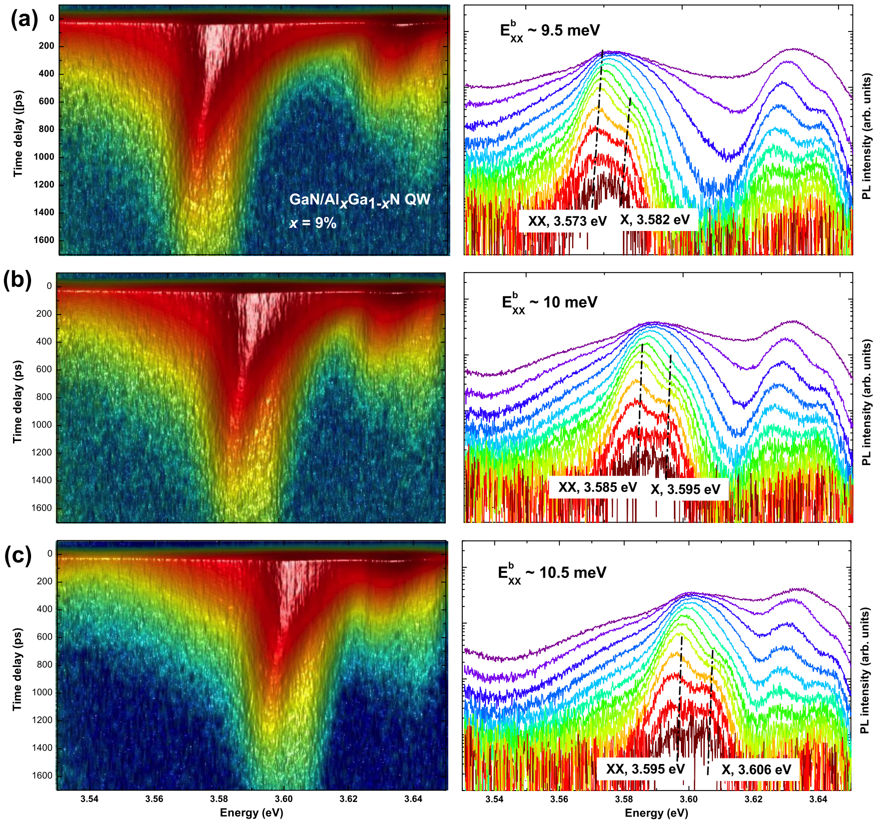

Figure 3.11 – a, b, c) Streak camera images issued from tr-PL measurements taken at T = 4.2 $K$ on a 9% GaN/Al$_x$Ga$_{1-x}$N QW of continuously decreasing thickness from (a) to (c) and corresponding tr-PL spectra at different time delays ranging from 100 to 1500 ps displayed in semi-logarithmic scale. The exciton and biexciton energies at long delays after excitation are estimated by fitting the PL spectra with two Voigt functions. The binding energy of the biexciton rises with increasing (decreasing) the QW emission-energy (thickness).

and hence increases the dipole-dipole repulsion in the biexciton complex. This usually leads to a reduction in the biexciton binding energy when the QW thickness increases.

From Fig. 3.11 we deduce an increase in the biexciton binding energy from 9.5 meV for the thickest QW region shown in (a) to 10.5 meV for the thinnest part shown in (c), which is consistent with results obtained on the same sample by Stokker-Cheregi *et al.* [11]. Note that for very thick QW regions and/or high Al contents in the barriers (cf. section 3.4), the repulsive interactions may overcome the biexciton binding energy leading to the absence of biexcitons in the PL spectra. Except for the dependence of the biexciton binding energy on the QW thickness in SQW-2, all other observations about the role of biexcitons in the Mott transition remain the same as observed in SQW-1.

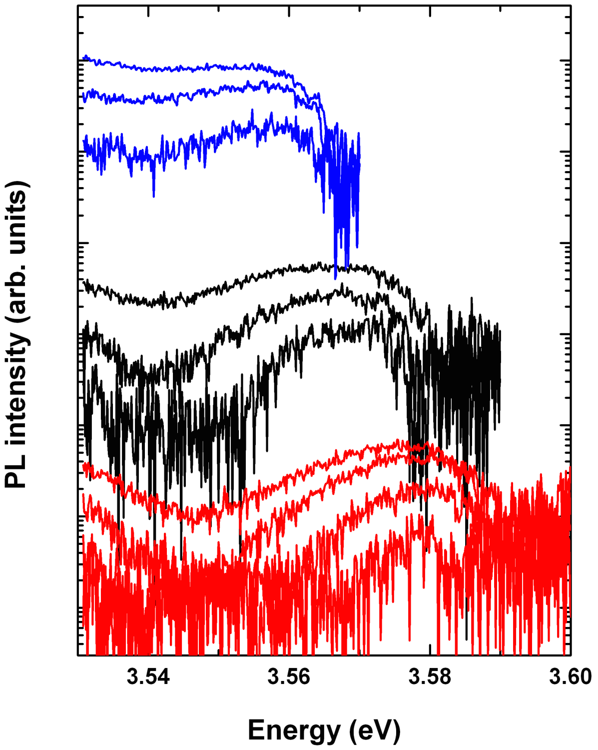

Figure 3.12 – The evolution of the peak on the low-energy tail of the QW emission, extracted by deconvolution of the EHP emission from time resolved spectra in Fig. 3.11(a-c). The set of spectra shown in blue, black and red color are corresponding to the streak image (a), (b), and (c) in Fig. 3.11, respectively, while in each set of spectra time delay increases from the top to the bottom spectrum. The spectra are shifted for clarity.

It worth noticing a distinct shoulder that appears on the low-energy tail of the QW emission (see Fig. 3.11). This shoulder cannot be reproduced by the EHP lineshape model employed before (see, for instance, the result of the EHP lineshape modeling in Fig. 3.2(a)). In order to evidence the evolution of this peak, that appears at the same time as the onset of the Mott transition, and evolves with the rising the injected density, we have subtracted the EHP emission from the tr-PL spectra in Fig. 3.11. The results of this deconvolution are shown in Fig. 3.12 (the spectra are shifted for clarity). The emission energy has a clear dependence upon density increase, which allows us safely excluding the LO-phonon replica of the barrier as an origin of this transition. Moreover, we exclude the so-called P-band transition due to the exciton-exciton scattering, as reported in case of ZnO heterostructure [126, 76], as the origin of this peak since it appears at the same time as the EHP emission: there are no more excitons in the QW. Unfortunately, the low intensity of this transition and the large homogeneous broadening of the QW emission at low-energy side conceals the accurate features of this transition. However, we tentatively attribute this transition to the so-called shakeup process observed previously in the case of two dimensional electron gases in GaAs QWs [127, 128]. In this process, a recombining electron-hole pair excites the surrounding electrons *via* the Coulomb interaction, causes a decrease in the emitted photon energy by the amount left to the electron gas. A more detailed study of this transition, however, stays beyond the scope of our investigation.

## 3.4 Temperature dependence of the Mott transition

### 3.4.1 Sample

In this section, the results of an optically induced Mott transition obtained on a 3.2 nm thick single GaN/$Al_{0.09}Ga_{0.91}N$ QW (SQW-3) at temperatures between 4K to 150 K will be discussed. The investigated single QW was grown by MOVPE on a *c*-plane GaN free-standing substrate and has bottom and top $Al_{0.09}Ga_{0.91}N$ barriers with respective thicknesses of 150 and 30 nm. The fundamental transitions of the QW consist of $X_A$ and $X_B$ transitions located around 3.5 eV (see PLE spectrum displayed in Fig. 3.13 (a)), separated in energy of about 8 meV. The linewidth of the excitonic transitions is also about 8 meV. In the PLE of the SQW-3, the band-edge (BE) transition, the first LO phonon replica of excitons and the strong absorption of the barrier can also be identified.

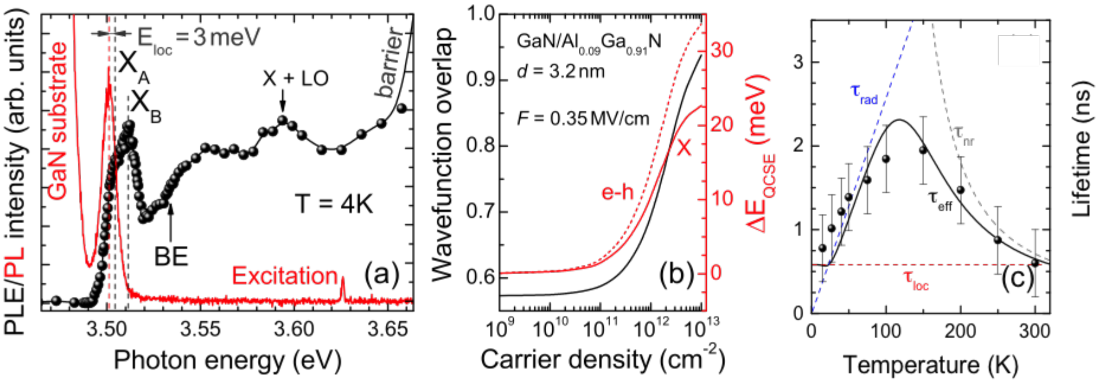

Figure 3.13 – **(a)** PLE spectrum (black dots and solid line as a guide to eye) of the QW recorded at 4 K revealing two fundamental excitons $X_A$ and $X_B$ and the BE absorption at higher energies. PL spectrum (red) with excitation energy 3.627 eV is shown for comparison with PLE. **(b)** SP simulations results for the normalized wave-function overlap (black) and the QW ground-state energy shift for excitons (red solid) and free carriers (red dashed) as a function of the carrier density $n$. **(c)** Effective exciton lifetime in SQW-3 as a function of the lattice temperature measured at low injection ($n < 10^{11} cm^{-2}$): comparison of experimental data (dots) with the experimental error bars, and modeling (black line). The modeled dependences of radiative (blue), non-radiative (gray), and localized exciton recombination (red) are also shown (adapted from Ref. [91]).

Performing a similar SP simulation to the SQW-3, at zero carrier density the $E_X^b$ and the normalized wave-function overlap was estimated to 30 meV and 0.57 (cf. Fig. 3.13(b)). The value obtained for $E_X^b$ from SP simulations coincides with the the identified BE absorption in the PLE. The-state-of-the-art exciton linewidth in this sample ($\sim 0.25 E_X^b$) as well as the large binding energy of exciton in this sample allows probing the Mott transition at temperatures up to 150 K.

Moreover, from the temperature dependence of the exciton effective lifetime $\tau_{eff}$, the radiative recombination governs the recombinations in this sample over the whole studied temperature range from $0K$ to $150K$. The $\tau_{eff}$-values versus the lattice temperature are shown in Fig. 3.13(c) obtained from temperature dependent tr-PL measurements. This set of tr-PL measurements have been performed with a much larger excitation spot $\sim 50\ \mu m$, yielding a considerably lower carrier density $n < 10^{11} cm^{-2}$. Therefore, the carrier density is always below the $n_{\text{crit}}$ for the Mott transition.

The effective lifetime of excitons can be modeled, considering the thermal equilibrium between the free and localized exciton populations according to Ref. [129]. The radiative lifetime of exciton, then, is given by [130]:

$$\tau_r = \frac{6Mk_BT}{\hbar^2 k_{\parallel}^2}\tau_0, \tag{3.19}$$

where $\tau_0$ denotes the radiative lifetime of free excitons at $0K$, M is the exciton effective mass, and $k_{\parallel}$ is the in-plane wave-vector of free excitons within the light cone. The linear dependence of the free exciton lifetime on temperature originates from the fact that, when raising the temperature, excitons populate more the states outside the light-cone. The effective free exciton lifetime in presence of non-radiative recombination can be modified according to:

$$\frac{1}{\tau_{eff}} = \frac{1}{\tau_r} + \frac{1}{\tau_{nr}}, \tag{3.20}$$

where $\tau_{nr}$ usually features a thermally activated behavior with a characteristic activation energy $E_A$, given by [129]:

$$\tau_{nr} = \tau_{nr,0} \exp\big(-\frac{E_A}{k_BT}\big). \tag{3.21}$$

Eventually, in the presence of disorder in our structure, we should consider the effect of localization. The latter was modeled by considering a thermal equilibrium between free exciton and localized exciton populations *via* Saha's law. Considering a characteristic decay time for localized exciton $\tau_{loc}$, the effective decay time of exciton in the QW can be written as:

$$\frac{1}{\tau_{eff}} = (\frac{n_{loc}}{\tau_{loc}} + \frac{n_{fr}}{\tau_{fr}})/(n_{loc} + n_{fr}), \tag{3.22}$$

where $n_{loc}$ and $n_{loc}$ denote the localized excitons and free excitons densities, respectively.

Here, due to isolation of localized excitons from the non-radiative centers, the localized excitons decay time behaves like the case of 0D excitons and their decay time is expected to be temperature independent. The value of $\tau_0$ was considered to be 10 ps in our simulations, consistent with the decreased e-h wave-function overlap in our structure (~ 0.57) at low carrier densities [129]. The results of this fitting to the experimentally observed effective lifetime of exciton in SQW-3 is shown in Fig. 3.13(c), with the fitting parameters of: $\tau_{nr,0} = 110ps$, $\tau_{loc} = 580ps$, $n_{loc} = 5 \times 10^{10} cm^{-2}$, $E_{loc} = 8meV$, and $E_A = 45meV$. The effective lifetime of excitons increases monotonously up to ~150 K, revealing the dominant radiative recombination in the QW and, therefore, the high structural quality of the sample.

In addition to the narrow exciton linewidth, the high quality of the present QW is evidenced by a small localization energy $E_{loc} = 3meV$ obtained by comparing the PLE spectrum to the PL spectrum. We deduce the exciton Bohr radius for this sample to be $a_B = 2.7nm$, and thus a hard-sphere limit for $n_{\text{crit}}$ of $4.4 \times 10^{12} cm^{-2}$.

As a final note on the sample properties, it worth mentioning the absence of the biexciton transition in this sample. As discussed in section 3.3.8, the QCSE can play an important role in the exciton and biexciton binding energy. The larger thickness of SQW-3 combined with the large built-in electric field value in this sample (~ 350 kV/cm), results in an efficient reduction of the e-h wave-function overlap. Owing to the larger height of the barrier in SQW-3, the maximum allowed carrier density in the QW can be higher compared to last two samples investigated, and can be up to $10^{13} cm^{-2}$.

### 3.4.2 Temperature dependence of the Mott transition

The streak image recorded at 4K is presented in Fig. 3.14(a). It evidences the emission originating from the substrate (around 3.48 eV), the barrier (around 3.68 eV), and the QW in between them. The QW emission right after the pulse arrival features all characteristics of an EHP emission: a broad emission (~100 meV) extending up to the barrier energy with saturated amplitude. Increasing the time delay, the width of the PL emission of the QW shrinks down on the high energy side, while it remains saturated on its low energy side up to ~1 ns after the excitation. The GaN substrate features a long rise time, originated from the carrier transfer from the QW barriers to the substrate as the main sources of the carrier density in the substrate.

The streak images recorded at different temperatures were analyzed by the same model discussed in section 3.1.3 (cf. Fig. 3.14(c) and (d)). In the present case the joint DOS was convoluted with a Gaussian of 8 meV width to take into account the inhomogeneous broadening. The EHP lineshape fitting was performed with the effective masses of $m_e^* = 0.2m_0$, $m_A^* = 1.8m_0$, and $m_B^* = 0.45m_0$ deduced from $k.p$ simulations [10]. The experimental results were well reproduced with the aforementioned EHP lineshape fitting. Similarly, additional Lorentzian/Gaussian functions were employed to reproduce the emission of the GaN substrate an the barrier, in order to fit the whole PL spectra.

When increasing the time delay, the high energy tail of the QW emission progressively shrinks down, following the reduction in the carrier density in the QW through radiative recombinations of the carriers. Moreover, the slope in the high energy tail of the EHP emission progressively decreases by time because of the cooling of the EHP. Eventually, at carrier densities out of the fitted range ($n < 10^{12} cm^{-2}$) the QW emission recovers its symmetric lineshape. The main characteristics of the PL spectra evolution upon the carrier density remain the same over the whole measured temperature range. However, when increasing the temperature, they became more blurred due to increase in the carrier temperature and, therefore, the homogenous broadening.

The carrier density beyond the possible range for the fitting, was determined by extrapolating the carrier density based on the integrated PL intensity $I_{PL}$ decay according to:

$$I_{PL} \propto \frac{n}{\tau_{rad}(n)}. \tag{3.23}$$

Here, the impact of the QCSE on the radiative lifetime $\tau_{rad}(n)$ within the e-h wave-function overlap was iteratively taken into account. The estimated carrier density can vary by ±10%, considering the uncertainty in the electron effective mass $m_e^*$ in GaN. Also, one can take into account the effect of the non-parabolicity of the A and B valence bands close to the zero in-plane wave-vector in the lineshape fitting to the EHP emission. However, a marginal impact was observed for the lineshape analysis, owing to the dominant inhomogeneous broadening [91].

Fig. 3.14(b) displays the QW peak energy and its FWHM evolution as a function of the estimated $n$ values. According to the FWHM of the QW transition two regimes of carrier density can be distinguished. At carrier densities $n < 10^{12} cm^{-2}$, the emission band is symmetric, while it blueshifts and becomes broader when raising $n$. The blueshift of the emission is well reproduced in our SP simulations, originating from the progressive screening of the electric field in the QW (~350 kV/cm) with rising $n$. As discussed before for SQW-1, the impact of QCSE screening on both the exciton binding energy and the band to band transition energy was considered within this model, yielding the density-dependent exciton energy according to Eq. 3.3. The increase in the linewidth of the PL band is ascribed to the enhanced collisional broadening, which is characteristic of a dense exciton gas [92, 116].

Towards higher carrier densities, the PL emission becomes asymmetric without any clear peak, featuring an enormous FWHM. At carrier densities $n > 10^{13} cm^{-2}$, the modeled e-h quasi-Fermi levels separation $\Delta E_{\mathrm{F}}$ exceeds the bandgap resulting in a plateau-like emission (cf. Fig 3.14(c-d)). The fitted bandgap $E_m$ redshift in this density regime with increasing $n$, due to the BGR effect [89].

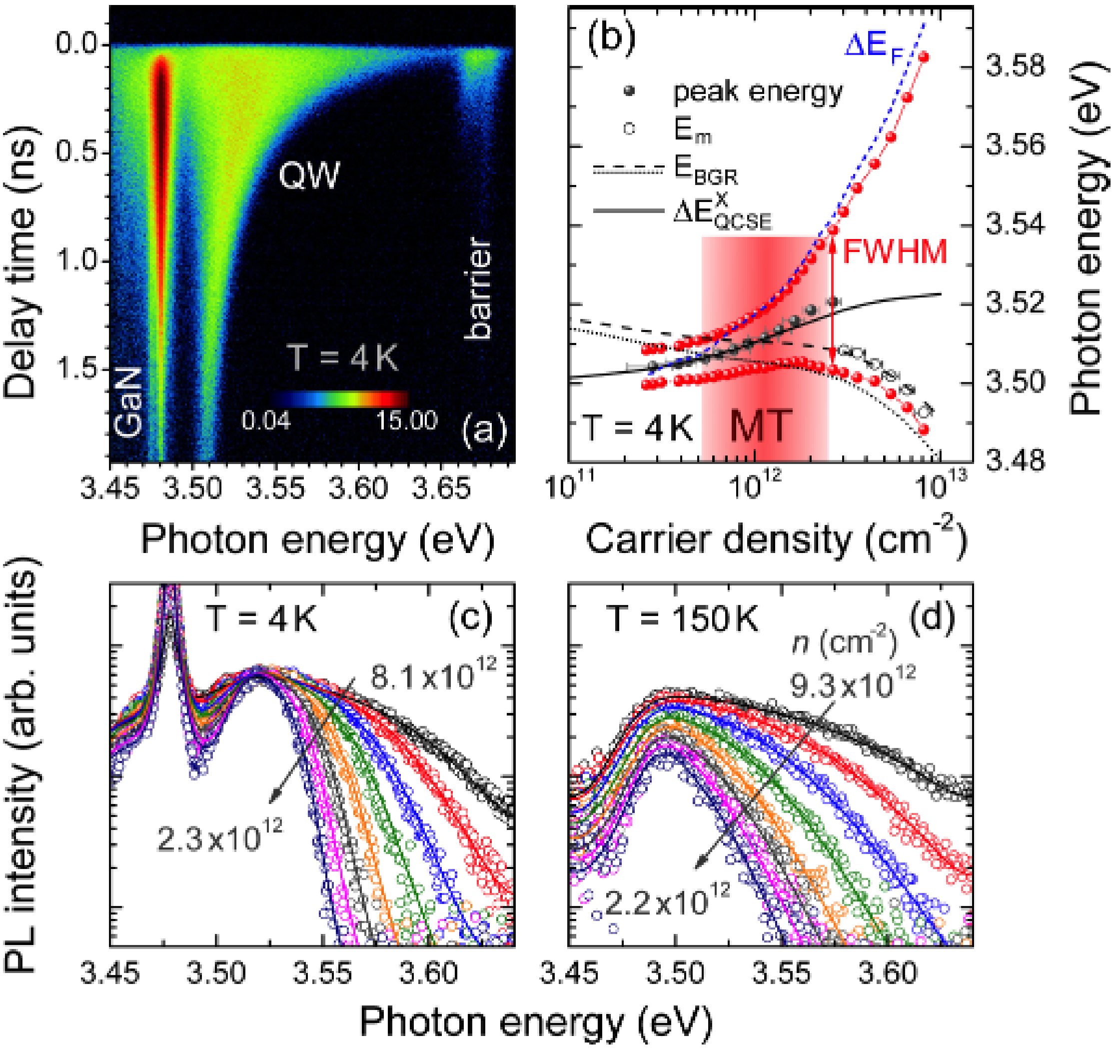

Figure 3.14 – **(a)** Streak camera image recorded at 4 K. **(b)** Fingerprint of the MT at 4K: Evolution of peak energy, upper and lower half maximum energy (red dots), $E_m$, $\Delta E^X_{QCSE}$ , $\Delta E_F$ (blue dashed line), and $E_{BGR}$ (black dashed line, the result of cw-PL is shown for comparison as a dotted line, cf. Fig. 3.15) as a function of $n$. The Mott transition range is shaded in red. **(c), (d)** Spectral profiles at different time delays: comparison of experimental data (dots) and modeling (lines) at 4 (steps of 60 ps) and 150 K (steps of 180 ps), respectively.

Note that the estimated $E_m$ change is lower than in the forthcoming cw-PL experiments (cf. results in Fig. 3.15) and may be even suppressed for the highest $n$ values. This effect appears for all temperatures in tr-PL measurements and is most likely due to feeding of carriers from the AlGaN barrier, a process disturbing the equilibrium shortly after the pulse excitation.

In summary, the Mott transition appears as a smooth transition in our tr-PL measurements. However, for carrier densities $n > 3 \times 10^{12} cm^{-2}$ the QW emission obviously originates from the EHP emission. Whereas, for carrier densities $n < 5 \times 10^{11} cm^{-2}$ the emission is governed by an excitonic gas as no further change in the emission lineshape can be distinguished down to the lowest densities (see Fig. 3.14(b)). Therefore, from this lineshape criterion, the carrier density corresponding to the crossover between EHP emission and excitonic emission can be estimated to $n_{crit} = 1.56 \pm 1 \times 10^{12} cm^{-2}$ at 4K. The latter value is significantly below the one estimated from the hard-sphere criterion for the present QW, determined to be $4.4 \times 10^{12} cm^{-2}$ for $a_B$ of 2.7 nm in SQW-3 according to Ref. [131].

The second set of measurements has been carried out by cw-PL measurements, while results confirming the ones in obtained by tr-PL technique. The excitation power density in our cw-PL measurements could be changed over four orders of magnitude, i.e. from 0.3 to 3600 $W/cm^2$. The obtained cw-PL spectra (cf. Fig. 3.15) resemble the ones obtained by tr-PL in Fig. 3.14. Therefore, the same lineshape analysis was applied to this set of measurements. The only noticeable difference being the BGR induced redshift in the bandgap energy, at high carrier densities, which is more pronounced compared to the one observed in tr-PL measurements. The latter can be understood as the absence of relaxation of the non-equilibrium population after excitation, as it is the case after the pulse excitation in our tr-PL measurements. As in the previous part of this chapter, the shift in the bandgap energy by BGR can be modeled by equation 3.1. The bandgap was fitted with $\alpha = 3.8 \times 10^{-6} eV cm^{2/3}$ at 4 K, a value very close to the prediction of Ref. [90].

Several criteria were applied to deduce the Mott density from our cw-PL measurements in addition to the bare lines shape analysis applied to tr-PL results. Indeed, the clear observation of BGR in the cw-PL measurements allows identifying an additional criteria for the Mott transition according to the transparency limit $\Delta E_{\mathrm{F}} = E_{\mathrm{BGR}}$, i.e., when the quasi-Fermi level separation exceeds the band-edge. The latter defines also the onset of gain from an EHP [96], a purely fermionic effect that excludes any excitonic absorption at the band-edge. Another criterion can be the crossing between $E_X$ and $E_{\mathrm{BGR}}$, i.e., where the exciton binding energy $E_X^b$ vanishes [89, 88].

Both criteria (as it was shown before on Fig 3.1, according to the values from our cw-PL experiments) yield a $n_{\mathrm{crit}}$ value of around $7 \times 10^{11} cm^{-2}$, in a good agreement with the estimated value from previous lineshape criterion (indicated by the red background in Fig. 3.15(c)). It worth noticing that tr-PL and cw-PL do not necessarily have to yield identical $n_{\mathrm{crit}}$ values, since the exciton screening in tr-PL can only be due to cold carriers, while in cw-excitation the static hot carrier population can potentially alter the screening efficiency [87].

Similar to our tr-PL results, when raising the temperature, the Mott transition characteristics do not vary significantly in our cw-PL results (see Fig. 3.15(b)). However, comparing the cw-PL results at 4K and 150K, some slight modifications should be highlighted. First, the

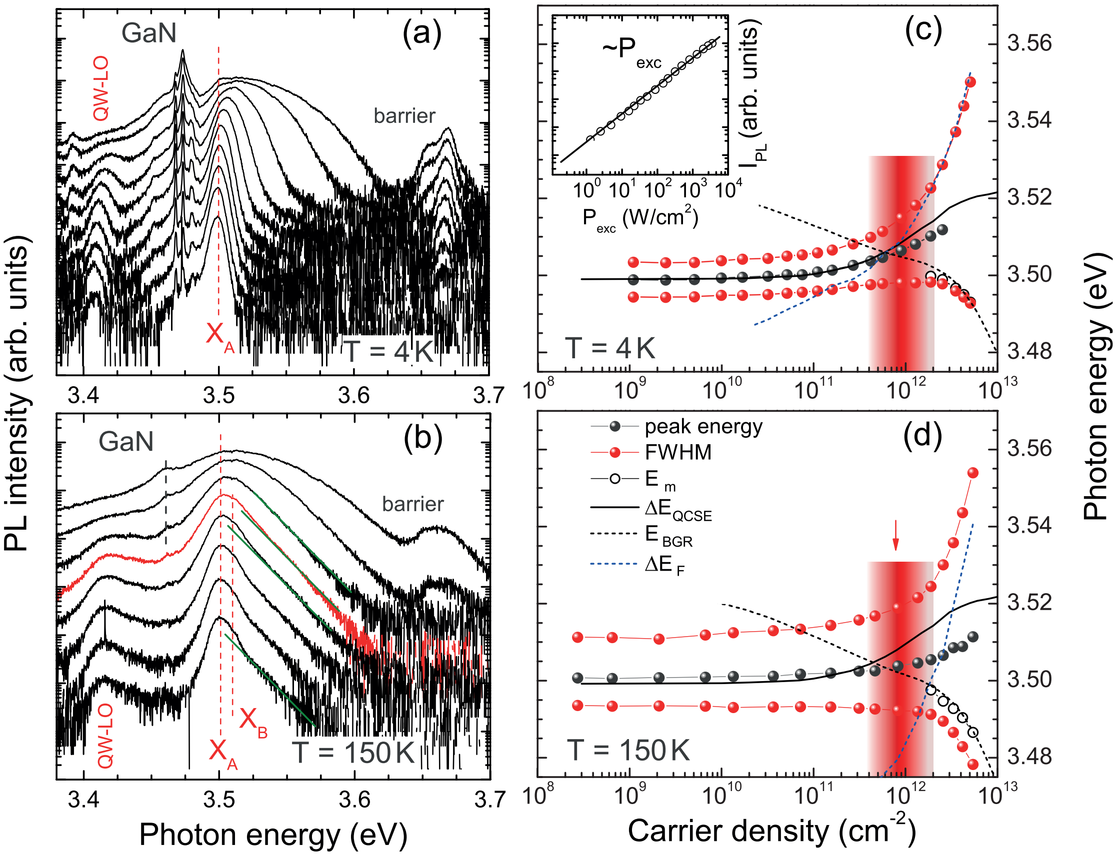

Figure 3.15 – **(a),(b)** the injection-dependent cw-PL spectra measured at 4 and 150 K, respectively. In (b) exponential fits of the high-energy tail are shown with green lines. The red spectrum marks the transition from a mono-exponential tail to an excitonic lineshape. **(c),(d)** the Mott transition characters at 4 and 150 K, respectively. The Mott transition range is marked with a red background and the red arrow in (d) marks the position of the red spectrum in (b). The inset in (c) shows IPL as a function of excitation power density $P_{exc}$ at 4 K.

plateau-like emission at high carrier densities is slightly blurred at 150K due to the increase in the homogenous broadening at higher temperatures, consistent with our tr-PL measurements. Additionally, the exciton B transition ($X_B$) emission is more populated at elevated temperatures, appearing as a high-energy shoulder to the QW emission and still present at carrier densities far below $n_{\mathrm{crit}}$.

Another criterion can be defined by the appearance of a mono-exponential tail on the high-energy side of the QW emission, as marked by the red spectrum in the Fig. 3.15(b). However, the latter criterion is valid for the continuous states of the QW, i.e. the band-edge emission. Indeed, even if the band-edge emission was not resolved in our PL spectra, the mono-exponential tail of the QW emission evidences its emergence.

Figure 3.16 – Values for $n_{\mathrm{crit}}$ deduced from various criteria: $\Delta E_{\mathrm{F}} = E_{\mathrm{BGR}}$ (blue), disappearance of an excitonic lineshape (cf. Fig.3.15(d), shown by green), and $E_X = E_{\mathrm{BGR}}$ (black). Results of tr-PL at 4 K are shown with open circles. The red background marks the confidence interval. The orange and green open circles show, respectively, the lower and upper values for the carrier density, for which the slope of IPL versus $n$ deviates from a linear slope (cf. section 3.4.3).

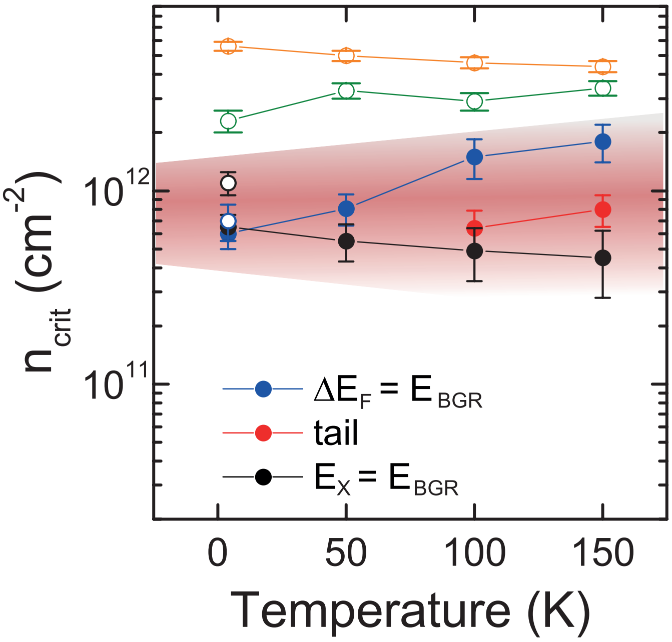

Fig. 3.16 summarizes the results of the estimated $n_{\mathrm{crit}}$ when applying different criteria. No significant change in the estimated $n_{crit}$ can be distinguished. However, the two other criteria defined before lead to different dependence of the $n_{crit}$ to the temperatures: whereas the larger value of $\alpha_{\mathrm{BGR}} = 4.1 \times 10^{-6} eV cm^{2/3}$ was found at 150 K, the raise of $T_{\mathrm{car}}$ caused an expected increase of the estimated $n_{\mathrm{crit}}$ with rising the temperature according to $\Delta E_{\mathrm{F}} = E_{\mathrm{BGR}}$ criterion, the increase of the $\alpha_{\mathrm{BGR}}$ leads to a contrast condition for the estimated $n_{\mathrm{crit}}$ evolution based on the $E_X = E_{\mathrm{BGR}}$ criterion.

The absence of a distinct temperature dependence of the Mott density is in contrast to the interpretation of an increasing screening length as employed in Ref. [86]. However, the screening efficiency can be modified by dynamical effects [100, 132]. It also can depend on the $k_B T / E_X^b$ [87], which in our study remains significantly below unity contrary to that of Ref. [86]. Eventually, our findings, despite the difference in dimensionality of the investigated structure, agree well to the findings and considerations of Klingshirn and co-workers for ZnO [76], where $n_{\mathrm{crit}}$ is defined by the BGR redshift and exhibits thus only a weak temperature dependence.

In the end, no clear trend can be identified for $n_{\mathrm{crit}}$ as a function of the temperature, and the estimated Mott density applying all the above-mentioned criteria yields a value in range of 0.5 to $2 \times 10^{12} cm^{-2}$. This value is more than one order of magnitude larger than the one determined in InGaAs/GaAs QWs [94]. Moreover, the BGR was only observed for the values above the $n_{\mathrm{crit}}$, in agreement with the finding of Ref. [94], which cannot be understood by the present theories and demands developing a comprehensive theory.

In conclusion, the results of Mott-transition investigation in a polar GaN/AlGaN QW have been reported in this section over a significant range of lattice temperatures using non-resonant optical carrier injection. It was found to be connected to a strong modification in the QW emission spectrum and to occur at constant QW carrier densities around $10^{12} cm^{-2}$ whatever the temperature, which contradicts the simplistic interpretation in terms of a static screening length [86].

There is a certain interest to extend the studied temperature range towards higher temperatures. However, when raising the temperature, apart from difficulties in the analysis that arises from the increase in the homogeneous broadening and increase of non-radiative recombinations, one should also consider the exciton dissociations due to the mass action law. The samples with larger $E_X^b$ such as ZnO QWs can be an ideal case for such study, given that the high-quality of the samples suppress non-radiative recombination over the whole studied temperature range.

### 3.4.3 Dynamics of the carriers at high carrier injection

It worth highlighting another important aspect of the study on SQW-3. The strict linearity of PL intensity with increasing pump power shown in the inset of Fig.3.15(c) and the absence of any ultrafast initial decay in our tr-PL experiments (cf. Fig. 3.17) exclude Auger-scattering as a non-radiative loss process in the present QW up to densities as high as $5 \times 10^{12} cm^{-2}$. Note that the latter value for the carrier density is far beyond the Bernard-Duraffourg limit [96].

Figure 3.17(a) shows the evolution of the spectrally integrated QW emission intensity IPL recorded under high injection tr-PL (excitation spot diameter $< 5\mu m$, and pulse energy 3.5 pJ). The longer decay time at 150K compared to 4K results from the increased carrier temperatures affecting Eq. 3.19, and the dominant impact of radiative recombination within this temperature range [129]. With respect to the high-excitation density (cf. deduced carrier densities in Fig. 3.17(b)) and the high quality of the sample, we neglect carrier localization effects in the following: luminescence stems exclusively from free electrons and holes or free excitons.

The non-exponential character of the PL intensity and $n$ evolution can be ascribed to two different effects. The built-in electric field due to the QCSE leads to a displacement of the electron and hole wave-functions, $\Psi_e(z)$ and $\Psi_h(z)$ (z marking the growth axis), towards opposite sides of the QW [19]. The wave-function overlap $\phi_{e,h}$ is reduced according to:

$$\phi_{e,h}^2 = \int_{-\infty}^{\infty} \Psi_{\mathrm{e}}^*(\mathrm{z}) \Psi_{\mathrm{h}}(\mathrm{z})\, \mathrm{d}z. \tag{3.24}$$

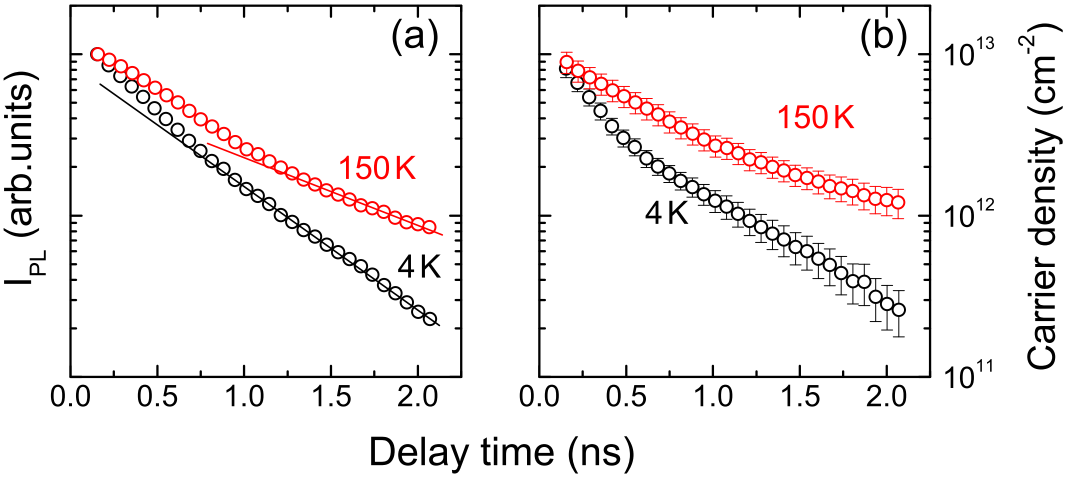

Figure 3.17 – **(a)** Decay of the normalized PL intensity and **(b)** the deduced QW carrier density $n$ in tr-PL recorded at 4 (black) and 150K (red). Solid lines in (a) act as a guide to the eye for the nearly exponential slope at long time delays.

When increasing carrier population in the QW, the electric field in the QW will be partially screened. This increases $\phi_{eh}$, which causes a density dependent radiative lifetime $\tau_{rad}(n)$ *via* the inverse proportionality relation $\tau_{rad} \propto 1/\phi_{e,h}^2$ [130]. This results in an intrinsically non-exponential decay for the free exciton recombination.

The second effect that can contribute to the carrier dynamics is the bimolecular recombination in an EHP. Contrary to the excitonic recombination, the spontaneous recombination rate for uncoupled e-h pairs $R_{spont}$ also depends on the occupancy of states according to:

$$R_{spont} = \sum_{j=A,B} \frac{1}{\tau_{rad,j}} \int_{E_m}^{\infty} D_j^{cv}.f_{e,j}(E) f_{h,j}(E), \tag{3.25}$$

which, in case of partial non-degeneracy, results in an additional non-exponential contribution to the carrier dynamics.

Nevertheless, there is no ultrafast initial decay in our tr-PL experiments , which allows us to exclude Auger-scattering as a non-radiative loss process in the present QW up to densities as high as $5 \times 10^{12} cm^{-2}$. However, this statement does not necessarily need to apply directly for InGaN-based LEDs, even though they are supposed to operate at much lower carrier densities. Indeed, Auger effects occurring in In-containing QWs might be significantly enhanced, owing to the lower bandgap and the strongly increased carrier lifetime [79, 78]. Moreover, the effect of localization might increase the local carrier density in the localized state, which are believed to be the active regions, and hence increase the efficiency of the Auger process owing to its strong dependence to the carrier density [133].

Therefore, we performed the same investigation on InGaN-based QWs, in which quite different dynamics have been observed. The next chapter deals with the dynamics of the carriers at high carrier injection in InGaN/GaN QWs. Our investigation method can provide a precise determination of the carrier concentration in QW *via* monitoring the emission lineshape as a function of carrier injection. The latter allows comparing the results with existing theories, and therefore an accurate estimation of the Auger non-radiative recombination efficiency.

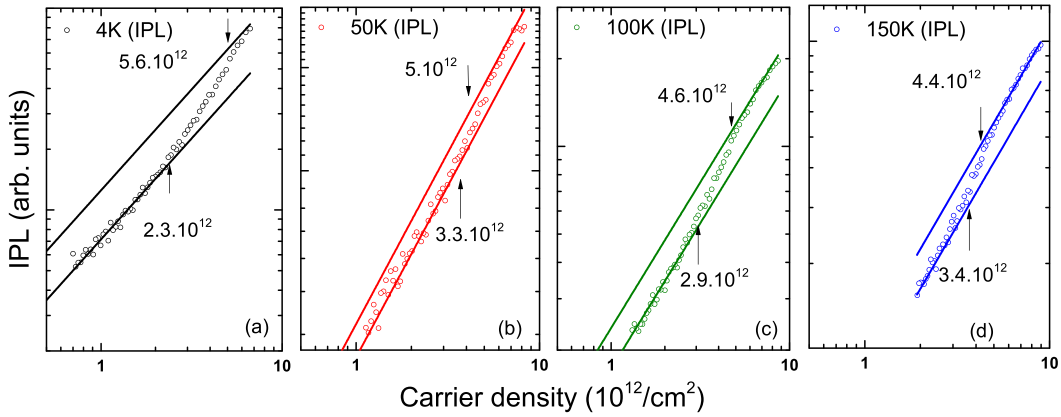

Figure 3.18 – **(a-d)** Evolution of the PL intensity as a function of the estimated carrier density $n$ in the QW for T= 4K, 50K, 100K and 150K, respectively. Arrows for each graph mark the carrier densities corresponding to the deviation of the IPL slope from the linear slope.

As a final note, we shall briefly discuss the evolution of the QW IPL as a function of the carrier density in the QW. Since no non-radiative recombination was identified in this sample and the effective lifetime was shown to be dominated by radiative recombination at temperatures up to 150K, one can rely on the change of the slope of IPL versus carrier density in the QW to determine another criterion for the Mott density. Indeed, at low injection regime IPL is expected to be linearly dependent on the carrier density in the QW, since:

$$IPL = \frac{n_X}{\tau_r}, \tag{3.26}$$

where $n_X$ and $\tau_r$ denote exciton density and radiative lifetime of exciton.

However, assuming the emission is dominated by EHP emission, when increasing the carrier density different regimes for can be defined according to Eq. 3.25. Whereas a linear dependence of IPL on the carrier density above degeneracy limit ($n_{\text{deg}}$), i.e. when the electron and hole Fermidistribution at BE becomes equal to one, in non-degenerate case ($n_{\text{th}} < n < n_{\text{deg}}$) a quadratic dependence is expected, where $n_{\text{th}}$ denotes the carrier density at which a transition from excitonic gas to EHP occurs.

Figure 3.18 shows the integrated IPL over the whole QW emission as a function of the estimated $n$, where the solid lines show the linear slope and open circles represent. At all temperatures, IPL follows a linear slope at low injection densities. However, when increasing the carrier density, IPL starts to deviate from linear dependence at $n_{\text{th}}$, and its slope become super-linear. Upon further increase of the carrier density, the slope of IPL becomes again linear at $n_{\text{deg}}$. Considering this dependence of IPL on carrier density, another upper and lower limit for the Mott transition can be identified, as marked by arrows in Fig. 3.18.

The lower ($n_{\text{th}}$) and upper ($n_{\text{deg}}$) limit carrier densities deduced according this argument are shown by green and orange open circles on Fig. 3.16, respectively. Both limit densities stay above the values deduced for the $n_{\text{crit}}$ according to aforementioned criteria. Indeed, the upper limit value predict a value higher than the one obtained from $\Delta E_{\text{F}} = E_{\text{BGR}}$, since the non-zero $T_{\text{car}}$ leads to a smooth variation of Fermi-distributions of electron and hole at their corresponding Fermi levels. Thus, to reach non-degenerate case density, i.e., $f_e(E_m) = f_h(E_m) = 1$, a higher carrier density in the QW is needed. The monotonous decrease of $n_{\text{deg}}$ when raising the temperature, can be attributed to the temperature dependence of the bandgap.

However, to interpret the values deduced for the lower limit, contribution of several physical effects should be considered. The QCSE screening leads to enhancement of the carrier recombination rates according to Eq. 3.24. However, this effect should increase the efficiency of exciton recombinations, and hence, causes an increase in the slope of excitons IPL. Accordingly, this effect is expected to reduce the value of $n_{\text{th}}$, that is not clearly the case here. Therefore, we tentatively attribute the shift of the observed transition towards higher carrier densities to the fact that the Mott transition is a smooth transition: in absence of a sharp transition from excitonic gas to EHP, the mixture of excitons and e-h pairs with different recombination rate can modify the collected IPL density for a given $n$. Thus, the lowered recombination rate of excitons can compensate the super-linear slope expected for EHP plasma recombinations, and leads to the observation of $n_{\text{th}}$ at higher carrier densities.

# 4 Efficiency droop signature in III-Nitrides LEDs: a time resolved PL investigation on InGaN/GaN QWs

.

The content of this chapter deals with the tr-PL spectroscopy of InGaN/GaN QWs, in order to investigate the internal quantum efficiency (IQE) in those QWs. The results of this investigation is of crucial importance for both industrial research and fundamental studies, since InGaN QWs make the ”heart” of the blue and green light-emitting diodes (LEDs). The aim of this chapter is to provide a clearer picture of carrier dynamics in these QWs, when the injection density increases. Indeed, some intrinsic differences in dynamics of these InGaN QW compared to those of GaN QWs investigated in the last chapter, shall be highlighted here. Moreover, the samples investigated here featuring various design and characteristics that allows us to investigate the role of several physical phenomena on the IQE. The experimental technique is the same as the one applied for GaN QWs in the last chapter. This technique has several advantages compared to those utilized in the literature. First, it allows simplifying the problem by just looking at the active region of an operating LED. Additionally, and perhaps most importantly, it allows us determining with a reasonable accuracy the carrier density in the QW and hence have a quantitative estimation of various recombination rates in InGaN QWs under high injection condition.

## 4.1 Efficiency droop

Nowadays, LEDs are used in a wide range of applications, from displays, sensing applications, communications, to lighting and illumination. LEDs are of center of interest for lighting application owing to their enormous higher efficiencies when comparing to other technologies. For instance, an LED can generate white light with a 20 times greater efficiency than a conventional incandescent light source with a tungsten filament [134]. Replacing on global scale the conventional light sources with LEDs, then, can lead to enormous energy savings, substantial financial savings, and reduction in the emission of global-warming-causing $CO_2$, and several other environmental benefits [135].

Figure 4.1 – Efficiency versus current curves of GaN-based UV, blue and green LEDs, showing a decrease in efficiency when raising the injection current. The green LEDs undergo the largest efficiency droop (adapted from Ref. [135]).

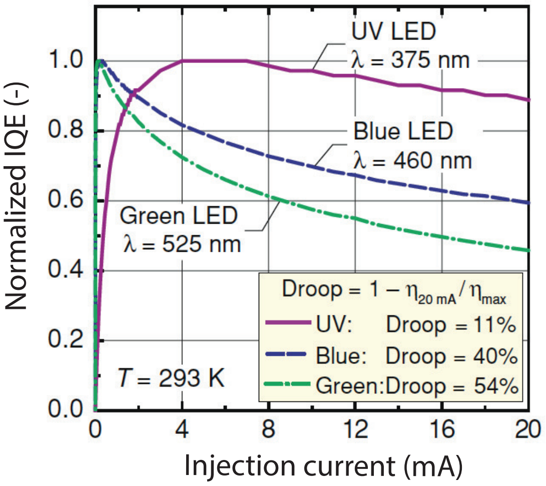

Among all technologies available for solid-state lighting, III-nitride LEDs are the most attractive and promising one, since blue LEDs can be combined with phosphors to realize a white light source. Since the demonstration of the first high-brightness blue LED by Shuji Nakamura and coworkers[1], the development of highly efficient white LEDs passed a successful period.

However, some physical issues remain which prevent their use for high power and highly efficient LEDs. One of particular importance is the drop of external quantum efficiency (EQE) of an LED with increasing the driving current [136], a problem that is so-called the ”efficiency droop”. Typical GaN-based LEDs have a peak in their efficiency at current densities less than 10 $A/cm^2$, and for larger current densities the efficiency gradually decreases. As shown in Fig. 4.1, although an InGaN blue LED has a very high efficiency at low currents, it can suffer more than 40% loss of efficiency at a higher current, which is the desired operating current. The efficiency droop is a particularly severe issue for high-power LEDs, which operate at current densities far beyond the efficiency peak. Although, some solutions have been suggested such as reducing the sheet carrier density by utilizing core-shell nano-rods [137, 138], increasing the thickness [139, 140, 141, 142], or the number [143, 144] of QWs, and improving the lateral current spreading [145]– for details one can refer to [146]– most of these solutions only shift the current density at which the peak efficiency occurs, and do not suggest a fundamental solution for solving the droop problem. Moreover, Even if some of these approaches have been successfully demonstrated in laboratory LED prototypes, no unequivocal design rules have been established yet [146].

In the following we will summarize some mechanisms suggested for the efficiency droop. Efficiency droop is caused by a non-radiative carrier loss mechanism that has a minor effect at low current densities, and becomes dominant at high currents. Generally speaking, non-radiative processes can occur either inside or outside the QW regions. Defect-related Shockley-Read-Hall (SRH) recombinations and Auger recombination are the main non-radiative recombination processes that occur inside the QWs, whereas leakage of carrier leads to the non-radiative recombination outside the QWs. The main mechanisms responsible for the carrier leakage can be invoked as: electron leakage[78], ineffective electron barrier layer (EBL) [78, 147, 148, 149], and ineffective hole injection [150, 151, 152]. Since our investigation focuses on the optically injection properties of InGaN QWs, we concentrate on those mechanisms that occurring inside the QW. In the following, we will briefly introduce the two main mechanisms of non-radiative recombinations that can occur inside the QW.

### 4.1.1 Auger recombination in III-Nitrides

One of the most generally considered mechanisms for the efficiency droop in GaInN/GaN LEDs is the Auger recombination. In a direct Auger process, an electron recombines with a hole, transferring the released energy for exciting a third carrier (another electron (e-e-h Auger) or another hole (e-h-h Auger)), rather than emitting a photon. In simplified terms, the rate of Auger recombination is proportional to the cube of free carrier density. Therefore, at high carrier densities, depending upon the value of the Auger coefficient C, the Auger recombination can become the dominant recombination channel and drive the efficiency down.

It is predicted that only Auger coefficients greater than $10^{-31} cm^6 s^{-1}$ can cause a significant droop in the efficiency, which emphasizes the importance of an accurate estimation of the value of Auger coefficient [136]. Since resonant optical excitation can ensure symmetric concentration of electrons and holes in the QWs, it was considered as a reasonable approach to investigate the efficiency droop. Many measurements have been performed on single QW, multiple QWs (MQW), and double- heterostructure (DH) devices, which were summarized in Ref. [136], and, nevertheless, conflicting results have been reported: whereas some claim on no droop signature in PL efficiency, others report droop evidences in PL investigations.

In addition to several experimental reports on Auger recombination, several theoretical efforts have also been conducted on the role of Auger recombination in InGaN LEDs. Hader et al. reported a very small Auger coefficient of C= $3.5 \times 10^{-34} cm^6 s^{-1}$ for the direct band-to-band Auger losses in InGaN QWs based on fully microscopic many-body models [153]. Kioupakis et al. performed atomistic calculations and proposed that the droop can be caused by indirect Auger recombination, mediated by electron-phonon coupling and alloy scattering [79]. Delaney et al. reported that interband Auger recombination can be significant in InGaN due to the proximity of a higher-level conduction band [154]. According to their findings, the Auger coefficient for bulk InGaN has strong dependence on the bandgap energy, with a maximum value of around $2 \times 10^{-30} cm^6 s^{-1}$ when the bandgap of InGaN is around 2.5 eV. However, the experimental evidences do not fully support the idea that interband Auger coefficient decreases very rapidly when the bandgap deviates from 2.5 eV, since the efficiency droop was observed over a wide range of emission energies.

These are, however, part of the controversial experimental and theoretical prediction conducted on the Auger coefficient. Two rather sophisticated and convincing experimental approaches were tried to provide a direct evidence of the presence and importance of Auger recombination that should be mentioned here. First was done by Iveland *et al.* by detecting high-energy carriers emitted from a cesiated InGaN/GaN LED under electrical injection condition, where the correlation found between the lost carriers and the emitted electron density was assigned to the Auger recombination [80, 155]. Second one reported by Binder et al. [156] on the measured photoluminescence on a test structure containing both type of QWs emitting UV and green luminescence. Upon resonant excitation in the green QW, up to carrier densities at which the emission efficiency showed significant droop, UV luminescence was observed. The authors attributed these high-energy carriers to those missed in the green photons due to droop and calculated a lower limit of 1% of the droop which must be ascribed to Auger processes.

Although, both groups demonstrate a proportionality of the missing current to the measured high-energy carriers, which arise from Auger recombination, they cannot provide a quantitative number for the droop. Moreover, the former experimental approach is only sensitive to e-e-h Auger processes and the latter is limited by the need for both types of high-energy carriers to be first captured efficiently and then recombine radiatively in the UV QW [157].

### 4.1.2 Density activated defect recombination (DADR)

Hader *et al.* [158] propose an alternative explanation for the droop, according to the fact that most of the theoretical calculations predicted a very small Auger recombination rate in GaN. They argue that a loss process with an alternative density dependence can also reproduce the experimental observations, a process called the density-activated defect recombination (DADR). The physical model behind this concept is the following: at low pumping currents and correspondingly low carrier densities, electrons and holes get localized in the local in-plane potential minima in the QW. These potential minima are caused by fluctuations in either the QW composition and/or by QW width fluctuations. They prevent the carriers to reach the defective regions with low IQE. However, when increasing the carrier density, carriers gradually escape from these minima and start to fill the entire quantum well including regions with low IQE. The same effect would be expected if the recombination centers are surrounded by potential barriers.

According to this rather simple and reasonable picture, the authors suggested a semi-empirical function for the non-radiative recombination rate, that becomes activated at high carrier densities. However, the validity of this model was only justified by a reasonable agreement between the fitting and the observed experimental results, and no clear experimental proof is reported on that up to now.

### 4.1.3 ABC model: applications and limits

Because of the importance of unambiguous identifying the droop mechanisms, several arguments based on modeling and simulations were also proposed in the literature. One of the simplest and, perhaps, the most popular approach is the so-called ABC model, in which three principal channels of the electron and hole recombination in the active region of a LED is considered: non-radiative SRH recombination, bimolecular radiative recombination, and non-radiative Auger recombination. The terms A, B, and C are then standing for the rate of each mentioned recombination mechanism.

In particular, the ABC model has been invoked to explain the non-thermal droop in InGaN-based LED structures in terms of Auger recombination, providing a good agreement with the available observations of [159, 160]. Since that time, the ABC model was extensively applied to variety of experimental data to probe the dominancy of Auger recombination in the non-thermal droop of III-nitride LED efficiency.

An oversimplified form of the ABC model can be derived under the following assumptions that are not necessarily accurate assumptions. First, the recombination constants A, B, and C are assumed to be independent of the carrier concentration, that is not a valid assumption considering the carrier delocalization effect, Fermi-filling effect, and variation in the carrier temperature when increasing the carrier density. Let us nevertheless start by this assumption on the carrier density-independent of A, B, and C terms. Then, a basic rate equation for the active region of LED can be given as:

$$\frac{dn}{dt} = P - An - Bnp - C_{ccv}nnp - -C_{cvv}npp, \tag{4.1}$$

where P denotes the pumping rate of carriers in the QW, $C_{ccv}$ and $C_{cvv}$ stands for electron-electron-hole (e-e-h) and electron-hole-hole (e-h-h) Auger recombinations. To simplify more this ABC model, one can assume that the non-equilibrium concentrations of electrons $n$ and holes $p$ in the LED active region are equal. This means that, under electrical injection condition, the electron leakage from the active region is neglected, providing a balance between the currents flowing through the LED structure. Moreover, Eq. 4.1 should be modified in case of a high level of residual doping. However, we neglect this effect for the moment. Then, with symmetric electron and hole concentration, the ABC model can be simplified to:

$$\frac{dn}{dt} = P - An - Bn^2 - Cn^3. \tag{4.2}$$

Under steady-state condition, the IQE can be defined as following:

$$IQE = \frac{IPL}{P} = \frac{Bn^2}{An + Bn^2 + Cn^3}. \tag{4.3}$$

The main reason for the wide popularity of the ABC model relies on its capability of excellent fitting the efficiency behavior of high-quality blue LEDs under variation of their operating current over a wide range (~5-7 orders of magnitude [161]). However, the ABC model has been criticized by several authors for its oversimplified treatment of the physical processes might occur in an operating LED. Moreover, it was shown that an uncertainty in defining the carrier density can simply cause an enormous uncertainty on the A, B, and C deduced from this model by several orders of magnitude [162, 163].

Some disagreements also appeared with a number of observations, largely on green LEDs [164]. Some authors tried to include some effects such as the dependence of the recombination rates on the non-equilibrium carrier concentration, by adding some higher order dependent recombination (more than three) to the ABC model [165, 166]. Apart from the better fitting, no better vision on the underlying physical processes leading to the droop was provided by these modifications [163].

In the following, some of the main phenomena that might affect the recombination rate will be introduced. At low injection regime, two main mechanisms may control the LED efficiency. One is the electron/hole localization by composition or QW thickness fluctuations in the InGaN QWs [167, 168]. The fluctuations of In-rich inclusions in a QW are capable of capturing carriers, and thus preventing them from their diffusion towards the non-radiative recombination centers at threading dislocations. Consequently, the rate of the SRH recombination can becomes dependent on the localization energy, temperature and quasi-Fermi level positions relatively to the conduction and valence band edges [168]. This effect can modify the low density side of the IQE, as shown in Fig. 4.2(a).

Another mechanism, that might affect the estimation of IQE at low-current regime, is the possible existence of a difference in the concentrations of electrons and holes injected into the well. This effect might also be sustained by the residual doping concentration in the QW, which can lead to asymmetry in electron-hole concentrations. This results in IQE which does not vanish at low currents, but tends to a constant value (see Fig. 4.2(b)). The violation of the electron-hole concentration symmetry also requires to take into account both e-e-h and e-h-h Auger recombination, which adds some more complexity to the ABC model.

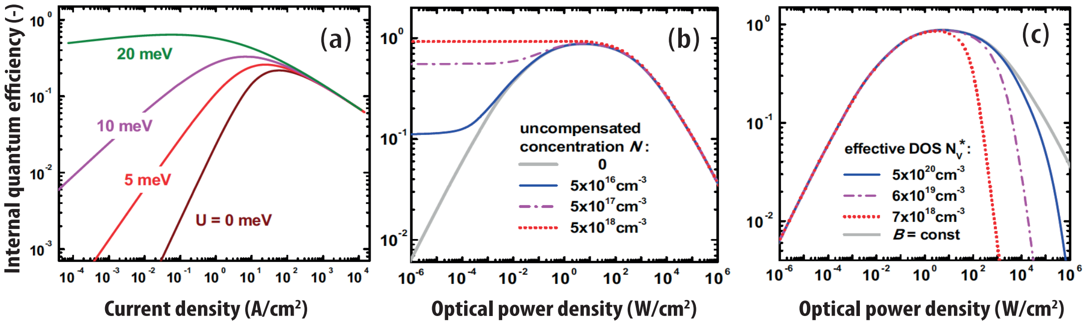

Figure 4.2 – **(a)** Room-temperature IQE as a function of the current density calculated by ABC model accounting for the effect of composition fluctuations in 2.5 nm green InGaN SQW on non-radiative carrier recombination at threading dislocations. The curves correspond to various localization energies U. The recombination constants $B = 1 \times 10^{-12} cm^3/s$ and $C = 1 \times 10^{-31} cm^6/s$ were used in the calculations. **(b-c)** IQE versus optical power density calculated for the case of (b) deviation from the electric neutrality in the QW and (c) degeneration of holes. Calculations were made for 3 nm single QW emitting at 450 nm and recombination constants $A = 10^6 s^{-1}$, $B = 5 \times 10^{-12} cm^3/s$, and $C = 1 \times 10^{-31} cm^6/s$ (adapted from Ref. [163]).

A tendency of the violation of the electric neutrality in InGaN QWs, when raising the current density, has been predicted theoretically for both polar and non-polar LED structures [169, 170]. However, up to now, one cannot distinguish unambiguously the effect of the above mentioned mechanisms in the IQE of LED under low-current operation [163].

At high injection densities, some other effects might cause deviation from the simple ABC model. The first one might be the LED self-heating. To exclude this effect from the experimental results, the IQE measurements should be carried out under pulsed injection at high currents, with the use of a good heat sink. The second effect can be the enhancement of the current crowding at high operating currents. This effect can lead to localization of the photon-emission regions under the electrodes, and thus increasing the optical losses due to the incomplete light reflection from the metal. Consequently, the light extraction efficiency from a LED die becomes current-dependent. To reduce this effect, chip designs to have accessing electrodes for both n- and p-contact layers on one side of the LED was suggested as a solution [171, 172].

Another effect, that is frequently discussed in literature, is the electron leakage into the p-side of an LED structure at high-current densities [136]. According to Ref. [136], any distinction of this effect from those caused by Auger recombination, can be hardly done in the measurements based on the electrical injection. However, some simulations demonstrate a noticeable changes in the slope of the IQE as a function of the injected current at high current densities, that has also strong correlation with the onsets of the electron leakage [163]. The controversy in the reports might be attributed, at least partly, to the difference in the material properties chosen for simulations, or to the LED structure design and the bandgap engineering there [163].

Finally, Fermi-filling effect should be mentioned as another reason of the high-current deviations from the predictions of ABC model. A modeling of this effect was tried through some semi-empirical dependence of the radiative recombination constant $B$ in a bulk semiconductor to the hole concentration, according to [153, 173]:

$$B(p) = \frac{1}{\tau_R(N_V^{3D} + p)}, \tag{4.4}$$

where p is the non-equilibrium hole concentration, $N_V^{3D}$ is the effective 3D density of states of the valence band, $\tau_R$ is the specific radiation time. The reason to consider the hole concentration, is implied in the fact that the electron effective mass is much lighter than the hole one, and thus the Fermi-filling of the valence band is more detrimental.

However, the validity of this simple function was debated, when applying the same assumptions to a narrow QW, i.e., when only the ground state for electrons and holes is confined. The expression predicts an exponentially fast reduction of the B-constant with the hole concentration, in contrast to the power-like dependence typical for bulk materials, according to:

$$B(p) = \frac{1 - exp(-\frac{p}{N_V^{2D}})}{(\tau_R p)}, \tag{4.5}$$

where $N_V^{2D}$ denotes the two dimensional density of states for holes. This means, in particular, that the B-constant reduction becomes substantial only if holes are degenerate. The experimental data reported in [174, 175] demonstrate an evident shift of the current corresponding to the hole degeneration to lower values when decreasing the temperature. In contrast, some temperature dependent measurements conducted on commercial blue LEDs did not reproduce this effect [160]. Therefore, it is still debated in the literature, whether a significant role can be played by the Fermi-filling effect at high currents in the state-of-the-art LEDs or not [163].

However, most of the aforementioned effects can play a role in the electrically injection measurements. Since, our measurement scheme is based on the pulsed optical injection, one can simply exclude the violation of the electric neutrality effect, self-heating, current crowding, and electron leakage in our measurements. The effect of the Fermi-filling can also be included in our estimations, because we are able to obtain a reasonable estimation of the carrier density in the QW. Indeed most of the uncertainties exist in the literature on the recombination rates deduced from ABC model can be circumvented in our method. In the last part of this chapter, after providing evidences of the droop in our samples, we will try to estimate the recombination rate according to the ABC model.

## 4.2 The experimental framework

In order to perform tr-PL experiments, the samples were excited with a third harmonic ($\lambda$ = 280 nm) of a femtosecond mode-locked Ti:sapphire laser, in order to have enough excitation power in UV. Unless stated otherwise, the excitation beam was focused on the sample by means of a 3 mm focal length UV objective (NA = 0.55), that allows for an excitation spot diameter below 5 $\mu m$.

The center of the PL spot on the sample was 100 times magnified and sent through a 50 $\mu m$ pinhole placed in the collection line, which allowed us to probe a region with a quite uniform excitation density. As mentioned before, this spatial filtering allows to obtain a well defined carrier density in the lateral direction. Using QWs in our investigation yield a uniform carrier distribution along the depth of the sample. This statement is also valid in case of multiple QW sample, because of their narrow separating barriers and small thickness of the total structure leading to only a marginal variation in the carrier density between QWs .

The collected PL was analyzed spectrally and temporally using a 32 cm focal length monochromator equipped with a CCD on one exit, and a streak camera in synchronous scan mode on the other exit (temporal resolution ~ 5 ps). To be able to measure the whole QW emission, a 150 groove/mm grating was used to disperse the PL spectra, which allows us to reach a spectral resolution of about 1 meV. The latter is basically limited by the size of the entrance slit of the spectrometer.

## 4.3 samples structure

In order to investigate the droop mechanism, mainly two sets of InGaN/GaN QWs shall be investigated in this chapter. The first set consists of InGaN/GaN QWs, grown on $c$-plane free-standing GaN substrate. The change in the QW thickness and the In composition of the QW allows us studying the effect of quantum confined Stark effect (QCSE) on the droop phenomenon. The high quality of these samples and the low value of In composition of the QW, moreover, make it possible to compare the carrier dynamics with single GaN/AlGaN QW (SQW-3), investigated thoroughly in the last chapter. Although, in industrial LEDs, higher In contents might be used in the QW structures, in our $c$-plane InGaN/GaN QWs we preferentially chose to study low In content. This was done not only to prevent experimental issues arise from long lifetime of high In content $c$-plane InGaN QWs, but also to probe the role can be played by slight In composition at dynamics of the carriers. It will be shown that even this small fraction of In used in our QWs, makes a dramatic change in the dynamics of carrier compared to those of the *c*-plane GaN/AlGaN QWs.

The second set of investigated QWs are *m*-plane InGaN/GaN multiple QW samples (5 QWs in each), with the state-of-the-art quality evidenced by the pure radiative recombination of carriers up to room temperature at low injection densities. The change in the growth condition leads to a low localization in one of these *m*-plane samples, whereas in the second one quasi-QD like behavior was observed owing to the high disorder in the QW thickness or the In composition.

The details of the structure of the investigated samples can be summarized as following:

- **sample C-SQW-1, and C-SQW-2:** These samples consist of a single $In_{0.06}Ga_{0.94}N$ QW, embedded in between of two GaN barriers. The QW thickness is 2nm and 3.5 nm for sample C-SQW-1, and C-SQW-2, respectively. The top and bottom barrier thicknesses in both samples are 50 nm and 200 nm, respectively. The QW structures have been grown by MOCVD on top of a 100 nm $Al_{0.04}Ga_{0.96}N$-template on Free-stranding GaN substrate. The built-in electric filed is estimated to be as strong as 1.25 MV/cm in these two samples.

- **sample C-SQW-3:** This sample consists of a single $In_{0.09}Ga_{0.91}N$ QW with QW thickness of 2 nm, embedded in between of two GaN barriers. The top and bottom barrier thicknesses are 50 nm and 200 nm, respectively. The QW structure have been grown by MOCVD on top of a 100 nm $Al_{0.04}Ga_{0.96}N$-template on Free-stranding GaN substrate. The built-in electric filed amounts to about 1.7 MV/cm in the QW.

- **sample M-MQW-1:** This sample consists of five non-polar QWs of InGaN, with thickness of 3nm. The QWs were separated by 7nm thick GaN barriers, and capped by the last 7 nm thick GaN barrier. The In composition of QW was estimated to be around 9-10% from our Schrödinger-Poisson simulations. The *m*-plane sapphire substrate was overgrown by a 1 $\mu m$ thick GaN buffer layer prior to the growth of the QWs. The growth temperature was set to 750 °C and all growth conditions were optimized to have low localization.

- **sample M-MQW-2:** This sample also consists of five non-polar QWs of InGaN, with thickness of 3nm. This sample share the same structure design with sample M-MQW-2, however, the growth temperature was set to 1250 °C and all growth conditions were optimized to have high localization in the QW. The average In composition in this sample was estimated to be 13%, a value obtained from a Schrödinger-Poisson simulations.

Table 4.1 summarize the design characteristics of all investigated samples, such as the substrate, QW and barrier design, number of QWs, QW thickness $d_{QW}$, barrier thickness $d_B$, and the FWHM of the PL spectrum at low injection densities. In case of single QW samples, the thicknesses of lower and upper barriers are listed, respectively.

Table 4.1 – Characteristics of the investigated sample: the substrate, QW and barrier design, number of QWs, QW thickness $d_{QW}$, barrier thickness $d_B$ (lower and upper one, respectively, in case of single QW samples), and the FWHM of the PL spectrum at low injection densities.

| | Substrate | Structure | number of QWs | $d_{QW}$ (nm) | $d_B$ (nm) | FWHM (meV) |
|---|---|---|---|---|---|---|
| SQW-3 | *c*-plane | $GaN/Al_{0.09}Ga_{0.91}N$ | 1 | 3.2 | 150-30 | 8 |
| C-SQW-1 | *c*-plane | $In_{0.06}Ga_{0.94}N/GaN$ | 1 | 2 | 200-50 | 32 |
| C-SQW-2 | *c*-plane | $In_{0.06}Ga_{0.94}N/GaN$ | 1 | 3.5 | 200-50 | 32 |
| C-SQW-3 | *c*-plane | $In_{0.09}Ga_{0.91}N/GaN$ | 1 | 2 | 200-50 | 26 |
| M-MQW-1 | *m*-plane | $In_{0.10}Ga_{0.90}N/GaN$ | 5 | 3 | 7 | 45 |
| M-MQW-2 | *m*-plane | $In_{0.13}Ga_{0.87}N/GaN$ | 5 | 3 | 7 | 150 |

## 4.4 PL investigation at low carrier injection

In the following we will briefly introduce the optical properties of the investigated InGaN QWs at low carrier injection in order to show their high quality. Some differences in the recombination dynamics at low excitation density shall be highlighted, which can explain the observed differences in dynamics at high carrier injection conditions.

### 4.4.1 Temperature dependence of radiative lifetime and carrier localization effect: S-shape behavior and IQE at low injection

Figure 4.3(a-c) shows the PL spectra of *c*-plane InGaN/GaN QWs (C-SQW-1, C-SQW-2, and C-SQW-3, respectively) at low excitation densities as a function of temperature. The QW exciton emission (X) and the first and second LO-phonon replicas are labeled on the spectra. The GaN barrier emission is also marked by an arrow at around 3.45 eV. There is also another transition on the low energy side of the GaN barrier, that is most probably due to the 2D electron gas at the interface of the buried AlGaN layer below the GaN barriers.

The QW emission energies for these three samples are shown in Fig. 4.4(a), deduced from a fitting of the QW emission peak (X) with a Gaussian function. In all these samples, when raising the temperature, the QW emission energy undergoes first a redshift and then a blueshift and eventually a monotonous redshift. This evolution of the emission energy, the so-called S-shape behavior, is well-understood in InGaN QWs in presence of localization, in terms of the change in the carrier dynamics due to inhomogeneity and carrier localization with

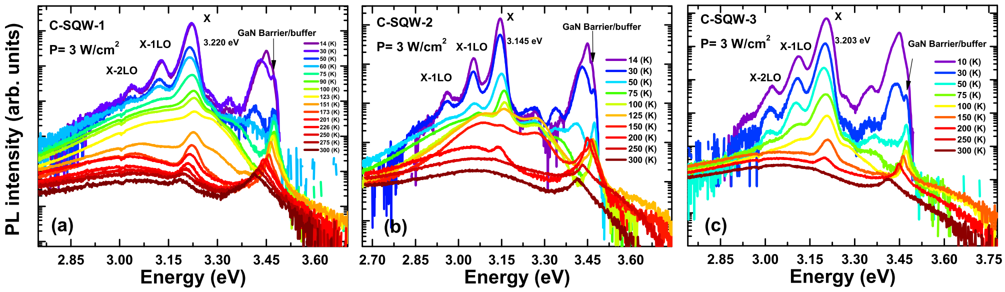

Figure 4.3 – The time-integrated PL spectra of the $c$-plane InGaN/GaN QWs: C-SQW-1(**a**), C-SQW-2 (**b**), and C-SQW-3 (**c**), at low excitation fluence ($\sim 1nJ/cm^2$) as a function of temperature. The QW exciton emission (X), the first and second LO-phonon emissions, and the GaN barrier/buffer layer are labeled on the spectra.

increasing temperature [176, 177, 178]. Indeed, increasing the temperature at first causes relaxation of the excitons from shallow localized sates towards deeper localized centers, and hence leads to a redshift of the emission energy. However, for further increase of the lattice temperature, excitons get delocalized and behave like 2D excitons. In case of the completely delocalized excitons, then one expect the emission energy as a function of temperature follows the Varshni's law [45].

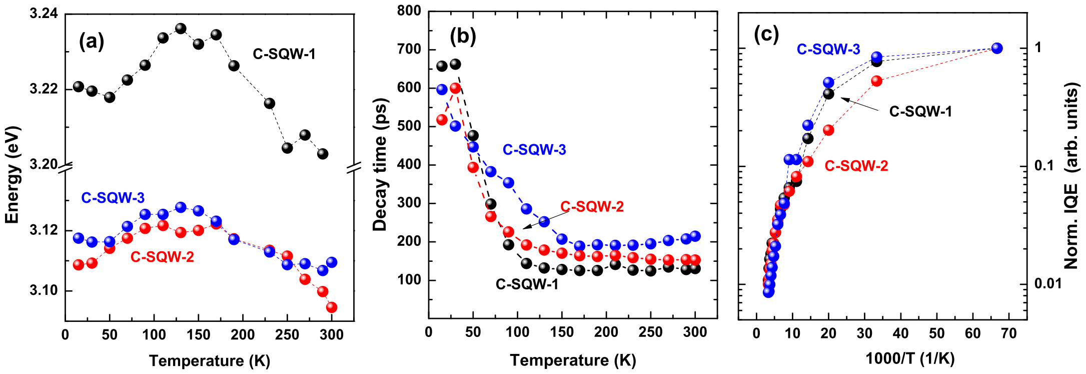

Figure 4.4 – **(a-c)** Evolution of the QW emission energy, effective lifetime, and IQE as a function of temperature for C-SQW-1(black), C-SQW-2 (red), and C-SQW-3 (blue), deduced from low excitation fluences tr-PL measurements ($\sim 1nJ/cm^2$).

The effective lifetime of the QW emission was measured in these samples through tr-PL measurements, as shown in Fig. 4.4(b). In the low temperature range, the effective lifetime remains constant or even slightly increases when increasing the temperature. However, as a general trend in all samples, the effective lifetime quenches fast when increasing the temperature above 50K and remains constant for high temperatures to a value of about 150-200 ps. The latter value is attributed to the non-radiative lifetime in these samples and evidences that the dynamics of delocalized carriers are governed by the SRH recombination at those temperatures. It worth noticing that the onset of delocalization, i.e., when exciton emission energy starts to follow the Varshni's law, appears in the same temperature range where the effective lifetimes also starts quenching (see Fig. 4.4(a-b)).

The normalized IQE for this sample, with assumption of a negligible non-radiative recombination at low temperatures, i.e., IQE= 100%, was extracted from these measurements (see Fig. 4.4(c)). The extracted normalized IQE, also shows a quenching for temperatures higher than 50K, linked with the delocalization temperature of carriers in these QWs.

Figure 4.5(a) and (b) show the evolution of the QW emission energy and corresponding energies to its upper and lower FWHM as a function temperature for the two $m$-plane QWs, M-MQW-1 and M-MQW-2, respectively. In case of sample M-MQW-1, the QW emission energy undergoes a redshift and consequently a blueshift in the emission energy, when raising the lattice temperature from 4K to approximately 170 K. For a further increase of temperature, the emission energy starts to monotonously redshift, and follows the expected Varshni's law (see Fig. 4.5(a)).

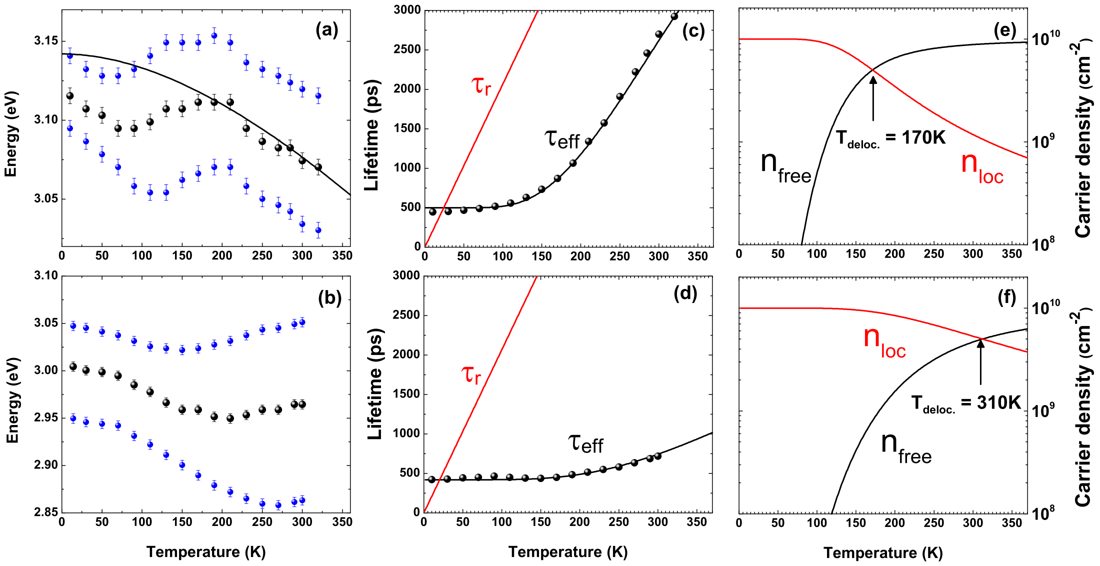

Figure 4.5 – **(a-b)** Evolution of the QW emission energy and the energies corresponding to its HWHM for samples M-MQW-1 and M-MQW-2, respectively. **(c-d)** Measured QW effective lifetime (black circles), as well as the modeled radiative (red solid line) and effective lifetime (black solid line) for samples M-MQW-1(c) and M-MQW-2(d). **(e-f)** The carrier densities of free and localized excitons, deduced from modeling, are shown for M-MQW-1 (e) and M-MQW-2 (f). The temperature, at which the free and localized carrier densities becomes equivalent, i.e., delocalization temperature, is marked by an arrow.

However, in the case of M-MQW-2 sample, the S-shape behavior of the emission energy is pushed towards much higher temperatures. The emission energy start to redshift at temperatures higher than 70K up to 200K, and then starts to blueshift from 200K up to 300K. The second redshift of the emission energy is expected to appear for temperatures higher than 300K. This extended S-shape variation of the emission peak clearly evidences deeper localization centers in this sample, which is also consistent with the larger FWHM measured at 10K for this sample (150 meV), compared to the one of M-MQW-1 (45 meV).

Consistent to the previous reports on the S-shape behavior of InGaN QWs [177, 176], the broadening of the emission spectrum for both samples decreases when the emission energy undergoes a redshift, and increases when the emission energy blueshifts. It worth also noticing the asymmetry in the broadening of the emission energy in Fig. 4.5(a) and (b). This asymmetry arises from the non-thermal inhomogeneous tail on the low-energy side, which is caused by either In fluctuations or QW thickness fluctuations in these samples [176].

Temperature dependence of the QW effective lifetime of two samples was measured at low excitation fluences of about $\sim 1nJ/cm^2$. The carrier density in the QW at that excitation power is estimated to be about $10^{10}cm^{-2}$, a value much lower than the estimated Mott density for these QWs. Under this condition, the effective lifetime $\tau_{eff}$ was measured integrating over the whole QW emission energy. As shown in Fig. 4.5(c), the $\tau_{eff}$ of M-MQW-1 remains constant when increasing the temperature up to ~100K, and then starts to monotonously increase for higher temperature. It clearly follows a linear dependence on the temperature for T > 170K. The $\tau_{eff}$ was modeled with the same model introduced for GaN/AlGaN QWs in the last chapter (cf. section 3.4.1). Here, due to isolation of the localized excitons from the non-radiative centers, the localized excitons decay time behaves similar to the case of 0D excitons and their decay time is expected to be temperature independent. The black solid line in Fig. 4.5(c) shows the results of this fitting, with the fitting parameters of: $\tau_{loc} = 500ps$, $n_{loc} = 8 \times 10^{11}cm^{-2}$, and $E_{loc} = 40meV$. The value of $\tau_0$ was considered to be 10 ps in our simulations [129]. The value of the non-radiative lifetime and the activation energy for the non-radiative recombinations were considered to be $\tau_{nr,0} = 100ps$, and $E_A = 200meV$. However, since no signature of non-radiative recombination was observed in the investigated range, these rather large values have no impact on the modeling results.

Anyway, despite the simplicity of the applied model, a good agreement was observed between the experimental values and model predictions. The carrier density for free and localized carriers are shown as a function of temperature for sample M-MQW-1 in Fig. 4.5(e). Approximately, at T= 170K, the estimated density of free and localized carriers becomes equal. This temperature stays in reasonable agreement with the delocalization temperature of carriers deduced from the variation of the QW emission energy.

The effective lifetime of M-MQW-2, however, features very different characteristics as a function of temperature (see Fig. 4.5(d)): apart from slight increase at low temperatures below 100K, it remains constant when increasing the temperature up to ~200K, and then starts to monotonously increase for higher temperatures. The small increase in the $\tau_{eff}$ at around 100K, can be attributed to relaxation of exciton into deeper localized states, consistent with the onset of emission redshift of the emission energy at those temperatures. However, applying the same for the $\tau_{eff}$ shows that even up to room temperature, the localized exciton dominate the population of carriers in the QW (see Fig. 4.5(f)). This is also consistent with the smaller raise of $\tau_{eff}$ to ~700 ps at room temperature, evidencing the fact the carriers are still localized at those temperatures. The black solid line in Fig. 4.5(d) shows the results of this fitting, with the same fitting parameters applied for M-MQW-1, except the value of $n_{loc}$ and $E_{loc}$ that were found to be $3 \times 10^{12} cm^{-2}$, and $60 meV$, respectively.

The higher localization energy and the higher density of localization centers estimated for the sample M-MQW-2 lead to the conclusion the dynamics of this sample should be governed by deep localized centers in this sample even up to room temperature. However, carrier dynamics in the sample M-MQW-1 should be less affected by the localization centers, particularly, for temperatures above 170K, at which carriers get completely delocalized.

It worth also commenting on the state-of-the-art quality of these $m$-plane QW samples. The fact that, at high temperatures, effective lifetime of carriers shows a linear dependence on the temperature evidences the dominant radiative recombination in these samples at those temperatures, which is not the case for instance for $c$-plane QWs investigated here. This implies the negligible SRH recombination in these samples, when carriers delocalize from localization centers. This statement can also be directly applied to high injection conditions, where one expects the activation of non-radiative recombinations due to overflow of carriers from localization centers with high IQE towards non-radiative centers.

In the end, from these low injection measurements, the normalized IQE was observed to decrease from 100% at 10K to 35% and 46% at 300K for sample M-MQW-1 and M-MQW-2, respectively. One might attribute this high value of IQE observed at room temperature solely to the higher localization energy in these samples. However, from our modeling we could show that, at least in case of M-MQW-1, carriers are expected to be mainly delocalized, and still the effective lifetime is dominated by the radiative part. Therefore, a smaller density of defects or non-radiative centers is the main reason for high IQE observed in these samples.

## 4.5 Carrier dynamics under high injection condition

The content of this section deals with carrier dynamics of the aforementioned InGaN/GaN QWs under high injection condition. In the first part we shall present the experimental evidences for the very different dynamics in InGaN/GaN QWs compared to those of GaN/AlGaN QWs probed in the last chapter. Despite the low In content used in our InGaN/GaN QWs, a dramatic difference was observed, hinting on the intrinsic modification of the optical properties with introducing In into III-nitride QWs. Afterward, the difference in the dynamics of polar and non-polar InGaN QWs will be presented.

### 4.5.1 Dynamic of carrier recombination: comparison between GaN/AlGaN and low In content InGaN/GaN QWs

In this part, a comparison between dynamics of the carrier recombination in a single GaN/AlGaN QW (SQW-3) and $c$-plane InGaN/GaN QW (C-SQW-3) shall be presented. In order to get rid of the SRH non-radiative recombinations, all measurements have been performed at low temperature (T = 4 K). As observed on the streak image obtained at high injection for two samples in Fig. 4.6(a) and (b), the PL spectra features a broad emission at early delays, evidencing the phase-space filling of the 2D density of states. At longer time delays, however, the emission spectrum of the QW get narrower due to continuous decrease of the carrier density in the QW *via* radiative/non-radiative recombination of carriers. Eventually, at very long time delays, the QW emission becomes quite narrow and symmetric in both samples, consistent with the expected characteristics of the excitonic emission.

However, there are some substantial differences between the two streak images that shall be highlighted. Whereas the emission energy of both QWs is expected to blueshift when increasing the carrier density, mainly due to the QCSE screening effect, it is more pronounced on the InGaN QW. Considering the small inhomogeneous linewidth of C-SQW-3, the filling of the localized states cannot cause this shift of the emission energy. However, the value of the blueshift of the emission energy in C-SQW-3 stays consistent with the larger built-in electric field in this QW, which is estimated to be about 1.25MV/cm instead of 0.35 MV/cm in SQW-3.

More importantly, concerning the dynamics, the behavior of InGaN/GaN and GaN/AlGaN QWs are drastically different (see Fig. 4.6(d)): a distinct fast decay component ($\tau \sim 110ps$) in the PL intensity is present at early time delay in the case of InGaN QWs, whereas the PL intensity decays smoothly in case of GaN QWs with a long initial decay time of ~ 380 ps. Several physical phenomena might be responsible for this fast recombination dynamics in C-SQW-3. At first sight, this observed fast dynamic can be attributed to the QCSE screening effect, which is expected to be more significant in case of C-SQW-3. However, the QCSE screening effect leads to enhancement of electron-hole wave-function overlap and should

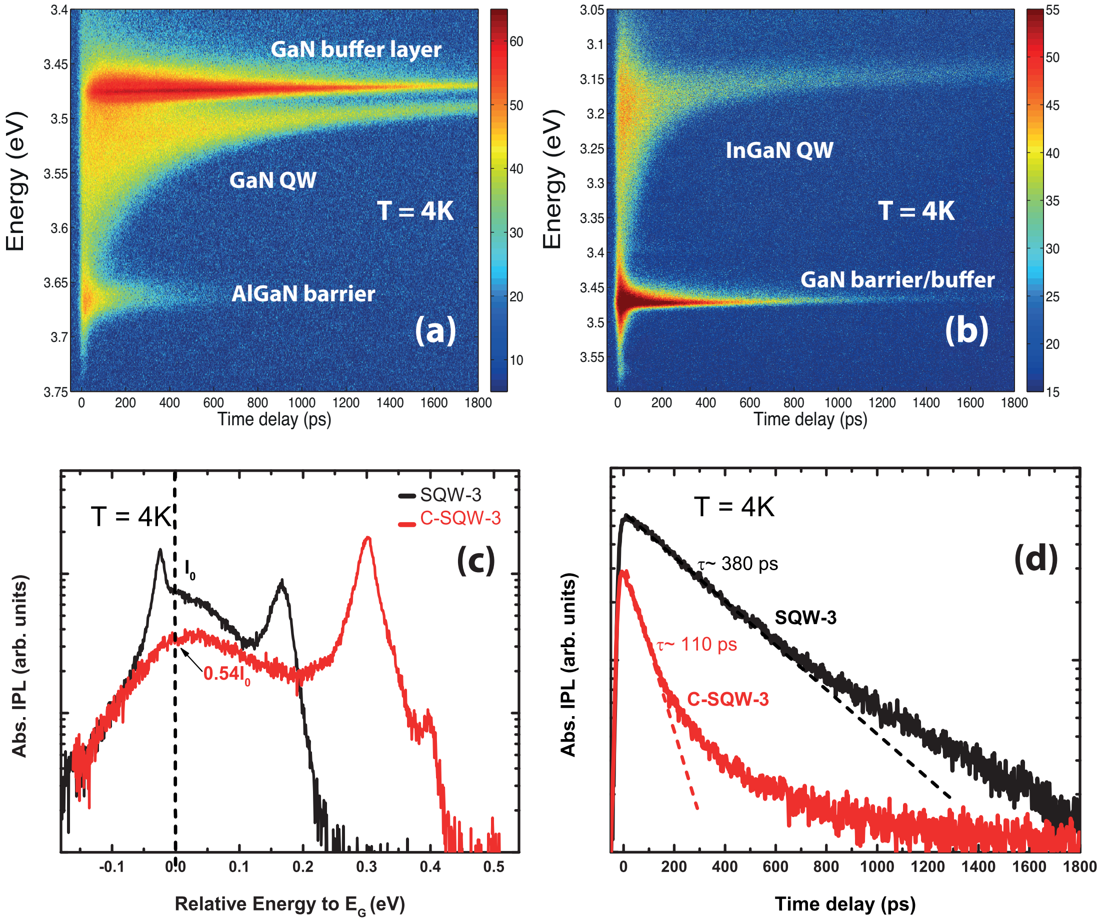

Figure 4.6 – **(a-b)** Streak image obtained at 4K on samples SQW-3 and C-SQW-3 under high injection conditions (excitation fluence ~ 300 $\mu J/cm^2$). The color code represents the absolute IPL. **(c)** The PL spectra obtained by integration over the first 30 ps after the excitation from steak images in (a) and (b). The energy axis is shifted to the QW ground state emission energy of the samples for comparison. $I_0$ is the IPL observed for SQW-3 (reference sample). **(d)** The IPL decay for SQW-3 (black) and C-SQW-3 (red), as well as the initial decay time deduced from fitting with mono-exponential decay functions.

increase the radiative recombination rate according to:

$$\tau_r \propto \frac{\tau_{r0}}{\phi_{e,h}^2}, \tag{4.6}$$

where $\phi_{e,h}$ denotes the electron-hole wave-function overlap integral, which is given by Eq. 3.24.

If we recall the spontaneous emission rate, which is given by:

$$R_{spont}(E) = \sum_{j=A,B} \frac{1}{\tau_{rad,j}} D_j^{cv}.f_{e,j}(E) f_{h,j}(E), \tag{4.7}$$

the IPL at the position of the bandgap in degenerate case, i.e., where $f_{e,j}(E_g) = f_{h,j}(E_g) = 1$, is only proportional to the optical transition matrix elements, and the joint density of states $D_j^{cv}$. This is with the assumption that the built-in electric field in the QW is also fully screened, which is consistent with the saturation of IPL at early delays in our measurements (cf. Fig. 4.7).

Since C-SQW-3 consists of a rather low In content, we do not expected a large change neither in the effective masses of conduction and valence bands nor in the matrix element, when comparing with SQW-3 sample. In order to be able to compare the absolute IPL of the two samples, a set of measurements with exactly the same conditions were conducted on these samples. However, the observed absolute IPL at the energy of the bandgap (see Fig. 4.6(c)) is smaller by factor of two in C-SQW-3 compared to SQW-3, which indicates that radiative recombination rate (lifetime) in C-SQW-3 should be half (twice) of the one of SQW-3 sample. Nevertheless, the effective recombination lifetime in this sample is much shorter, evidencing a strong non-radiative recombination mechanism governing the carrier dynamics in this sample.

There might be some errors in the absolute IPL intensity measured here, induced mainly by the time-window, over which the IPL was integrated (here, about 30ps). However this effect was observed to be marginal, when trying different integration time-windows. The light extraction efficiency should also be quite similar in the two samples, because of the same growth conditions and reasonably similar surface roughness. The latter effect, however, should be treated more carefully concerning $m$-plane QWs, which feature much larger surface roughness and hence larger expected light extraction efficiency.

This fast component evidences a strong non-radiative recombination at early delays (i.e., high carrier density), which may be responsible for the efficiency droop. There is, indeed, an intrinsic difference between InGaN/GaN QWs and GaN/AlGaN QWs, which despite the low In content used in sample C-SQW-3 structure, leads to drastic difference in the dynamics.

### 4.5.2 Signature of droop in $c$-plane and $m$-plane InGaN/GaN QWs at low temperature

In this section the results of a set of measurements on $c$-plane and $m$-plane samples will be discussed. In these measurements, all experimental conditions remain unchanged, in order to be able to compare the collected absolute IPL from samples. Some notable differences in carrier dynamics were observed between $c$-plane and $m$-plane InGaN/GaN QWs.

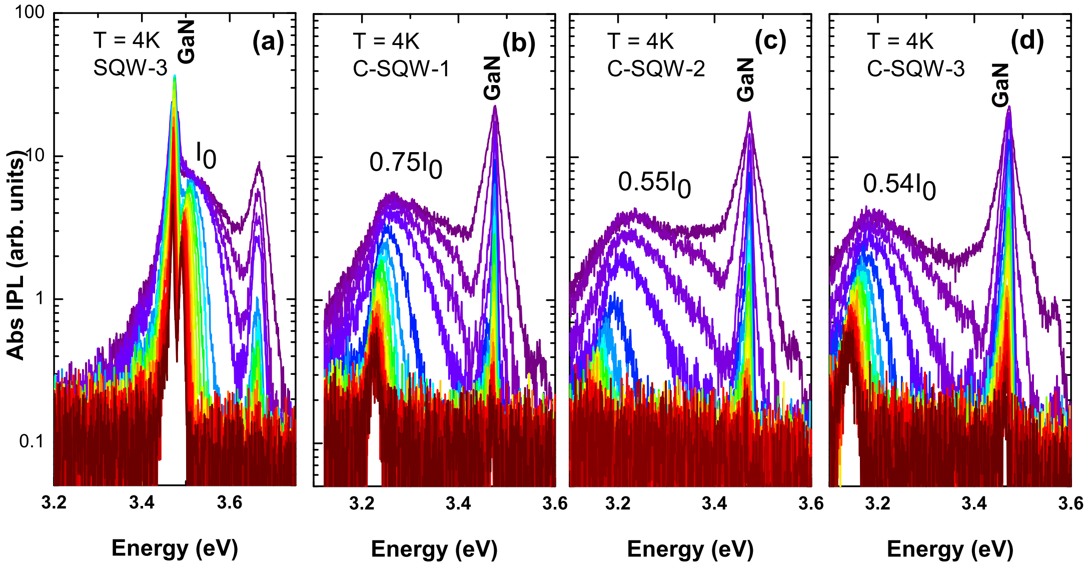

Figure 4.7 – **(a-d)** Time resolved spectra obtained at 4K and under high injection conditions for sample SQW-3, C-SQW-1, C-SQW-2, and C-SQW-3, respectively. The IPLs at the energy of QWs ground state transition are compared to the one of SQW-3 ($I_0$). The PL spectra are extracted for every 50 ps after the excitation up to time delay of 250 ps, and after that for every 100 ps.

Figure 4.7(a-d) shows the tr-PL spectra obtained at 4K at high excitation densities on sample SQW-3 and three $c$-plane InGaN/GaN single QW samples. The first notable point is that in all these measurements, the IPL at early delay is saturated, which evidences the $k$-space filling and at the same time the complete screening of the built-in electric field in the QWs. The term $I_0$ here is the observed IPL in the reference sample at the energy of the bandgap. In all samples, the absolute IPL stays in the range of 0.5-0.75 $\times I_0$. As discussed before, this difference is in the acceptable range considering the possible difference in the electron/hole effective masses in these samples, caused by different In-composition and the difference in the QW confinement energies.

Considering the aforementioned arguments, a longer effective decay time is expected in these samples assuming negligible non-radiative processes. However, similar fast dynamics were observed in all these $c$-plane InGaN QWs, as shown in Fig. 4.8. Whereas, the initial IPL decay time in our reference sample (SQW-3) stays about 380 ps, in all $c$-plane InGaN QWs, IPL has at least three times faster decay. This states a sharp contrast to the longer radiative lifetime of expected for carriers in these InGaN/GaN QWs, and can only be justified by the presence of a fast non-radiative recombination process that govern dynamics of carrier at early delays and high densities. It worth also noticing that for longer time delays, the decay time of IPL

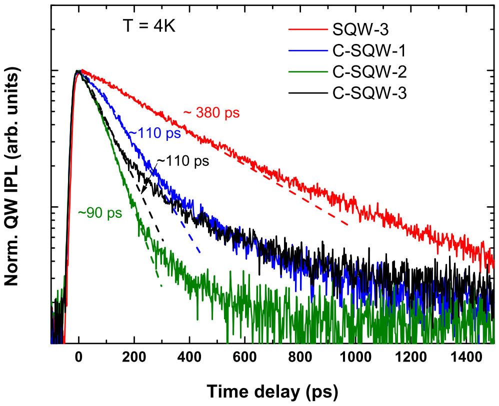

Figure 4.8 – The IPL decays, integrated over the whole QW emission energy, for samples SQW-3 and three other $c$-plane InGaN QWs. The dashed lines show the initial decay time at early delays, and the decay times deduced from fitting with a mono-exponential decay function.

increases. This effect can be explained by the combined effect of the recovered built-in electric field in the QW, localization of carriers, recovering of excitonic enhancement, and reduction of non-radiative recombinations.

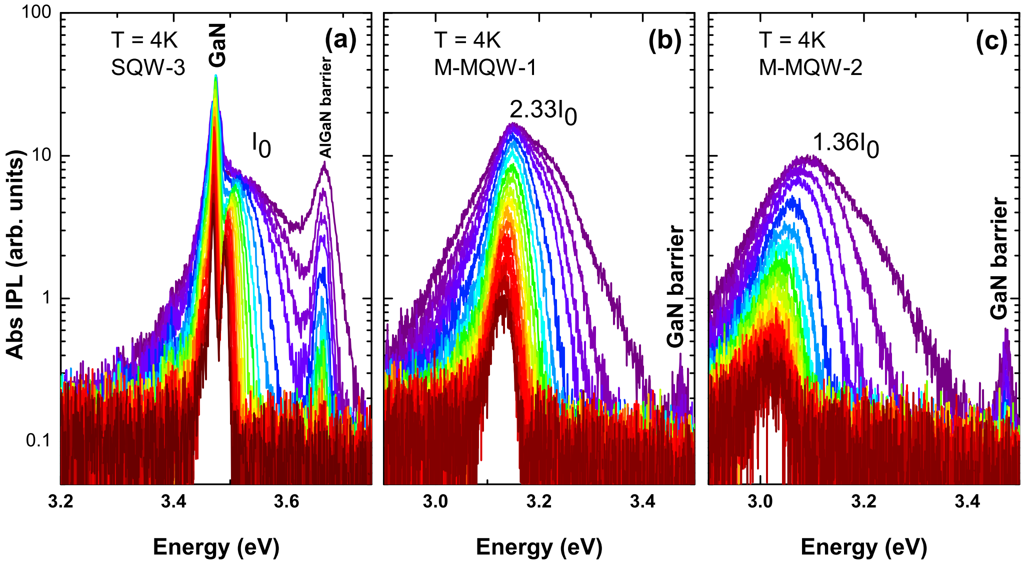

Figure 4.9 – **(a-c)** Time resolved spectra obtained at 4K and under high injection conditions of sample SQW-3, M-MQW-1, and M-MQW-2, respectively. The IPLs at the energy of QWs ground state transition are compared to the one of SQW-3 ($I_0$). The PL spectra are extracted for every 50 ps after the excitation up to time delay of 250 ps, and after that for every 100 ps.

Figure 4.9(a-c) shows the tr-PL spectra obtained at 4K at high excitation densities on sample SQW-3 and the two $m$-plane InGaN/GaN multiple QW samples. Here, comparing the absolute IPL is not, however, as straightforward as it is for $c$-plane QWs. Several physical phenomena should be considered in order to get a quantitative comparison of IPLs. First, one should

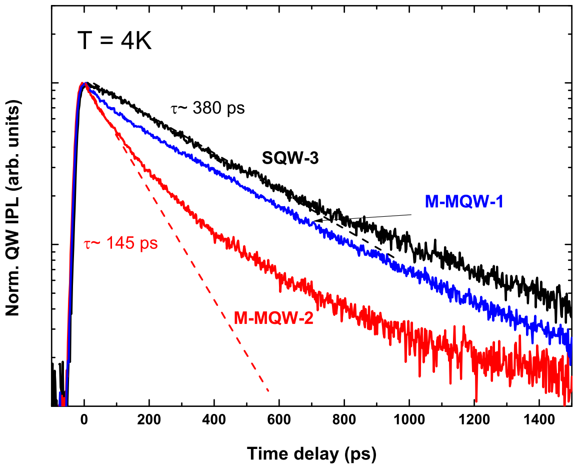

Figure 4.10 – The IPL decays, integrated over the whole QW emission energy, for samples SQW-3 and the two *m*-plane InGaN QWs. The dashed lines shows the initial decay time at early delays, and the decay time deduced from fitting with a mono-exponential decay function.

consider the different extraction efficiency between *c*-plane and *m*-plane QWs, where it is expected to be much higher in *m*-plane QWs due to the higher surface roughness [179, 180]. Second, to be able to compare IPL, one should ensure the same carrier density is captured in *m*-plane samples, that consist of multiple QWs and different barrier thickness from *c*-plane samples. Nevertheless, since both *m*-plane QWs were grown under the same growth condition and feature the same structure design, the carrier density should be the same in both samples just after the pulse excitation. Assuming, the same or reasonably close effective masses for electron and hole in both samples, the difference in the IPL seems noticeably large.

Another remarkable difference might be the continuous shift of the emission energy in sample M-MQW-2 (see Fig. 4.9(c)), which does not saturate even at early delays. This is an evidence of large localization centers densities in this multiple QW sample, that is still not saturated even at those large excitation densities, consistent with our estimation about the localization densities in this sample from our low injection measurements ($n_{loc} \sim 3\times10^{12} cm^{-2}$).

Additionally, the dynamics of carriers in sample M-MQW-1 differs significantly from those of M-MQW-2 (see Fig. 4.10): whereas IPL decays almost mono-exponentially in M-MQW-1, it shows a noticeable time/carrier density- dependence in M-MQW-2. As shown by the red dashed line, IPL of M-MQW-2 decays with a very fast decay component of about 145 ps and then at longer delay times this decay time increases. Once again, comparing the absolute IPL in both samples and the dynamics of IPL decay of the QW provide a clear evidence of some non-radiative recombinations occurring in M-MQW-2 sample, i.e., the *m*-plane multiple QW with higher localization density.

## 4.6 Temperature and power-dependence of non-radiative recombinations

Figure 4.11 shows the decay of IPL, integrated over entire QW emission energies, as a function of the excitation power at T= 300K (a), and as a function of the excitation power density at T= 300K (b) for one of *c*-plane InGaN QW (C-SQW3). The same dynamics exist in the two other *c*-plane QWs. In the *c* -plane QWs, the PL intensity shows a very fast decay at low temperatures (T= 4, and 100K), which was attributed to a fast non-radiative recombination process as discussed before in detail. However, when raising the temperature to 300K, the decay time of IPL becomes longer, and more interestingly, it becomes mono-exponential. This IPL decay time at 300K shows no dependence on the injection density (see 4.11(b)). The value of this decay time remains unchanged at ~ 200ps upon decreasing the excitation density by several orders of magnitude. This value of 200 ps is close to that observed for the IPL decay time in low-injection measurements for this sample at room temperature (see Fig. 4.4(b)).

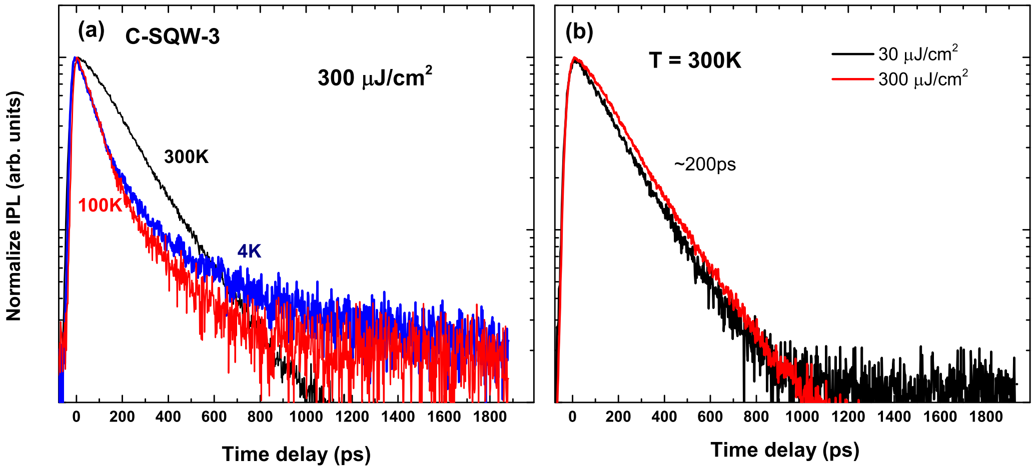

Figure 4.11 – **(a)** Temperature dependence of the QW IPL decays for sample C-SQW3.**(b)** Injection power-dependence of the QW IPL decays at T= 300K for sample C-SQW3.

The observed dynamics in sample C-SQW3 evidence that the recombination dynamics are dominated by SRH non-radiative recombination at room temperature. According to the existing literature [129, 52, 53], non-radiative lifetime due to SRH ($\tau_{nr}$, hereafter) should be exponentially thermally activated, and should therefore decrease when raising the temperature. Assuming that $\tau_{nr}$ is even constant (~ 200 ps) over the whole studied temperature range, which indeed means an underestimated value for $\tau_{nr}$ at low temperatures, the observed decay time of IPL at low temperatures in this sample cannot be explained by SRH process. In fact, at high injection densities applied here, the localization centers are completely filled and due to carriers overflow, they are not anymore isolated from non-radiative centers. Therefore, assuming the SRH process as the dominant process for the observed non-radiative recombination at low temperatures, the effective lifetime of carriers should be longer than 200 ps, that is in a sharp contrast to our experimental results. This allows us to exclude safely the aforementioned DADR process, proposed by Ref. [158], as the origin of the observed droop.

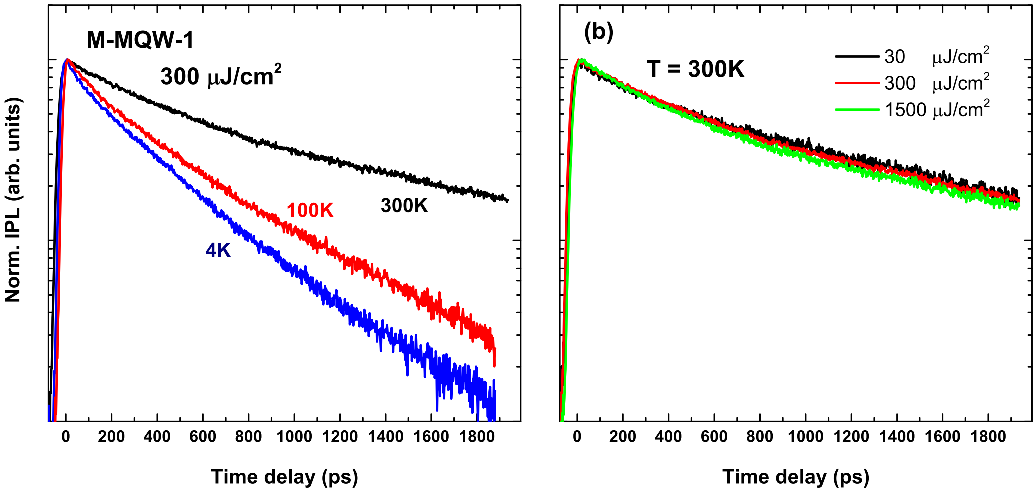

Figure 4.12 – **(a)** Temperature dependence of the QW IPL decays for sample M-MQW1.**(b)** Injection power dependence of the QW IPL decays at T= 300K for sample M-MQW1.

Let us now discuss IPL dynamics in the two $m$-plane samples. As shown before, at low temperatures, no droop signature was observed on sample M-MQW1 under high injection condition. Moreover, at low injection, the IPL decay for this sample is governed by radiative recombination up to room temperature, as is evidenced by the linear increase of the effective decay time in that temperature range. At high injection condition, whatever the temperature, the decay of IPL shows no evidence of fast non-radiative recombination at all temperatures up to room temperature (see Fig. 4.12(a)). More interestingly, when raising the temperature, the effective lifetime of carriers increases significantly, following the same trend as under low injection conditions. Additionally, when increasing the excitation power, only a marginal change in dynamics was spotted (see Fig. 4.12(b)). These two pieces of evidence clearly show that, even at the high excitation regime reached in our measurements, no signature of the droop appears in this sample. The small dependence of the IPL decay on the excitation power, can either originate from the change in the bimolecular recombination rate or only a marginal contribution of the non-radiative recombinations.

However, the carrier dynamics in sample M-MQW-2 appeared to be completely different from C-SQW3 and M-MQW-1. Despite the increase of the effective lifetime of IPL, when raising the temperature (see Fig. 4.13(a)), it still features a non-exponential behavior and a strong dependence on the injection density (see Fig. 4.13(b)). These observations can be interpreted as follows: the droop mechanism responsible for the observed fast non-radiative dynamics,

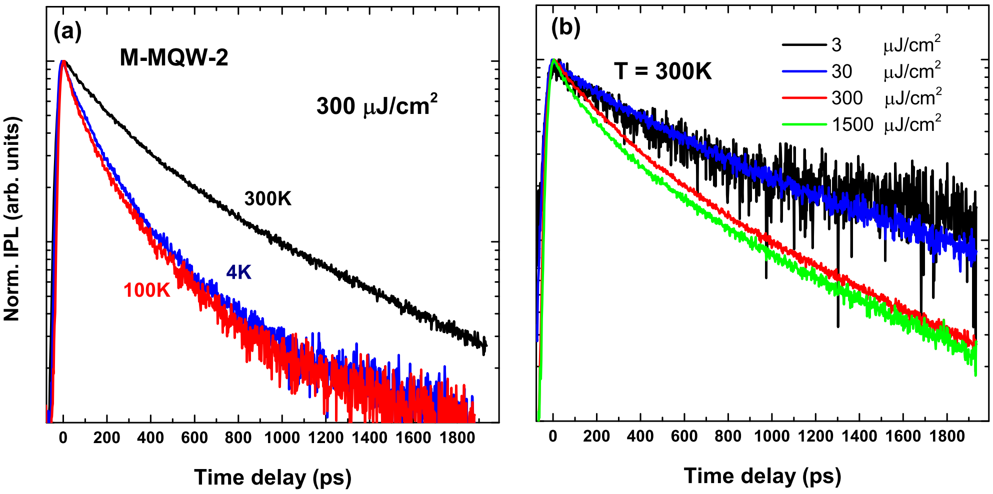

Figure 4.13 – (**a**) Temperature dependence and (**b**) the injection power dependence of the QW IPL decays at T= 300K, for sample M-MQW2.

becomes less rapid when increasing temperature, but still shows up in the dynamics up to room temperature. More importantly, the absence of any droop signature in M-MQW-1 and its distinct impact on the carrier dynamics in M-MQW-2 hints on its link with the localization.

It worth noticing that from low injection measurements, we have shown negligible SRH recombination in these two m -plane QWs. As has been discussed above, the fact that, despite the negligible SRH recombination in our $m$-plane QWs, still one of them shows evidences of droop, casts very strong doubts on the validity of the DADR model as an explanation of droop mechanism in III-nitride LEDs. Our measurements therefore clearly favor the second possible mechanism for the droop under optical injection: Auger recombination. In fact, both clear experimental evidences have been given for Auger recombination in III-nitride LED [80, 156], and some theoretical proposals [33, 79, 181, 154] also support the existence of Auger recombination. To be more specific, we will now try in the next section to obtain a quantitative estimation of Auger rate in our samples through the detailed comparison of the ABC model with our tr-PL results. Nevertheless, to have quantitative estimation of Auger rate in our samples, in the next section we will try simple ABC model to our tr-PL results.

## 4.7 Estimation of Auger coefficient

In order to estimate the Auger coefficient C from our measurements, the experimental IPL decays were fitted, at 4K, with the ABC model. The carrier density was extracted from the same lineshape analysis introduced in the previous chapter, using, for each structure, the electron and hole effective masses deduced from $k.p$ simulations. In order to prevent the possible influence of the feeding of carriers from the barriers, the fit was performed starting only at delays of about 150 ps. At such delays, the luminescence from the barrier has completely vanished, meaning there is no more significant carrier density in the barriers. The estimated carrier density for all samples is in the range of few times $10^{12} cm^{-2}$, a carrier density which is above the Mott density for typical GaN QWs [182, 91].

In our fitting, the SRH non-radiative recombination rate is considered to be negligible in all the studied samples. As discussed before, the SRH could in no way explain the fast non-radiative dynamics in $c$-plane InGaN QWs at low temperatures. In case of $m$-plane, it was shown at that when carriers get delocalized, the carrier dynamics still is governed by the radiative recombination term. In addition to these arguments, the high IQE observed at low temperature in all these samples, allows us to exclude safely the SRH term in our modeling.

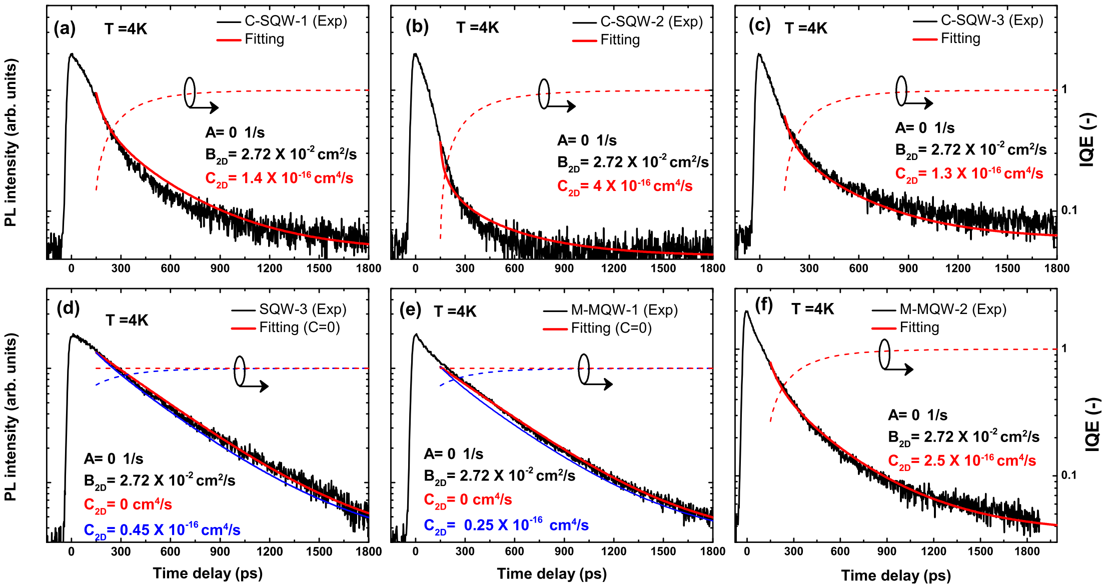

Figure 4.14 – **(a)** Fitting of the IPL decays (solid lines) as well as the experimentally observed IPL decay of the investigated samples: C-SQW-1(a), C-SQW-2(b), C-SQW-3(c), SQW-3 (d), M-MQW-1(e), M-MQW-2(f). In all the fittings the SRH recombination rate A was set to zero. The characteristic radiative lifetime $\tau_{rad}$ was considered to be the same, and dependence of the B on the carrier density due to the Fermi-filling effect was included. The reported value for B, is the one at low density regime. The only fitting parameter to fit all the curves was the Auger coefficient C. The carrier density (in $cm^{-2}$) at the time delay of 150 ps which fitting started is $9.6 \times 10^{12}$, $9.5 \times 10^{12}$, $10 \times 10^{12}$, $4.5 \times 10^{12}$, $5 \times 10^{12}$, and $6.2 \times 10^{12}$ for C-SQW-1, C-SQW-2, C-SQW-3, SQW-3, M-MQW-1, and M-MQW-2, respectively. The dashed lines represent the value of IQE as a function of the time delay. In order to obtain an upper limit for the value of C, for samples SQW-3 (d) and M-MQW-2 (e), the fitting was repeated with increasing C to a value, for which the fittings start to deviate from the experimental data (blue).

We employed in our calculations the radiative recombination rate deduced from Eq. 4.7, with the effective masses used in our PL lineshape fitting. The only free parameters is $\tau_{rad}$. It has been taken to be the same in all samples and we use the same value as the one for samples SQW-3 and M-MQW-3, i.e., the samples show no droop signature in their IPL decays. To avoid complexity at this stage, the Auger coefficient was chosen to be independent of the carrier density. Knowing A and B parameters in all samples, then, the C coefficient was tuned as the only fitting parameter to find the best fit to all QW IPL decay curves.

Figure 4.14 shows the best results for the fitting, upon the mentioned conditions. Despite the simplicity, the ABC model is known to have a huge flexibility to fit any non-exponential IPL decay curve by tuning A, B, and C and playing with the carrier density [162]. Therefore, knowing of the carrier density is of crucial importance to reduce the number of fitting parameters. Nevertheless, a reasonably good agreement is obtained between the fits and the experimental curves. This allows a good accuracy on the estimated C coefficient. In the three $c$-plane InGaN QWs, however, the fitted curves deviate from the experimental results for long time delays (see Fig. 4.14(a-c)). This might originate from the fact that in our preliminary fitting results, the effect of QCSE screening was neglected for simplicity. Although, this effect might become significant at long time delays, i.e., at low carrier densities, it should have only a marginal impact on the fit at early time delays. We have also neglected the effect of the carrier temperatures at this stage, but this could be included in our ABC model.

Table 4.2 summarize the results of the fitting for values of A, B, and C parameters for all samples. B and C parameters are converted to the units for 3D case, in order to be able to compare with the reports in the literature. The Auger coefficient for $c$-plane QWs is found to be in the same range for C-SQW-1 and C-SQW-3 ($\sim 1.3-1.4\times10^{-16}cm^4/s \approx 5\times10^{-30}cm^6/s$). However, the estimated C for sample C-SQW-2 ($\sim 4\times10^{-16}cm^4/s \approx 5\times10^{-29}cm^6/s$ ) is noticeably larger than the two others. The difference between $c$-plane QWs most probably originates from their difference in the QW thickness, since they share quite similar optical properties and growth conditions. This observation is consistent with the theoretical prediction by Vaxenburg *et al.* on the dependence of the Auger recombination rate on the polarization field in InGaN QWs [183]. According to their prediction, not only can the polarization field induce a reduction of the radiative recombination rate and hence an increase of the carrier density in polar QWs, but it can also trigger the Auger-induced efficiency droop. They found a dependence of the Auger rate on both the built-in electric field, and the QW thickness in presence of the same built-in electric field. However, our results state a contrast to other theoretical prediction (Kioupakis *et al.* [33]), according to which both Auger and radiative recombination rates should be modified in the same manner by the polarization electric field.

In case of M-MQW-1 sample, the IPL decay curve was reproduced well with an Auger coefficient of zero. Nevertheless, to estimate an upper limit for the Auger coefficient, the C

Table 4.2 – The fitting parameters applied in the ABC model to fit IPL decays at 4K. B and C parameters were converted to the 3D units, by considering the QW thickness of samples. $IQE_0$ is the value of the IQE extracted from our fitting for each sample at the time delay corresponding to the beginning of fitting curves (t = 150 ps).

| | $A$ $(1/s)$ | $B_{2D}$ $(10^{-2}cm^2/s)$ | $B_{3D}$ $(10^{-9}cm^3/s)$ | $C_{2D}$ $(10^{-16}cm^4/s)$ | $C_{3D}$ $(10^{-30}cm^6/s)$ | IQE$_0$ (%) |
|---|---|---|---|---|---|---|
| C-SQW-1 | 0 | 2.72 | 5.43 | 1.4 | 5.60 | 15 |
| C-SQW-2 | 0 | 2.72 | 9.50 | 4 | 49 | 6 |
| C-SQW-3 | 0 | 2.72 | 5.43 | 1.3 | 5.2 | 14 |
| SQW-3 | 0 | 2.72 | 8.69 | < 0.45 | < 4.6 | >71 |
| M-MQW-1 | 0 | 2.72 | 8.14 | < 0.25 | < 2.25 | >70 |
| M-MQW-2 | 0 | 2.72 | 8.14 | 2.5 | 23 | 27 |

parameter in our fitting was increased until a noticeable deviation from the experimental IPL was observed (shown by blue curve in Fig. 4.14(e)). The maximum possible value for C in this samples was found to be smaller than ~ $0.25 \times 10^{-16} cm^4/s$. At the first sight, this value (~ $2.5 \times 10^{-30} cm^6/s$), might seem still large compared to the reports on the Auger coefficient in the literature [160, 159, 162]. However, the absence of the droop signature in this sample is justified by the larger value of B. Indeed, even if this value of C is large, owing to have large bimolecular recombination rate, the IQE stay stays reasonably large in this sample (> 70 %).

Nevertheless, a much larger value (~ $2.5 \times 10^{-16} cm^4/s$) was found in case of the other $m$-plane multiple QW sample (M-MQW-2). This value is about ten times larger than the upper limit value found in case of M-MQW-1 sample. This huge difference can only be attributed to the much larger localization effects that exist in sample M-MQW-2. Some reports claim that the localization effect can enhance the Auger recombination rate $via$ the increase of the local carrier density [184]. However, at large injected carrier densities in our measurements (~ $10^{12} - 10^{13} cm^{-2}$), the local carrier density cannot be significantly modified by localization centers: the depth of the localization centers (few meV- few tens of meV) is too small to add a significant density of states to the density of states of the QW. Therefore, we tentatively attribute this large value of Auger induced by localization effect to the fact that the localization centers, owing to the 3D confinement of carriers, can enhance the Auger recombination rate through the softening of $k$-selection rules in the Auger scattering process. Although most of the theoretical works predict a negligible Auger rate in III-nitride QWs, it is important to recall the work by Kioupakis *et al.* [79], which demonstrates that phonon or alloy scattering in III-nitrides can significantly enhance the Auger recombination thanks to the relaxation of the momentum conservation during such type of scattering. In a similar way, one can expect that softening of the $k$-selection rules, induced by the localization effect, leads to a similar effect on the Auger recombination. The theoretical investigation of this effect is beyond the scope of this thesis. However, there is a certain interest to investigate theoretically the impact of the localization in 2D continuum on the efficiency of the Auger process, and estimate the possible value for Auger rate in InGaN QWs.

## 4.8 Conclusion and perspectives

In conclusion, we provided a clear experimental evidence of the signature of droop in InGaN/-GaN QWs under large optical excitation. By comparing the dynamics between GaN and InGaN QWs, we showed that there are some intrinsic changes caused by adding In to III-nitride heterostructures. Moreover, two types of polar and non-polar QWs have been investigated in this chapter so as to uncover the role played by the polarization field in the efficiency droop. With engineering the localization effect in our $m$-plane QWs, we could unambiguously demonstrate that the Auger recombination efficiency in InGaN QWs is linked with the localization effect: the efficiency of the Auger process can rise significantly with increasing the localization. Our experimental scheme provides us the possibility to determine accurately the carrier density in the QW, and hence deduce reliably the Auger coefficient from our measurements. Indeed, new theoretical efforts are demanded to fully understand the impact of each aforementioned physical phenomena in the efficiency droop. There is certainly an interest to employ such kind of measurements into single QW LED structures, while the applied bias can simulate a more realistic situation for the measurements, and make our results directly applicable to LEDs. We believe that our work can help to understand better the physical origin of the droop in III-nitride LEDs.

# 5 Exciton hopping under a uniform strain gradient in ZnO microwires

For a long time, strain engineering has been considered as a powerful strategy to tune the electro-optical properties of semiconductors [17, 18]. At the same time, strain is an unavoidable phenomenon that has an enhanced contribution to the properties of semiconductor nanostructures [16]. Therefore, proper design of devices based on strain effect in semiconductor nanostructures demands a better understanding of the strain effects on the electronic and optical properties of semiconductor nanostructures. To exemplify the strain effect on the electro-optical properties in semiconductors, we can point out the strain-induced Stark shift of the emission energy in III-Nitride semiconductors [19], the strained silicon application in mobility enhanced transistors [18], and bandgap engineering of nanowires with core-shell structure with strain [20]. Moreover, semiconductor nanowires are interesting for fundamental studies of strain effects, since a large range of both compressive and tensile strain can be applied to them by simply deforming the nanowires without introducing dislocations, owing to their higher elastic strain limits [15]. Applying the large values of tensile strain is another advantage of micro/nanowires, while this is not easy to reach in bulk structures [21]. In fact, tensile strain in bulk structures can only be achieved in strained epitaxial layers, but is limited to small values. The mechanical-optical coupling properties of ZnO micro/nanowires have raised a huge interest for application in piezoelectric-optical devices as well as photon-mechanical devices [16].

This chapter deals with the exciton dynamics in bent ZnO microwires (MWs) under a uniform strain gradient at low temperatures. Starting with the evidence of exciton movement under a strain gradient, it then focuses on a theoretical model to explain the mechanism of this movement, taking into account the fact that the majority of excitons are bound to donors at low temperatures in our samples. Eventually, the validity of the proposed model is examined by performing measurements on a sample with different design over a finite range of temperatures. As an introduction to this chapter, the growth of the investigated samples and the experimental techniques shall be introduced.

The results shall be discussed in this chapter have been previously published, or are submitted, as the following papers:

- *Exciton drift in semiconductors under uniform strain gradients : Application to bent ZnO microwires*
X. Fu, G. Jacopin, M. Shahmohammadi, R. Liu, M. Benameur, J.-D. Ganière, J. Feng, W. Guo, Z. M. Liao, B. Deveaud, and D. Yu, ACS Nano, **8(4)**, 3412-3420, (2014).

- *Hopping process of bound excitons under an energy gradient*
G. Jacopin, M. Shahmohammadi, J.-D. Ganière, and B. Deveaud, APL., **104(4)**, 042109, (2014).

- *Donor-bound exciton hopping under a uniform strain gradient*
M. Shahmohammadi, G. Jacopin, X. Fu, J.-D. Ganière, D. Yu, and B. Deveaud, submitted to APL (2015).

## 5.1 Experimental scheme

### 5.1.1 Sample growth

Hexagonal ZnO MWs align along the $c$-axis [0001] have been explored in this study. The ZnO MWs were grown by chemical vapor deposition (CVD) in a horizontal quartz tube furnace on Si substrate. A zinc oxide substrate with purity of about 99.9999% was used in combination with graphite powder (molar ration of 1:1) in an aluminum boat for growth. Before growth, the furnace was purged with Argon to avoid contaminations in the furnace. The growth was performed at $1050°C$ in the presence of oxygen flow (3.0 sccm). Afterwards, the Si substrate covered with grown ZnO MWs was cooled down to room temperature. The SEM image of the grown MWs is shown in Fig. 5.1, on this image the typical diameter of wires is ranging between 2 to 3 $\mu m$ (see the inset).

### 5.1.2 Standard four-point bending configuration

In order to apply strain on ZnO MWs, the ZnO MWs were mounted in a dedicated module allowing to obtain a four-point bending configuration according to the ASTM E855-08 standard [185]. This configuration allows us to reach a pure compressive/tensile strain across the MWs and, at the same time, have a precise control on the applied strain value. As shown in Fig. 5.2(a), the lattice constant along the $c$-axis varies linearly by the distance from the neutral plane of the MW. Knowing the curvature radius of the neutral plane $\rho$, the strain value at any point across the MW can be evaluated by:

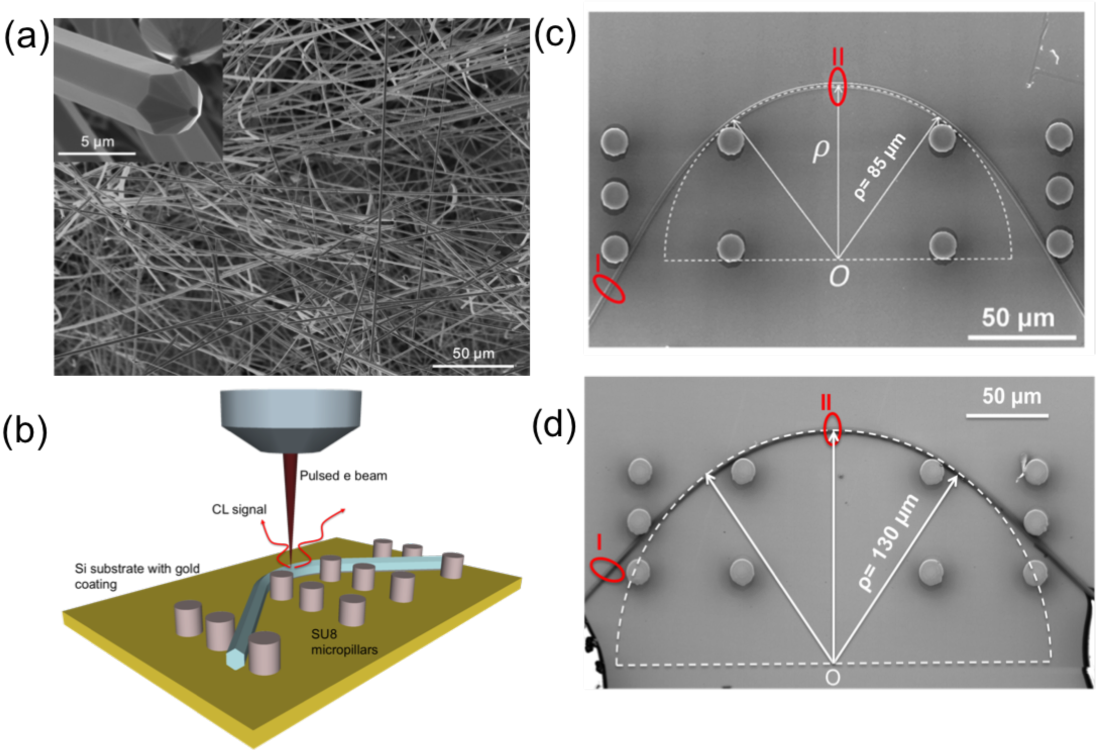

Figure 5.1 – **(a)** The SEM image of the ZnO MW ensembles after the growth with an average diameter between 2 and 3 $\mu m$. The inset shows that the ZnO MWs are grown along the [0001] direction and have an hexagonal cross section. **(b)** Schematics of a ZnO MW in four-point bending configuration in between of SU8 micropillars. The MW is excited by either pulsed or cw electron beams. **(c-d)** The SEM image of the ZnO MWs called sample I and sample II with diameters of d= 2.24 $\mu m$ and d= 2.33 $\mu m$, respectively. The straight and bent segments of the MWs are labeled by as "I" and "II", respectively. $\rho$ shows the radius of curvature of the neutral strain plane in the two samples, which has been designed to be larger in sample II compared to sample I (130 $\mu m$ instead of 85 $\mu m$).

$$\varepsilon_c = \frac{c_r - c_0}{c_0} = \frac{r}{\rho}, \tag{5.1}$$

where $c_r$ denotes the lattice constant at given distance $r$ from the neutral plane. Indeed for points on the outer side of the neutral plane the strain value is positive (tensile), whereas points in the inner side have negative value of strain (compressive strain). In a first-order approximation, the bandgap is expected to increase (decrease) by applying compressive (tensile) strain to a direct bandgap semiconductor (shown by the color code in Fig. 5.2(b)).

To fabricate the SU8 micropillars, SU8 photoresist was spin coated on the Si substrate with speed of 500 rpm for 10 s in the first step and then with 3000 rpm for 60s. The pre-baking was

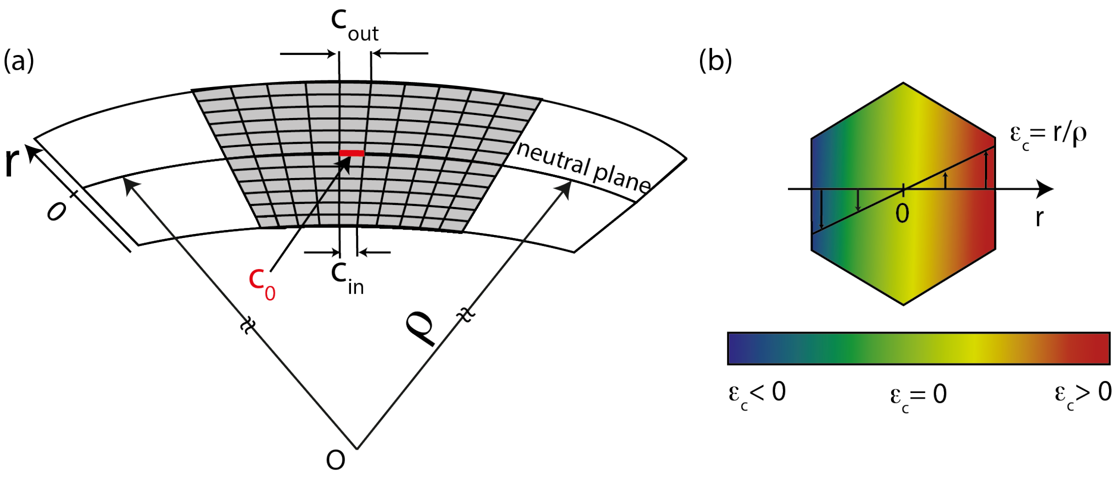

Figure 5.2 – **(a)** Schematics of a ZnO MW under pure bending configuration, showing the variation of lattice constant $c$ across the MW. The terms $C_{in}$, $C_0$, and $C_{out}$ stands for the lattice constant values at the most inside region, the neutral plane and the most outside region of the MW cross section. **(b)** Variation of the emission energy, i.e., the bandgap (color code), and the uniaxial strain value along the $c$-axis $\varepsilon_c$, across the MW cross section.

performed in a furnace at 65 $°C$ for 1 minute and then 95 $°C$ for 3 minutes. The lithography process was done under UV exposure with power intensity of 13 $mW/cm^2$ for a duration of 12 s with a predesigned mask. After the lithography process, the surface of micropillars and Si substrate was coated with a layer of gold with 20 nm thickness to avoid charging effect in the cathodoluminescence (CL) measurements. The lithography mask for SU8 micropillars was designed in a way to have the possibility of applying different values of the strain gradient across the ZnO MWs.

Some of the ZnO MWs were detached from the growth substrate and individually transferred to the substrate designed for applying the four-point bending deformation. The MWs were mounted between the SU8 micropillars by means of two needle-shape glass tips under an optical microscope. The applied deformation was verified to be elastic since ZnO MWs could resume their original straight state once they were taken out of the SU8 pillars.

As shown in SEM images of Fig. 5.1(c-d), using different micropillars to mount the ZnO MWs, different degrees of strain gradient can be achieved. The SEM images in Fig. 5.1(c) and (d) correspond to ZnO MWs that have been probed in section 5.2 and section 5.4, respectively. The difference in the measured dynamics will be discussed in detail later in section 5.4.

### 5.1.3 Experimental techniques

To probe dynamics of excitons under a uniform strain gradient, we used mainly time resolved (tr) CL as a powerful technique that can provide us a good vision on dynamics tanks to its high spatial (50 nm) and temporal resolution (30 ps) [72]. In addition to tr-CL experiments, continuous wave (cw) CL measurements were carried out as a complementary technique to provide results on the spatial variation of the ZnO MWs optical properties with a large dynamical range, thanks to the higher excitation current in the cw mode. Eventually, some polarization resolved PL measurements were performed to probe the polarization properties of the near band edge emission of the probes ZnO MWs.

Time resolved CL experiments have been performed with an Attolight Alalin Chronos 4027 system. The excitation was done with ~1 ps electron pulses and the repetition rate of 80MHz. We used an acceleration voltage of 6 kV in all the measurements. The Attolight tr-CL system allows us to switch from pulsed mode to cw mode. The CL signal was collected by the reflective optics of the CL microscope and sent to a Jobin-Yvon spectrometer (iHr320) equipped with a Synapse CCD camera as well as a streak camera synchronized with the electron pulse. The luminescence of the samples was analyzed by a 600 groove/mm grating. The photoluminescence (PL) measurements were carried out by exciting a single straight ZnO MW using the third harmonic ($\lambda$ = 280 nm) of a picosecond mode-locked Ti:sapphire laser (the average power and repetition rate of 50 $\mu W$ and 80 MHz, respectively).

## 5.2 Exciton drift under a uniform strain gradient

### 5.2.1 Continuous wave CL measurements

Figure 5.3 shows the results of cw-CL experiments on sample $I$ obtained by scanning the excitation spot across the ZnO MW at 8K. The line scanning cw-CL spectra were collected on both straight and pure bending regions of the MW– indicated by regions $I$ and $II$ in the SEM image of Fig. 5.1(c-d), respectively. The CL spectrum on the straight part consists of a sharp emission line at 3.360 eV attributed to donor-bound exciton ($D^\circ X$) emission line, and two other emission lines at 3.292 eV and 3.222 eV attributed to the two-electron-satellite (TES) and the first LO phonon replica of $D^\circ X$, respectively. According to the existing literature, the LO phonon energy in ZnO is measured to be ≈ 72 meV [47]. Most-importantly, when the excitation spot was scanned across the straight region of MW, the CL spectrum remains unchanged.

However, the CL spectra collected across the bent region of MWs have quite different features from those on the straight part (see Fig. 5.3(b)): the luminescence features a broad emission, when excited within the compressive region (lower part of figure), while its broadening pro-

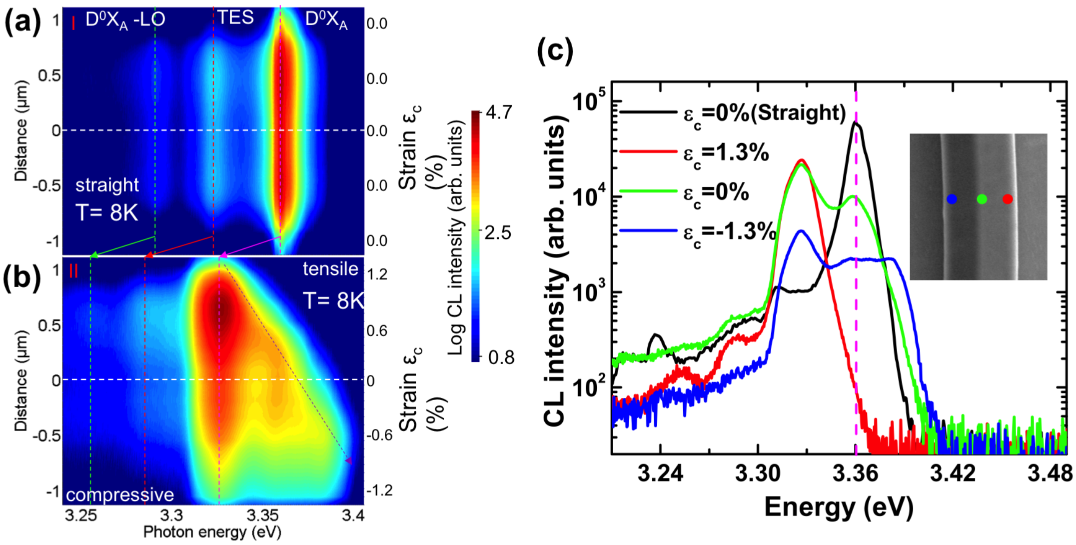

Figure 5.3 – **(a, b)** Line scanning cw-CL spectra along the straight cross section "I" and the pure bending cross section "II" of the ZnO MW (sample I). The neutral strain plane across the MW is set as zero for position. **(c)** cw-CL spectrum at the straight cross section (black), and three different spots across the bent cross section of the MW with local strain value of $\varepsilon_c = -1.3\%$ (red), $\varepsilon_c = 0\%$ (green), and $\varepsilon_c = +1.3\%$ (blue).

gressively shrinks down by moving the excitation spot towards the tensile part across the MW (upper part of the figure). In addition to the change in the broadening of CL spectra from compressive to tensile region, the highest emission energy of the CL spectra also redshifts moving from compressive to tensile region, shown by the red dashed line on the figure. The emission energy in the neutral plane across the MW (shown by a horizontal dashed line) appears at the same emission energy than the emission of the CL at the straight part of wire. The CL spectra of the straight part, and three spots on the bent segment of the MW are compared in Fig. 5.3(c), where the changes in the emission energy and the broadening of the spectrum appear even more clearly. The change in the emission energy in addition to the position dependence of the CL emission broadening can be an evidence of the exciton movements. However, to shed light on the exciton dynamics and to safely exclude other explanation for the observed change in the CL spectra, like valence band crossing [186, 187] or charge accumulation due to the transverse piezoelectric field across the MW [188], we decided to perform tr-CL measurements.

The CL spectral mapping of Sample *I* at room temperature is shown in Fig. 5.4. Similar to measurements at 8K, no shift in the emission energy or broadening can be distinguished, when the excitation spot was scanned across the straight segment of the MW (see Fig. 5.4(a)). The spectral line scanning on the bent region of the MW features the redshift of CL emission energy by moving from compressive to tensile region across the MW (see Fig. 5.4(b)). However, a remarkable difference can be identified with respect to the previous measurements performed at 8K: the CL spectrum remains narrow, independent of the excitation position across the MW.

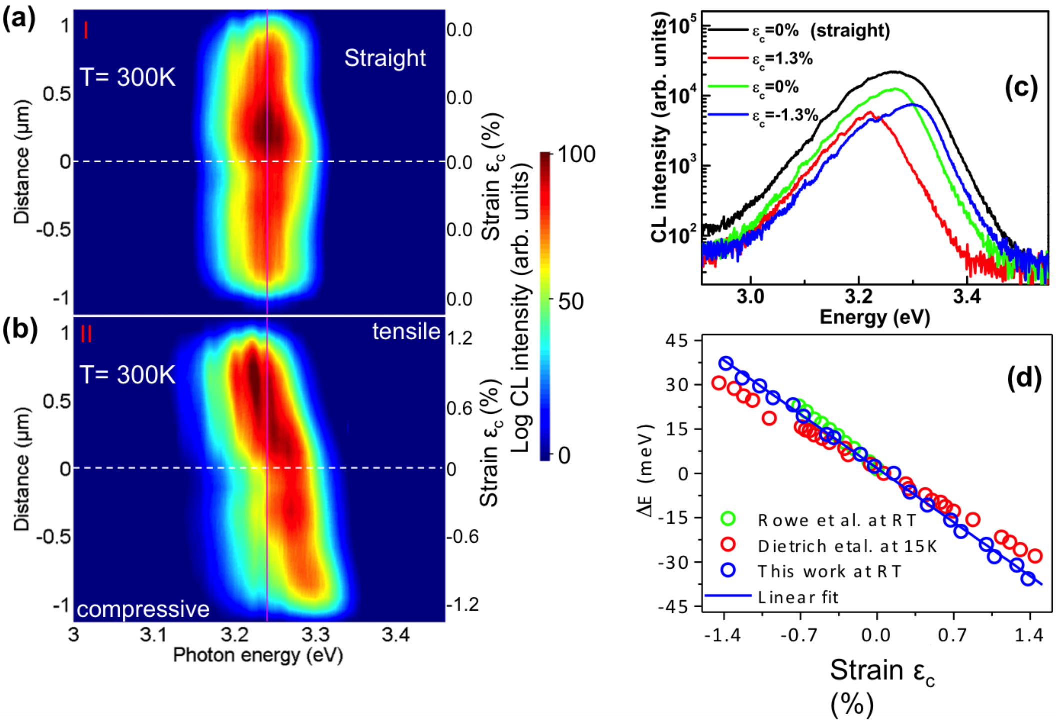

Figure 5.4 – **(a)** and **(b)** Room temperature line scanning cw-CL spectra across the straight and the bent segment of the ZnO MW (sample I), respectively. The geometric neutral plane of the MW is set as zero for the position axis, negative in inside and positive in outside.**(c)** Typical room temperature CL spectra with excitation spot at the outermost ($\varepsilon_c = 1.3\%$), middle ($\varepsilon_c = 0\%$) and innermost ($\varepsilon_c = -1.3\%$) part of the MW at the pure bending cross section ”II”, as well as that at the straight part ”I”. **(d)** Energy shift of the NBE luminescence peak as a function of local strain distribution in the pure bending cross section ”II” of the probed ZnO MW in our study (blue), and the previous experimental reports in the literature by Diterich *et al.* on bent ZnO MWs (red circles), and Rowe *et al.* on bulk ZnO (green circles).

Another aspect of the spectral line scanning across the bent region of MW at room temperature is its agreement with previous reports in the literature by Refs. [21, 189], i.e., the linear variation of the emission energy (bandgap) versus the local uniaxial strain across the MW. Estimating the curvature radius of the bent region of the probed ZnO MW, the deformation potential amounts to $\partial E_{ex}/\partial\varepsilon_c \approx -27.3 meV\%$. The latter value is very close to the one extracted from experimental results on homogeneously stressed ZnO reported by Row and coworkers (about -29.5 meV/%) [189], and is larger than the reports of Dietrich and coworkers on bent ZnO MWs about (-20.4 meV/%)[21].

The fact that the CL emission linewidth is position independent across the bent region of the MW at room temperature originates from the shorter lifetime of excitons at room temperatures

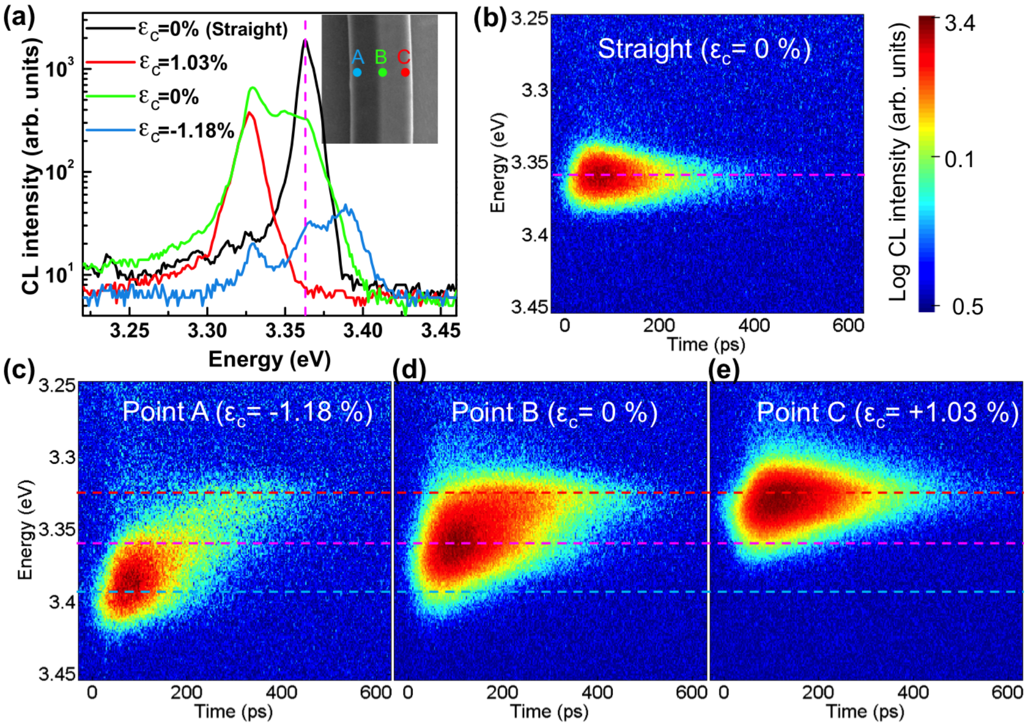

Figure 5.5 – **(a)** Time integrated CL spectra obtained by pulse excitation at point A (inside: $\varepsilon_c = -1.18\%$), B (middle: $\varepsilon_c = 0\%$), and C (outside: $\varepsilon_c = +1.18\%$) on the pure bending cross section as well as the straight part of the ZnO MW sample I. The inset shows the relative position of the excitation spots A, B, and C on the bent cross section of the MW. **(b-e)** Streak camera images showing emission energy as a function of time after the pulsed electron excitation the straight part (b) and points A, B, and C of the purely bent section (c, d, e). The intensity is color coded in logarithmic scale. The pink dashed line indicates the emission energy of the $D^{\circ}X_A$ luminescence in strain-free part of the MW. The blue and red dashed lines show the emission energies of 3.392 and 3.322 eV, corresponding to the highest and the lower part of the time integrated CL spectra, respectively.

due to the thermally activated non-radiative recombinations. In fact, the effective lifetime of excitons is much shorter than the time needed for the drift of excitons from one side of MW toward the other side. This interpretation is confirmed by our temperature dependent time resolved PL measurements, where a very short lifetime was observed for excitons at room temperature ($\tau_{eff.}|_{(T=300K)} \leq 40ps$).

To reveal the differences between measurements at 8K and room temperature and directly observe exciton dynamics, we further performed tr-CL experiments at 8K. Figure 5.5(a) depicts the time integrated CL spectra obtained at 8K under pulsed electron excitation (pulse duration~ 1ps) by exciting the straight part (segment I) of the MW (black), and three equally spaced spots across the bent region (segment II) of the MW: Point A on the inside part of segment II ($\varepsilon_c = -1.18\%$), point B approximately on the neutral strain plane ($\varepsilon_c = 0\%$), and point C on the outside region ($\varepsilon_c = +1.18\%$). The relative position of the three probed spots are shown on the inset of Fig. 5.5(a). The time integrated spectra look similar to those obtained by cw-CL, except for the change in the ratio of the CL intensity of the low-energy to the high-energy part of CL spectra. This change most presumably originated from the fact that the quality of the probed ZnO MWs changes by keeping them for long time in high vacuum. Indeed, a huge increase in the relative intensity of the defect band (originated from oxygen vacancies) to the NBE intensity was observed when keeping the ZnO MWs in vacuum. For subsequent measurements (presented in section 5.4), we therefore were careful to minimize as much as possible the time spent by the sample under vacuum.

The streak image corresponding to the straight part of the MW is shown in Fig. 5.5(b). In this image, the emission energy of the CL spectrum shows no variation with time and the CL intensity decays mono-exponentially with a time constant of about 105 ps. However, the streak images obtained when exciting on points A, B, and C dramatically differ from the one obtained on the straight part. The most remarkable feature is the "comma shape" of these time resolved streak image (Fig. 5.5(c)), which directly illustrates that the NBE emission energy undergoes a time dependent redshift of the emission energy. The same feature exists in the streak image corresponding to point B (Fig. 5.5(d)), however, the highest emission energy is approximately the same as the emission of the straight part. Finally, in the streak image obtained for point C no time dependent energy shift exists. The time dependent redshift of the emission energy, observed for different points across the bent region of the MW, directly evidences the movement of excitons from the region of the MW under compressive strain (inside of the MW) towards the region of the MW under tensile strain (outside of the MW).

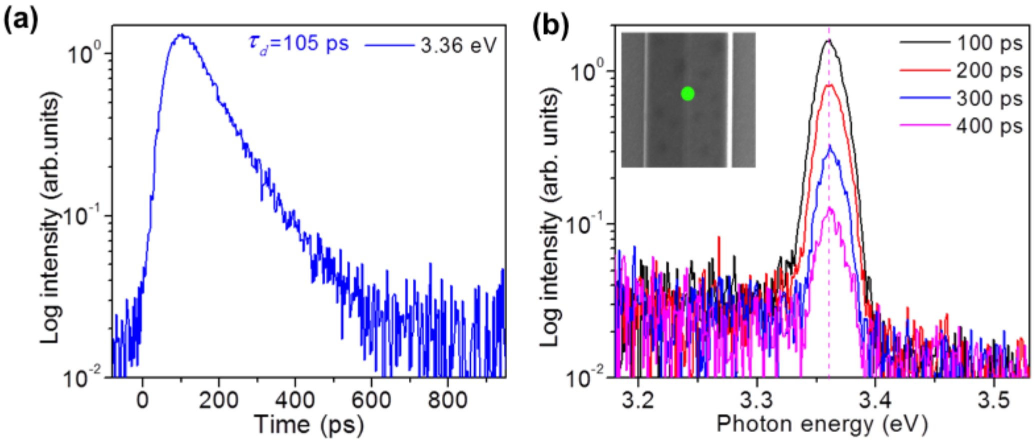

Figure 5.6 – **(a)** The CL intensity decay of $D^\circ X_A$ exciton, **(b)** the CL spectra at different time delays after excitation. The intensity decay and CL spectrum traces are extracted from the streak image obtained by excitation on the straight part of the MW shown in Fig. 5.4(b).

Figure 5.6 represents the CL spectra at different time delays after the excitation and the corresponding CL intensity decay extracted from streak images in Fig. 5.5(b) for the straight part of the MW. The CL intensity decays mono-exponentially with a time decay constant of 105 ps (deduced from the fitting with a mono exponential decay function). The CL spectra obtained by integrating the streak image on a narrow time window at different delays. No shift in the energy can be spotted from 100 ps time delay after the excitation up to 400 ps, corresponding to time delay at which the signal intensity vanishes almost completely.

Figure 5.7 presents the time dependent decay traces at different emission energies (top row) as well as the CL spectra at different time delays after excitation (bottom row) extracted from the streak images in Fig. 5.5. In the decay traces corresponding to innermost point A (see Fig. 5.5(a)), the higher emission energy (blue) shows very short rise time and decay time, while the lower emission energy (red) evidences longer rise and decay times. To compare the rise and decay times we considered the rise time $\tau_r$ and decay time $\tau_d$ to be the time for signal to rise from 10% to 90% of the maximum value and the mono-exponential decay time resulting from fitting with a mono-exponential decay function, respectively.

For the CL intensity at emission energy of 3.375 eV, we found $\tau_r \approx 60ps$ and $\tau_d \approx 70ps$ , respectively. While at intermediate energy of 3.358 eV, the rise time and decay time changes to $\tau_r \approx 90ps$ and $\tau_d \approx 100ps$, respectively. For the excitons at even lower energy of 3.325 eV, the decay time remains at about 100 ps. Most importantly, the rise time at this energy significantly extends to 260 ps, corresponding to the time needed for the high-energy luminescence to disappear completely.

As seen clearly in Fig. 5.7(b), the emission peak gradually red shifts from 3.392 to 3.322 eV, for time windows shifting from 88 to 450 ps after excitation. The emission peak becomes increasingly broad with time while a structure can be observed at about 3.365 eV that becomes a peak at 280 ps (the origin of this structure will be discussed latter). The behavior of both the decay traces and time dependent spectra directly illustrate the exciton dynamics in the pure bending cross section: the excitons that are formed upon pulsed electron beam excitation at the inside (with larger bandgap) drift towards the outside of the bent MW (with smaller bandgap).

Similar exciton dynamic features can be observed with excitation at the central point B (Fig. 5.7(c-d)). The rise and decay times at 3.365 eV are 70 and 80 ps, respectively, and increase to 160 and 100 ps at 3.325 eV. The time dependent CL spectrum red shifts from 3.365 to 3.322 eV for time slots changing from 120 to 460 ps. On the contrary, no sign of exciton movement can be spotted at the outmost point C (Fig. 5.7(e-f)).The time dependent CL spectrum only slightly red shifts from 3.331 to 3.322 eV, and the rise and decay times at 3.325 eV (70 ps and 100 ps) are similar to those of the straight segment. Indeed, created at the energy minimum in the cross section of the MW, excitons do not have any possibility to move along the strain

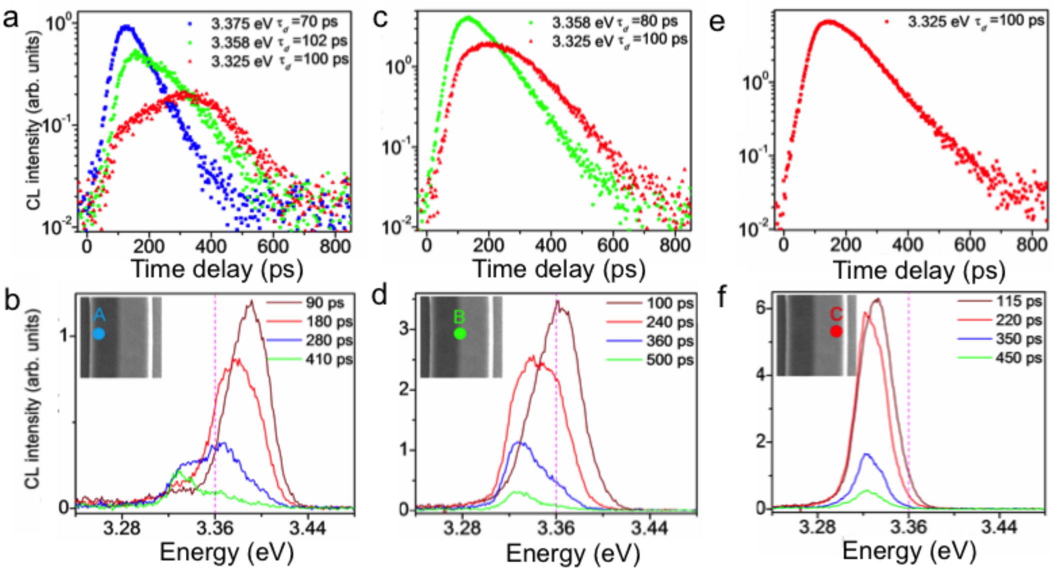

Figure 5.7 – The CL intensity decays **(a, c, e)** as well as the time-resolved CL spectra at different time delays **(b, d, f)** obtained for excitation spot positioned at the inside, middle, and outside of the purely bent section of the MW. The emission energy corresponding to each CL intensity decay is indicated in the figures. The first column (a, b) corresponds to point A ($\varepsilon_c = -1.18\%$), the second column (c, d) to point B ($\varepsilon_c = 0\%$), and the third column (e, f) to point C ($\varepsilon_c = 1.03\%$).

gradient. The small shift observed for point C can be due to the uncertainty in the position of the excitation spot, which might not be exactly at the edge of the MW.

In order to explain the observed exciton dynamics in the probed MWs, in the first approximation, a drift-diffusion model has been used. In the drift-diffusion model the strain gradient has been considered as the driving force for excitons since it results in a continuous variation of the electronic band structure [190, 191]. Our cw-CL measurements indeed evidence the fact that the bandgap varies linearly with the strain gradient across the bent region of the MW. Therefore, the excitons generated at positions with higher energy bandgap can drift along the strain gradient, as shown schematically in Fig. 5.8(a). Indeed, the variation in bandgap caused by the strain gradient across the MW leads to a potential variation for excitons.

Therefore, an equivalent built-in field for excitons can be evaluated as:

$$E = \frac{\partial E_{ex}(r)}{\partial r} = \frac{\partial E_{ex}(r)}{\partial \varepsilon_c} \frac{\partial \varepsilon_c}{\partial r}, \tag{5.2}$$

where $E_{ex}(r)$ denotes the exciton potential within the cross section in the pure bending region of the MW. The term $\partial E_{ex}(r)/\partial \varepsilon_c = -27.3 meV/\%$ expresses the deformation potential of exci-

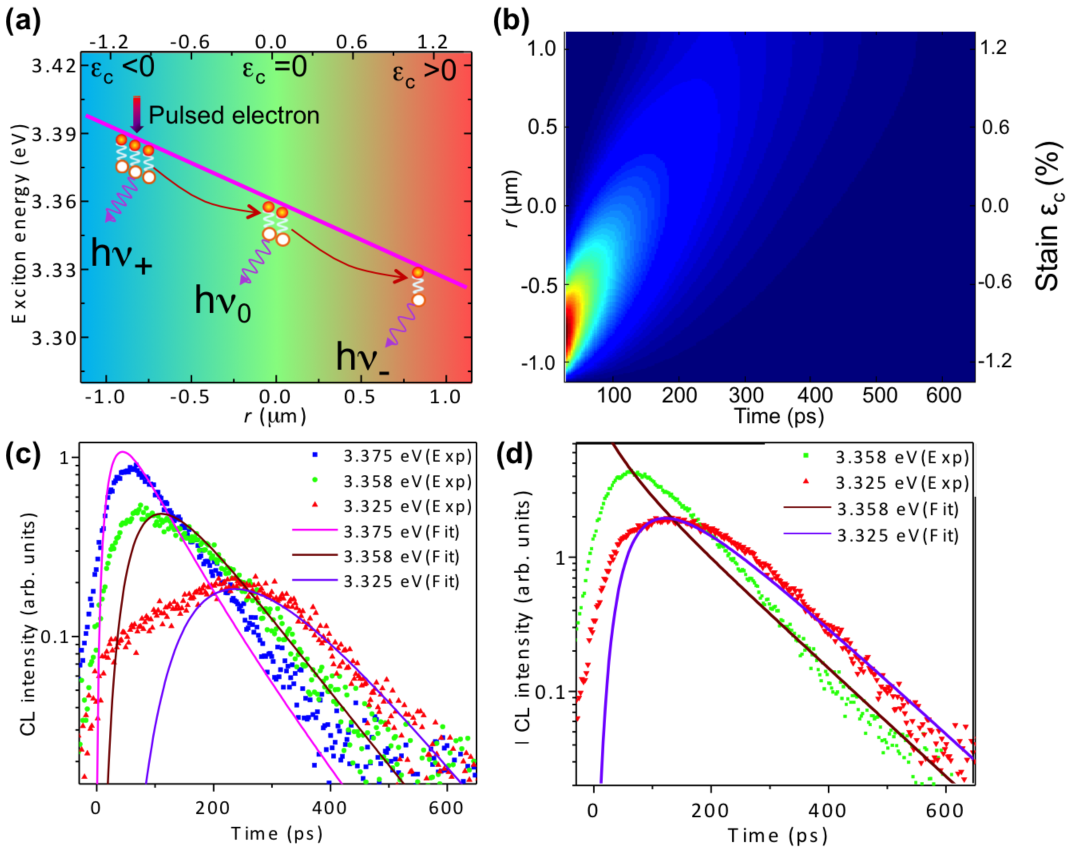

Figure 5.8 – **(a)** Schematic diagram of donor-bound exciton drift mechanism in the cross section of the purely bent ZnO MW after pulsed electron excitation at the inner side (high-energy region). The blue and red colors indicate the regions under compressive and tensile strains, respectively. **(b)** The results of the drift-diffusion model simulation for the time-dependent exciton density in the ZnO MW pure bending cross section after the pulsed excitation at the inner side (point A). **(c, d)** The best fitting results of the experimental decay traces at different photon energies with pulsed excitation at the innermost point A and the middle point B, respectively.

tons, and $\partial\varepsilon_c/\partial r = 1/\rho = 1.25\%/\mu m$ denotes the uniform strain gradient in the pure bending cross section.

Considering the obtained equivalent built-in field E as the driving force of exciton drift, the time dependent drift-diffusion equation for excitons can be written as

$$\frac{\partial}{\partial t}n(r,t) = -\frac{1}{\tau}n(r,t) + D\frac{\partial^2 n(r,t)}{\partial r^2} - \mu E\frac{\partial n(r,t)}{\partial t}, \tag{5.3}$$

where n, $\tau$ , $D$, and $\mu$ denote the exciton density, effective lifetime, diffusion coefficient, and mobility across the MW, respectively. The exciton effective lifetime contains both the radiative

$\tau_r$ and non-radiative $\tau_{nr}$ lifetime of excitons according to:

$$\frac{1}{\tau} = \frac{1}{\tau_r} + \frac{1}{\tau_{nr}}. \tag{5.4}$$

The change in the local strain across the bent region can cause a change in the effective mass of the conduction and valence band. Consequently, the exciton mobility and diffusion coefficient can vary from the region under compressive strain to regions with tensile strain. Nevertheless, in the range of the applied strain ($|\varepsilon_c| < 1.5\%$), the change in the effective mass was estimated to be less than 5%, deduced from a $k.p$ simulation with ZnO parameters taken from [192]. Therefore, within our simple model we disregarded the impact of the local strain on the mobility and diffusion constant. The latter parameters were considered to be constant in the whole cross section of the bent segment in the MW. The variation in the exciton binding energy was also assumed to be negligible over the whole applied strain range.

Finally, in order to apply proper boundary conditions to our simulations, the surface recombination velocity was implemented by adding another term due to the non-radiative recombination at the edge of the MW ($|r| = d/2$) [193]:

$$\frac{\partial}{\partial t} n(d/2,t) = -\frac{1}{\tau} n(d/2,t) + D\frac{\partial^2 n(d/2,t)}{\partial r^2} - \mu E\frac{\partial n(d/2,t)}{\partial t} - \frac{1}{\tau_{surf.}} n(d/2,t) \tag{5.5}$$

where $\tau_{surf.}$ denotes the exciton lifetime at surface of the MW.

Figure 5.8(b) shows the results of the finite element simulation for the exciton density as a function of time and the position across the bent segment of the MW. The excitation spot in the simulation was assumed to be in the innermost point (point A in Fig. 5.7). The excitons drift from the excitation spot towards the tensile region, as shown by this simulation results. The decay traces at different emission energies for excitation at point A and B in Fig. 5.7(a) and (c) are fitted reasonably well by this drift-diffusion model (see the solid lines in Fig. 5.8(c) and d)). From these fits, we deduced an exciton mobility of about $1400 \pm 100 cm^2 eV^{-1} s^{-1}$ at 8 K in this probed ZnO MW (sample I). This value can be compared with the simple estimation one can obtain directly from the streak image in Fig. 5.5(c). By comparing the difference in the rise time of the high-energy (3.392 eV) and low-energy (3.322 eV) part of the streak image, it takes 400 ps for excitons to travel from the inner most part to the outermost part of the bent region ($d \approx 1.8 \mu m$ deduced from SEM images). Therefore, the average speed of excitons is about 5 nm/ps. knowing the equivalent E field of $E \approx 312.5 eV/cm$ (70 meV over 2.24 $\mu m$), this corresponds to an exciton mobility of 1450 $cm^2 eV^{-1} s^{-1}$, a value close to the one deduced from our drift-diffusion model. Therefore, from our tr-CL measurements we obtain a direct and rather precise estimation of the exciton mobility, or exciton speed. For the reasons that will be discussed in detail later, a drift-diffusion model cannot fully explain the observed dynamics at low temperature. Therefore, we favor using the term exciton speed for donor-bound excitons instead of the term exciton mobility.

The difference between the cw-CL results at low and room temperature is another aspect that can be well described by the results of this drift-diffusion model. Indeed, the exciton generated at 8K can move towards the outside region of the MW thanks to their fast movement and long lifetime at low temperatures. Therefore, only a small portion of excitons recombine at the position of the excitation. The latter explains the weak emission intensity of the blue-shifted as well as the intense emission of the low-energy part of the CL spectra obtained by exciting the bent segment of the MW in compressive regions (see Fig. 5.3(b)). However, at room temperature, the smaller exciton mobility due to the larger phonon and defect scattering rates and the shorter exciton lifetime due to thermally activated nonradiative recombinations prevent excitons to drift under strain gradient. Therefore, excitons recombine radiatively at the excitation spot, which leads to a continuous shift of the NBE luminescence upon moving the excitation spot across the bent segment of the MW (see Fig. 5.4(b)). It worth emphasizing the fact that the movement mechanism of excitons at room temperature is expected to be different from the one at low temperatures since the luminescence is dominated by free excitons, as will be discussed later.

Since the luminescence of the studied ZnO MWs is dominated by donor-bound excitons, any movement is unexpected according to traditional theories: they should be immobile. However, bound excitons have been shown to be able to move by hopping from one donor state to others even at low temperatures. This movement that occurs *via* phonon coupling has already been reported for donor-bound excitons in nitrogen traps in GaAsP:N and GaInP:N [194].This hopping process of excitons can be an efficient process even at low temperatures. Also the hopping of donor-bound excitons is more favorable at low temperatures compared to the possible drift of free excitons trapped onto donors on their drift along the strain gradient field. In our measurements, the free exciton emission was observed only as a shoulder of the donor-bound exciton emission in the luminescence spectra. This means that the capture of free excitons to donors is an efficient and fast process that occurs at times scales much faster than the radiative lifetime of excitons. In addition, we observed the variation of the emission energy as a function of the applied strain for the whole spectrum. The latter observation allows us safely excluding the presence of the motionless donor-bound excitons. In other words, these observations clearly evidence the motion of donor-bound excitons even if we cannot discard the possibility of free exciton drift. The details of the hopping process model and the results of this model based on a Monte-Carlo simulation will be presented in detail in the following section, while further experiments on the validity of this model will be discussed in section 5.4.

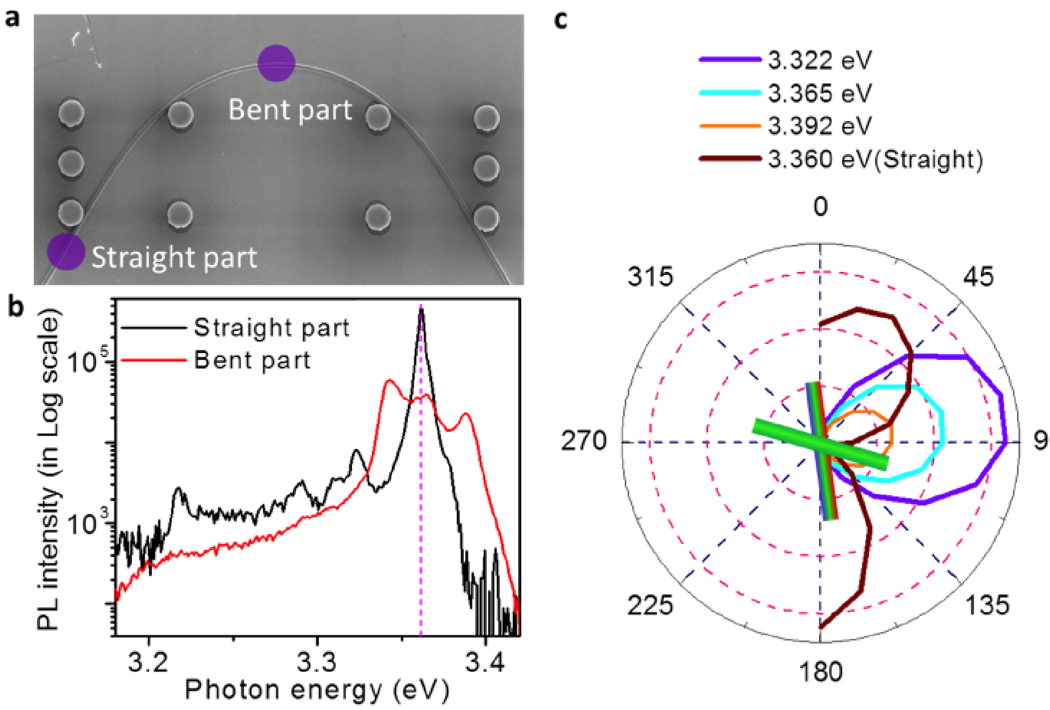

Figure 5.9 – **(a)** SEM image of the 4PB MW and shows the positions for the polarized PL measurement. **(b)** PL spectra at straight part and pure bent part. **(c)** Polarization properties of the $D^0X_A$ emission peak at the straight segment (3.360 eV) and the three emission peaks (3.322 eV, 3.365 eV and 3.392 eV) at the pure bending segment.

### 5.2.2 Whispering gallery modes (WGMs)

In our cw-CL experiments at low temperatures (see Fig. 5.3(b)), in addition to the broad emission and blue-shifted emission of the CL for excitation in the compressive part of the MW, there is a component with an emission energy that does not vary when changing the excitation spot across the MW. This peak was also observed in the time integrated CL spectra shown in Fig. 5.5(a).

One possible explanation for this peak might be the strain-induced valence band crossing [186]. Figure 5.10(a) represents the polarization resolved PL measurements carried on the both of straight and bent regions a single ZnO MW. As shown in Fig. 5.10(b), the luminescence of the straight part of the ZnO MW is dominated by a narrow emission line at 3.360 eV, attributed to donor-bond exciton emission $D^\circ X_A$. The PL on the bent segment features a broad luminescence with three peaks at 3.322 eV, 3.365 eV, and 3.392 eV. As shown in Fig. 5.10(c), all the three emission lines of the bent region have the same polarization with respect to the MW axis as the emission of the $D^\circ X_A$ in the straight part of the MW. The angle between the polarization for the emissions of the bent segment and the straight segment of the MW is due to the difference in the initial orientation of these two parts of the MW with the polarizer. These results implies that there is no valence band crossing induced by the bending deformation.

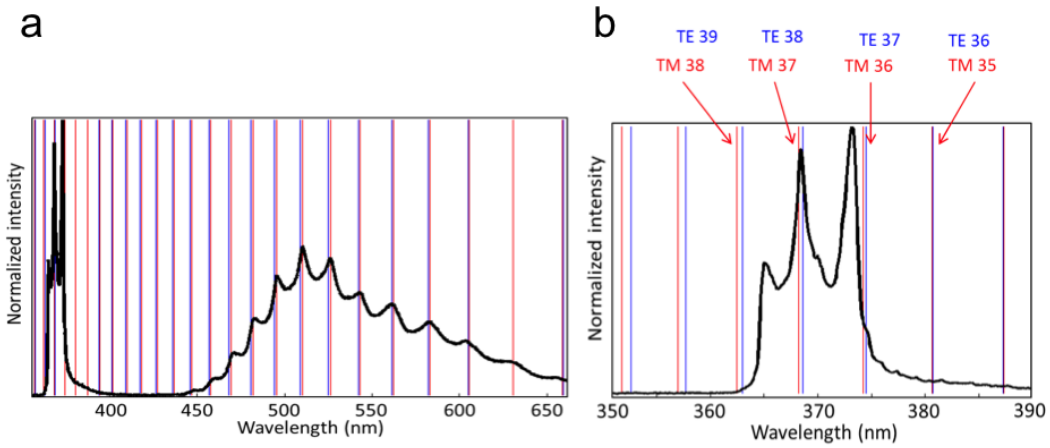

Figure 5.10 – **(a)** Result of fitting the CL spectrum (both the UV and yellow bands) obtained at the pure bending cross section with the spectral position of WGMs. **(b)** Fitting result with WGMs for the middle peak in the UV band. The middle peak is assigned the mode TM37.

Therefore, we tentatively attribute this additional peak to the one of whispering gallery modes (WGMs) that are known to exist in ZnO MWs [195]. Since the WGM emissions originate from the light propagation in the whole cross section of the MW, their emission energy is not expected to vary with scanning the excitation spot across the MW. To confirm this assignation, we computed numerically the expected position of the different cavity modes. Assuming the total internal reflection along the cross-section of the MW, we can obtain the following condition for WGMs [195]:

$$R = \frac{hc}{3\sqrt{3}nE}[N + \frac{6}{\pi} arctan(\beta\sqrt{3n^2-4})] \tag{5.6}$$

where R is the radius of the wire, h is the Planck constant, n is the refractive index (for TE and for TM modes), E is the photon energy, $\beta$ is a factor, which depends on the polarization ($\beta = 1/n_{\perp}$ for TE modes and $\beta = 1/n_{\parallel}$ for TM modes), and N is the mode number. The dependence of the refractive index upon polarization and wavelength has been taken from Ref. [196]. In Fig. 5.10, we superimpose a spectrum of a MW with the expected position of the different modes of both polarizations (TE and TM mode are shown by blue and red color, respectively). The diameter of the wire was used in the simulation as a fitting parameter to reproduce the positions of the observed modulation peaks: the best fit was obtained for R =1271 nm (from SEM image, we deduce R = 1195 nm). This fitting procedure allows us to assign the modulation in the luminescence of the yellow band as well as the middle peak in the NBE emission of the bent MWs to the WGMs.

Although the results of the fit for the position of the peaks are in a good agreement with the experimental results, due to the strong dispersion of the reflective index near the energy of the band edge, it is not possible to predict precisely the position of this peak. Also, we do not exclude the possibility of the strong coupling of the NBE emission to the WGMs [197], which needs further studies that lies beyond the scope of this chapter.

### 5.2.3 Degradation of the ZnO MWs quality in high vacuum

It worth briefly commenting on the differences between the results of the time integrated CL spectra in Fig. 5.5(a) and the cw-CL spectra in Fig. 5.3(c). Although both set of measurements were performed on the bent segment of the same ZnO MW, a remarkable difference in the relative intensity of the high-energy to low-energy part of the CL spectra can be spotted: the red shifted peak is weaker than the high-energy peak in the time integrated spectrum with pulse excitation at inside. The reasonable interpretation is that the ZnO MWs were kept for a long time (more than 24 hours) in high vacuum during cw-CL measurements. As reported before in Ref. [198, 199], keeping ZnO MWs in high vacuum for a long time can induce oxygen vacancy defects. Thus, the ZnO MWs had a lower quality (shorter lifetime for excitons) when performing time resolved measurements. The differences between results obtained on sample II (discussed in section 5.4) and those on sample I can also be interpreted the same way: tr-CL measurements have been performed directly on the ZnO MWs in sample II to reduce the time that ZnO MWs spend in the vacuum.

## 5.3 Hopping of donor-bound excitons in doped semiconductors at low temperatures

As discussed in the last section, the luminescence of the probed ZnO is dominated by the donor-bound exciton emission at low temperatures. Because of their bounding to donors, they are not expected to move. Nevertheless, we observed the shift of the emission energy for whole NBE emission and not just for free excitons. This means that the donor-bound excitons are observed to move quite efficiently at low temperature. The motion of impurity bound excitons has already been observed in inhomogeneous materials such as GaAsP:N and GaInP:N [200, 201], InGaN [202], and MgZnO [203]. In these materials, the bond excitons movement was attributed to the transfer of excitons from one donor to another one with a lower energy, by tunneling between the two states. This process has been also reported in the case of well defined energy level of impurities in GaP [204].

The advantage of our experimental scheme is the possibility to estimate the precise exciton

Figure 5.11 – Scheme of the hopping mechanism of donor-bound excitons in an energy gradient.

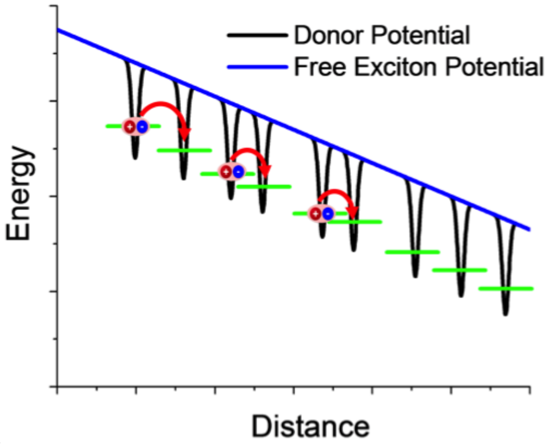

movement speed and hence to get a precise estimation of the jump rate of excitons between different states. The strain-induced variation of the bandgap provides a potential variation for excitons as shown in Fig. 5.11. The well-defined binding energy of donor-bound excitons $D^\circ X$ leads to a "donor ladder". Therefore, the next donor level along the energy gradient has always a lower energy.

We performed a Monte-Carlo (MC) simulation based on Miller-Abrahams formalism [205] for the jump rate of $D^\circ X$s from one donor state to another in order to simulate the observed dynamics. The temperature dependent simulation predicts a strong decrease in the exciton movement speed when temperature is raised. The effect of the $D^\circ X$ Bohr radius as well as the doping concentration was also studied within this model.

The hopping rate $v_{ij}$ from the donor state i to another state j with corresponding energies of $E_i$ and $E_j$ is given by [206, 205]:

$$v_{ij} = \begin{cases} v_0 e^{-2\frac{R_{ij}}{a_0}} & \text{if } E_j < E_i, \\ \\ v_0 e^{-2\frac{R_{ij}}{a_0}} e^{\frac{E_i - E_j}{k_B T}} & \text{if } E_j > E_i, \end{cases} \tag{5.7}$$

where $v_0$ denotes the typical time constant of the hopping process, $a_0$ is the Bohr radius of the $D^\circ X$s, $R_{ij}$ is the distance between the two donors, and $k_B$ is the Boltzmann constant. Accordingly, the hopping rate from one state to another is exponentially decreases when the distance between the donors is increased. The term $e^{\frac{E_i - E_j}{k_B T}}$ shows that the hopping from one state to another with higher energy needs to be thermally activated. Indeed, at T= 0K, excitons can only hop to the next donors with a lower energy, while hopping to states with higher energies is only possible when the temperature is raised.

In order to determine the mean speed of donor-bound excitons hopping along the energy gradient, we performed the MC simulation with following assumptions. The position of N donor levels was randomly chosen in a finite 3D volume. The homogenous energy gradient $E_\sigma$ was arbitrarily applied along the z-axis defined by

$$E_\sigma = \frac{\Delta E}{\Delta z} \tag{5.8}$$

where $\Delta E$ denotes the total energy difference over the distance $\Delta z$. The assumption of a homogenous energy gradient is consistent with our cw-CL measurements at room temperature, as discussed before. Then, the transition time $\tau_i$ from a given donor to the next one was determined by the sum of the all the hopping rates from this donor to any other:

$$\frac{1}{\tau_i} = \sum_{i \neq j} v_{ij}. \tag{5.9}$$

To choose the next donor, we chose randomly a number $\Gamma$ between 0 and $1/\tau_i$ and used the cumulative distribution function $f_{cum}$, defined by

$$f_{cum}(j) = \sum_{\substack{k=1 \\ k \neq i}}^{j} v_{ik}. \tag{5.10}$$

If $f_{cum}(j) < \Gamma < f_{cum}(j+1)$, the next donor level where the exciton will be bound to is donor j. This method allows us to choose the donor that has the highest possibility. In other words, this condition reproduces the exciton behavior for choosing the next donor. The simulation was repeated until the donor-bound excitons travels along the z-axis a given distance $d >> \frac{1}{\sqrt[3]{N_d}}$, where $N_d$ denotes the donor concentration. By averaging the total time for exciton $\tau_{tot}$ to travel distance $d$ along z-axis for several simulations, we can estimate the mean speed of excitons.

Figure 5.12 shows an example of the exciton trajectory in an energy gradient at T= 0K for donor concentration of $N_d = 10^{18} cm^{-3}$ and an exciton Bohr radius of $a_0 = 5nm$. Owing to the strain gradient and in the absence of any thermally activated motion towards donor levels with higher energies, excitons always move in the direction of the energy gradient. For this specific case, assuming $v_0 = 10^{13} s^{-1}$ [201], we deduced an exciton mean speed of 5.4 nm/ps along the z-axis.

To estimate the mean exciton speed as a function of the physical parameters in our system, we carried out the MC simulations for a volume with dimensions of $L_x = L_y = L_z = 300nm$, and for 10 000 trials for T= 0K. The results of these MC simulations are shown in Fig. 5.13. It worth emphasizing that we favor using the term of exciton speed instead of the exciton mobility

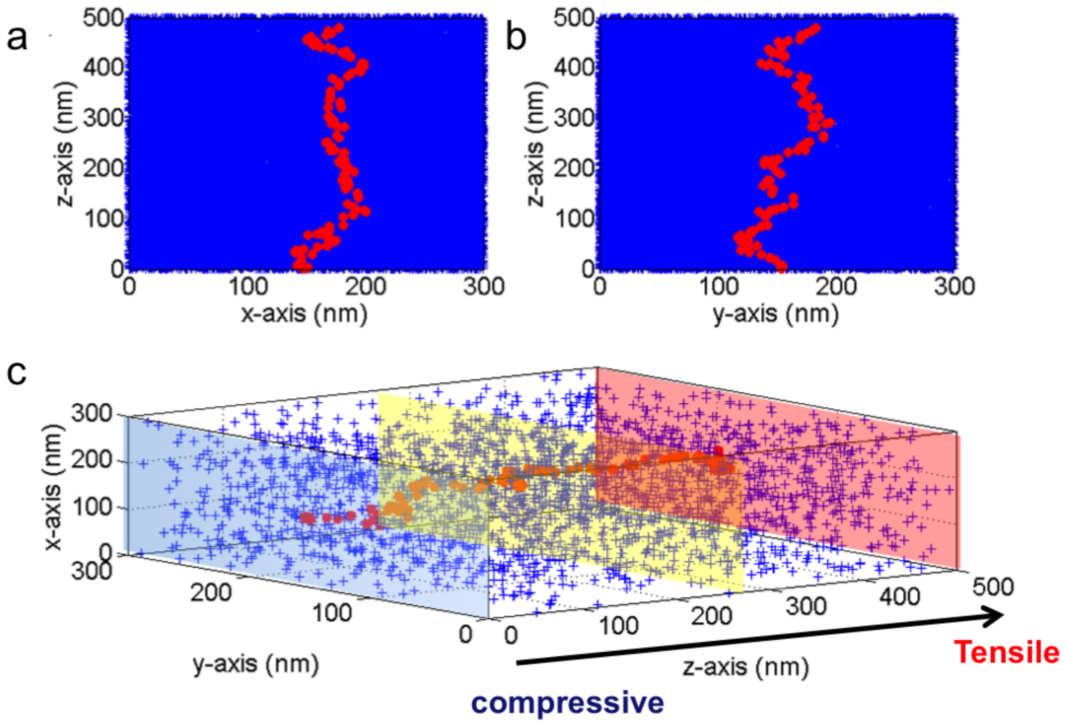

Figure 5.12 – Example of the trajectory of an exciton at T= 0K in an energy gradient along the z-axis for a donor concentration of $N_d = 10^{18} cm^{-3}$ and a Bohr radius $a_0 = 5nm$. Blue crosses show the donor positions and red dots show the donors in the exciton pass. **(a, b)** x-z, and y-z projection, **(c)** 3D view.

since at T= 0K the exciton movement speed does not depend on the energy gradient $E_\sigma$ (see equation 5.6).

The exciton mean speed was found to be strongly dependent on the exciton Bohr radius. As shown in Fig. 5.13(a), for a given doping concentration of $N_d = 10^{18} cm^{-3}$ and hopping rate of $\nu_0 = 10^{13} s^{-1}$, the average speed of excitons changes from $v = 3.2 \times 10^{-3} nm/ps$ for $a_0 = 2nm$ to $v = 590nm/ps$ for $a_0 = 15nm$.

Fig. 5.13(b) shows the dependence of the exciton average speed on temperature. For $T \neq 0K$, the value of the energy gradient can play a role owing to the exponential dependence of the hopping rate on the energy difference between the initial and final state within the donor ladder for excitons $(E_i - E_j) = E_\sigma(z_i - z_j)$. Considering that the value $R_{high} = \frac{E_\sigma}{k_B T \times \sqrt[3]{N_d}}$ defines the possibility for excitons to hop to states with higher energies, two extreme cases can be imagined: if $R_{high} >> 1$ excitons can move only towards the states with lower energies, while for $R_{high} << 1$ excitons have the same probability to move to either higher or lower energy

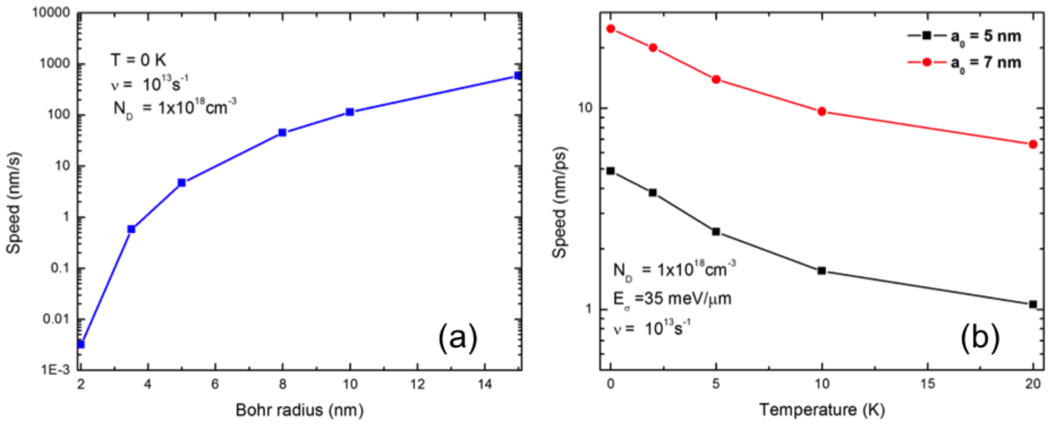

Figure 5.13 – **(a)** The exciton average speed along the z-axis at T= 0K as a function of the exciton Bohr radius. **(b)** The exciton average speed as a function of temperature for exciton Bohr radius of 5 nm (black), and 7 nm (red) for a doping concentration of $N_d = 10^{18} cm^{-3}$.

states, i.e., do not "feel" anymore the energy gradient. Indeed, when the temperature is raised, excitons also have the possibility to move against the energy gradient. Therefore, when raising the temperature, the average exciton speed is expected to decrease due to this thermally activated motion (see Fig. 5.13(b)).

Table I, summarize the results of the MC simulation of the excitons mean speed for an energy gradient of 35 $meV/\mu m$, for two different Bohr radii of donor-bound excitons when the temperature is raised from 0 K to 20 K.

| | $a_0 = 5nm$ | $a_0 = 5nm$ |
|---|---|---|
| T= 0K | 4.95 nm/ps | 24.9 nm/ps |
| T= 20K | 1.1 nm/ps | 6.6 nm/ps |

Table 5.1 – Average speed of excitons deduced from MC simulations for two different Bohr radii at T= 0K and T= 20K.

In addition to MC simulations, we carried out simulations by assuming an effective medium. Within this model, a homogeneous distribution was considered for donors instead of the random distribution. Following the previous discussion, the mean transition time for an exciton at a given position in then given by:

$$\frac{1}{\tau} = \sum_{j=1}^{\infty} v_{ij} \approx \int_{-\infty}^{+\infty} \int_{-\infty}^{+\infty} \int_{-\infty}^{+\infty} N_d v(x, y, z) dx dy dz. \tag{5.11}$$

Here, $N_d$ denotes the doping concentration, and the $v(x, y, z)$ for motion in either direction

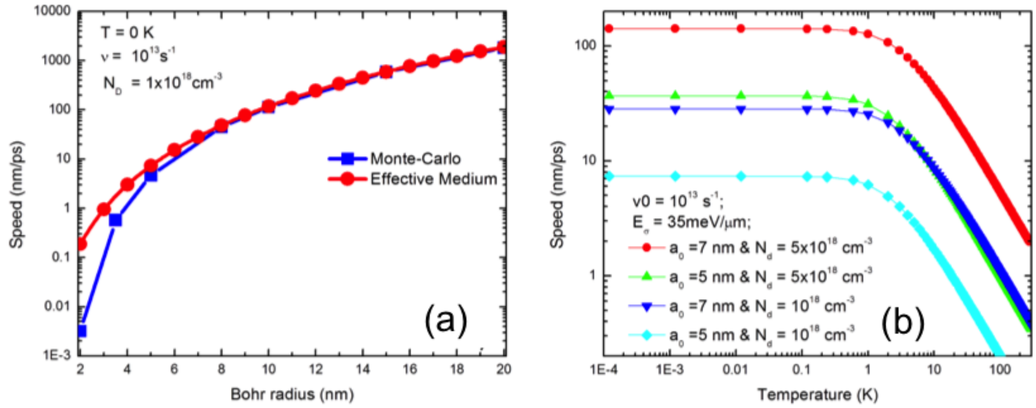

Figure 5.14 – **(a)** The average speed of excitons as a function of the exciton Bohr radius obtained by the MC simulation (blue) and the effective medium approximation (red). **(b)** The average exciton speed in an energy gradient of 35 $meV/\mu m$ as a function of temperature for different exciton Bohr radii and different doping concentrations.

along energy gradient is defined as:

$$v(x,y,z) = \begin{cases} v_0 e^{-2\frac{\sqrt{(x-x_0)^2+(y-y_0)^2+(z-z_0)^2}}{a_0}} & \text{if } z > z_0 \\ v_0 e^{-2\frac{\sqrt{(x-x_0)^2+(y-y_0)^2+(z-z_0)^2}}{a_0}} e^{-\frac{E_\sigma(z_0-z)}{k_B T}} & \text{if } z < z_0 \end{cases} \tag{5.12}$$

Then, the mean hopping distance for excitons in such a medium can be approximated by:

$$d = \tau \int_{-\infty}^{+\infty} \int_{-\infty}^{+\infty} \int_{-\infty}^{+\infty} (z - z_0) N_d v(x,y,z) dxdydz. \tag{5.13}$$

One of the advantage of this model is to reach an analytical solution at T= 0K for exciton mean speed given by:

$$\begin{cases} \frac{1}{\tau} = \frac{\pi}{2} N_d v_0 a_0^3 \\ d = \frac{3}{4} a_0 \\ v = \frac{d}{\tau} = \frac{3\pi}{8} N_d v_0 a_0^4. \end{cases} \tag{5.14}$$

Figure 5.14 compares the results of this effective medium simulation with the results obtained by the MC simulation at T= 0K and for doping concentration of $10^{18} cm^{-3}$. There is a good agreement between the results the two models for $a_0 > \sqrt[3]{N_d}$. However, for $a_0 < \sqrt[3]{N_d}$, the effective medium approach overestimates the exciton mean speed.

For finite temperatures, however, it is not possible to obtain an analytical solution from our effective medium model. Figure 5.14(b) shows the results of such simulations of the exciton mean speed as a function of temperature for different exciton Bohr radius and doping concentration. The energy gradient in all these simulations was assumed to be about $35 meV/\mu m$, taken from our results in the previous section of this chapter. For a given exciton Bohr radius, an increase in the doping concentration can lead to 3 to 4 times enhancement of the exciton average speed. More importantly, even if the exciton mean speed does not vary significantly from 1 to 10K, it quenches very fast when the temperature is raised above 10 K. This fast decrease of the exciton speed is however valid for donor-bound excitons at low temperatures. It does not mean that excitons cannot drift under the strain gradient/energy gradient at temperatures above 10K. Indeed, if the exciton dynamics are dominated by the hopping process of donor-bound excitons at low temperatures, at higher temperatures it is expected to be dominated by the standard drift of free excitons. The transition between these two drift processes is referred in literature as the *mobility edge* [207, 208]. However, when raising the temperature, for the reason of the decrease of the exciton lifetime in our sample we could not study these changes in the exciton dynamics.

In the following section, the results of the tr-CL measurements on sample II (the ZnO MW shown in Fig. 5.1(d)) will be discussed. The higher quality of this sample compare to sample I, allows us to probe the dynamics from 4K to 30K. The change in the observed dynamics, as will be discussed later, shows the validity of the hopping process as the main mechanism of the donor-bound exciton movement at low temperatures.

## 5.4 Temperature dependence of the exciton hopping speed

Section 5.2 dealt with the evidences of exciton movement in the presence of an energy gradient induced by the strain variation across the bent ZnO MW (sample I) at low temperatures. The exciton movement speed was estimated to be 5 $nm/ps$ at 8 K in sample I. Nevertheless, no exciton movement was observed at room temperature, which was attributed to the short exciton lifetime exciton at room temperature. A simple drift-diffusion model was employed in that section to reproduce the experimental results and to estimate the exciton mobility or the exciton movement speed. However, as it was briefly discussed there, the luminescence of the studied wires at low temperature is dominated by donor-bound excitons and not by free excitons. This is consistent with the high unintentional doping concentration in our samples that can amount to $>10^{18} cm^{-3}$ and the large binding energy of donor-bound excitons in the studied ZnO MWs.

The MC simulations in the previous section shows the possibility of an efficient exciton transport mechanism based on exciton tunneling between adjacent energy states. At high enough doping concentration, $D^{\circ}X$s can hop from one donor state to the next one, which has a lower energy. This is indeed possible because the mean distance between donors is comparable to the exciton Bohr radius. Considering the donor concentration of $>10^{18} cm^{-3}$ in our samples, the mean distance between two neighboring donors is approximately 10 nm, a value comparable to the Bohr radius of $D^\circ X$s ($a_0$ =3-5 nm). Moreover, the strain gradient makes a ladder-like energy potential for $D^\circ X$s that lead to their movement only towards tensile regions ( i.e., lower energies for excitons) at T= 0K. Since the hopping rate between the two adjacent states is independent of their energy difference at very low temperatures, the average speed of exciton is expected to be independent of the energy gradient. However, when raising the temperature, a backward motion of excitons can be activated by thermal energy. The impact of this thermally activated backward motion of excitons is a dramatic decrease in their average speed. According to our model, the average speed of $D^\circ X$s is expected to decrease by almost a factor of 10 when raising the temperature from 0K to 30K. Exciton mobility limited by phonon scattering also decreases with temperature, but this effect appears at much higher temperatures.

In this section, the temperature dependence of the $D^\circ X$ movement speed under uniform strain gradient in sample II is studied. The higher quality of the ZnO MWs in sample II allows us to investigate the exciton dynamics from T= 4K up to 30 K. Over this studied temperature range, $D^\circ X$ dominates the carrier recombination. More importantly, only a limited decrease in the exciton effective lifetime was observed. As shown in Fig. 5.1(d) sample II was designed in order to undergo a smaller strain gradient across the bent region of the ZnO MW (since it has larger curvature radius of neutral plane $\rho$), that allows us to comment on the strain gradient effect by comparing with the results of sample I.

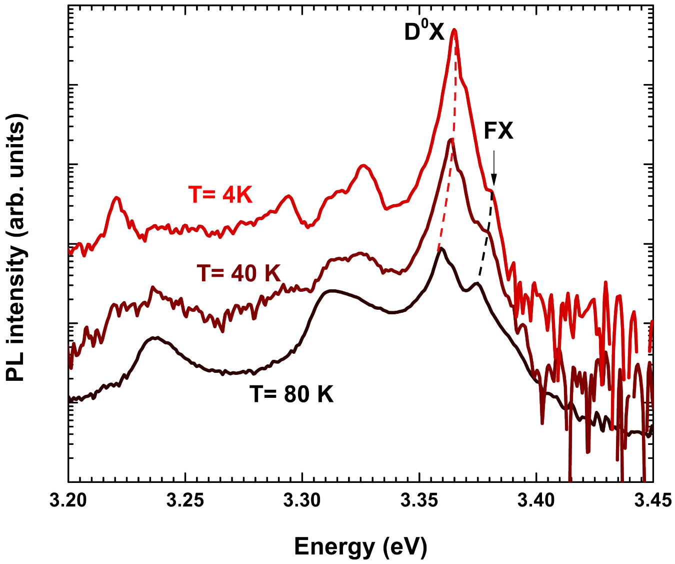

Figure 5.15 – The typical PL spectra of a single ZnO MW at different temperatures from 4K to 80K. PL spectra have been vertically shifted for clarity.

The typical low temperature PL spectra of a single straight ZnO MW are displayed in Fig. 5.15. As indicated by arrows, the NBE emission of these MWs is composed of an intense emission at 3.364 eV and a weaker emission at 3.380 eV, which appears as a shoulder. According to the existing literature [47], the 3.364 eV and 3.380 eV emission lines are attributed to $D^{\circ}X$ and FX transitions, respectively. Increasing the temperature changes the ratio of $D^{\circ}X$ to FX intensity and at higher temperatures $D^{\circ}X$ slightly decreases in favor of FXs. Anyway, for temperatures below 40K, the luminescence is still dominated by $D^{\circ}X$ emission by more than one order of magnitude.

The CL spectrum line scanning across the straight region ”I” at 4K, and the bent region ”II” are displayed in part (a) and (b-d) of Fig. 5.16, for different temperatures. No spectral shift was spotted for region I at 4K when the excitation spot was scanned across the MW. However, the CL spectra for region II at 4K (cf. Fig. 5.16(b)) consist of a broad emission when the excitation was done at the interior side of the MW (the lower part of the figure). The CL spectrum progressively redshifts and narrows by moving the excitation spot towards the tensile region (the upper part of figure). The blue and red dashed lines depict the highest and the lowest emission energies corresponding to the inner and outer edges of the bent region of the ZnO MW. The CL spectra mappings for higher temperatures (Fig. 5.16(c) and (d)) feature a similar redshift of the emission energy when moving the excitation spot from the compressive part to the tensile part across the MW. However, the intensity of the low-energy part of the CL spectrum appears to have a strong temperature dependence: when raising the temperature the low-energy part of the CL spectra disappears. This is even more clear on the time integrated CL spectra shown in Fig. 5.16(e) at the compressive part of the MW for different temperatures. Note that in these normalized CL spectra, the CL intensity of the lowest energy decreases when the temperature is raised (shown by a red arrow in the figure). Figure 5.16(f) demonstrates the CL intensity decay as a function of time for different temperatures probed in region I. The effective decay time amounts to $\sim 105ps$ and remains constant over the whole measured temperature range.

Before comparing the time resolved measurements for different temperatures, it worth commenting on the dynamics at 4K, at which the largest movement speed of $D^{\circ}X$ is expected. The streak images obtained at 4K for different excitation spots across the region II of the ZnO MW are displayed in Fig. 5.17. These measurements have been performed at four equally spaced excitation spots across the bent region of the ZnO MW, shown on the SEM image in Fig. 5.17(a). The local strain values is $\varepsilon_c$ = -0.57 %, -0.19 %, +0.19 %, and +0.57 % for points A, B , C, and D, respectively. The streak image in Fig. 5.17(b) features a clear time-dependent redshift of the CL spectrum in addition to a delayed rise at lower energies. These features provide a clear evidence of the exciton movement from region with higher energies ( i.e., with compressive strain) towards regions with lower energies (tensile strain), as it was discussed in details before for sample I. The streak images corresponding to the middle points across the MW (Fig. 5.17(c) and (d)) also depict the same characteristics. The main difference is that the energy of the CL emission at early delays after the excitation shifts towards lower values compared to the

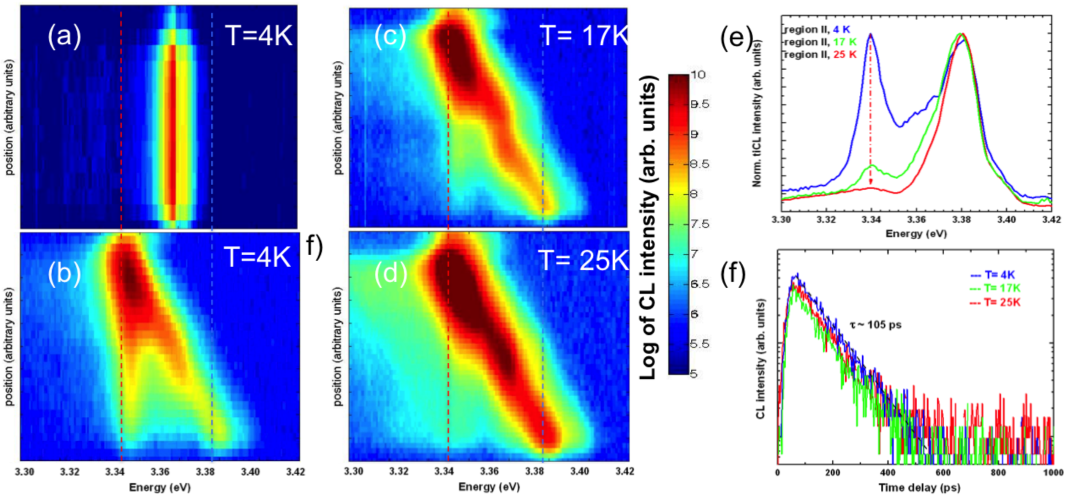

Figure 5.16 – **(a)** Time integrated CL spectral mapping across the straight part of MW (part I) as a function of the excitation spot position across the MW. The color coded intensity is in logarithmic scale. **(b-d)** Time integrated CL spectra cross the bent region of MW (part II) as a function of the excitation position across the MW atT= 4K, 17K and 25K, respectively. The local strain value changes from $\varepsilon_c$ =-0.77% in the compressive region (lower part of each panel) to $\varepsilon_c$ =+0.77% at the tensile part (upper part of each panel). **(e)** Normalized time integrated CL spectra, when the excitation was done in the compressive part of the MW cross section at different temperatures from 4 K to 25K. The red arrow underlines the decrease in intensity of the low-energy part of the CL spectra by temperature. **(f)** The CL decay on the straight part of ZnO MW as a function of temperature, while no significant change in the exciton lifetime can be spotted for all temperatures from 4 K to 25K.

results in Fig. 5.17(b). This is due to the linear dependence of the bandgap energy on the local strain when moving across the MW and, therefore, evidences the one-directional movement of excitons towards the tensile region. Eventually, in the streak image recorded at point D (Fig. 5.17(e)) no time-dependent redshift in the CL spectrum can be distinguished.

The time delay traces of these CL experiments are displayed in Fig. 5.18(a-c) for different temperatures. In this set of measurements, the excitation was always performed in the compressive part of the MW (point A in Fig. 5.17(a)). The CL intensity decays are obtained by integrating the streak images at the highest energy part and the lowest energy part of the streak images. The short rise time of the CL intensity at compressive region (blue) and the delayed rise time for tensile region (red) demonstrate the presence of exciton movement in all these measurements. As mentioned before, no change in the effective lifetime of the excitons was observed in this temperature range. However, the ratio of the CL intensity in the tensile region compared to the compressive region decreases upon raising the temperature. In addition to the CL component with a long rise-time, another component with a mono-exponential decay and a much shorter rise time exists in the CL decay of the tensile region. This component

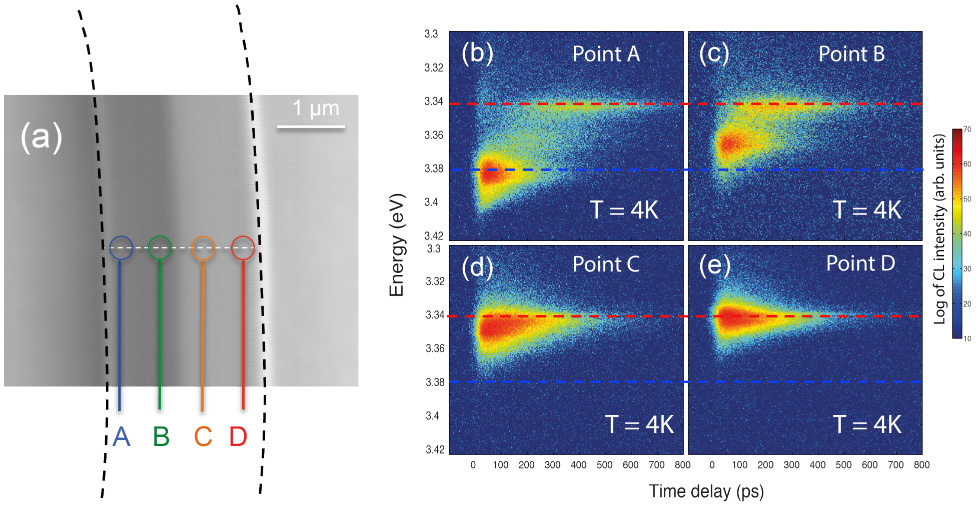

Figure 5.17 – **(a)** SEM image of ZnO MW recorded in pulsed mode. The position of four equally-spaced excitation spots of A to D are displayed on the SEM image. **(b-e)** Streak-camera images obtained by exciting points A, B, C, and D across the bent region of MW at 4K, respectively. Points A, B, C, and D of the purely bent section have local strain value of $\varepsilon_c \approx$ -0.57%, -0.19%, +0.19%, and +0.57%, respectively.

features the same decay time as the CL intensity of the compressive part of the MW and a constant intensity ratio to the CL intensity of the compressive region of the MW for all temperatures. According to these characteristics, this component is interpreted as originating from the reabsorption of the luminescence in the regions of the MW with lower bandgap, consistent with the effective light confinement in our high quality probed ZnO MW.

As discussed before in the text, the exciton hopping rate is predicted to be independent of the energy gradient [209]. Therefore, the exciton mobility cannot be a measure of the efficiency of $D^\circ X$ movement through hopping process at low temperatures. Instead of the drift-diffusion model in section 5.2, the following equation has been solved by finite difference methods to estimate the exciton speed from our measurements, where the term $\mu E$ due to exciton drift is replaced by the exciton average speed. The carrier density as a function of time and position across the bent MW is then given by:

$$\frac{\partial}{\partial t} n(r,t) = -\frac{1}{\tau} n(r,t) + D\frac{\partial^2 n(r,t)}{\partial r^2} - v\frac{\partial n(r,t)}{\partial t}, \tag{5.15}$$

where n, $\tau$ , $D$, and $v$ denote carrier density, exciton effective lifetime, diffusion coefficient, and exciton average speed across the MW. The surface recombination has been implemented in the boundary conditions in the same way discussed before in section 5.2.

The effective lifetime of excitons is taken to be 105 ps, from our tr-CL measurements on the

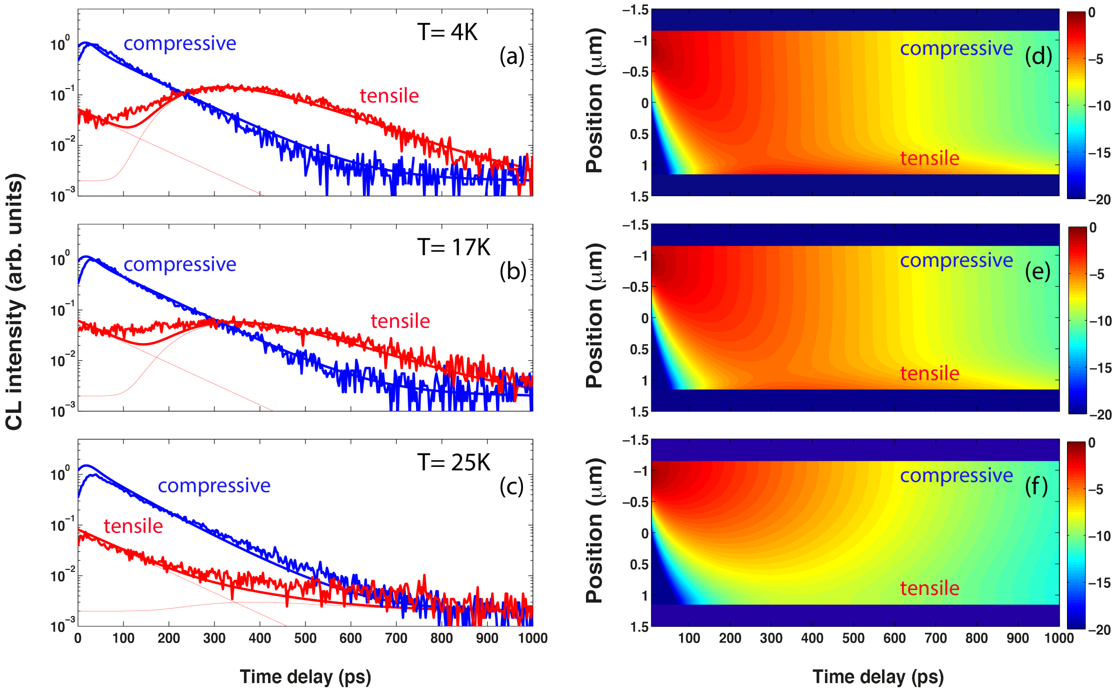

Figure 5.18 – **a-c)** The experimental CL intensity decay at the highest (blue) and lowest (red) emission energy extracted from streak images recorded under excitation at point A in the bent region of the MW at 4K, 17K, and 25K. The results of drift-diffusion simulation are shown as continuous lines for comparison with experimental data. **d-f)** simulation result for the exciton density distribution across the bent region of MW as a function of time delay after the excitation for 4K, 17K and 25 K, respectively. The excitation spot is always at the region with the highest bandgap energy across the MW.

straight part of the MW and was kept constant for all temperatures. The exciton movement speed $v$ and the diffusion constant $D$ were tuned as the main fitting parameters to reproduce properly the decay time and rise time of CL decays at the compressive and tensile part of the MW, as well as their relative intensity in the simulations. The intense CL in the tensile region of the MW indicates the accumulation of the excitons at the edge of the MW in absence of a fast non-radiative channel, that is consistent with the smaller value of the surface recombination velocity $v_{surf.} = 5.10^{3} cm/s$ compared to the value for previous MWs in sample I. A mono-exponential decay function with a constant proportion to the CL intensity at compressive part is added to simulation results to mimic the component from reabsorption of light in the tensile region of MW. Additionally, the simulation results of CL decay have been convoluted with a Gaussian function with temporal broadening of 30 ps to account for the temporal resolution of our experimental system.

The exciton movement speed from these simulations was estimated to $v$= 5.8 $nm/ps$ at 4K, $v$= 4.2 $nm/ps$ at 17K, and $v$= 0.4 $nm/ps$ at 25K. The diffusion coefficient was considered to be constant over this temperature range and estimated to D= 7 ± 3 $cm^2/s$: the results of the fitting only show a small dependence on D. The results of these finite element simulations for the CL intensity decay are compared with the experimental results in Fig. 5.18(a-c): a good agreement between simulation and experiments is observed.

To check the estimated value of exciton speed, we can simply perform an estimation from time resolved decays in Fig. 5.17, as we did before. Comparing the rise time of the CL intensity at energies corresponding to the compressive and tensile part of MW, it takes about 350 ps for an exciton to drift from the high-energy side to the low-energy side of the MW (see Fig. 5.17(a)). The distance between these two points is about $d \approx 2\ \mu m$, i.e., distance from the excitation spot to the outside region of MW. Thus, the average speed of excitons is determined to be 5.7 nm/ps at 4K, which is in a close agreement to our simulation results.

However, it is not possible to precisely determine the diffusion constant since the simulation results do not vary significantly with diffusion constant. Still, the estimated value for diffusion coefficient is reasonable comparing it with the previous reports in the literature. Considering D= $7 \pm 3\ cm^2/s$ and exciton lifetime $\tau$=100 ps, the diffusion length amount to $l_D = \sqrt{D\tau} \approx 250\ nm$, which is in a reasonable agreement with $l_D$=140 nm measured in bulk ZnO using CL techniques in Ref. [210]. Note further that according to the Einstein-Smoluchowski relation[211], the ratio of the diffusion constant to the mobility should be linearly dependent on the temperature in a non-degenerate semiconductor at quasi-equilibrium condition. However, since the movement of $D^\circ X$ excitons is governed by hopping process and not by a Brownian motion in the case for FXs, this relation can be violated. The universality of the Einstein relation was debated by several authors[212, 213, 214] for exciton hopping in disordered materials. However, this investigation is beyond the scope of this chapter.

As a final note, comparing the results obtained in sample I and II ZnO MWs, some remarkable differences should be noticed. First, the strain gradient is lower in sample II than the one for the sample I. This is due to the larger curvature radius of the bent region in sample II. Therefore, the energy difference between the tensile and compressive region of this MW and the energy gradient $\partial E/\partial r$ across the MW is smaller in sample II (both MWs have the same diameter $\approx 2\mu m$). Nevertheless, the estimated value for exciton movements speed at $T \leq 10K$ remains approximately the same in both MWs.

As discussed in detail in Ref. [209], at low temperature $D^\circ X$s can hop from one energy state to the next one as long as the next donor is placed at a lower energy. This process is independent of the energy difference between two donor states at low temperature, where no thermal activation for backward motion of excitons exists. Then, the detrimental parameters in the hopping process speed are the exciton Bohr radius and the distance between adjacent donors, i.e., the doping concentration. Since ZnO MWs in both studies have been grown in the same growth conditions, neither the type of dopant nor the doping concentration is expected to vary in these two samples. The latter confirms the main outcomes from our theoretical proposal that at low temperatures energy gradient is not detrimental in the hopping speed of impurity bound excitons. Moreover, our experimental results shows that in the presence of the same doping concentration hopping speed of $D^\circ X$s has a strong dependence on temperature. The 10-fold decrease of the exciton movement speed from 4K to 25 K, originates from backward motion of excitons that becomes thermally activated by raising the temperature. This strong temperature dependence of exciton speed confirms our assumption that the exciton hopping is the main process of exciton movement at low temperatures.

## 5.5 Conclusion

In conclusion, we presented a direct study of exciton movement under a uniform strain gradient in ZnO MWs at low temperatures. The excitons, despite their binding to donor levels in our unintentionally doped samples, were observed to move efficiently under the uniform energy slope caused by the strain gradient. Designing two different samples with different values of the energy gradient across their bent region, the same movement speed for impurity bound excitons has been observed in both samples. Indeed, at low enough temperatures, donor-bound excitons can hop across the MW given that they can find a donor level at lower energy. In other words, in absence of a thermally activated motion of excitons, they can only move in the low energy direction of the energy slope, independent of the value of the energy or strain gradient. The observed dramatic dependence of the exciton movement speed on temperature is interpreted as the thermal activation of exciton movements to donor levels at higher energies, i.e., against the energy gradient direction. All these observations confirm the validity of the proposed theoretical model as the main movement mechanism of impurity bound excitons under an energy gradient at low temperatures.

In the studied samples in this chapter, the exciton lifetime was observed to be limited by non-radiative recombination as soon as the temperature was raised to moderate temperatures. Therefore, all our studies were carried out in a finite range of temperature below 30K. Getting ZnO MW samples with higher qualities can be interesting to probe the dynamics of excitons at still higher temperatures and follow the free exciton speed, when the dominant portion of excitons would change from donor-bound excitons to free excitons.

# 6 Excitonic diffusion in InGaN/GaN core-shell nanowires

The discussion in this chapter is mainly based on the following publication that has been submitted recently:

- *Exciton diffusion in presence of In composition fluctuations in GaN/InGaN core-shell nanowires*
G. Jacopin, M. Shahmohammadi, J.-D. Ganière, H. Zhang, R. Ciechonski, G. Vescovi and O. Kryliouk, M. Tchernycheva and B. Deveaud, submitted (2015).

## 6.1 Introduction

Since the first demonstration of a high-brightness blue LED by Shuji Nakamura *et al.* [1], the development of highly efficient white LEDs has been at the center of a huge interest. Although, the successful realization of high brightness III-Nitride LEDs leaded to their penetration into the lighting market as one of the most promising technologies, some physical issues still remain unsolved for their use at high power with high efficiency. One of the issues with a peculiar importance is the drop of efficiency under high injection, the so-called ”efficiency droop” problem. Even if its origin is understood [80], the possibility to circumvent it is still under investigation. Nevertheless, the nitride community is still puzzled with the physical origin of the efficiency droop.

The importance of the efficiency droop has already been discussed in detail in chapter 4. Whatever the origin of the droop, a reduction in the local carrier density in the QW for a given driving current can postpone the efficiency droop to higher driving currents. Since nearly a decade, the use of core-shell nanowires (NWs) has been proposed to reduce the current density in a LED, and as a consequence, the effects of a large carrier densities [215]. Nevertheless, the increase of the active surface area is effective only if the carrier density in the QW is homogeneous along the entire wire. To fulfill this requirement, the current injection should be homogeneous along the wire [22]. Additionally, once the carriers are in the QW, caution should be taken to prevent accumulation of carriers at one side of the NW. Indeed, it has been shown that the growth of core-shell structure often leads to the alloy gradient along the wire [22]. This In gradient may result in an accumulation of carriers in the In-rich part of the QW. However, only a few investigations on the drift of carriers in such NWs can be found in the literature, where this carrier accumulation effect could be carefully quantified. Indeed, this would require good spatial resolution, comparable or even smaller than the NW size (for instance, smaller than 100 nm) and also a high temporal resolution (better than 50 ps).

As was discussed in the last chapter, the use of our tr-CL can provide a powerful technique to investigate the local dynamics of excitons in a nanostructures. In this chapter, we present the results of an investigation of the carrier diffusion in a graded InGaN/GaN QW NW. Despite the presence of an energy gradient along the NW, because of large fluctuations in the localization energy, carriers cannot diffuse over long distances at low temperatures. This means that the dynamics of carriers is governed by the local energy fluctuations instead of the energy gradient along the NW. However, when raising the temperature from 4 K to 250 K, a strong change in the dynamics was observed: excitons could overcome the local energy barriers in the localization landscape owing to the absorption of thermal energy and reach to farther localized centers *via* tunneling. The analysis of the CL lifetime as a function of temperature reveals an isotropic motion of excitons in the investigated NWs. An analytical model based on an effective medium approximation was used to reproduce the observed dynamics as a function of temperature.

## 6.2 Sample structure and experimental details

The investigated samples are InGaN/GaN core-shell NWs grown by metal organics vapor phase epitaxy (MOVPE) on n-doped GaN/sapphire substrates, using a SiN mask with submicrometer openings to define the structure position and dimension. The NWs structure consists of the following elements (see Fig. 6.1(a)): the core of the NWs appears under the form of a needle of n-doped GaN with a doping concentration estimated to be between $5 \times 10^{18}$ and $10^{19}$ cm$^{-3}$. The first shell is the active region and consists in an undoped 5-10 nm thick QW, capped with an AlGaN electron-blocking layer. The structure growth is finished with a p-doped GaN shell with approximate thickness of 150 nm and doping concentration of about $5 \times 10^{19}$ cm$^{-3}$. The growth technique used here results in an array of identical NWs with a density of $5 \times 10^7$ NW/cm$^2$, with NWs dimensions of about 900 nm and 2.5 $\mu$m in diameter and length, respectively. According to the CL and TEM analysis performed previously on the same sample, no InGaN QW exists on the top of the NWs, i.e., on the semipolar planes (see Fig. 6.1(a)) [22].

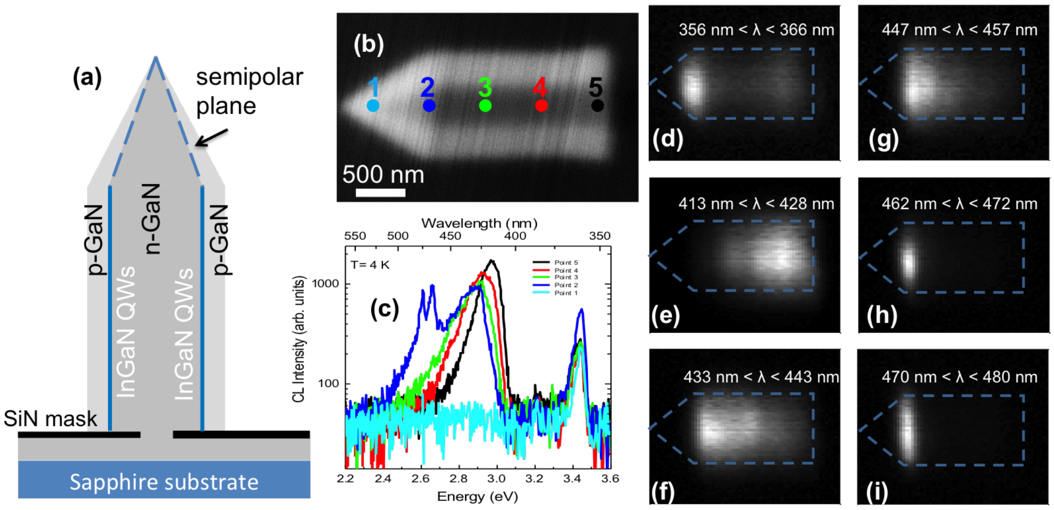

Figure 6.1 – **(a)** Schematic of the InGaN/GaN NW grown on Sapphire substrate. **(b)** SEM image obtained in the pulsed electron mode operation of the microscope. **(c)** CL spectra corresponding to excitation at different spots along the NW (Point 1 to point 5 refer to the positions indicated on the SEM image in part (b)). **(d)-(i)** Monochromatic CL mappings integrated over different emission wavelengths. The approximate boundaries of the NW structure are marked by the dashed lines.

In order to analyze the optical properties of a single NW in CL, NWs were detached from their growth substrate and dispersed on a heavily doped n-type Si substrate. The SEM image of a single NW obtained in the tr-CL setup by pulsed electron excitation at 6 keV, is shown in Fig. 6.1(b). The spatial resolution of our tr-CL setup can be estimated from this image to be better than 50 nm.

All tr-CL experiments have been carried out in an Attolight Alalin Chronos 4027 microscope coupled with Jobin Yvon spectrometer (iHr320) and a Synapse CCD camera. We used a grating with 150 grooves/mm to analyze the CL signal. The CL spectra as well as streak images have been recorded in a pulsed mode operation (~1ps electron pulse, 80.5 MHz repetition rate, and average electron current ~10 pA). For all the measurements, the excitation voltage was set to 6kV, which leads to a reasonable generation volume (with a radius of ≈ 300 nm) and, therefore, a good spatial resolution in our tr-CL measurements.

## 6.3 CL mapping of the InGaN/GaN core-shell NWs

Figure 6.1(c) shows the CL spectra, obtained when the excitation was performed at different spots along the NW at 4K (the point corresponding to each spectrum is shown by the same color in Fig. 6.1(b)). Exciting the NW at point 1, i.e., top edge of the NW, only a single peak was observed at 3.45 eV. This emission peak is attributed to the GaN near band edge (NBE) emission, confirming the absence of any semi-polar InGaN/GaN QW on the top of the NW. For other points, however, a strong luminescence was observed at about 2.8-3 eV that blueshifts monotonously when moving the excitation spot from the top of the NW towards its bottom, i.e., from point 2 to point 5. This shift in the emission energy is attributed to the presence of a gradient in the In composition of the non-polar $m$-plane QW along the NW.

In addition to the emission of the QW, the CL spectrum of point 2 features sharp emission lines on the low-energy side of the CL spectrum. These sharp emission peaks might originate from In-rich regions, located on the top of the NW, that behave similar to quantum dots (QDs) at low temperatures with emission linewidth of about 10 meV. The latter is basically limited by the spectral resolution of our CL system, and not necessarily by the properties of these quasi-QDs. We also discard the high carrier injection density as an origin of the observed linewidth of these QDs. Nevertheless, the features observed here provide evidence of the high collection efficiency in our tr-CL microscope.

Figure 6.1(d-i) presents the monochromatic CL mapping of the same NW, at the corresponding emission wavelength, extracted from 64 × 64 hyperspectral mappings at 4K. The CL intensity of the GaN emission peak is concentrated mainly on the top side of the NW (see Fig. 6.1(d)). This is due to the fact that other parts along the NW, carriers in the GaN barrier are efficiently captured into the InGaN QWs. However, due to the absence of QWs on the top region of the NW, carriers stay for a long time in the GaN barrier. The CL mapping of the QW emission spectrum at different energies are shown in Fig. 6.1(e-g). Comparing the mapping of Fig. 6.1(e) and (f), evidently, the high-energy regions are more located at the lower side of the NW. Eventually, the two CL mapping in Fig. 6.1(h-i) depict the spatial distribution of the regions corresponding to the sharp features in CL of the point 2, and the CL stems locally form the positions around point 2.

## 6.4 Temperature dependence of exciton dynamics, probed over the entire length of the NW

To probe the dynamics of excitons caused by the presence of the inhomogeneity of In composition along the NWs and to reveal better the role of the temperature in these dynamics, a set of tr-CL experiments along the NW and at different temperatures have been performed. The streak images have been recorded when exciting over the entire length of the NW and at different temperatures from 4K to 250K (see Fig. 6.2). Apart from the change in the effective decay time, which presumably originates from the increase of the non-radiative recombination effect at elevated temperatures, a distinct difference in dynamics appears: whereas at low temperatures (T <100K) no time dependent redshift of the emission energy exists, an enhanced redshift of the emission energy appears when raising the temperature above 150K.

At low temperatures, excitons get efficiently trapped into the first encountered shallow localization centers, and because of their low thermal energy, they cannot escape from these shallow levels. The characteristic time for this capture process has been demonstrated to be less than 20 ps [216, 203]. This is, however, below the temporal resolution of our tr-CL microscope (~ 50 ps), and cannot be detected. If any exciton movement would occur after this time delay, for example through a hopping process, it should appear as redshift in the emission energy. However, such a behavior is clearly not observed here at low temperatures, i.e., below 100K (see Fig. 6.2(a-c)).

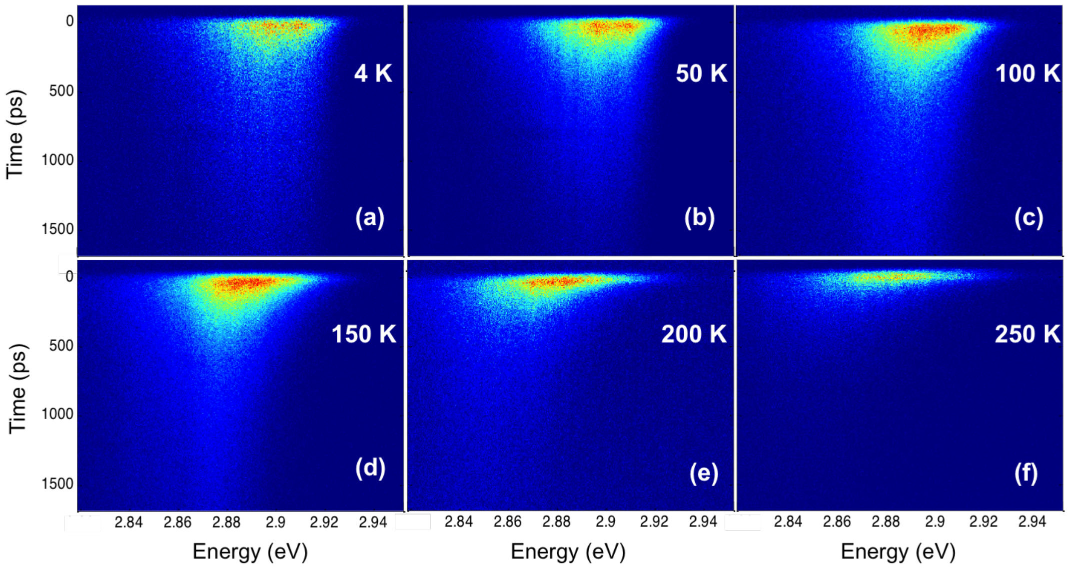

Figure 6.2 – Streak image recorded by excitation over the entire length of the NW at different temperatures: 4K **(a)**, 50K **(b)**, 100K **(c)**, 150K **(d)**, 200K **(e)**, 250K **(f)**. The intensities are normalized.

When raising the temperature above 100$K$ (see Fig. 6.2(d-f)), a distinct spectral shift of the emission appears after the electron pulse excitation, evidencing the exciton motion in the QW region. Two main possibilities can be considered for the observed spectral shift with a strong thermally activated nature: (i) the observed S-shape and its explanation [176], and (ii) drift of free carriers along the energy gradient of the QW. Other explanations related to high injection densities can be safely excluded here since the probe current is extremely small (~ 10 pA) for such high-injection effects to play a role [91, 182].

## 6.5 tr-CL measurements along the NW

In order to determine more precisely the origin of this shift, we performed tr-CL experiments at several temperatures for different excitation spots along the NW. The results obtained at 200K are shown in Fig. 6.3(b-d). The shift in the emission energy is highlighted by the white dashed arrows, and evidences that the behavior of the shift is dependent on the excitation spot. Indeed, the exciton lifetime is long enough to allow traveling over whole length of the NW and to reach the potential minima along the NW. In this case, the final value of the shifted energy should be the same wherever is the position of the excitation spot [68]. By contrast, our observations do not confirm this predicted drift effect due to the In-gradient along the NW.

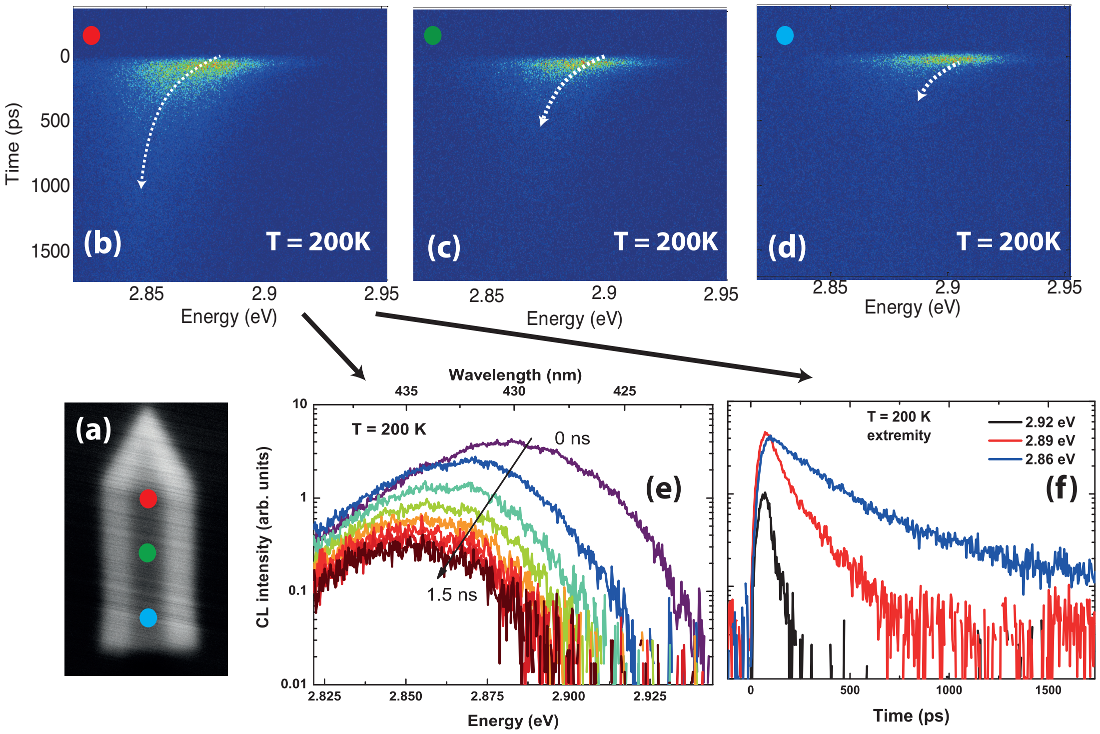

Figure 6.3 – **(a)** SEM image of a single NW recorded under pulsed electron operation. **(b)-(d)** Streak images of the tr-CL measurements recorded at 200 K for three different points along the NW corresponding to the bottom (blue), middle (green), and top (red) of the NW. **(e)** and **(f)** the CL spectrum traces and intensity decays extracted from streak image shown in (b), taken at the top of the NW.

However, we observe a strong energy shift at early delays that reduces when increasing the time delay. This behavior can only be understood as hopping process in a random distribution of localization centers [203, 200]. It worth also noticing the drastic change in the overall decay time from the top to the bottom of the wire (will be discussed later in section 6.7). The CL spectra for different delay times taken at the extremity of the non-polar QW is reported on Fig. 6.3(e). The peak position of the CL emission spectra progressively shifts from 2.88 eV at $t = 0$

ps to 2.85 eV at $t$=1500 ps. The large broadening of the CL spectrum at early delay is a strong evidence for the hopping process. Indeed, within the first few ps after the excitation, excitons experience a highly disordered landscape, leading to a large linewidth of the CL at early delays. This is indeed justified by the fact that our probe size (~ 100 nm) in our measurements is much larger than the size of localization centers. After that, excitons minimize their energies through several hopping steps to their nearest localization centers.

Figure 6.3(f) shows the CL intensity decay profiles corresponding to three different energies extracted from the streak image in Fig. 6.3(b). A remarkable difference can be identified depending on the emission energy: there is a significant difference in the effective lifetime, while it changes form 30 ps at 2.92 eV to ~130 ps and 280 ps at 2.89 eV and 2.86 eV. At the same time, the rise time raises of about 25 ps from 2.92 eV to 2.86 eV. These evidences together show the transfer of excitons from high to low energy levels.

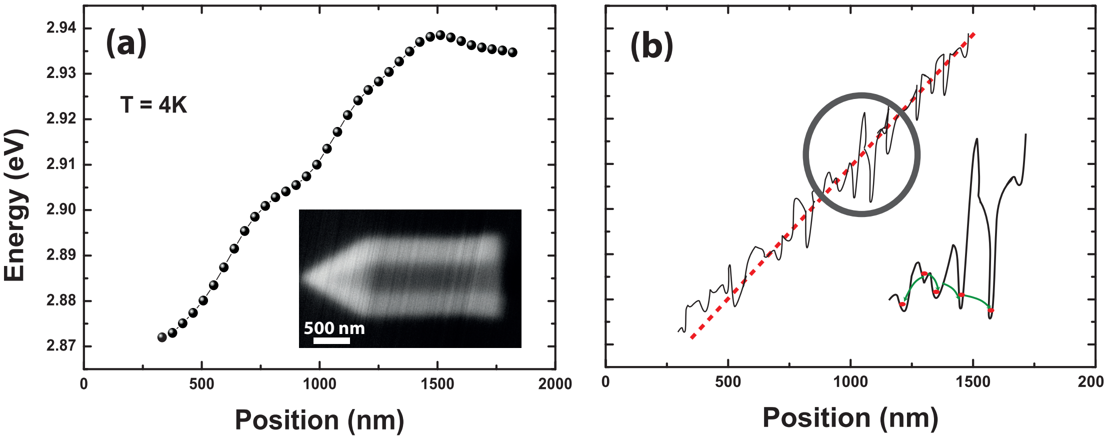

Figure 6.4 – **(a)** Energy profile of the CL emission along the NW, extracted from cw-CL mapping at T = 4K. Inset shows the SEM of the NW. **(b)** Schematics of the energy landscape for the excitons along the NW, including the energy fluctuations caused by the localization effect. The inset shows the behavior of exciton (red circle) with respect to this energy profile. Owing to large fluctuations in the energy profile, exciton does not necessarily follow the overall potential slope (red dashed line), and its trajectory is governed by the local potential profile.

One might attribute the strange time dependence of the energy shift to a non-linear potential profile that might exist along the NW, in our samples. Contrary to the strained ZnO MWs in the previous chapter, here the potential profile can have any dependence to position. In order to identify this effect, we have extracted the QW emission energy as a function of the position along the NW, from the cw-CL measurements at 4K (see Fig. 6.4(a)). We have preferentially chosen 4K measurements, since excitons have the least motion along the QW, and thus their emission energy is a measure of the local energy potential. The results show that the energy gradient caused by the In fluctuations approximately varies linearly along the NW. Therefore, assuming excitons have a constant movement speed along the NW, the emission energy should vary linearly with time, which is in sharp contrast to our observations.

Figure 6.4(b) shows schematically, the possible trajectory of excitons in the potential profile in our samples. Indeed, due to large local energy fluctuations, excitons can find states with lower energies that are not necessarily along the overall energy slope. This effect can become more pronounced at elevated temperatures, when excitons can overcome the energy barriers surrounding the shallow localization states.

## 6.6 Modeling of the exciton tunneling dynamics

To confirm that the observed dynamics are happening via the hopping process of excitons in an disordered potential provided by localization centers in our samples, the expected emission profile was simulated using the analytical formalism developed by Müller *et al.* in Ref. [203]. Within this model, a Gaussian distribution is assumed for the energy and spatial distribution of the localized states in order to reduce the complexity of the analysis, without any loss of generality. By simulating the hopping process between localization centers, the expected energy profile of the emission can be modeled as a function of time.

At low temperatures, most carriers relax into local potential minima within the first few picoseconds after the excitation [216]. As the thermal energy is not large enough to overcome the potential barriers between localization centers, lower lying localized states can be reached only by phonon-assisted tunneling [217, 218, 219]. Assuming that an exciton can reach $k$ different localized states, it will most probably relax into the lowest of these. The resulting distribution of the smallest out of k Gaussian random numbers can then be estimated and is simply given by [220]:

$$p_k(y) = k[1 - F(y)]^{k-1} f(y) = k\big(1 - \frac{erf(y/\sqrt{2}) + 1}{2}\big)^{k-1} \frac{\exp(-\frac{1}{2}y^2)}{\sqrt{2\pi}}, \tag{6.1}$$

where $f(y)$ and $F(y)$ denote the normal distribution and the corresponding commutative distribution, respectively.

Assuming a random spatial distribution for localization centers within the crystal with an average density of $n$, the number of reachable states within a certain tunneling volume $V_t$ follows a Poisson distribution $N^k e^{-N}/k!$, with an expectation value of $N = nV_t$. To calculate the occupation probability of the localized states, Eq. (6.1) should then be summed over all

$k \geq 0$, which leads to:

$$p_N(y) = \frac{N}{\sqrt{2\pi}} exp\Big(-N\frac{erf(y/\sqrt{2})+1}{2} - \frac{y^2}{2}\Big). \tag{6.2}$$

Since Eq. 6.1 vanishes for k = 0, Eq. 6.2 has to be normalized by $(1-e^{-N})^{-1}$. The PL line shape then can be derived from Eq. 6.2 by substituting $y = \frac{E-E_0}{\sigma}$, where $E_0$ is the mean exciton transition energy and $\sigma$ corresponds to the standard deviation determining the spectral linewidth of the distribution.

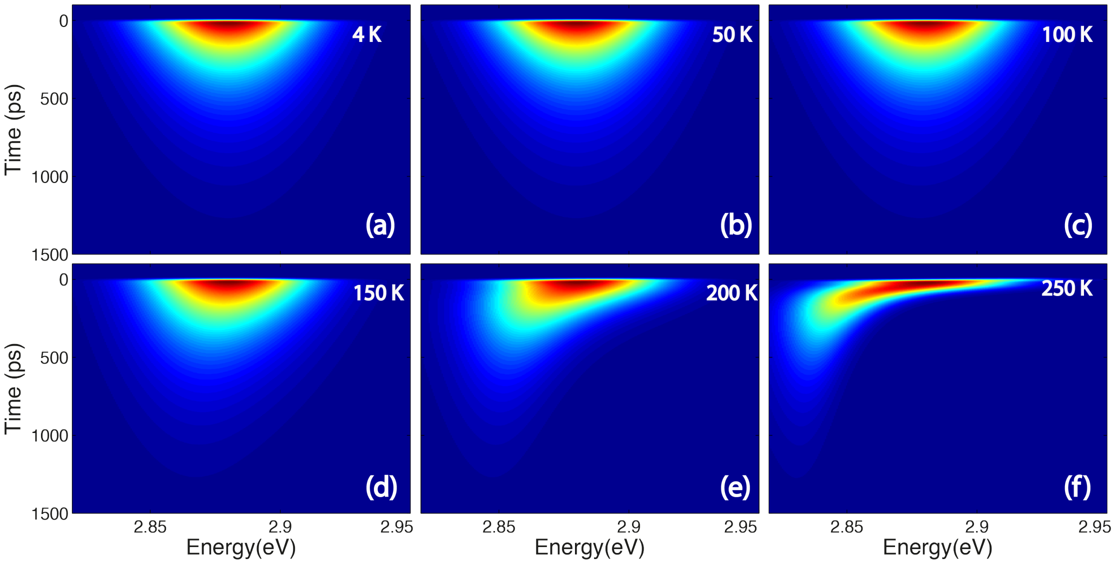

Figure 6.5 – **(a)** Results of the simulation of the luminescence emission profile as a function of time delay after excitation at different temperatures. At T< 100K, a negligible shift in the emission energy is observed, confirming the absence of any exciton hopping between the localization centers. When raising the temperature (T> 100K), a clear comma shape appears in simulations due to the activation of exciton hopping to reach the potential minima within a larger area in the QW.

In a first-order approximation, for excitons below the mobility edge, the probability of presence decreases exponentially as a function of distance from the center of mass [209, 221]. Therefore, the tunneling probability from an initial state to a given final states decrease also exponentially with the tunneling length $r_{t,0}$ as a function of the distance between the two states, . On average, the time to reach the more distant target state increases by the factor $e$, defining a time-dependent tunneling distance according to:

$$r_t(t) = r_{t,0} ln\Big(\frac{t}{t_0}\Big). \tag{6.3}$$

For simplification, the dependence of the extension of the exciton wave-function on the localization energy as well as the concrete potential environment around the localized state was neglected. The strongest variations are expected for the states energetically near the mobility edge. However, since most excitons rapidly relax into local potential minima well below the mobility edge, this means only a slow variation of $r_{t,0}$ is expected. Therefore, the tunneling length can be approximated by a constant. Statistically, within the time t, an exciton can reach all states inside the volume $V_t(t) = \frac{4}{3}\pi r_t^3$, leading to the average number of reachable states as:

$$N(t) = n \times \frac{4}{3} r_t^3(t). \tag{6.4}$$

Indeed, the time dependence of $r_t(t)$ images the fact that the number of reachable states for excitons is also a function of time. Here, the time $t_0$ has no direct physical meaning. However, it can be interpreted as the time delay at which the tunneling distance $r_t$ is large enough to reach all states during the thermalization process of an exciton.

To implement the temperature dependence of dynamics in our simulations, we assumed that the tunneling distance $r_t$ increases exponentially when raising the temperature, according to:

$$r_t(t,T) = r_{(t,T=0)} exp(\frac{T}{T_0}), \tag{6.5}$$

with $T_0 = 80K$, a value chosen in order to obtain a reasonable agreement with our temperature dependent measurements. Eventually to mimic the decrease of the carrier density, when increasing the time delay, the emission profile was multiplied by an exponential decay function with a typical decay time of excitons in our samples (~ 300 ps).

In an oversimplified view, this assumption can be justified by the fact that, when raising the temperature, excitons can overcome the barriers between localization centers and reach to larger number of the localization centers. Therefore, excitons trapped in shallow localization centers, can reach to final states positioned at much further distances from their initial positions.

Note further that, in our simplified model, no prior assumption on microscopic parameters such as an energy dependence of the exciton relaxation time constant [219, 222] or energy dependence of the transition rates [219] have been made. Figure 6.5 shows the results of this simulation preformed at different temperatures. The localization levels were considered to have a mean energy of 2.8 eV with standard deviation of about ~ 20 meV. The latter was taken to be a value close to the broadening of our measured CL spectra. The $t_0$ was found to be 20 ps for having a proper agreement between experiments and simulations.

This model, despite its oversimplified assumptions, can reproduce qualitatively the main

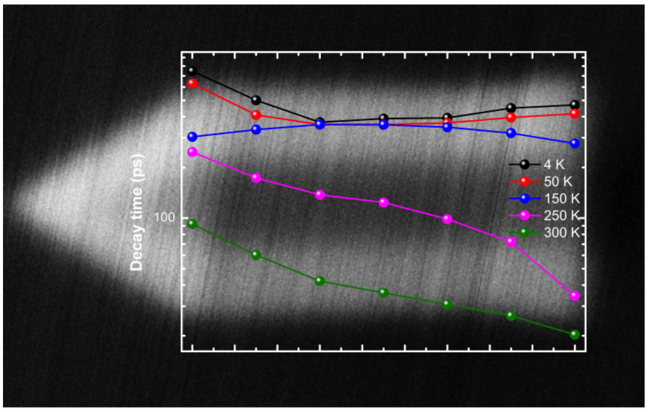

Figure 6.6 – CL lifetime of excitons along the NW at different temperatures, ranging from 4 K to 300 K. The lifetime was deduced from a mono-exponential fit to the total CL intensity of the QW.

features of the experimental observations in Fig. 6.2: at low temperatures, there is no shift in the emission energy, whereas with raising temperature a characteristic comma shape of the emission profile as a function of time delay appears. Moreover, the shift in the emission energy peak energy is fast at early delays and then slows down at longer delays, in agreement with experimental results (see Fig. 6.5(e-f)). Therefore, this model reproduces qualitatively the experimental results. However, to extract precise quantitative values from it, one needs to have an accurate knowledge of distribution of the localized centers along the NW. This would demand a better understanding of the potential profile caused by the In corporation in the QW and along the NW, which can be certainly an interesting task for future research.

## 6.7 Temperature dependence of the exciton lifetime along the NW

It worth commenting on the variation of the exciton effective lifetime along the NW. Figure 6.6 shows the effective lifetime deduced from our tr-CL experiments at different temperatures as a function of the position along the NW (resulting from a mono-exponential fitting of the integrated CL intensity over the whole emission spectrum of the QW). At low temperature (i.e., below 50K), the lifetime is approximately constant along the wire. The slight increase of lifetime at the top of the NW is attributed to the high In segregation in the m-plane QW at those positions of the NW. Indeed, even if there is no Stark effect here, the increase of In composition leads to an increase of localization, which results in an increase of lifetime [223]. However, when raising the temperature above 150 K, a decrease in the lifetime appears when moving towards the bottom of the NW.

This change in the effective lifetime is attributed to our preparation technique. Indeed, in order to disperse the NWs on the Si substrate, we detached the NWs from the growth substrate. As a matter of fact, this cleaving process introduces a large non-radiative recombination at the free surface at the bottom of the NW. Therefore, the excitons that can reach this surface experience a shorter effective lifetime.

At low temperature, this effect has only a minor impact on the exciton lifetime along the NW, because carriers are not mobile enough to reach non-radiative centers. However, when raising the temperature, the excitons can diffuse over larger larger distances and reach the surface defects introduced by our sample preparation technique. By probing the lifetime along the wire, we have an indirect estimation of the diffusion length of excitons: excitons can move less than 100 nm at temperatures below 50 K, while this length increases to ~200 nm at 150K and to a value more than 1 $\mu$m at 250K and 300K. The latter explains why the exciton lifetime is affected by this surface non-radiative recombinations over the whole length of the NW.

## 6.8 Conclusion

Our measurements confirm the motion of carriers in InGaN NWs, when the temperature is raised. However, the carriers do not necessarily drift along the In gradient. This stands in sharp contrast to our previous experimental observations in exciton hopping in bent ZnO microwires at low temperature discussed in chapter 5. The difference can be understood as follows: in the case of ZnO microwires, we observed the motion of bound excitons thank to the perfect energy ladder along the gradient of energy [209], whereas here, even in the presence of an energy gradient along the NW, the strong potential disorder provided by the localization centers prevents excitons to ”feel” the energy gradient. Indeed, with an In content as large as 15%, even perfect random alloy composition was predicted to lead to the formation of randomly distributed localization centers [224]. In such case, it has been shown that the hopping is much less efficient at low temperature and can be thermally activated at higher temperatures [203].

To summarize, we have investigated through tr-CL experiments the motion of carriers in an inhomogeneous non-polar core-shell InGaN QW in GaN NW, where the random alloy fluctuation suppresses any directional drift along the In gradient, i.e., the energy gradient caused by that. Nevertheless, the exciton motion through this hopping process can be thermally activated up to 1 $\mu m$ in distance. Eventually, the redshift of the emission energy was qualitatively reproduced using a model for the hopping process of exciton s in between localization centers. An isotropic motion of carriers independent of the energy gradient orientation was observed. Our results therefore confirm the possible potential of the core-shell NWs for lighting devices, since strong carrier accumulation at high In content centers can be suppressed by the randomly distributed localization centers. Indeed, the short lifetime of $m$-plane QW combined with the large active area and the homogeneous distribution of carrier along the QW can decrease the carrier density in the QW for a given operation current and as a consequence might help to eliminate the drop of the efficiency of blue LEDs.

# Conclusion and perspectives

In this PhD thesis, we have investigated the dynamics of carriers in wide bandgap semiconductor nanostructures. The time-resolved photo- and cathodoluminescence techniques used here, allows us to track, at the nanometer and picosecond scales, the transport and recombination mechanisms of the carriers in those nano-structures. We present in the following the main outcomes of the present work as well as some perspectives for the further investigations.

In chapter 3, a crossover from excitons to biexcitons and finally to an electron-hole plasma in a 2D system was observed as a function of carrier density. The stability of biexciton molecules against Coulomb screening and collisions at high carrier density was traced back to the robustness in the biexciton binding energy. The appearance of an electron-hole plasma emission spectrum from the biexciton energy implies the important role can be played by biexcitons in the Mott transition.

The robustness of biexcitonic molecules might seem surprising if one considers their smaller binding energy compared to that of excitons. However, one might attribute this to a more complex interplay between correlation and exchange processes occurring in those molecules built from four particles, when interacting with nearby carriers. In most of the existing theories on the Mott transition, the existence of biexcitons was neglected [120, 100], likely because of their reduced stability in smaller bandgap QW heterostructures like GaAs. Therefore, considering the important role that can be played by those quasiparticles across the Mott transition, our results call for additional theoretical investigations

Then, the temperature dependence of the Mott density in a $c$-plane GaN/AlGaN QW was investigated over a significant range of lattice temperatures. The Mott density was found to have no distinct dependence on the temperature and to be around $10^{12} cm^{-2}$ in our investigated $c$-plane GaN/AlGaN QW. There is a certain interest to extend the studied temperature range towards higher temperatures. However, when raising the temperature, apart from difficulties in the analysis that arises from the increase in the homogeneous broadening and increase in the non-radiative recombinations, one should also consider the exciton dissociation due to the mass action law. The samples with larger exciton binding energy such as ZnO QWs can then be a proper choice for such a study, given the fact that the high-quality of the samples suppresses non-radiative recombination over the whole studied temperature range.

In chapter 4, we performed the same investigation on InGaN/GaN QWs, in which quite different dynamics have been observed. From the dynamics of the PL intensity, we could provide a clear experimental evidence on the droop signature in InGaN/GaN QWs. While, absolutely no ultrafast initial decay was observed in the investigated GaN/AlGaN QWs up to densities as high as $5 \times 10^{12} cm^{-2}$. Therefore, by comparing the dynamics between GaN and InGaN QWs, we demonstrated that, indeed, there are some intrinsic properties caused by adding In to III-nitride heterostructures. Moreover, the difference in the dynamics observed between various $c$-plane and $m$-plane QWs investigated in this chapter, can help to uncover the role played by the polarization field in the efficiency droop. The engineered localization density in our $m$-plane QWs, also allows us studying solely the effect of localization on the droop in those state-of-the-art quality samples. Our experimental scheme provided us the possibility to determine accurately the carrier density in the QW, and hence deduce reliably the Auger coefficient from our measurements by proper fittings. Indeed, new theoretical efforts are demanded to fully understand the impact of each aforementioned physical phenomena in the efficiency droop. There is also certainly an interest to employ such kind of measurements into single QW LED structures, while the applied bias can simulate a more realistic situation for the measurements, and make our results directly applicable to LEDs.

In chapter 5, we presented a direct observation of exciton movement under a uniform strain gradient in ZnO microwaves at low temperatures. Donor-bound excitons, despite their binding to donor levels in our unintentionally doped samples, were observed to move efficiently under the uniform energy slope caused by the strain gradient. Varying the energy gradient across the bent region of microwires, the same movement speed for impurity bound excitons has been observed. This means that, in the absence of any thermally activated motion of excitons, excitons can only move in the low energy direction of the energy slope, independent of the value of the energy or strain gradient. The observed dramatic dependence of the exciton movement speed on temperature was interpreted as the thermal activation of exciton movements to donor levels at higher energies, i.e.,. against the energy gradient direction. All these observations confirm the validity of the proposed theoretical model as the main movement mechanism of impurity bound excitons under an energy gradient at low temperatures.

In the investigated samples, the exciton lifetime was observed to be limited by non-radiative recombination as soon as the temperature is raised. Therefore, all our studies were carried out in a finite range of temperature below 30K. Studying samples with higher quality can be interesting to probe the dynamics of excitons at still higher temperatures and follow the free exciton speed, when the dominant portion of excitons would change from donor-bound excitons to free excitons. Even if the hopping process is limited to low temperatures in our investigated ZnO microwires, in other disordered systems such as InGaN nanowire or organic semiconductors, which have usually a large disorder, such a transport may persist up to room temperature.

In the last chapter, we have investigated the motion of the carriers in an inhomogeneous non-polar core-shell InGaN QWs, while the random alloy fluctuation suppresses any directional drift along the In gradient, i.e., energy gradient caused by that. Nevertheless, exciton motion through hopping process have been demonstrated to be thermally activated up to 1 $\mu m$ in distance. The redshift of the emission energy was qualitatively reproduced using a model for the hopping process of exciton in between localization centers. An isotropic motion of carriers independent of the energy gradient orientation was observed. Our results therefore confirm the potential of core-shell NW for lighting devices, since strong carrier accumulation at high In-content centers can be suppressed by the randomly distributed localization centers. Indeed, the short lifetime of $m$-plane QW combined with the large active area and the homogeneous distribution of carrier along the QW can decrease the carrier density in the QW for a given operation current. These effects can help to shift the efficiency droop problem to higher driving currents.

# Bibliography

[1] S. Nakamura, T. Mukai, and M. Senoh, “Candela-class high-brightness InGaN/AlGaN double-heterostructure blue-light-emitting diodes,” *Appl. Phys. Lett.*, vol. 64, no. 13, p. 1687, 1994.

[2] “U.S. Department of Energy, Solid-State Lighting Research and Development: Multi-Year Program Plan,” 2012.

[3] S. Christopoulos, V. Högersthal, G. Baldassarri Höger, A. J. D. Grundy, P. G. Lagoudakis, a. V. Kavokin, J. J. Baumberg, G. Christmann, R. Butté, E. Feltin, J.-F. Carlin, and N. Grandjean, “Room-temperature polariton lasing in semiconductor microcavities,” *Phys. Rev. Lett.*, vol. 98, p. 126405, 2007.

[4] G. Christmann, R. Butte, E. Feltin, J.-F. Carlin, and N. Grandjean, “Room temperature polariton lasing in a GaNAlGaN multiple quantum well microcavity,” *Appl. Phys. Lett.*, vol. 93, p. 051102, 2008.

[5] I. Iorsh, M. Glauser, G. Rossbach, J. Levrat, M. Cobet, R. Butté, N. Grandjean, M. A. Kaliteevski, R. a. Abram, and A. V. Kavokin, “Generic picture of the emission properties of III-nitride polariton laser diodes: Steady state and current modulation response,” *Phys. Rev. B*, vol. 86, p. 125308, 2012.

[6] N. F. Mott, “Metal-insulator transition,” *Rev. Mod. Phys.*, vol. 40, no. 4, p. 677, 1968.

[7] K. G. Lagoudakis, M. Wouters, M. Richard, A. Baas, I. Carusotto, R. Andre, L. S. Dang, and B. Deveaud-Pledran, “Quantised Vortices in an Exciton-Polariton Fluid,” *Nat. Phys.*, vol. 4, p. 706, 2008.

[8] A. Amo, J. Lefrere, S. Pigeon, C. Adrados, C. Ciuti, I. Carusotto, R. Houdre, E. Giacobino, and A. Bramati, “Observation of Superfluidity of Polaritons in Semiconductor Microcavities,” *Nat. Phys.*, vol. 5, p. 805, 2008.

[9] J. Kasprzak, M. Richard, S. Kundermann, A. Baas, P. Jeambrun, J. M. J. Keeling, F. M. Marchetti, M. H. Szymańska, R. André, J. L. Staehli, V. Savona, P. B. Littlewood, B. Deveaud, and L. S. Dang, “Bose-Einstein condensation of exciton polaritons.,” *Nature*, vol. 443, p. 409, 2006.

[10] G. Rossbach, J. Levrat, E. Feltin, J.-F. Carlin, R. Butté, and N. Grandjean, “Impact of saturation on the polariton renormalization in III-nitride based planar microcavities,” *Phys. Rev. B*, vol. 88, p. 165312, 2013.

[11] F. Stokker-Cheregi, A. Vinattieri, E. Feltin, D. Simeonov, J. Levrat, J.-F. Carlin, R. Butte, N. Grandjean, and M. Gurioli, “Impact of quantum confinement and quantum confined Stark effect on biexciton binding energy in GaN/AlGaN quantum wells,” *Appl. Phys. Lett.*, vol. 93, p. 152105, 2008.

[12] F. Stokker-Cheregi, A. Vinattieri, E. Feltin, D. Simeonov, J.-F. Carlin, R. Butte, N. Grandjean, and M. Gurioli, “Biexciton kinetics in GaN quantum wells: Time-resolved and time-integrated photoluminescence measurements,” *Phys. Rev. B*, vol. 77, p. 125342, 2008.

[13] Y. Hayamizu, M. Yoshita, Y. Takahashi, H. Akiyama, C. Ning, L. Pfeiffer, and K. West, “Biexciton gain and the Mott transition in GaAs quantum wires,” *Phys. Rev. Lett.*, vol. 99, no. 16, p. 167403, 2007.

[14] M. Yoshita, Y. Hayamizu, H. Akiyama, L. Pfeiffer, and K. West, “Exciton-plasma crossover with electron-hole density in T-shaped quantum wires studied by the photoluminescence spectrograph method,” *Phys. Rev. B*, vol. 74, p. 165332, 2006.

[15] T. Zhu and J. Li, “Ultra-strength materials,” *Prog. Mater. Sci.*, vol. 55, pp. 710–757, 2010.

[16] B. Wei, K. Zheng, Y. Ji, Y. Zhang, Z. Zhang, and X. Han, “Size-dependent bandgap modulation of zno nanowires by tensile strain,” *Nano Lett.*, vol. 12, p. 4595, 2012.

[17] R. He and P. Yang, “Giant piezoresistance effect in silicon nanowires.,” *Nat. Nanotechnol.*, vol. 1, p. 42, 2006.

[18] M. Ieong, B. Doris, J. Kedzierski, K. Rim, and M. Yang, “Silicon device scaling to the sub-10-nm regime.,” *Sci. (New York)*, vol. 306, p. 2057, 2004.

[19] M. Leroux, N. Grandjean, M. Laugt, J. Massies, B. Gil, P. Lefebvre, and P. Bigenwald, “Quantum confined Stark effect due to built-in internal polarization fields in (Al,Ga)N/GaN quantum wells,” *Phys. Rev. B*, vol. 58, no. 20, p. R13371, 1998.

[20] G. Jacopin, L. Rigutti, S. Bellei, P. Lavenus, F. H. Julien, A. V. Davydov, D. Tsvetkov, K. A. Bertness, N. A. Sanford, J. B. Schlager, and M. Tchernycheva, “Photoluminescence polarization in strained GaN/AlGaN core/shell nanowires,” *Nanotechnology*, vol. 23, p. 325701, 2012.

[21] C. P. Dietrich, M. Lange, F. J. Klüpfel, H. Von Wenckstern, R. Schmidt-Grund, and M. Grundmann, “Strain distribution in bent ZnO microwires,” *Appl. Phys. Lett.*, vol. 98, p. 031105, 2011.

[22] M. Tchernycheva, P. Lavenus, H. Zhang, A. V. Babichev, G. Jacopin, M. Shahmohammadi, F. H. Julien, R. Ciechonski, G. Vescovi, and O. Kryliouk, “InGaN/GaN core-shell single nanowire light emitting diodes with graphene-based P-contact,” *Nano Lett.*, vol. 14, no. 5, p. 2456, 2014.

[23] J. Levrat, *Physics of Polariton Condensates in GaN-based Planar Microcavities.* PhD thesis, EPFL, 2012.

[24] T. Lei, M. Fanciulli, R. J. Molnar, T. D. Moustakas, R. J. Graham, and J. Scanlon, “Epitaxial growth of zinc blende and wurtzitic gallium nitride thin films on (001) silicon,” *Appl. Phys. Lett.*, vol. 59, no. 8, p. 944, 1991.

[25] H. Angerer and D. Brunner, “Determination of the Al mole fraction and the band gap bowing of epitaxial,” *Appl. Phys. Lett.*, vol. 71, no. 11, p. 1504, 1997.

[26] L. Gorgens, O. Ambacher, M. Stutzmann, C. Miskys, F. Scholz, and J. Off, “Characterization of InGaN thin films using high-resolution x-ray diffraction,” *Appl. Phys. Lett.*, vol. 76, no. 5, p. 577, 2000.

[27] T. Peng, J. Piprek, G. Qiu, J. O. Olowolafe, K. M. Unruh, C. P. Swann, and E. F. Schubert, “Band gap bowing and refractive index spectra of polycrystalline Al[sub x]In[sub 1-x]N films deposited by sputtering,” *Appl. Phys. Lett.*, vol. 71, no. 17, p. 2439, 1997.

[28] O. Ambacher, J. Majewski, C. Miskys, A. Link, M. Hermann, M. Eickhoff, M. Stutzmann, F. Bernardini, V. Fiorentini, V. Tilak, B. Schaff, and L. F. Eastman, “Pyroelectric properties of Al(In)GaN/GaN hetero- and quantum well structures,” *J. Phys. Condens. Matter*, vol. 14, p. 3399, 2002.

[29] R. Butté and N. Grandjean, “Effects of polarization in optoelectronic quantum structures,” in *Polariz. Eff. Semicond. From Ab InitioTheory to Device Appl.*, pp. 467–511, Springer, 2008.

[30] N. Akopian, G. Bahir, D. Gershoni, M. D. Craven, J. S. Speck, and S. P. Denbaars, “Optical evidence for lack of polarization in (11 2- 0) oriented GaN (AlGa) N quantum structures,” *Appl. Phys. Lett.*, vol. 86, p. 202104, 2005.

[31] P. Waltereit, O. Brandt, A. Trampert, H. Grahn, J. Menniger, M. Ramsteiner, M. Reiche, and K. Ploog, “Nitride semiconductors free of electrostatic fields for efficient white light-emitting diodes,” *Nature*, vol. 406, p. 865, 2000.

[32] N. F. Gardner, J. C. Kim, J. J. Wierer, Y. C. Shen, and M. R. Krames, “Polarization anisotropy in the electroluminescence of m-plane InGaN-GaN multiple-quantum-well light-emitting diodes,” *Appl. Phys. Lett.*, vol. 86, p. 111101, 2005.

[33] E. Kioupakis, Q. Yan, and C. G. Van de Walle, “Interplay of polarization fields and Auger recombination in the efficiency droop of nitride light-emitting diodes,” *Appl. Phys. Lett.*, vol. 101, p. 231107, 2012.

[34] K. Kojima, A. A. Yamaguchi, M. Funato, Y. Kawakami, and S. Noda, “Impact of nonpolar AlGaN quantum wells on deep ultraviolet laser diodes,” *J. Appl. Phys.*, vol. 110, p. 043115, 2011.

[35] J. E. Northrup, “GaN and InGaN (1122) surfaces: Group-III adlayers and indium incorporation,” *Appl. Phys. Lett.*, vol. 95, p. 133107, 2009.

[36] Y. Yoshizumi, M. Adachi, Y. Enya, T. Kyono, S. Tokuyama, T. Sumitomo, K. Akita, T. Ikegami, M. Ueno, K. Katayama, and T. Nakamura, “Continuous-wave operation of 520 nm green InGaN-based laser diodes on semi-polar {202-1} GaN substrates,” *Appl. Phys. Express*, vol. 2, p. 092101, 2009.

[37] S.-H. Park and S.-L. Chuang, “Crystal-orientation effects on the piezoelectric field and electronic properties of strained wurtzite semiconductors,” *Phys. Rev. B*, vol. 59, no. 7, p. 4725, 1999.

[38] Y. Sun, S. E. Thompson, and T. Nishida, *Strain effect in semiconductors: Theory and device applications.* New York: Springer, 2010.

[39] U. M. E. Christmas, a. D. Andreev, and D. A. Faux, “Calculation of electric field and optical transitions in InGaN/GaN quantum wells,” *J. Appl. Phys.*, vol. 98, p. 073522, 2005.

[40] I. Vurgaftman and J. R. Meyer, “Band parameters for nitrogen-containing semiconductors,” *J. Appl. Phys.*, vol. 94, no. 6, p. 3675, 2003.

[41] P. Gopal and N. A. Spaldin, “Polarization, piezoelectric constants, and elastic constants of ZnO, MgO, and CdO,” *J. Electron. Mater.*, vol. 35, no. 4, p. 538, 2006.

[42] B. Gil, O. Briot, and R. L. Aulombard, “Valence-band physics and the optical properties of GaN epilayers grown onto sapphire with wurtzite symmetry,” *Phys. Rev. B*, vol. 52, no. 24, p. R17028, 1995.

[43] M. Feneberg, R. A. R. Leute, B. Neuschl, K. Thonke, and M. Bickermann, “High-excitation and high-resolution photoluminescence spectra of bulk AlN,” *Phys. Rev. B*, vol. 82, p. 075208, 2010.

[44] J. Wu, W. Walukiewicz, K. M. Yu, J. W. Ager, E. E. Haller, H. Lu, W. J. Schaff, Y. Saito, and Y. Nanishi, “Unusual properties of the fundamental band gap of InN,” *Appl. Phys. Lett.*, vol. 80, no. 21, p. 3967, 2002.

[45] Y. Varshni, “Temperature dependence of the energy gap in semiconductors,” *Physica*, vol. 34, p. 149, 1967.

[46] R. Pässler, “Temperature dependence of fundamental band gaps in group IV, III-V, and II-VI materials via a two-oscillator model,” *J. Appl. Phys.*, vol. 89, no. 11, p. 6235, 2001.

[47] B. K. Meyer, H. Alves, D. M. Hofmann, W. Kriegseis, D. Forster, F. Bertram, J. Christen, A. Hoffmann, M. Straß burg, M. Dworzak, U. Haboeck, and A. V. Rodina, "Bound exciton and donor-acceptor pair recombinations in ZnO," *Phys. status solidi*, vol. 241, no. 2, p. 231, 2004.

[48] F. Bernardini, V. Fiorentini, and D. Vanderbilt, "Spontaneous polarization and piezoelectric constants of III-V nitrides," *Phys. Rev. B*, vol. 56, no. 16, p. R10024, 1997.

[49] F. Bernardini and V. Fiorentini, "Non-linear macroscopic polarization in III-V nitride alloys," *Phys. Rev. B*, vol. 64, p. 085207, 2001.

[50] N. Grandjean, B. Damilano, S. Dalmasso, M. Leroux, M. Lauugt, and J. Massies, "Built-in electric-field effects in wurtzite AlGaN/GaN quantum wells," *J. Appl. Phys.*, vol. 86, no. 7, p. 3714, 1999.

[51] T. Bretagnon, P. Lefebvre, P. Valvin, R. Bardoux, T. Guillet, T. Taliercio, B. Gil, N. Grandjean, F. Semond, B. Damilano, A. Dussaigne, and J. Massies, "Radiative lifetime of a single electron-hole pair in GaN AlN quantum dots," *Phys. Rev. B*, vol. 73, p. 113304, 2006.

[52] S. F. Chichibu, T. Koida, M. D. Craven, B. A. Haskell, T. Onuma, T. Sota, J. S. Speck, S. P. DenBaars, and S. Nakamura, "Reduction of bound-state and nonradiative defect densities in nonpolar (1120) AlGaN/GaN quantum wells by the use of lateral epitaxial overgrowth technique," *Phys. status solidi*, vol. 2, no. 7, p. 2700, 2005.

[53] J. K. Son, S. N. Lee, H. S. Paek, T. Sakong, K. H. Ha, O. H. Nam, and Y. Park, "Radiative and non-radiative transitions in blue quantum wells embedded in AlInGaN-based laser diodes," *Phys. status solidi*, vol. 4, no. 7, p. 2780, 2007.

[54] H. Yoshida, M. Kuwabara, Y. Yamashita, K. Uchiyama, and H. Kan, "Radiative and nonradiative recombination in an ultraviolet GaN/AlGaN multiple-quantum-well laser diode," *Appl. Phys. Lett.*, vol. 96, p. 211122, 2010.

[55] E. Grilli, M. Guzzi, R. Zamboni, and L. Pavesi, "High-precision determination of the temperature dependence of the fundamental energy gap in gallium arsenide," *Phys. Rev. B*, vol. 45, no. 4, p. 1638, 1992.

[56] C. Neumann, A. Nöthe, and N. O. Lipari, "Two-photon magnetoabsorption of ZnTe, CdTe, and GaAs," *Phys. Rev. B*, vol. 37, no. 2, p. 922, 1988.

[57] P. Y. Yu and M. Cardona, *Fundamentals of semiconductors: Physics and materials properties.* Heidelberg: Springer, 4th ed., 2010.

[58] G. Steude, T. Christmann, B. Meyer, A. Goeldner, A. Hoffmann, F. Bertram, J. Christen, H. Amano, and I. Akasaki, "Optical Investigations of AlGaN on GaN Epitaxial Films," *MRS Proc.*, vol. 74, no. 17, p. 2456, 1998.

[59] K. Kornitzer, T. Ebner, K. Thonke, R. Sauer, C. Kirchner, V. Schwegler, M. Kamp, M. Leszczynski, I. Grzegory, and S. Porowski, "Photoluminescence and reflectance spectroscopy of excitonic transitions in high-quality homoepitaxial GaN films," *Phys. Rev. B*, vol. 60, no. 3, p. 1471, 1999.

[60] G. Bastard, E. E. Mendez, L. L. Chang, and L. Esaki, "Exciton binding energy in quantum wells," *Phys. Rev. B*, vol. 26, no. 4, p. 1974, 1982.

[61] J. Shah, *Ultrafast Spectroscopy of Semiconductors and Semiconductor Nanostructures.* Springer-Verlag Berlin Heidelberg, 2nd ed., 1999.

[62] P. M. Corfdir, *Physics of the Ultrafast Dynamics of Excitons in GaN Nanostructures PAR.* PhD thesis, EPFL, 2011.

[63] A. Morel, P. Lefebvre, T. Taliercio, T. Bretagnon, B. Gil, N. Grandjean, B. Damilano, and J. Massies, "Two-dimensional "pseudo-donor-acceptor-pairs" model of recombination dynamics in InGaN/GaN quantum wells," *Phys. E*, vol. 17, p. 64, 2003.

[64] J.-M. Bonard and J.-D. Ganiere, "Quantitative analysis of electron-beam-induced current profiles across p-n junctions in GaAs/Al0.4Ga0.6As heterostructures," *J. Appl. Phys.*, vol. 79, no. 9, p. 6987, 1996.

[65] "Simulations have been done with CASINO, Version 2.4.8.1, available online for free (http://www.gel.usherbrooke.ca/casino/What.html).."

[66] B. G. Yacobi and D. B. Holt, *Cathodoluminescence Microscopy of Inorganic Solids.* New York: springer, 1st ed., 1990.

[67] C. A. Klein, "Bandgap dependence and related features of radiation ionization energies in semiconductors," *J. Appl. Phys.*, vol. 39, p. 2029, 1968.

[68] X. Fu, G. Jacopin, M. Shahmohammadi, R. Liu, M. Benameur, J.-D. Ganière, J. Feng, W. Guo, Z. M. Liao, B. Deveaud, and D. Yu, "Exciton drift in semiconductors under uniform strain gradients: Application to bent ZnO microwires," *ACS Nano*, vol. 8, no. 4, p. 3412, 2014.

[69] A. Steckenborn, H. Münzel, and D. Bimberg, "Cathodoluminescence lifetime pattern of GaAs surfaces around dislocations," *J. Lumin.*, vol. 24-25, no. 1, p. 351, 1981.

[70] P. Corfdir, J. Ristić, P. Lefebvre, T. Zhu, D. Martin, A. Dussaigne, J.-D. Ganìre, N. Grandjean, and B. Deveaud-PÍdran, "Low-temperature time-resolved cathodoluminescence study of exciton dynamics involving basal stacking faults in a-plane GaN," *Appl. Phys. Lett.*, vol. 94, p. 201115, 2009.

[71] P. Corfdir, P. Lefebvre, L. Balet, S. Sonderegger, A. Dussaigne, T. Zhu, D. Martin, J.-D. Ganìre, N. Grandjean, and B. Deveaud-PÍdran, "Exciton recombination dynamics in a -plane (Al,Ga)N/GaN quantum wells probed by picosecond photo and cathodoluminescence," *J. Appl. Phys.*, vol. 107, p. 043524, 2010.

[72] M. Merano, S. Sonderegger, A. Crottini, S. Collin, P. Renucci, E. Pelucchi, A. Malko, M. H. Baier, E. Kapon, B. Deveaud, and J.-D. Ganière, “Probing carrier dynamics in nanostructures by picosecond cathodoluminescence.,” *Nature*, vol. 438, p. 479, 2005.

[73] C. F. Klingshirn, *Semiconductor Optics.* Berlin: Springer-Verlag, Berlin, 1997.

[74] H. Haug and S. Koch, “Semiconductor laser theory with many-body effects,” *Phys. Rev. A*, vol. 39, no. 4, p. 1887, 1989.

[75] T. Ogawa, Y. Tomio, and K. Asano, “Quantum condensation in electron-hole systems: excitonic BEC-BCS crossover and biexciton crystallization.,” *J. physics. Condens. matter*, vol. 19, p. 295205, 2007.

[76] C. Klingshirn, R. Hauschild, J. Fallert, and H. Kalt, “Room-temperature stimulated emission of ZnO: Alternatives to excitonic lasing,” *Phys. Rev. B*, vol. 75, p. 115203, 2007.

[77] J. Ding, H. Jeon, T. Ishihara, M. Hagerott, A. Nurmikko, H. Luo, N. Samarth, and J. Furdyna, “Excitonic Gain and Laser Emission in ZnSe-Based Quantum Wells,” *Phys. Rev. Lett.*, vol. 69, p. 1707, 1992.

[78] M. H. Kim, “Origin of efficiency droop in GaN-based light-emitting diodes,” *Appl. Phys. Lett.*, vol. 91, p. 183507, 2007.

[79] E. Kioupakis, P. Rinke, K. T. Delaney, and C. G. Van De Walle, “Indirect Auger recombination as a cause of efficiency droop in nitride light-emitting diodes,” *Appl. Phys. Lett.*, vol. 98, p. 161107, 2011.

[80] J. Iveland, L. Martinelli, J. Peretti, J. S. Speck, and C. Weisbuch, “Direct measurement of auger electrons emitted from a semiconductor light-emitting diode under electrical injection: Identification of the dominant mechanism for efficiency droop,” *Phys. Rev. Lett.*, vol. 110, no. 17, p. 177406, 2013.

[81] A. Pasquarello and L. C. Andreani, “Variational calculation of Fano linewidth: Application to excitons in quantum wells,” *Phys. Rev. B*, vol. 44, p. 3162, 1991.

[82] L. J. Schowalter, F. M. Steranka, M. B. Salamon, and J. P. Wolfe, “Evidence for separate Mott and liquid-gas transitions in photoexcited, strained germanium,” *Phys. Rev. B*, vol. 29, no. 6, p. 2970, 1984.

[83] L. M. Sander and D. Fairobent, “Mott transition of the electron-hole liquid in Ge,” *Solid State Commun.*, vol. 20, p. 631, 1976.

[84] F. Binet, J. Duboz, J. Off, and F. Scholz, “High-excitation photoluminescence in GaN: Hot-carrier effects and the Mott transition,” *Phys. Rev. B*, vol. 60, no. 7, p. 4715, 1999.

[85] J. Shah, M. Combescot, and A. H. Dayem, “Investigation of exciton-plasma mott transition in Si,” *Phys. Rev. Lett.*, vol. 38, no. 25, p. 1497, 1977.

[86] H. Schweizer, A. Forchel, A. Hangleiter, S. Schmitt-Rink, J. P. Löwenau, and H. Haug, "Ionization of the direct-gap exciton in photoexcited germanium," *Phys. Rev. Lett.*, vol. 51, no. 8, p. 698, 1983.

[87] S. Schmitt-Rink, D. Chemla, and D. Miller, "Theory of transient excitonic optical nonlinearities in semiconductor quantum-well structures," *Phys. Rev. B*, vol. 32, no. 10, p. 6601, 1985.

[88] R. Zimmermann, "Nonlinear optics and the Mott transition in semiconductors," *Phys. status solidi*, vol. 146, no. 1, p. 371, 1988.

[89] G. Manzke, D. Semkat, and H. Stolz, "Mott transition of excitons in GaAs-GaAlAs quantum wells," *New J. Phys.*, vol. 14, p. 095002, 2012.

[90] S. Schmitt-Rink, C. Ell, S. Koch, H. Schmidt, and H. Haug, "Subband-level renormalization and absorptive optical bistability in semiconductor multiple quantum well structures," *Solid State Commun.*, vol. 52, no. 2, p. 123, 1984.

[91] G. Rossbach, J. Levrat, G. Jacopin, M. Shahmohammadi, J.-F. Carlin, J.-D. Ganière, R. Butté, B. Deveaud, and N. Grandjean, "High-temperature Mott transition in wide-band-gap semiconductor quantum wells," *Phys. Rev. B*, vol. 90, p. 201308(R), 2014.

[92] C. Ciuti, V. Savona, C. Piermarocchi, A. Quattropani, and P. Schwendimann, "Role of the exchange of carriers in elastic exciton-exciton scattering in quantum wells," *Phys. Rev. B*, vol. 58, p. 7926, 1998.

[93] S. Utsunomiya, L. Tian, G. Roumpos, C. W. Lai, N. Kumada, T. Fujisawa, M. Kuwata-Gonokami, A. Löffler, S. Höfling, A. Forchel, and Y. Yamamoto, "Observation of Bogoliubov excitations in exciton-polariton condensates," *Nat. Phys.*, vol. 4, p. 700, 2008.

[94] L. Kappei, J. Szczytko, F. Morier-Genoud, and B. Deveaud, "Direct observation of the Mott transition in an optically excited semiconductor quantum well," *Phys. Rev. Lett.*, vol. 94, p. 147403, 2005.

[95] S. Wachter, M. Maute, H. Kalt, and I. Galbraith, "Coherent exciton interactions: Dependence on excitation fluence and polarization," *Phys. Rev. B*, vol. 65, p. 205314, 2002.

[96] M. G. A. Bernard and G. Duraffourg, "Laser Conditions in Semiconductors," *Phys. status solidi*, vol. 1, no. 7, p. 699, 1961.

[97] F. Kreller, M. Lowisch, J. Puls, and F. Henneberger, "Role of biexcitons in the stimulated emission of wide-gap II-VI quantum wells," *Phys. Rev. Lett.*, vol. 75, no. 12, p. 2420, 1995.

[98] N. Cain, M. O'Neill, J. Nicholls, T. Stirner, W. Hagston, and D. Ashenford, "Photoluminescence of CdTe/CdMnTe multiple quantum wells excited near the Mott transition," *J. Lumin.*, vol. 75, p. 269, 1997.

[99] J. Singh, D. Birkedal, V. Lyssenko, and J. Hvam, “Binding energy of two-dimensional biexcitons,” *Phys. Rev. B*, vol. 53, no. 23, p. 15909, 1996.

[100] S. Ben-Tabou de Leon and B. Laikhtman, “Mott transition, biexciton crossover, and spin ordering in the exciton gas in quantum wells,” *Phys. Rev. B*, vol. 67, p. 235315, 2003.

[101] G. Brown, I. Blewett, I. Galbraith, A. Kar, and B. Wherrett, “Observation of exciton-energy renormalization by the biexciton gas in semiconductors,” *Phys. Rev. B*, vol. 63, p. 081201, 2001.

[102] M. Kuno, *Introductory nanoscience: Physical and chemical concepts.* Garland Science, 1st ed., 2011.

[103] P. T. Landsberg, “Electron Interaction Effects on Recombination Spectra,” *Phys. status solidi*, vol. 15, no. 2, p. 623, 1966.

[104] A. Selloni, S. Modesti, and M. Capizzi, “Luminescence line-shape analysis of the electron-hole plasma in direct-gap Ga-Al-As: Random-phase-approximation approach,” *Phys. Rev. B*, vol. 30, no. 2, p. 821, 1984.

[105] B. Deveaud, F. Clérot, A. Regreny, and K. Fujiwara, “Radiative properties of a highly excited quantum well,” *Superlattices Microstruct.*, vol. 58, no. 14, p. 85, 1990.

[106] M. Asada, “Intraband relaxation time in quantum well lasers,” *IEEE J. Quantum Electron.*, vol. 25, no. 9, p. 2019, 1989.

[107] E. Feltin, D. Simeonov, J. F. Carlin, R. Butté, and N. Grandjean, “Narrow UV emission from homogeneous GaN/AlGaN quantum wells,” *Appl. Phys. Lett.*, vol. 90, p. 021905, 2007.

[108] P. Corfdir, J. Levrat, G. Rossbach, R. Butté, E. Feltin, J. F. Carlin, G. Christmann, P. Lefebvre, J.-D. Ganière, N. Grandjean, and B. Deveaud-Plédran, “Impact of biexcitons on the relaxation mechanisms of polaritons in III-nitride based multiple quantum well microcavities,” *Phys. Rev. B*, vol. 85, p. 245308, 2012.

[109] D. Birkedal, J. Singh, V. Lyssenko, J. Erland, and J. Hvam, “Binding of Quasi-Two-Dimensional Biexcitons,” *Phys. Rev. Lett.*, vol. 76, no. 4, p. 672, 1996.

[110] J. Haynes, “Experimental observation of the excitonic molecule,” *Phys. Rev. Lett.*, vol. 17, no. 16, p. 860, 1966.

[111] J. C. Kim, D. R. Wake, and J. P. Wolfe, “Thermodynamics of biexcitons in a GaAs quantum well,” *Phys. Rev. B*, vol. 50, no. 20, p. 15099, 1994.

[112] R. T. Phillips, D. J. Lovering, G. J. Denton, and G. W. Smith, “Biexciton creation and recombination in a GaAs quantum well,” *Phys. Rev. B*, vol. 45, no. 8, p. 4308, 1992.

[113] H. Souma, T. Goto, T. Ohta, and M. Ueta, “Formation and radiative recombination of free excitonic molecule in CuCl by ruby laser excitation,” *J. Phys. Soc. Japan*, vol. 29, no. 3, p. 697, 1970.

[114] K. Cho, “Emission line shapes of exciton molecules in direct and indirect gap materials,” *Opt. Commun.*, vol. 8, no. 4, p. 412, 1973.

[115] H. W. Yoon, D. R. Wake, J. P. Wolfe, and H. Morkoç, “In-plane transport of photoexcited carriers in GaAs quantum wells,” *Phys. Rev. B*, vol. 46, no. 20, p. 13461, 1992.

[116] B. Deveaud, F. Clérot, N. Roy, K. Satzke, B. Sermage, and D. Katzer, “Enhanced radiative recombination of free excitons in GaAs quantum wells,” *Phys. Rev. Lett.*, vol. 67, no. 17, p. 2355, 1991.

[117] B. Deveaud, F. Clérot, A. Regreny, K. Fujiwara, K. Mitsunaga, and J. Ohta, “Capture of photoexcited carriers by a laser structure,” *Appl. Phys. Lett.*, vol. 55, no. 25, p. 2646, 1989.

[118] H. Reinholz, “Mott effect for an electron–hole plasma in a two-dimensional structure,” *Solid State Commun.*, vol. 123, p. 489, 2002.

[119] N. Ben Brahim Aouani, L. Mandhour, R. Bennaceur, S. Jaziri, T. Amand, and X. Marie, “Thermodynamic equilibrium of screened exciton system by electron-hole plasma in the two-dimensional structure,” *Solid State Commun.*, vol. 108, no. 4, p. 199, 1998.

[120] R. Maezono, P. López Ríos, T. Ogawa, and R. J. Needs, “Excitons and biexcitons in symmetric electron-hole bilayers,” *Phys. Rev. Lett.*, vol. 110, p. 216407, 2013.

[121] D. S. Citrin, “Radiative lifetimes of excitons in quantum wells: Localization and phase-coherence effects,” *Phys. Rev. B*, vol. 47, no. 7, p. 3832, 1993.

[122] R. T. Phillips, G. C. Nixon, T. Fujita, M. Y. Simmons, and D. A. Ritchie, “Excitonic trions in undoped GaAs quantum wells,” *Solid State Commun.*, vol. 98, no. 4, p. 287, 1996.

[123] D. Chemla, D. Miller, P. Smith, A. Gossard, and W. Wiegmann, “Room temperature excitonic nonlinear absorption and refraction in GaAs/AlGaAs multiple quantum well structures,” *IEEE J. Quantum Electron.*, vol. 20, no. 3, p. 265, 1984.

[124] M. Colocci, M. Gurioli, and A. Vinattieri, “Thermal ionization of excitons in GaAs/AlGaAs quantum well structures,” *J. Appl. Phys.*, vol. 68, no. 6, p. 2809, 1990.

[125] K. Korona, “Erratum: Dynamics of excitonic recombination and interactions in homoepitaxial GaN [Phys. Rev. B 65, 235312 (2002)],” *Phys. Rev. B*, vol. 66, p. 235312, 2002.

[126] T. Guillet, C. Brimont, P. Valvin, B. Gil, T. Bretagnon, F. Mdard, M. Mihailovic, J. Zuniga-Prez, M. Leroux, F. Semond, and S. Bouchoule, “Laser emission with excitonic gain in a ZnO planar microcavity,” *Appl. Phys. Lett.*, vol. 98, p. 211105, 2011.

[127] G. Finkelstein, H. Shtrikman, and I. Bar-Joseph, “Mechanism of shakeup processes in the photoluminescence of a two-dimensional electron gas at high magnetic fields,” *Phys. Rev. B*, vol. 56, no. 16, p. 10326, 1997.

[128] P. O. Holtz, Q. X. Zhao, B. Monemar, M. Sundaram, J. L. Merz, and A. C. Gossard, “Shake-up intersubband processes in quantum-well luminescence,” *Phys. Rev. B*, vol. 50, no. 7, p. 4439, 1994.

[129] P. Corfdir, J. Levrat, A. Dussaigne, P. Lefebvre, H. Teisseyre, I. Grzegory, T. Suski, J.-D. Ganière, N. Grandjean, and B. Deveaud-Plédran, “Intrinsic dynamics of weakly and strongly confined excitons in nonpolar nitride-based heterostructures,” *Phys. Rev. B*, vol. 83, p. 245326, 2011.

[130] F. Della Sala, A. Di Carlo, P. Lugli, F. Bernardini, V. Fiorentini, R. Scholz, and J. M. Jancu, “Free-carrier screening of polarization fields in wurtzite GaN/InGaN laser structures,” *Appl. Phys. Lett.*, vol. 74, no. 14, p. 2002, 1999.

[131] X. F. He, “Excitons in anisotropic solids: The model of fractional-dimensional space,” *Phys. Rev. B*, vol. 43, no. 3, p. 2063, 1991.

[132] S. Schmitt-Rink and C. Ell, “Excitons and electron-hole plasma in quasi-two-dimensional systems,” *J. Lumin.*, vol. 30, p. 585, 1985.

[133] H. Y. Ryu, D. S. Shin, and J. I. Shim, “Analysis of efficiency droop in nitride light-emitting diodes by the reduced effective volume of InGaN active material,” *Appl. Phys. Lett.*, vol. 100, p. 131109, 2012.

[134] E. F. Schubert and J. K. Kim, “Solid-state light sources getting smart.,” *Sci. (New York)*, vol. 308, no. 5726, p. 1274, 2005.

[135] J. Cho, E. F. Schubert, and J. K. Kim, “Efficiency droop in light-emitting diodes: Challenges and countermeasures,” *Laser Photon. Rev.*, vol. 7, no. 3, p. 408, 2013.

[136] J. Piprek, “Efficiency droop in nitride-based light-emitting diodes,” *Phys. status solidi*, vol. 207, no. 10, p. 2217, 2010.

[137] S. Albert, A. Bengoechea-Encabo, X. Kong, M. A. Sanchez-Garcia, E. Calleja, and A. Trampert, “Monolithic integration of InGaN segments emitting in the blue, green, and red spectral range in single ordered nanocolumns,” *Appl. Phys. Lett.*, vol. 102, p. 181103, 2013.

[138] A. Waag, X. Wang, S. Fündling, J. Ledig, M. Erenburg, R. Neumann, M. Al Suleiman, S. Merzsch, J. Wei, S. Li, H. H. Wehmann, W. Bergbauer, M. Straß burg, A. Trampert, U. Jahn, and H. Riechert, “The nanorod approach: GaN NanoLEDs for solid state lighting,” *Phys. status solidi*, vol. 8, no. 7-8, p. 2296, 2011.

[139] A. Laubsch, W. Bergbauer, M. Sabathil, M. Strassburg, H. Lugauer, M. Peter, T. Meyer, G. Brüderl, J. Wagner, N. Linder, K. Streubel, and B. Hahn, "Luminescence properties of thick InGaN quantum-wells," *Phys. status solidi*, vol. 6, no. S2, p. S885, 2009.

[140] M. J. Cich, R. I. Aldaz, A. Chakraborty, A. David, M. J. Grundmann, A. Tyagi, M. Zhang, F. M. Steranka, and M. R. Krames, "Bulk GaN based violet light-emitting diodes with high efficiency at very high current density," *Appl. Phys. Lett.*, vol. 101, p. 223509, 2012.

[141] M. Maier, K. Köhler, M. Kunzer, W. Pletschen, and J. Wagner, "Reduced nonthermal rollover of wide-well GaInN light-emitting diodes," *Appl. Phys. Lett.*, vol. 94, p. 041103, 2009.

[142] N. F. Gardner, G. O. Müller, Y. C. Shen, G. Chen, S. Watanabe, W. Götz, and M. R. Krames, "Blue-emitting InGaN-GaN double-heterostructure light-emitting diodes reaching maximum quantum efficiency above 200 A cm2," *Appl. Phys. Lett.*, vol. 91, p. 243506, 2007.

[143] D. S. Meyaard, Q. Shan, J. Cho, E. Fred Schubert, S. H. Han, M. H. Kim, C. Sone, S. Jae Oh, and J. Kyu Kim, "Temperature dependent efficiency droop in GaInN light-emitting diodes with different current densities," *Appl. Phys. Lett.*, vol. 100, p. 08106, 2012.

[144] C. S. Xia, Z. M. Simon Li, Z. Q. Li, Y. Sheng, Z. H. Zhang, W. Lu, and L. W. Cheng, "Optimal number of quantum wells for blue InGaN/GaN light-emitting diodes," *Appl. Phys. Lett.*, vol. 100, p. 263504, 2012.

[145] C. K. Li and Y. R. Wu, "Study on the current spreading effect and light extraction enhancement of vertical GaN/InGaN LEDs," *IEEE Trans. Electron Devices*, vol. 59, no. 2, p. 400, 2012.

[146] G. Verzellesi, D. Saguatti, M. Meneghini, F. Bertazzi, M. Goano, G. Meneghesso, and E. Zanoni, "Efficiency droop in InGaN/GaN blue light-emitting diodes: Physical mechanisms and remedies," *J. Appl. Phys.*, vol. 114, p. 071101, 2013.

[147] H. P. T. Nguyen, K. Cui, S. Zhang, M. Djavid, A. Korinek, G. A. Botton, and Z. Mi, "Controlling electron overflow in phosphor-free InGaN/GaN nanowire white light-emitting diodes," *Nano Lett.*, vol. 12, no. 3, p. 1317, 2012.

[148] H. P. Chen, Y. C. Wen, Y. H. Chen, C. H. Tsai, K. L. Lee, P. K. Wei, J. K. Sheu, and C. K. Sun, "Femtosecond laser-ultrasonic investigation of plasmonic fields on the metal/gallium nitride interface," *Appl. Phys. Lett.*, vol. 97, p. 201102, 2010.

[149] K. J. Vampola, M. Iza, S. Keller, S. P. DenBaars, and S. Nakamura, "Measurement of electron overflow in 450 nm InGaN light-emitting diode structures," *Appl. Phys. Lett.*, vol. 94, p. 061116, 2009.

[150] U. Kaufmann, P. Schlotter, H. Obloh, K. Köhler, and M. Maier, "Hole conductivity and compensation in epitaxial GaN:Mg layers," *Phys. Rev. B*, vol. 62, no. 16, p. 10867, 2000.

[151] T. Oto, R. G. Banal, K. Kataoka, M. Funato, and Y. Kawakami, “100 mW deep-ultraviolet emission from aluminium-nitride-based quantum wells pumped by an electron beam,” *Nat. Photonics*, vol. 4, p. 767, 2010.

[152] K. B. Nam, M. L. Nakarmi, J. Li, J. Y. Lin, and H. X. Jiang, “Mg acceptor level in AlN probed by deep ultraviolet photoluminescence,” *Appl. Phys. Lett.*, vol. 83, no. 5, p. 878, 2003.

[153] J. Hader, J. V. Moloney, B. Pasenow, S. W. Koch, M. Sabathil, N. Linder, and S. Lutgen, “On the importance of radiative and Auger losses in GaN-based quantum wells,” *Appl. Phys. Lett.*, vol. 92, p. 261103, 2008.

[154] K. T. Delaney, P. Rinke, and C. G. Van De Walle, “Auger recombination rates in nitrides from first principles,” *Appl. Phys. Lett.*, vol. 94, p. 191109, 2009.

[155] J. Iveland, M. Piccardo, L. Martinelli, J. Peretti, J. W. Choi, N. Young, S. Nakamura, J. S. Speck, and C. Weisbuch, “Origin of electrons emitted into vacuum from InGaN light emitting diodes,” *Appl. Phys. Lett.*, vol. 105, p. 052103, 2014.

[156] M. Binder, A. Nirschl, R. Zeisel, T. Hager, H. J. Lugauer, M. Sabathil, D. Bougeard, J. Wagner, and B. Galler, “Identification of nnp and npp Auger recombination as significant contributor to the efficiency droop in (GaIn)N quantum wells by visualization of hot carriers in photoluminescence,” *Appl. Phys. Lett.*, vol. 103, p. 071108, 2013.

[157] A. Nirschl, M. Binder, M. Schmid, M. M. Karow, I. Pietzonka, R. Zeisel, M. Sabathil, B. Galler, and D. Bougeard, “Transport and Capture Properties of Auger-Generated High-Energy Carriers in (AlInGa)N Quantum Well Structures,” *arXiv:1504.04734v1*, 2015.

[158] J. Hader, J. V. Moloney, and S. W. Koch, “Density-activated defect recombination as a possible explanation for the efficiency droop in GaN-based diodes,” *Appl. Phys. Lett.*, vol. 96, p. 221106, 2010.

[159] Y. C. Shen, G. O. Mueller, S. Watanabe, N. F. Gardner, A. Munkholm, and M. R. Krames, “Auger recombination in InGaN measured by photoluminescence,” *Appl. Phys. Lett.*, vol. 91, p. 141101, 2007.

[160] A. Laubsch, M. Sabathil, W. Bergbauer, M. Strassburg, H. Lugauer, M. Peter, S. Lutgen, N. Linder, K. Streubel, J. Hader, J. V. Moloney, B. Pasenow, and S. W. Koch, “On the origin of IQE-’droop’ in InGaN LEDs,” *Phys. status solidi*, vol. 6, no. S2, p. S913, 2009.

[161] I. E. Titkov, S. Y. Karpov, A. Yadav, V. L. Zerova, M. Zulonas, B. Galler, M. Strassburg, I. Pietzonka, H.-j. Lugauer, E. U. Rafailov, and S. Member, “Temperature-Dependent Internal Quantum Efficiency of Blue High-Brightness Light-Emitting Diodes,” *IEEE JQE*, vol. 50, no. 11, p. 911, 2014.

[162] J. Piprek, F. Römer, and B. Witzigmann, “On the uncertainty of the Auger recombination coefficient extracted from InGaN / GaN light-emitting diode efficiency droop measurements,” *Appl. Phys. Lett.*, vol. 106, p. 101101, 2015.

[163] S. Karpov, “ABC-model for interpretation of internal quantum efficiency and its droop in III-nitride LEDs: a review,” *Opt. Quantum Electron.*, vol. 47, no. 6, p. 1293, 2015.

[164] Q. Dai, Q. Shan, J. Cho, E. F. Schubert, M. H. Crawford, D. D. Koleske, M. H. Kim, and Y. Park, “On the symmetry of efficiency-versus-carrier-concentration curves in GaInN/GaN light-emitting diodes and relation to droop-causing mechanisms,” *Appl. Phys. Lett.*, vol. 98, p. 033506, 2011.

[165] P. G. Eliseev, M. Osin’ski, H. Li, and I. V. Akimova, “Recombination balance in green-light-emitting GaN/InGaN/AlGaN quantum wells,” *Appl. Phys. Lett.*, vol. 75, no. 24, p. 3838, 1999.

[166] Q. Dai, Q. Shan, J. Wang, S. Chhajed, J. Cho, E. F. Schubert, M. H. Crawford, D. D. Koleske, M. H. Kim, and Y. Park, “Carrier recombination mechanisms and efficiency droop in GaInN/GaN light-emitting diodes,” *Appl. Phys. Lett.*, vol. 97, p. 133507, 2010.

[167] S. F. Chichibu, A. Uedono, T. Onuma, B. A. Haskell, A. Chakraborty, T. Koyama, P. T. Fini, S. Keller, S. P. Denbaars, J. S. Speck, U. K. Mishra, S. Nakamura, S. Yamaguchi, S. Kamiyama, H. Amano, I. Akasaki, J. Han, and T. Sota, “Origin of defect-insensitive emission probability in In-containing (Al,In,Ga)N alloy semiconductors.,” *Nat. Mater.*, vol. 5, p. 810, 2006.

[168] S. Y. Karpov, “Effect of localized states on internal quantum efficiency of III-nitride LEDs,” *Phys. status solidi*, vol. 4, no. 11, p. 320, 2010.

[169] M. V. Kisin, C.-L. Chuang, and H. S. El-Ghoroury, “Effect of active QW population on optical characteristics of polar, semipolar and nonpolar III-nitride light emitters,” *Semicond. Sci. Technol.*, vol. 27, p. 024012, 2012.

[170] M. V. Kisin, C. L. Chuang, and H. S. El-Ghoroury, “Non-equilibrium quantum well populations and active region inhomogeneity in polar and nonpolar III-nitride light emitters,” *J. Appl. Phys.*, vol. 111, p. 103113, 2012.

[171] A. Laubsch, M. Sabathil, J. Baur, M. Peter, and B. Hahn, “High-power and high-efficiency InGaN-based light emitters,” *IEEE Trans. Electron Devices*, vol. 57, no. 1, p. 79, 2010.

[172] O. B. Shchekin, J. E. Epler, T. A. Trottier, T. Margalith, D. A. Steigerwald, M. O. Holcomb, P. S. Martin, and M. R. Krames, “High performance thin-film flip-chip InGaN-GaN light-emitting diodes,” *Appl. Phys. Lett.*, vol. 89, p. 071109, 2006.

[173] A. David and M. J. Grundmann, “Droop in InGaN light-emitting diodes: A differential carrier lifetime analysis,” *Appl. Phys. Lett.*, vol. 96, p. 103504, 2010.

[174] K. Fujiwara, H. Jimi, and K. Kaneda, “Temperature-dependent droop of electroluminescence efficiency in blue (In,Ga)N quantum-well diodes,” *Phys. status solidi*, vol. 6, no. S2, p. S814, 2009.

[175] D. S. Shin, D. P. Han, J. Y. Oh, and J. I. Shim, “Study of droop phenomena in InGaN-based blue and green light-emitting diodes by temperature-dependent electroluminescence,” *Appl. Phys. Lett.*, vol. 100, p. 153506, 2012.

[176] Y. H. Cho, G. H. Gainer, A. J. Fischer, J. J. Song, S. Keller, U. K. Mishra, and S. P. DenBaars, “"S-shaped" temperature-dependent emission shift and carrier dynamics in InGaN/GaN multiple quantum wells,” *Appl. Phys. Lett.*, vol. 73, no. 10, p. 1370, 1998.

[177] H. Schömig, S. Halm, A. Forchel, G. Bacher, J. Off, and F. Scholz, “Probing Individual Localization Centers in an InGaN/GaN Quantum Well,” *Phys. Rev. Lett.*, vol. 92, no. 10, p. 106802, 2004.

[178] T. Langer, H.-G. Pietscher, F. A. Ketzer, H. Jönen, H. Bremers, U. Rossow, D. Menzel, and A. Hangleiter, “S shape in polar GaInN/GaN quantum wells: Piezoelectric-field-induced blue shift driven by onset of nonradiative recombination,” *Phys. Rev. B*, vol. 90, p. 205302, 2014.

[179] T. Fujii, Y. Gao, R. Sharma, E. L. Hu, S. P. DenBaars, and S. Nakamura, “Increase in the extraction efficiency of GaN-based light-emitting diodes via surface roughening,” *Appl. Phys. Lett.*, vol. 84, no. 6, p. 855, 2004.

[180] E. Matioli, S. Brinkley, K. M. Kelchner, S. Nakamura, S. Denbaars, J. Speck, and C. Weisbuch, “Polarized light extraction in m-plane GaN light-emitting diodes by embedded photonic-crystals,” *Appl. Phys. Lett.*, vol. 98, p. 251112, 2011.

[181] F. Bertazzi, M. Goano, and E. Bellotti, “Numerical analysis of indirect Auger transitions in InGaN,” *Appl. Phys. Lett.*, vol. 101, p. 011111, 2012.

[182] M. Shahmohammadi, G. Jacopin, G. Rossbach, J. Levrat, E. Feltin, J.-F. Carlin, J.-D. Ganière, R. Butté, and N. Grandjean, “Biexcitonic molecules survive excitons at the Mott transition,” *Nat. Commun.*, vol. 5, p. 5251, 2014.

[183] R. Vaxenburg, A. Rodina, E. Lifshitz, and A. L. Efros, “The role of polarization fields in Auger-induced efficiency droop in nitride-based light-emitting diodes,” *Appl. Phys. Lett.*, vol. 103, p. 221111, 2013.

[184] Y.-R. Wu, R. Shivaraman, K.-C. Wang, and J. S. Speck, “Analyzing the physical properties of InGaN multiple quantum well light emitting diodes from nano scale structure,” *Appl. Phys. Lett.*, vol. 101, p. 083505, 2012.

[185] X. W. Fu, Z. M. Liao, R. Liu, J. Xu, and D. Yu, “Size-dependent correlations between strain and phonon frequency in individual ZnO nanowires,” *ACS Nano*, vol. 7, no. 10, p. 8891, 2013.

[186] Z.-M. Liao, H.-C. Wu, Q. Fu, X. Fu, X. Zhu, J. Xu, I. V. Shvets, Z. Zhang, W. Guo, Y. Leprince-Wang, Q. Zhao, X. Wu, and D.-P. Yu, “Strain induced exciton fine-structure splitting and shift in bent ZnO microwires,” *Sci. Rep.*, vol. 2, p. 452, 2012.

[187] G. Signorello, E. Lörtscher, P. A. Khomyakov, S. Karg, D. L. Dheeraj, B. Gotsmann, H. Weman, and H. Riel, "Inducing a direct-to-pseudodirect bandgap transition in wurtzite GaAs nanowires with uniaxial stress.," *Nat. Commun.*, vol. 5, p. 3655, 2014.

[188] S. Xu, W. Guo, S. Du, M. M. T. Loy, and N. Wang, "Piezotronic effects on the optical properties of ZnO nanowires," *Nano Lett.*, vol. 12, p. 5802, 2012.

[189] J. Rowe, M. Cardona, and F. Pollak, "Valence band symmetry and deformation potentials of ZnO," *Solid State Commun.*, vol. 6, no. 4, p. 239, 1968.

[190] J. Bardeen and W. Shockley, "Deformation potentials and mobilities in non-polar crystals," *Phys. Rev.*, vol. 80, no. 1, p. 72, 1950.

[191] J. Feng, X. Qian, C. Huang, and J. Li, "Strain-engineered artificial atom as a broad-spectrum solar energy funnel," *Nat. Photonics*, vol. 6, p. 866, 2012.

[192] W. Lambrecht, A. Rodina, S. Limpijumnong, B. Segall, and B. Meyer, "Valence-band ordering and magneto-optic exciton fine structure in ZnO," *Phys. Rev. B*, vol. 65, p. 075207, 2002.

[193] B. Lambert, F. Clerot, B. Deveaud, A. Chomette, G. Talalaeff, A. Regreny, and B. Sermage, "Electron and hole transport properties in GaAs-AlGaAs superlattices," *J. Lumin.*, vol. 44, p. 277, 1989.

[194] S. Haacke, N. T. Pelekanos, H. Mariette, M. Zigone, A. P. Heberle, and W. W. Rühle, "Tunneling dynamics in CdTe/(Cd,Zn)Te asymmetric double-quantum-well structures," *Phys. Rev. B*, vol. 47, no. 24, p. 16643, 1993.

[195] T. Nobis, E. M. Kaidashev, A. Rahm, M. Lorenz, and M. Grundmann, "Whispering gallery modes in nanosized dielectric resonators with hexagonal cross section," *Phys. Rev. Lett.*, vol. 93, no. 10, p. 103903, 2004.

[196] H. Dong, Z. Chen, L. Sun, W. Xie, H. H. Tan, J. Lu, C. Jagadish, and X. Shen, "Single-crystalline hexagonal ZnO microtube optical resonators," *J. Mater. Chem.*, vol. 20, p. 5510, 2010.

[197] A. Trichet, E. Durupt, F. Médard, S. Datta, A. Minguzzi, and M. Richard, "Long-range correlations in a 97% excitonic one-dimensional polariton condensate," *Phys. Rev. B*, vol. 88, p. 121407(R), 2013.

[198] D. M. Hofmann, D. Pfisterer, J. Sann, B. K. Meyer, R. Tena-Zaera, V. Munoz-Sanjose, T. Frank, and G. Pensl, "Properties of the oxygen vacancy in ZnO," *Appl. Phys. A*, vol. 88, p. 147, 2007.

[199] X. Q. Wei, B. Y. Man, M. Liu, C. S. Xue, H. Z. Zhuang, and C. Yang, "Blue luminescent centers and microstructural evaluation by XPS and Raman in ZnO thin films annealed in vacuum, N2 and O2," *Phys. B*, vol. 388, p. 145, 2007.

[200] H. Mariette, “Picosecond spectroscopy in III–V compounds and alloy semiconductors,” *Phys. B+C*, vol. 146, p. 286, 1987.

[201] H. Mariette, J. A. Kash, D. J. Wolford, and A. Marbeuf, “Exciton transfer at low temperature in GaxIn1-xP:N and GaAs1-xPx:N,” *Phys. Rev. B*, vol. 31, no. 8, p. 5217, 1985.

[202] G. Franssen, A. Kamińska, T. Suski, A. Suchocki, K. Kazlauskas, G. Tamulaitis, A. Žukauskas, R. Czernecki, H. Teisseyre, P. Perlin, M. Leszczyński, M. Boćkowski, I. Grzegory, and N. Grandjean, “Observation of localization effects in InGaN/GaN quantum structures by means of the application of hydrostatic pressure,” *Phys. status solidi*, vol. 241, no. 14, p. 3285, 2004.

[203] A. Müller and M. Grundmann, “Tunneling dynamics of excitons in random semiconductor alloys,” *Phys. Rev. B*, vol. 87, p. 035134, 2013.

[204] P. L. Hugon and H. Mariette, “Stochastic transfer of excitations and exhancement of the NN±-pair luminescence in GaP: N,” *Phys. Rev. B*, vol. 30, no. 3, p. 1622, 1984.

[205] A. Miller and E. Abrahams, “Impurity conduction at low concentrations,” *Phys. Rev.*, vol. 120, no. 3, p. 745, 1960.

[206] V. Ambegaokar, B. I. Halperin, and J. S. Langer, “Hopping conductivity in disordered systems,” *Phys. Rev. B*, vol. 4, no. 8, p. 2612, 1971.

[207] M. Oueslati, M. Zouaghi, M. E. Pistol, L. Samuelson, H. G. Grimmeiss, and M. Balkanski, “Photoluminescence study of localization effects induced by the fluctuating random alloy potential in indirect band-gap GaAs1-xPx,” *Phys. Rev. B*, vol. 32, no. 12, p. 8220, 1985.

[208] N. Mott, “The mobility edge since 1967,” *J. Phys. C*, vol. 20, p. 3075, 1987.

[209] G. Jacopin, M. Shahmohammadi, J.-D. Ganière, and B. Deveaud, “Hopping process of bound excitons under an energy gradient,” *Appl. Phys. Lett.*, vol. 104, p. 042109, 2014.

[210] J. Yoo, L. S. Dang, B. Chon, T. Joo, and G.-C. Yi, “Exciton scattering mechanism in a single semiconducting MgZnO nanorod.,” *Nano Lett.*, vol. 12, p. 556, 2012.

[211] A. Einstein, “Über die von der molekularkinetischen Theorie der Wärme geforderte Bewegung von in ruhenden Flüssigkeiten suspendierten Teilchen,” *Ann. Phys.*, vol. 322, p. 549, 1905.

[212] L. Li, N. Lu, M. Liu, and H. Bässler, “General Einstein relation model in disordered organic semiconductors under quasiequilibrium,” *Phys. Rev. B*, vol. 90, p. 214107, 2014.

[213] G. A. Wetzelaer, L. J. A. Koster, and P. W. M. Blom, “Validity of the einstein relation in disordered organic semiconductors,” *Phys. Rev. Lett.*, vol. 107, p. 066605, 2011.

[214] K. Harada, A. G. Werner, M. Pfeiffer, C. J. Bloom, C. M. Elliott, and K. Leo, “Organic homojunction diodes with a high built-in potential: Interpretation of the current-voltage characteristics by a generalized einstein relation,” *Phys. Rev. Lett.*, vol. 94, p. 036601, 2005.

[215] F. Qian, S. Gradečak, Y. Li, C. Y. Wen, and C. M. Lieber, “Core/multishell nanowire heterostructures as multicolor, high-efficiency light-emitting diodes,” *Nano Lett.*, vol. 5, no. 11, p. 2287, 2005.

[216] S. Shevel, R. Fischer, E. Göbel, G. Noll, P. Thomas, and C. Klingshirn, “Picosecond luminescence of excitons localized by disorder in CdSxSe1-x,” *J. Lumin.*, vol. 37, p. 45, 1987.

[217] S. Permogorov, A. Reznitskii, S. Verbin, G. O. Muller, P. Flogel, and M. Nikiforova, “Localized Excitons in CdS1- xSex Solid Solutions,” *Phys. status solidi*, vol. 113, no. 2, p. 589, 1982.

[218] C. Gourdon and P. Lavallard, “Exciton Transfer between Localized States in CdS1-xSex Alloys,” *Phys. status solidi*, vol. 153, no. 2, p. 641, 1989.

[219] E. Cohen and M. D. Sturge, “Fluorescence line narrowing, localized exciton states, and spectral diffusion in the mixed semiconductor CdSxSe1-x,” *Phys. Rev. B*, vol. 25, no. 6, p. 3828, 1982.

[220] B. Arnold, N. Balakrishnan, and H. Nagaraja, *A First Course in Order Statistics.* Philadelphia: Society for Industrial Mathematics, 2008.

[221] S. Rodt, V. Türck, R. Heitz, F. Guffarth, R. Engelhardt, U. Pohl, M. Straß burg, M. Dworzak, A. Hoffmann, and D. Bimberg, “Lateral carrier transfer in CdxZn1-xSe/ZnSySe1-y quantum dot layers,” *Phys. Rev. B*, vol. 67, p. 235327, 2003.

[222] E. F. Schubert and W. T. Tsang, “Photoluminescence line shape of excitons in alloy semiconductors,” *Phys. Rev. B*, vol. 34, no. 4, p. 2991, 1986.

[223] M. Sugawara, “Theory of spontaneous-emission lifetime of Wannier excitons in mesoscopic semiconductor quantum disks,” *Phys. Rev. B*, vol. 51, no. 16, p. 10743, 1995.

[224] T.-J. Yang, R. Shivaraman, J. S. Speck, and Y.-R. Wu, “The influence of random indium alloy fluctuations in indium gallium nitride quantum wells on the device behavior,” *J. Appl. Phys.*, vol. 116, p. 113104, 2014.

# List of Acronyms

| | |
|---|---|
| 0..3D | zero..three-dimensional |
| BE | band-edge |
| BGR | bandgap renormalization |
| BS | beam-splitter |
| CB | conduction band |
| CCD | charge-coupled device |
| CVD | chemical vapor deposition |
| CL | cathodoluminescence |
| cw | continuous wave |
| DADR | density activated defect recombination |
| DH | double-heterostructure |
| EBL | electron barrier layer |
| e-h | electron-hole |
| EHP | electron-hole plasma |
| EQE | external quantum efficiency |
| FWHM | full width at half maximum |
| hh | heavy-hole |
| IQE | internal quantum efficiency |
| IR | infrared |
| JDOS | joint density of states |
| LED | light-emitting diode |
| lh | light-hole |
| LO | longitudinal-optical |
| MBE | molecular beam epitaxy |
| MC | Monte-Carlo |
| MCP | multiple-channel plate |
| MOVPE | metal-organic vapor phase epitaxy |
| MQW | multiple quantum wells |
| MT | Mott-transition |
| MW | microwire |
| NA | numerical aperture |
| NBE | near-band-edge |
| NW | nanowire |
| PL | photoluminescence |
| PLE | PL excitation spectroscopy |
| QCSE | quantum-confined Stark-effect |
| QD | quantum dot |
| QW | quantum well |
| SEM | scanning electron microscopy |
| SP | Schrödinger-Poisson |
| SQW | single quantum well |
| SRH | Shockley-Read-Hall |
| TES | two-electron-satellite |
| tr | time-resolved |
| UV | ultra-violet |
| VB | valence band |
| WGMs | Whispering Gallery modes |
| X | exciton |
| XX | biexciton |
| YAG | yttrium aluminium garnet |

Curriculum vitae

# *Mehran Shahmohammadi*

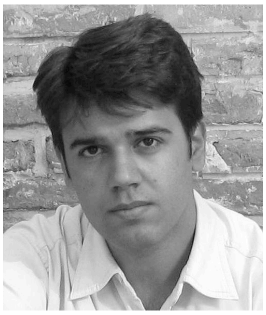

**Address** Rue de Verdeaux 17,
Renens, 1020, Switzerland
**Phone** +41 78 735 53 49
**Mail** mehran.shah@epfl.ch
shahmohammadimehran@gmail.com
**Nationality** Iranian

## EDUCATION

| | |
|---|---|
| 2011-2015 | **PhD in Photonics**,<br>Laboratory of Quantum Optoelectronics (LOEQ), EPFL, Switzerland |
| 2008-2011 | **M.S.E in Electronic (Semiconductor devices)**,<br>University of Tehran (UT), Iran |
| 2004-2008 | **B.S. Electrical Engineering (Electronics)**,<br>University of Tehran (UT), Iran |

## TECHNICAL SKILLS

- **Ultrafast optical spectroscopy:**
  - Cathodoluminescence, streak camera, lasers (pulsed and cw), optoelectronic devices, cryogenics, vacuum techniques, design and realization of setups for optical measurement
- **Clean room processes and microelectronics fabrication:**
  - Silicon micromachining (dry and wet etching)
  - Thin film deposition: RF sputtering, thermal and e-beam evaporation, CVD (RF/DC-PECVD, LPCVD)
  - Standard photo-lithography
  - Electron microscopy
- **Computer skills:**
  - Scientific Programs: C++/C, Matlab, Mathematica, Origin, Labview, Zemax, Sketchup.
  - Hardware Languages: Verilog, Labview, COMSOL, HSPICE, PSPICE.
  - Other Programs: Microsoft Office, LaTex.

## PROJECTS

- **PhD thesis:**
  - Ultrafast optical spectroscopy of wide bandgap semiconductors
  - Exciton transport in the strain gradient fields
  - High injection properties of III-Nitride QWs
  - Investigation into the efficiency of InGaN QWs for blue LEDs
  - Exciton transport in disordered InGaN/GaN QWs in core-shell nanowires
- **Master thesis:**
  - Ion Sensitive Field Effect Transistors (ISFETs) as pH-meters, using nano-porous Si gate
  - Standard fabrication of MOSFETs.

## SELECTED JOURNAL PUBLICATIONS

- *Biexcitonic molecules survive excitons at the Mott transition*
  M. Shahmohammadi, G. Jacopin, G. Rossbach, J. Levrat, E. Feltin, J.-F. Carlin, J.-D. Ganière, R. Butté, N. Grandjean, and B. Deveaud, Nat. Commun. **5**, 5251 (2014).
- *Exciton drift in semiconductors under uniform strain gradients: application to bent ZnO microwires*
  X. Fu, G. Jacopin, M. Shahmohammadi, R. Liu, M. Benameur, J.-D. Ganière, J. Feng, W. Guo, Z.-M. Liao, B. Deveaud, and D. Yu, ACS Nano **8**, 3412 (2014).
- *High-temperature Mott-transition in wide band-gap semiconductor quantum wells*
  G. Rossbach, J. Levrat, G. Jacopin, M. Shahmohammadi, J.-F. Carlin, J.-D. Ganière, R. Butté, B. Deveaud, and N. Grandjean, Phys. Rev. B **90**, 201308 (2014).
- *Hopping process of bound excitons under an energy gradient*
  G. Jacopin, M. Shahmohammadi, J.-D. Ganière, and B. Deveaud, Appl. Phys. Lett. **104**, 042109 (2014).
- *InGaN/GaN core-shell single nanowire light emitting diodes with graphene-based p-contact*
  M. Tchernycheva, P. Lavenus, H. Zhang, a V Babichev, G. Jacopin, M. Shahmohammadi, F. H. Julien, R. Ciechonski, G. Vescovi, and O. Kryliouk, Nano Lett. **14**, 2456 (2014).
- *Label-free detection of DNA hybridization using a porous poly-Si ion-sensitive field effect transistor*
  M. Mahdavi, A. Samaeian, M. Hajmirzaheydarali, M. Shahmohammadi, S. Mohajerzadeh, and M. a. Malboobi, RSC Adv. **4**, 36854 (2014).
- *Temperature-Dependence of Exciton Radiative Recombination in (Al, Ga) N/GaN Quantum Wells Grown on a-Plane GaN Substrates*
  P. Corfdir, A. Dussaigne, H. Teisseyre, T. Suski, I. Grzegory, P. Lefebvre, E. Giraud, M. Shahmohammadi, R. T. Phillips, J.-D. Ganiere, N. Grandjean, and B. Deveaud, Jpn. J. Appl. Phys. **52**, 08JC01 (2013).
- *High performance multilayered nano-crystalline silicon/silicon-oxide light-emitting diodes on glass substrates*
  S. Darbari, M. Shahmohammadi, M. Mortazavi, S. Mohajerzadeh, Y. Abdi, M. Robertson, and T. Morrison, Nanotechnology **22**, 375204 (2011).
- *High-Sensitivity Ion-Selective Field-Effect Transistors Using Nanoporous Silicon*
  N. Zehfroosh, M. Shahmohammadi, and S. Mohajerzadeh, IEEE Electron Device Lett. **31**, 1056 (2010).

## PATENTS

- *High Performance Ion-Selective Field Effect Transistors using Nano-Porous Silicon.*
  S. Mohajerzadeh, **M. Shahmohammadi**, N. Zehfroosh (US. Patent No: US8, 642,371 B2, Feb. 2014)

## HONORS AND AWARDS

- Ranked **2nd** among all master students in electronics at UT (2011).
- Ranked in top **10%** in bachelor among all electrical engineering students at UT (2004-2008).
- Granted engineering scholarship as an **Exceptional Talent Student** at UT (2008).
- Entitled prize "**exceptional performance in teaching**" for experimental physics lab at EPFL (2014).

## TEACHING EXPERIENCES

**Teaching assistant in the following courses:**
Experimental lab of semiconductor lasers, Microelectronics fabrication lab, Clean room access authorization, Electronic II, III, Experimental lab of Electronic I, II, Linear control systems, Engineering mathematics, and DC electric machines.

## LANGUAGE SKILLS

| | |
|---|---|
| • **English** | Full Proficiency |
| • **French** | B1 |
| • **Persian** | Native |
| • **Arabic** | Familiar |

## HOBBIES

| | |
|---|---|
| • **Sport** | Ski, volleyball, horse riding |
| • **Music** | Vocal |
| • **Other** | Painting, cooking, traveling |

## REFERENCES

• Prof. B. Deveaud,
Institute of Condensed Matter Physics,
EPFL, LOEQ, Switzerland,
benoit.deveaud@epfl.ch

• Dr. J.D. Ganiere,
Institute of Condensed Matter Physics,
EPFL, LOEQ, Switzerland,
jean-daniel.ganiere@epfl.ch

• Prof. N. Grandjean
Director, Institute of Condensed Matter Physics
EPFL, LASPE, Switzerland,
nicolas.grandjean@epfl.ch

• Prof. S. Mohajerzadeh,
Director, Institute of Electronic Engineering,
University of Tehran, TFNL, Iran,
mohajer@ut.ac.ir